University of Southampton

Faculty of Medicine

Schools of Cancer Sciences and Human Development and Health

Developing a 3-Dimensional Multicellular Bone Model of Osteosarcoma

by

Hannah Louise Smith

ORCID ID: 0000-0001-7186-1981

Thesis for the degree of Doctor of Philosophy

April 2022

University of Southampton

Abstract

Faculty of Medicine

Schools of Cancer Sciences and Human Development and Health

Doctor of Philosophy

Developing a 3-Dimensional Multicellular Bone Model of Osteosarcoma

by

Hannah Louise Smith

The main treatment for osteosarcoma patients remains a combination of surgery followed by neoadjuvant chemotherapy. The drug Mifamurtide, introduced in 2001, is routinely given concurrently with chemotherapy in the UK, and works by activating macrophages in an inflammatory manner. Unfortunately, there are mixed reviews on the therapeutic benefit of Mifamurtide, and few new drugs and therapies show efficacy in osteosarcoma clinical trials. Greater understanding of the osteosarcoma microenvironment, and the cellular interactions involved in tumour proliferation, could introduce novel targets for future therapies. To explore this a 3D multicellular model of osteosarcoma was developed, replicating some of the cellular interactions of stromal and immune cells in a human bone structure.

A range of stromal, myeloid and osteosarcoma cells were initially characterised in 2D assays for inclusion in the 3D bone model. These included; human bone marrow stromal cells (HBMSCs), macrophages derived from bone marrow and peripheral blood mononuclear cells (PBMCs), as well as two osteosarcoma cell lines, Saos-2 and MG63. The human bone structure of the 3D bone models were made from the femoral head of patients undergoing hip replacement surgery, and were cultured either in conditioned media for 20 days or incubated on the chorioallantoic membrane (CAM) of fertilised chicken eggs. Micro-computed tomography (μCT) and histological techniques were used to validate the 3D bone models; to determine whether bone remodelling occurred, as well as characterising the migration and biological activity of the inserted cells.

Characterisation of the two osteosarcoma cell lines showed distinct differences in tri-lineage differentiation, with Saos-2 cells promoting an osteogenic phenotype and consequently being used in the 3D bone models. Skeletal location also proved to be important in the tri-lineage characterisation of the HBMSCs, with cells isolated from the femoral diaphysis (FD) and femoral epiphysis (FE) demonstrating distinct phenotypes. HBMSCs from the FD were used in the development of the 3D bone models due to the higher osteogenic potential, which is also found in osteosarcoma patients. The third cell type included in the 3D model were monocyte-derived macrophages (MDMs) differentiated from PBMCs, which showed a similar phenotype to human bone marrow-derived macrophages, but could be produced in greater quantities. The Saos-2 cells,

FD HBMSCs and MDMs were introduced into the 3D bone models. Changes in the expression of CD68, CD105 and RANK were found between combinations of the three cell types, as well as those treated with and without Mifamurtide. No significant changes in bone formation or resorption were detected.

In summary, a 3D multicellular bone model of osteosarcoma has been developed that holds the potential to be used to test new drugs and therapies. While further analysis is needed to determine whether the stromal and immune cell interactions replicate those found in the osteosarcoma microenvironment, it has been shown that multiple cell types can be combined in a 3D human bone scaffold, cultured on the CAM and remain viable.

Table of Contents

List of Tables

List of Figures

Research Thesis: Declaration of Authorship

Print name: HANNAH SMITH

Title of thesis: Developing a 3-Dimensional Multicellular Bone Model of Osteosarcoma

I declare that this thesis and the work presented in it are my own and has been generated by me as the result of my own original research.

I confirm that:

1. This work was done wholly or mainly while in candidature for a research degree at this University;
2. Where any part of this thesis has previously been submitted for a degree or any other qualification at this University or any other institution, this has been clearly stated;
3. Where I have consulted the published work of others, this is always clearly attributed;
4. Where I have quoted from the work of others, the source is always given. With the exception of such quotations, this thesis is entirely my own work;
5. I have acknowledged all main sources of help;
6. Where the thesis is based on work done by myself jointly with others, I have made clear exactly what was done by others and what I have contributed myself;
7. Parts of this work have been published as:-

Smith, H.L., et al., *The Role of Pre-Clinical 3-Dimensional Models of Osteosarcoma.* Int J Mol Sci, 2020. **21**(15).

Signature: ..... Date: 12/4/2022

Acknowledgements

I would like to thank my supervisors; Prof Steve Beers, Dr Juliet Gray and Dr Janos Kanczler for their knowledge and support in the development of my PhD, as well as Dr Janos Kanczler's unwavering enthusiasm for all data produced in this thesis.

I would like to thank the Research Histology department, University Southampton Hospital, for performing multiplex immunohistochemistry on osteosarcoma patient samples used in this thesis. I would also like to thank the members of the Antibody and Vaccine group as well as the Bone and Joint group for the support and cake provided during the last three years, and my funders Willberry Wonder Pony charity, without which this project would not have been possible.

Finally I would also like to thank my family, in particular my sister Emma, who supported me throughout my PhD, both emotionally and with quite a lot of free food!

Definitions and Abbreviations

µCT ..... Micro Computed Tomography

2D ..... Two-Dimensional

3D ..... Three-Dimensional

ACAN ..... Aggrecan

ALP ..... Alkaline Phosphatase

ARS ..... Alizarin Red

ATCC ..... American Type Culture Collection

BMP ..... Bone Morphogenetic Protein

BSA ..... Bovine Serum Albumin

CAM ..... Chorioallantoic Membrane

COL1A1 ..... Collagen I

COL2A1 ..... Collagen II

ECM ..... Extracellular Matrix

EDTA ..... Ethylenediaminetetraacetic Acid

FABP4 ..... Fatty Acid Binding Protein 4

FCS ..... Fetal Calf Serum

FD ..... Femoral Diaphysis

FDA ..... Food and Drug Administration

FE ..... Femoral Epiphysis

GFP ..... Green Fluorescent Protein

GM-CSF ..... Granulocyte Macrophage Colony Stimulating Factor

hBMDM ..... Human Bone Marrow-Derived Macrophages

HBMSC ..... Human Bone Marrow Stromal Cell

HDBR ..... Human Developmental Biology Resource

HEMA ..... Poly-hydroxyethyl Methacrylate

HIF ..... Hypoxia Inducible Factors

HTA ..... Human Tissue Act

IFNγ..... Interferon Gamma

IL-4..... Interleukin 4

IL-6..... Interleukin 6

IL-11 ..... Interleukin 11

IL-13 ..... Interleukin 13

L-MTP-PE ..... Liposome Encapsulated Muramyl Tripeptide

LPS ..... Lipopolysaccharide

M-CSF..... Macrophage Colony-Stimulating Factor

MDM..... Monocyte-Derived Macrophages

MSC..... Mesenchymal Stem Cell

NFκB..... Nuclear Factor Kappa-Light-Chain-Enhancer of Activated B Cells

NMR..... Nuclear Magnetic Resonance

NOD ..... Nucleotide-Binding and Oligomerization Domain

NRES..... National Research Ethics Service

OCT ..... Optimal Cutting Temperature

PCW ..... Post Conception Weeks

PDL1..... Programmed Cell Death Ligand 1

PFA..... Paraformaldehyde

PI..... Propidium Iodide

PPARγ..... Peroxisome Proliferator-Activated Receptor γ

RANKL ..... Receptor Activator of Nuclear Factor–κB Ligand

Rb ..... Retinoblastoma

REC..... Research Ethics Committee

Rh ..... Recombinant Human

ROI..... Region of Interest

SOX9..... SRY-Box transcription factor 9

SP7 ..... Osterix

STAT3.....Signal Transducer and Activator of Transcription 3

TAMs .....Tumour Associated Macrophages

TBPf.....Trabecular Pattern Factor

TGFβ.....Transforming Growth Factor Beta

TILs.....Tumour Infiltrating Lymphocytes

TMB.....Tetramethylbenzidine

TRAP.....Tartrate-Resistant Acid Phosphatase

Tregs.....Regulatory T Cells

VEGF.....Vascular Endothelial Growth Factor

ZA.....Zoledronic Acid

Chapter 1 Introduction

1.1 Osteosarcoma

1.1.1 Epidemiology

Cancer is a broad term that covers a wide variety of biologically and genomically diverse tumours. While the molecular characteristics of tumours can differ markedly between different malignancies, they all initiate from genetic mutations that lead to uncontrollable cell growth and proliferation. Factors causing genetic mutation and consequently cancer cell initiation can be split into three groups: aging, hereditary disease and environmental factors. Aging is one of the most widely studied cancer risk factors as there is a strong correlation between an increase in age and cancer initiation. Between 2012 and 2016 54% of all US cancer diagnosis were found in patients over 65 years of age [1]. While age related cancer is heavily linked with accumulation of mutations due from environmental exposures to chemical and physical agents, the aging process itself can also be a cause of cancer initiation. Telomere dysfunction, DNA damage accumulation and mitochondrial dysfunction have all been shown to contribute to the aging process and have been linked to an increased risk of cancer development [1-3]. Hereditary cancer syndrome increases the risk of developing specific tumours from inherited mutations, and accounts for around 5% of all human cancers [4]. In most known hereditary syndromes the increased risk is due to a mutation of a single gene, which is present in every cell of the human body, most often linked with regulation of the cell cycle or repair of DNA damage [4]. The majority of cancer mutations are caused by environmental factors, highlighting the importance of preventing carcinogenic exposures where possible. Many different mutations are caused by environmental factors including man-made risks like smoking, which caused 27% of cancer deaths in 2014 [5], and alcohol consumption, which has been indirectly linked with increasing risk of developing multiple types of cancer [6]. Environmental factors could also come from naturally occurring risks including ultraviolet radiation from sunlight, as well as viral and bacterial infections; together estimated to cause around 20% of all malignancies [7].

Osteosarcoma, although a rare type of cancer, is the most frequent primary bone tumour, and accounts for >10% of all solid tumours in adolescents [8]. The incidence of osteosarcoma is bimodal, with peaks found in adolescent children and in the elderly [9]. Although the aetiology of osteosarcoma is still unknown, evidence suggests that it is a genomically unstable disease with abnormal karyotypes [10, 11]; a relatively high percentage of patients have somatic P53 and Retinoblastoma (Rb) deletions/point mutations [12-15]. A small percentage of osteosarcoma cases have been found in patients with hereditary cancer syndromes, which predispose the carrier to a wide variety of mesenchymal and epithelial cancers [15, 16]. In younger patients,

osteosarcoma most commonly invades the metaphyses of long bones, including the proximal tibia, humerus and distal femur [17]. These tumours have the ability to metastasise, most frequently to the lung [18], which is associated with poorer prognosis. Osteosarcoma has been graded into seven subtypes based on cellular pathology: osteoblastic, fibroblastic, chondroblastic, epithelioid, giant-cell rich, small cell and telangiectatic [19, 20], but due to the low frequency, it is unclear if these subtypes are associated with distinct genetic mutations. 5-year event free survival rates for osteosarcoma are reported to be approximately 50-60%, but are much lower in patients with metastasis, who have a 5-year event free survival rate of 30% [21, 22]. The second peak of incidence of osteosarcoma is found in patients aged 60-85 years. Initially all cases of osteosarcoma in the elderly were considered a secondary neoplasm, occurring at sites of pre-existing bone lesions, including irradiated bone and Paget's disease [17, 23]. However, it has been shown that around 50% of osteosarcoma in the elderly are primary tumours without pre-existing bone disease [23]. Elderly osteosarcoma patients have a higher rate of incidence of tumours in axial skeletal locations, including the skull and pelvis, compared with the appendicular skeletal axis of younger osteosarcoma patients. Unfortunately, the general poor health of elderly patients can limit the use of standard osteosarcoma treatments [23]. This may contribute to the inferior 5-year survival rate in the elderly population, reported to be between 24-40% [17, 24].

1.1.2 Treatment

The majority of patients with osteosarcoma undergo a combination of neoadjuvant chemotherapy followed by surgical resection of the tumour. The first line chemotherapy used to treat osteosarcoma has been largely unchanged for several decades, with the majority of patients receiving regimens consisting of methotrexate, doxorubicin and cisplatin. In 2001 Mifamurtide, an immunomodulating liposome encapsulated muramyl tripeptide (L-MTP-PE), was approved by the US Food and Drug Administration (FDA) [25], and is now used in routine clinical practice as a component of front line therapy. L-MTP-PE is a synthetic derivative of muramyl dipeptide, which is a constituent of bacterial cell walls [26]. It is recognised by multiple signalling molecules including nucleotide-binding and oligomerization domain (NOD)-like receptors present in monocytes and macrophages [27], this then activates the nuclear factor kappa-light-chain-enhancer of activated B cells (NFκB) pathway [28]. Liposome encapsulation promotes phagocytic uptake of the drug by macrophages, which results in the production of pro-inflammatory cytokines and tumoricidal effects [29, 30]. Muramyl dipeptide also activates NLRP3, a component of the inflammasome, which can cause dendritic cell recruitment and polarisation of T-helper cells [31]. Mifamurtide's mechanism of action is proposed to be through its activation of an immune response, similar to that induced during an infection, that can eradicate residual micro metastases which are still present after chemotherapy [32]. Comparative analysis of three cohort evaluations

of osteosarcoma patients treated with Mifamurtide, have shown three-year event free survival increase to between 65-92% [33-36], which while a broad range is an improvement compared with historical data of patients treated with surgery and chemotherapy alone. A randomised control clinical trial comparing chemotherapy with chemotherapy plus Mifamurtide also showed an 18% improvement in the 3-year event free survival [36]. Ongoing clinical trials have also been testing alternative pathways of macrophage activation for use in the clinic, this includes targeting CD47 [37] a protein shown to be overexpressed in osteosarcoma. Blocking of CD47 was reported to inhibit the interaction with macrophage signal regulatory protein α (SIRP α), resulting in phagocytosis of sarcoma cells [38]. Early studies have shown this method could be an effective target for future osteosarcoma treatment.

Several novel osteosarcoma therapeutic agents have undergone recent clinical trials, including bisphosphonates and inhaled Granulocyte Macrophage Colony Stimulating Factor (GM-CSF). Bisphosphonates are routinely used to treat osteoporosis, a degenerative disease, by reducing the degradation of bone through inhibiting the activation of osteoclasts [39]. Given the success of bisphosphonates in osteoporosis, their potential to treat or prevent bone metastases and osteosarcoma has been investigated. Anti-tumour efficacy has been demonstrated *in vitro* and *in vivo*, by the inhibition of proliferation in cancer cells, and consequently inducing apoptosis of the tumour [40, 41], while also enhancing the sensitivity of osteosarcoma cell lines to chemotherapy agents [42]. Early phase clinical trials showed the bisphosphonate Zoledronic acid (ZA) could be safely incorporated with chemotherapy [43, 44]. Unfortunately, recent phase three clinical trials have found that although the addition of ZA improved event free survival [45], it caused a reduction in overall survival, which could have been caused by the significant side effects including hypocalcemia, hypophosphatemia and, importantly, an increase in lung metastases [45, 46].

GM-CSF is a cytokine secreted by leukocytes that stimulates proliferation of multipotent progenitor cells and can be used to upregulate the level of Fas, which is normally downregulated on osteosarcoma metastatic cells [47, 48]. The binding of Fas and Fas ligand, expressed on activated T cells, induces apoptosis. By targeting this, the recurrence rate of osteosarcoma could potentially be reduced. Unfortunately, following promising phase one data [49], a phase two clinical trial using this treatment showed that although there was low toxicity of the drug, only a limited patient benefit was seen, with little to no improvement in overall survival [50]. GM-CSF is in ongoing clinical trials in combination with antibody therapies. Although new therapeutic targets and agents are being continually identified and developed to promote regression and cell death, few have been therapeutically active in osteosarcoma. Therefore, there is an increased need to

understand the growth of osteosarcoma and its microenvironment, in order to produce more robust and active therapies.

1.2 Human Bone and the Osteosarcoma Tumour Microenvironment

1.2.1 Bone

Bone is a major structural component of the human body, and can be classified as cortical or trabecular, with cortical bone being denser than trabecular bone and forming the surface of the skeleton around the medullary cavity [51]. As cortical bone is weight-bearing, it is compact, giving it resistance to bending and torsion. Trabecular bone forms small interconnecting bridges, resulting in a high surface density but low overall size. This spongy textured bone allows for a higher porosity, and is normally found in the epiphysis of long bones [51]. Bone growth and remodelling is predominantly regulated by two cell types, osteoblasts and osteoclasts. Osteoblasts are cuboidal cells that differentiate from mesenchymal stem cells (MSC). During the synthesis of bone matrix, osteoblasts secrete collagen proteins, forming an organic matrix known as the osteoid, which is then mineralised to form bone [52]. When mineralisation occurs some of the remaining osteoblasts are encased, forming small pockets called lacunae, here these osteoblasts differentiate into osteocytes [53]. Connecting all of these osteocyte lacunae are small tunnels know as canaliculi, which allow the transport of signalling molecules and interstitial fluid, important in bone mechanotransduction, as well as regulating both osteoblast and osteoclasts, and consequently bone remodelling [54]. Osteoclasts are multinucleated cells that differentiate from a monocyte/macrophage lineage when in the presence of macrophage colony-stimulating factor (M-CSF) and receptor activator of nuclear factor–κB ligand (RANKL), which can be secreted by osteoblasts, osteocytes and other stromal cells [54]. During bone remodelling osteoclasts are polarized, resulting in rearrangement of the actin cytoskeleton to produce an F-actin ring, sealing the osteoclast to the bone matrix, where it reabsorbs the bone and releases calcium, magnesium and various growth factors [54].

Interleukin-6 (IL-6) is a unique cytokine with many roles, particularly in the immune and central nervous system. It also plays a role in both osteoclast and osteoblast differentiation and activities [55]. IL-6 receptor is expressed on osteoblasts, albeit at low levels and has been shown to enhance differentiation and expression of osteoblastic markers, including alkaline phosphatase (ALP) [55]. IL-6 has also been reported to have an inhibitory effect on osteoblast differentiation, showing apoptotic effects. It has been suggested that the potentially opposing effects of IL-6 on osteoblasts is dependent on their differentiation stage, with immature osteoblasts being stimulated by IL-6, whilst at maturity IL-6 inhibits differentiation to induce an osteocyte phenotype [56]. IL-6 works indirectly on bone resorption by inducing RANKL secretion

consequently regulating osteoclast differentiation. Conversely recent evidence suggests IL-6 can also directly inhibit osteoclast formation, potentially by redirecting osteoclasts towards a macrophage lineage [57].

Bone formation and bone resorption are closely regulated by osteoblasts and osteoclasts respectively, but their function can be altered in the tumour microenvironment [58]. RANKL and other osteoclast stimulating factors, including IL-6 and IL-11, are also secreted by tumour cells in bone metastases [58] and osteosarcoma [59, 60], leading to an increase in bone resorption. This resorption releases growth factors, including transforming growth factor beta (TGFβ) and bone morphogenetic protein (BMP) that interact with the microenvironment to stimulate tumour growth, which in turn stimulates the tumour to induce further bone resorption [61] (**Figure 1-1**). As well as inducing bone resorption, osteosarcoma is pathologically defined by the production of an osteoid matrix by malignant cells, resulting in immature bone formation [62], although the level of osteoid deposition varies greatly between patients [62]. ALP is an enzyme abundant in osteoblasts and can be used as an early marker of osteogenic differentiation [63]. Serum analysis of patients has revealed ALP as a tumour marker with high specificity to osteosarcoma that can even be used for prognosis, as increased ALP at diagnosis has been associated with poorer overall survival [64], although this is not currently used clinically. In the tumour microenvironment IL-6 has been found to inhibit the proliferation of osteosarcoma cells, via the induction of cell cycle inhibitors, through the signal transducer and activator of transcription 3 (STAT3) signalling pathway (IL-6 receptors) [56], but although they can have a potent inhibitory effect directly on the tumour, they are indirectly involved in bone resorption, releasing growth factors which result in tumour proliferation.

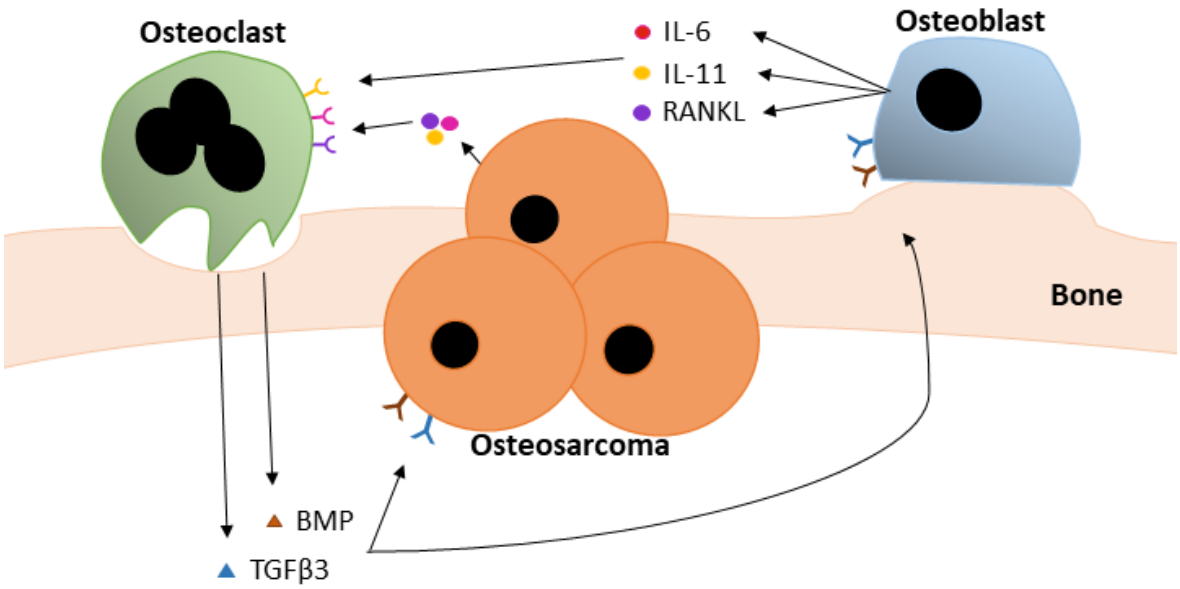

Figure 1-1. Manipulation of bone remodelling in the osteosarcoma microenvironment. *Osteosarcoma cells and osteoblasts both express osteoclast activation stimulating factors including RANKL, IL-6 and IL-11. These bind to receptors on osteoclasts and activate bone resorption. The resorption of bone results in the release of growth factors including BMPs and TGFβ3, stimulating the growth and proliferation of both the tumour and osteoblasts.*

1.2.2 Bone Marrow

Bone marrow is the main component in the medullary cavity of bone, with trabecular bone only accounting for 15% [65]. Bone marrow is routinely separated into two categories, namely 'red' and 'yellow', named by the colouration resulting from their differing phenotype. Nuclear magnetic resonance (NMR) imaging techniques have shown that red bone marrow is composed of approximately 60% haematopoietic cells and 40% adipocytes [65, 66]. Haematopoietic cells are a heterogenous population that allow for the generation of myeloid and lymphoid cells. This includes the differentiation of red blood cells, white blood cells and platelets, important in generating an effective immune system. Haematopoiesis occurs within a stromal cell framework, including endothelial and mesenchymal cells, these cells are important in bone metabolism and have been found to regulate haematopoiesis [67, 68].

In comparison yellow bone marrow is composed of around 95% adipocytes [65, 66], and although their purpose is still not completely understood, there have been data to suggest adipocytes also have a role in metabolism and in regulating haematopoiesis [69, 70]. During aging, red bone marrow, which occupies all bones during fetal development, gradually converts to yellow [65, 66]. In the femur this process starts in the diaphysis and progresses both proximally and distally within the bone (**Figure 1-2**). During adolescence, approximately 11 to 25 years of age, the conversion of

red bone marrow to yellow is still ongoing, meaning areas near the metaphysis and growth plates are in the process of being converted [65]. By adulthood red bone marrow is only found in the proximal metaphysis of the femur [66], although an increase in demand for haematopoietic cells can result in the conversion of yellow to red bone marrow [71], as found in some athletes. As discussed subsequently, the components of red and yellow bone marrow play an important role in tumorigenesis.

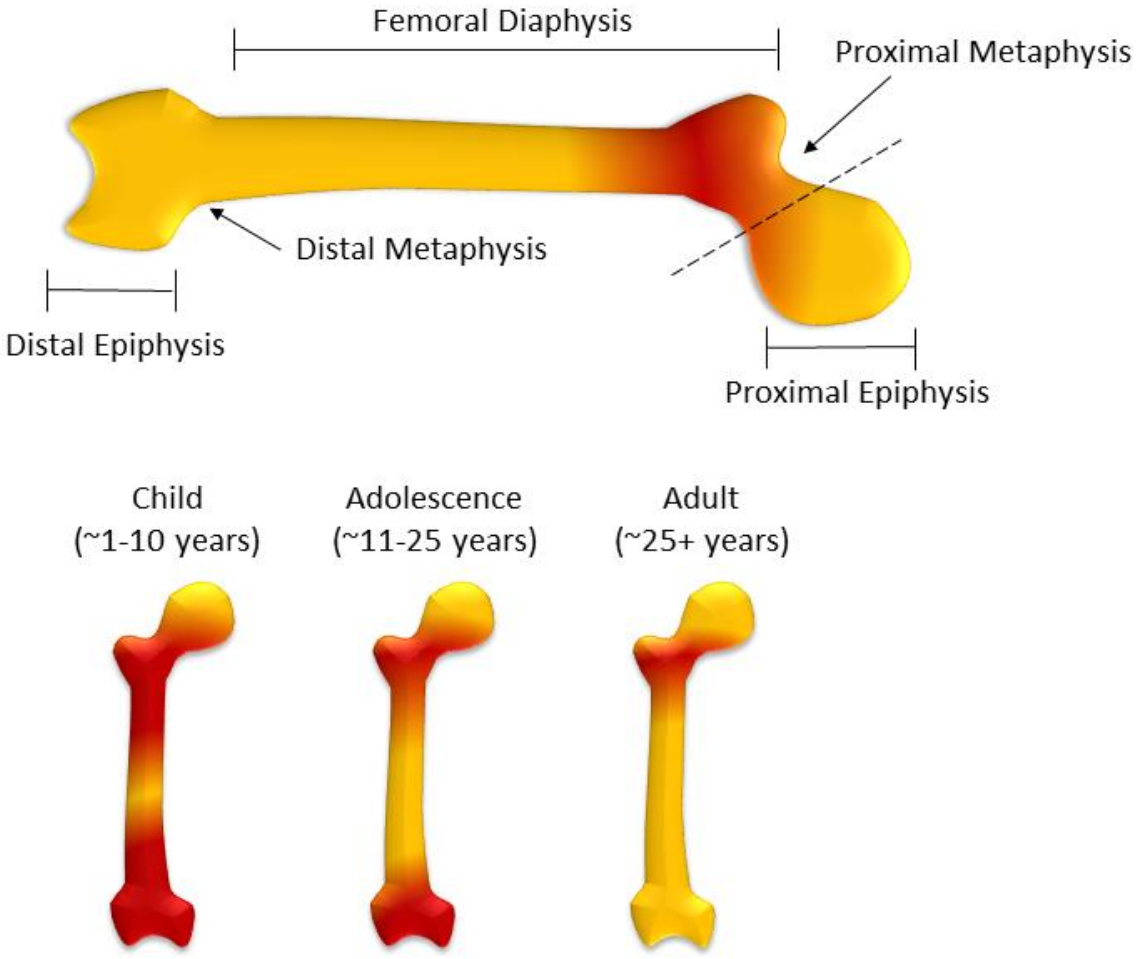

Figure 1-2. The conversion of red bone marrow to yellow bone marrow in the femur*. In long bones, yellow bone marrow conversion starts in the diaphysis and progresses outwards towards the epiphysis. By adulthood (~25+ years) the majority of the femur has converted to yellow bone marrow, except for the proximal metaphysis.*

The cell of origin for osteosarcoma is unclear, with current evidence suggesting it to be located somewhere on the MSC to osteoblast differentiation pathway [20]. Key phenotypic markers to accurately define MSCs have not yet been found, but they are understood to be stem-cell like precursors of important structural cells in bone, including osteoblasts, adipocytes and chondrocytes [72]. MSCs are proposed to be one of the cell types found in human bone marrow

stromal cells (HBMSCs), which are progenitors of skeletal components. HBMSCs are a key element in osteosarcoma, providing a major component of the tumour microenvironment. Stromal cells have been found to inhibit anti-tumour immune responses [73], and are key contributors in the growth and development of many cancers through the promotion of: angiogenesis [74-76], drug resistance [77], and tumour cell migration and metastasis [78] via extracellular matrix (ECM) remodelling. The effect of HBMSCs on osteosarcoma is less well studied, but evidence has shown that stromal cells also enhance migration, metastasis [79] and chemoresistance [80] via IL-6 secretion.

Stromal cells of mesenchymal origin are actively recruited to the osteosarcoma tumour site [80], where they act as if there was an unhealed wound, causing inflammation [81] and inducing the influx of circulating stromal cells into the surrounding tissue. Here they are manipulated by the tumour microenvironment to promote tumour growth, as well as recruit immunosuppressive monocytes, macrophages and regulatory T cells (Tregs) [82, 83]. There is also evidence the stromal cells can impede tumour growth by upregulating soluble factors, inhibiting angiogenesis, as well as inducing apoptosis [84]. It has been suggested that the contradictory evidence of naïve mesenchymal stromal cells in promoting tumour growth or inhibition, could be a result of differing cytokines present in the tumour microenvironment, to which these cells respond accordingly [85]. Mesenchymal stromal cells isolated from osteosarcoma tumours show similar morphology and phenotype to normal tissue derived cells, but they differ in functionality [85]. Tumour associated stromal cells exhibit a greater proliferative capacity and stronger migratory capability than those found in normal tissue [86, 87]. This could be an important target in the development of new treatments for osteosarcoma.

1.2.3 Macrophages

Macrophages are found in tissues throughout the human body. The majority are seeded during embryonic development, classed as tissue resident macrophages and are involved in tissue homeostasis and repair [88]. Other macrophages are derived from monocytes circulating in the blood and are involved with the pro-inflammatory immune response [88]. Macrophages have a wide range of differing phenotypes and characteristics; the extremes of this polarisation spectrum are known as M1-like and M2-like macrophages. In the healthy human body M1-like macrophages are classed as having a more pro-inflammatory phenotype [89], secreting pro-inflammatory cytokines including IL-6 [89], while M2-like macrophages stimulate proliferation and tissue repair [90]. Macrophages have been shown to play key roles in the development of osteosarcoma and other cancers, and are involved in a broad range of functions including regulating metastasis [91]. Macrophages can be actively recruited into the tumour microenvironment [92, 93], where they are then classed as tumour associated macrophages (TAMs). The majority of evidence suggests

TAMS are directly involved in tumour growth, with their presence correlating with metastasis and a poor outcome [94, 95], but there is also contrasting evidence to suggest TAMs act as anti-tumour effectors, with a positive correlation between TAM presence and increased overall survival [96]. TAMs generally express an M2-like phenotype in the majority of cancers, which promote angiogenesis facilitating metastases, and can be linked to poorer prognosis [97, 98]. They can also mediate the immune reaction by inhibiting activation of T cells via the programmed cell death protein 1 (PD-1) receptors, while also secreting chemokines to recruit regulatory T cells [99].

The role of macrophages in osteosarcoma is complex and remains controversial, with different forms of the disease resulting in differing macrophage recruitment and phenotype. TAMs can be recruited by osteosarcoma cells through the release of IL-34, directly ensuring infiltration into the osteosarcoma microenvironment [92]. Similarly, to other cancers, the majority of research shows correlations between an increase of M2-like TAMs with increasing tumour vascularisation and metastasis [95, 100, 101]. Other studies have linked an increase of CD68+ macrophages with the development of metastases but in the same study the number of M2-like macrophages did not change [95]. A higher level of M1-like TAMs have also been associated with non-metastatic form of osteosarcoma compared with the metastatic disease [100]. Figure 1-3 is a schematic representing the differences recorded in M1-like and M2-like TAMs in the osteosarcoma microenvironment.

Osteoclasts differentiate from a monocyte lineage, and can be formed from the fusion of osteal macrophages or from myeloid progenitor cells [102]. Differentiation of osteoclasts can also be regulated by macrophages through the expression of various cytokines, for example; the secretion of IL-10 and IL-4 by M2-like macrophages can inhibit osteoclast differentiation [103, 104]. It has also been found that inflammation in areas of tissue damage, for example bone fractures, leads to a higher infiltration of macrophages, which are known to differentiate into osteoclasts [103]. The interaction of macrophages and osteoclasts in bone cancer isn't very widely studied, but may prove to be a potential target for future therapies.

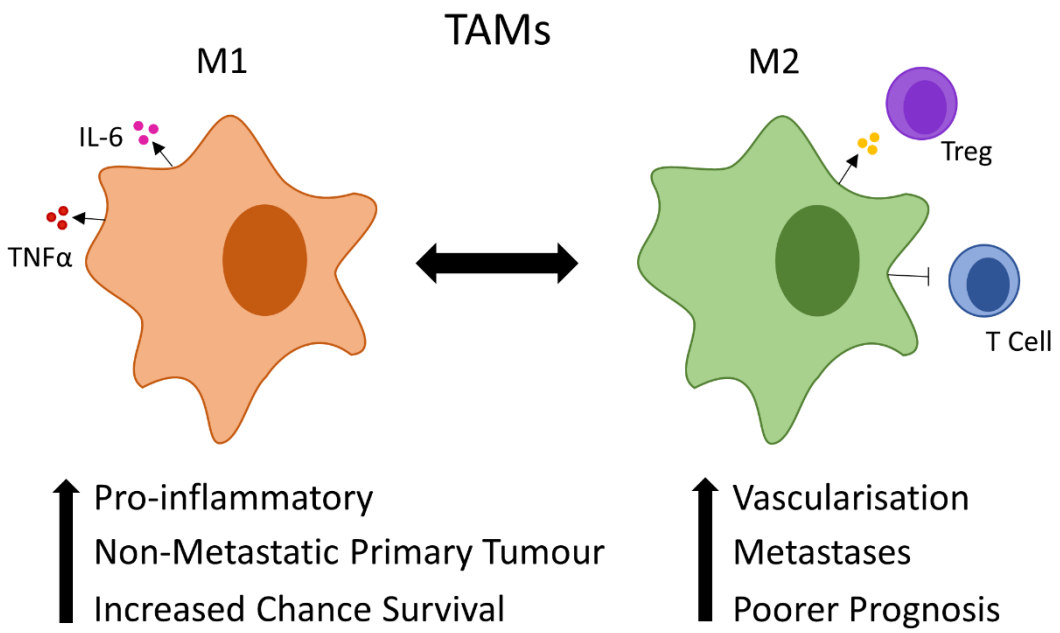

Figure 1-3. M1-like and M2-like TAMs in the tumour microenvironment*. M1-like TAMs secrete pro-inflammatory cytokines including IL-6 and TNFα. Increased numbers of M1-like TAMs have been linked with non-metastatic tumours, correlating with an increased chance of survival. M2-like TAMs secrete cytokines to recruit Tregs, while inhibiting the activation of T cells. They have shown to be increased in metastatic osteosarcoma and correlate with a higher level of vascularisation and a poorer prognosis.*

1.2.4 Lymphocytes

As discussed earlier, bone marrow is an important part of the immune system, with lymphocytes consisting of between 8-20% of all bone marrow mononuclear cells [105]. Lymphocytes are an important part of the osteosarcoma tumour microenvironment (Figure 1-4), which are transported through the bone marrow via blood vessels, and are found throughout the stroma including in follicle-like structures [105]. The interaction of these immune cells with structural bone cells, while in the presence of osteosarcoma is still poorly understood. It has been demonstrated that while cancer cells can recruit immune suppressive cells, including Tregs and TAMs, to the tumour site, they can also manipulate the function of inflammatory immune cells into a tumour-promoting phenotype, facilitating tumour growth [106].

In many cancers, having a higher number of tumour infiltrating lymphocytes (TILs) in the tumour stroma correlates with a better prognosis [107, 108]. Although there is patient variability, multiple studies have found high levels of CD3+ and CD8+ T cells in osteosarcoma samples [109, 110], suggesting osteosarcoma maybe a good target for immunotherapies. Interestingly skeletal location of osteosarcoma has an effect on the level of TIL infiltration, with osteosarcoma of the

jaw showing very low levels [111]. Although high levels of TILs have been found in a number of osteosarcoma patients, most commonly in the femur and tibia [109], there is also a positive correlation with programmed cell death ligand 1 (PDL1) expression on the osteosarcoma cells [112]. PDL1, expressed on the tumour cell surface, binds to PD1, present on CD8+ T cells, and inhibits the immune response [112]. This suggests that although CD8+ T cells are present in the tumour they are potentially being suppressed. Anti-PD1 immunotherapy drugs have been approved for use in the treatment of multiple cancers including melanoma and renal cell cancer [113, 114], and there are ongoing anti-PD1 clinical trials on sarcoma patients. In a phase 2 clinical trial, 5% of bone sarcoma patients treated with pembrolizumab, a PD1 inhibitor, showed an objective response, but this only equated to two patients [115]. Activating the CD8+ T cell response, either alone or in combination with other therapies may be an effective treatment strategy for osteosarcoma.

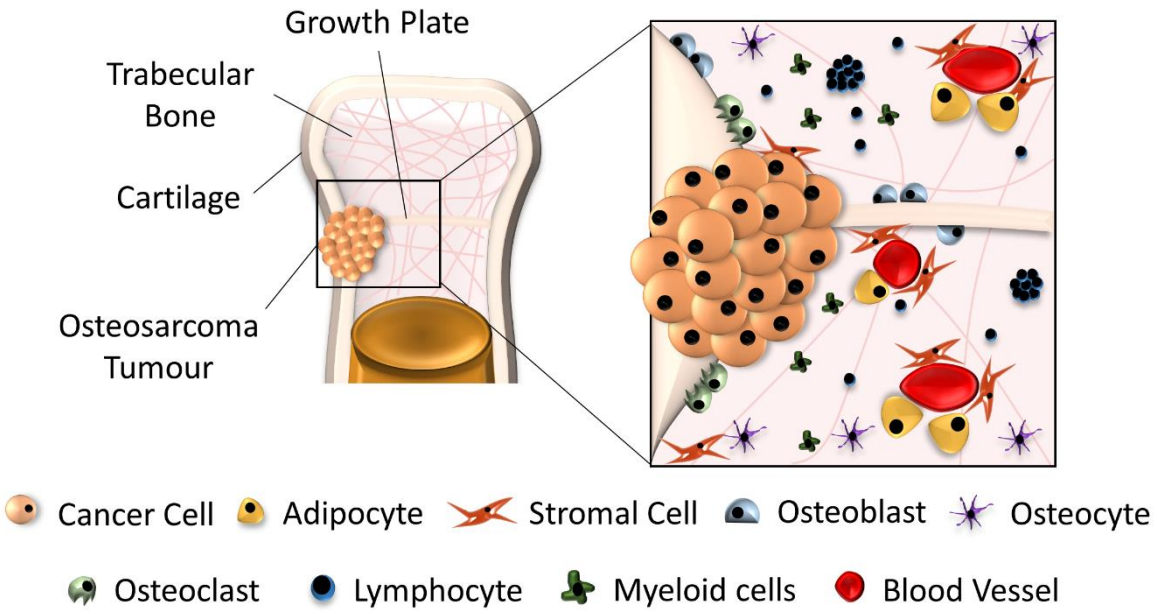

Figure 1-4. Formation of the osteosarcoma microenvironment*. The osteosarcoma microenvironment is a complex arrangement of structural cells, including stromal cells, osteoblasts, osteoclasts, osteocytes and adipose cells, alongside lymphocytes and myeloid immune cells, which are transported through the bone marrow by blood vessels. Osteosarcoma cells routinely form tumours along the growth plate that can protrude from the trabecular bone through the cartilage layer. Adapted from: Smith, H.L., et al., The Role of Pre-Clinical 3-Dimensional Models of Osteosarcoma. Int J Mol Sci, 2020. 21(15).*

1.2.5 Angiogenesis and Hypoxia

Angiogenesis, the formation of blood vessels, is a pivotal step in the progression and development of most cancers including osteosarcoma. Additional nutrients and oxygen are needed as a tumour increases in size, causing the onset of vascularisation. This has led to the generation of anti-angiogenic compounds, including vascular endothelial growth factor (VEGF) inhibitors [116]. VEGF is a key mediator of angiogenesis, both in healthy patients for wound healing, and also for tumour growth. Due to the overstimulation of VEGF production tumour vasculature is functionally and structurally abnormal, with irregularly shaped blood vessels, which can be haemorrhagic [117]. This suboptimal tumour blood supply results in a hypoxic environment as well as inducing further VEGF production [118, 119]. Higher expression of VEGF has also been associated with lower disease-free survival and lower overall survival of osteosarcoma patients [120]. VEGF inhibitors are currently in early clinical trials for osteosarcoma patients, with initial results showing limited responsiveness to these therapies, ending in stable disease rather than tumour regression. These included phase 2 clinical trials of two different small molecule multi-kinase inhibitors; Regorafenib, which showed no significant difference in overall survival of osteosarcoma patients [121], and Sorafenib, which only reached a 6-month progression free survival rate of 45%, less than the pre-specified target [122]. Both drugs target a range VEGF receptors, Regorafenib inhibits VEGF receptors 1-3 while Sorafenib targets VEGF receptors 2-3, alongside other stromal and oncogenic receptor tyrosine kinases. These results have meant few drugs are proceeding to phase 3 clinical trials [122-124].

While hypoxic regions are present in normal healthy bone, particularly around the growth plate [125], high levels of hypoxia in osteosarcoma patients are associated with poor prognosis [126]. Hypoxia inducible factors (HIF) signalling pathway is critical in regulating osteoblastic and vascular niches during cartilage development, with HIF1α regarded as a positive regulator of osteoblast activity and bone formation [127]. HIF1α is also involved with indirectly regulating osteoclast mediated bone resorption by stimulating cytokines and increasing mitochondrial metabolic rate supporting bone resorption [128]. Osteosarcoma normally occurs at the site of a growth plate, known to have pre-existing hypoxic regions, which could facilitate tumour initiation. While chronic hypoxia leads to tumour necrosis, a known factor of osteosarcoma tumours, in the early stages of cancer initiation hypoxia has been shown to inhibit apoptosis [129]. Overexpression of HIFs was significantly linked with poor prognosis and metastatic disease in osteosarcoma patients, presenting a potential therapeutic target [130, 131]. Hypoxic inhibitors have been generated to block hypoxic pathways, either directly or indirectly, and are increasingly being introduced in clinical trials, although they have not yet been used for osteosarcoma patients.

1.3 Pre-Clinical Modelling of Osteosarcoma- 3D Models

Outcomes for osteosarcoma are largely unchanged over several decades and novel therapeutic drug strategies are needed. 2-dimensional (2D) *in vitro* assays have been essential in the field of cancer research; producing novel insights into characterising protein production, cell biology and the tissue morphology of various subsets of cancer [132]. Unfortunately, they have many limitations including that the culture process can induce changes in morphology, as well as cause disruption of cellular and extracellular interactions [132]. With more awareness on the heterogeneity and complexity of the tumour microenvironment, robust and informative 3-dimensional (3D) models are being developed to mimic the cellular interactions found in human osteosarcoma. 3D models offer the potential to better understand micro-environmental interactions. There are a growing number of models including *in vivo*, *in vitro* and *in ovo* 3D models of osteosarcoma.

1.3.1 In Vivo Animal Models

As the origin and pathogenesis of osteosarcoma is still unknown, establishing a robust and representative animal model, that mimics all aspects of the human disease, is challenging. Initial rodent models for osteosarcoma were developed by exposing the tibia to chemical and radioactive carcinogens, which produced histologically accurate tumours and could still be utilised to represent the DNA damaging effect on pathogenesis [133]. Despite the success in generating this model, it does not represent the sporadic and spontaneous generation of this disease in humans, and is not routinely used to represent the aetiology of osteosarcoma [134]. The establishment of immunocompromised mice allowed for inoculation of a variety of human osteosarcoma cell lines; these can be injected subcutaneously, although cell grafts into the femur are considered more therapeutically relevant, as subcutaneous injection only allows for ectopic bone formation. These models have had success in providing insights into osteosarcoma migration, especially as these murine models allows for metastasis [135], and they are a useful tool for screening drugs [136, 137]. The fundamental limitation of this approach is the use of mature osteosarcoma cells, which does not provide information on tumour initiation, although it can be used to study angiogenesis. The lack of a tumour microenvironment before implantation, and a lack of an intact immune system, also means key interactions are lost [138].

The introduction of gene targeting technologies allowed for the development of transgenic mice that spontaneously develop osteosarcoma. There are several genetically modified mouse models for osteosarcoma; most based on the *P53* and *Rb* mutations [134]. Unfortunately, the *Rb* gene is essential for normal mouse development, and *Rb* transgenic mutations alone tend to result in serious defects, making them very hard to breed [139]. Even if these mice reach maturity they do

not tend to develop osteosarcoma [140]. There was more success in *P53* transgenic mice, where spontaneous osteosarcoma development was observed [141], but was accelerated with the combination of *P53* and *Rb* mutations [140, 142], which did not generate the same serious defects as *Rb* alone mutations. Importantly mice with *P53* mutations also developed lymphomas, carcinomas and adenocarcinomas [141, 143], sometimes before the establishment or characterisation of osteosarcoma could occur. Other genes have also been found to have been implicated in osteosarcoma pathogenesis including *c-fos*. Transgenic mice overexpressing the *c-fos* proto-oncogene showed a high level of penetrance and development of bone tumours, but mixed levels of malignancy, along with evidence of other diseases including woven bone and fibrous marrow [144, 145]. While mouse models allow us to gain some insight into the development of osteosarcoma, the high cost and limited representation of human osteosarcoma, means effective and robust alternatives are needed.

In vivo mouse models have advantages over *in vitro* assays, this includes in the investigation of osteosarcoma development and drug efficacy [136, 141]. Mice have a close genetic lineage to humans, and non-immunocompromised mice have a complete immune system. Murine models for osteosarcoma have given further insights into methods of tumour invasion and metastasis, when compared to current *in vitro* and *in ovo* 3D models [135]. Unfortunately, osteosarcoma models generated by injecting cells into the femur is a highly skilled and more costly process than *in vitro* assays. Alternative subcutaneous implantation and grafts are applicable for studying osteosarcoma establishment, but do not replicate the human microenvironment as they lack bone and cartilage [138]. Although mice are genetically similar to humans it has been shown that there are critical differences in cellular, molecular and immunological biology [146], thus also questioning the translation relevance of these models for the human disease.

Canine osteosarcoma is more common than the human equivalent, but it has been shown to be very similar histologically and have parallel genetic features to human osteosarcoma. The primary treatment method for human osteosarcoma, surgery and chemotherapy, is also the main treatment used in canines, which have been found to show a similar level of response [147]. The level of similarity between the two species shows increased relevancy compared to other animal models. Studies into canine osteosarcoma gene expression after chemotherapy, have identified significantly differentiated pathways between non-responders and responders, which were consequently found to be mirrored in human osteosarcoma [148]. Although gene expression pathways in canine osteosarcoma are not always found in human osteosarcoma [149], the frequency of canine osteosarcoma compared with the sporadic, rare nature of human osteosarcoma, as well as the closer histological similarities than mouse models, presents an

increased opportunity to identify further biological and genetic pathways that can impact new therapies and treatments.

1.3.2 In Vitro 3D Models

As an alternative to *in vivo* systems, *in vitro* 3D models have been developed to mimic cellular interactions and understand tumour development. *In vitro* 3D models are broadly separated into two groups, those with a scaffold and those without. 3D models without a scaffold normally entail the formation of spheroids/organoids. One method of looking at spheroid formation of osteosarcoma is using liquid overlays or ultra-low binding plates [150]. The liquid overlay, which can be a type of agar/agarose [151] or poly-hydroxyethyl methacrylate (HEMA) [152], is used to coat the plate, preventing the cells from adhering to the surface of the vessel, enhancing cellular interactions and allowing them to form spheroids. These methods have been used to study how hypoxic changes [153] can increase spheroid adhesion, and how drug responses can differ between spheroids and 2D cultures [152], in both osteosarcoma cell lines and other cancer cell lines. Ultra-low binding plates have been used more extensively to compare differences in chemoresistance of spheroids and monolayer cultures [154]. An alternative scaffold free method is the hanging drop method, this technique utilises gravity to generate multi-cell co-cultures [150], and have been combined and compared with 2D cultures [155] to show that cells grown in the hanging drop technique express increased levels of VEGF, compared with 2D cultures [155]. While these scaffold-free techniques are relatively low cost and have the advantage of being high throughput, they lack a number of components of the tumour microenvironment, including ECM-cell interactions, which influence the formation, and growth of osteosarcoma.

In the bone microenvironment mechanical signals are very important in modulating tumour behaviour [156]. Scaffolds allow for cell adhesion and an added dimension of cell-ECM signalling compared with scaffold-free models. The material selected to form a scaffold must be chosen appropriately to allow for correct, functional environmental signalling. Scaffolds can be made from natural material (collagen, Matrigel, silk), or synthetic (Hydrogel, polyethylene glycol, ceramics) [150, 156]. The hard brittle surface, and mechanical stiffness of ceramic scaffolds exhibit biocompatibility to bone because of their structural similarity [157], and studies have shown osteoblast differentiation and proliferation are enhanced when interacting with ceramic [158], unfortunately the brittleness of the scaffold means it has limited applications [159]. The success of synthetic scaffolds is the flexibility in fabrication and architecture whilst being able to control degradation [160], but in turn some have reduced levels of bioactivity [157]. Natural scaffolds generally have good levels of bioactivity but can show increased levels of degradation [156]. The choice of scaffold will depend on the scientific question, and whether mechanical stiffness or slow degradation is required. A mixture of synthetic and natural scaffolds have been

developed in stem cell research [161] that can overcome some of these disadvantages, but there is a limited amount of published work showing their use with osteosarcoma, especially when co-culturing with other important cell types found in the microenvironment.

The ECM is a major component of the tumour microenvironment, with studies showing that it acts in a pro-tumorigenic capacity, enhancing osteosarcoma cell invasion, with some evidence suggesting it provides a protective niche for drug resistance [162]. This has been studied mainly in 2D *in vitro* assays using multiple components of ECM, including fibroblasts [163] and acellular proteins [162]. There have also been a few 3D models incorporating components of the ECM, including the use of collagen sponges [156] and growth factors [164] to simulate aspects of the tumour microenvironment. The complete and integrated understanding of the osteosarcoma/ECM interaction is important as it makes up a large part of the vascular network, and one of the main limitations of *in vitro* 3D models is the lack of angiogenesis, important in tumour growth.

Innovative *in vitro* 3D models are evolving and becoming translationally relevant, as we understand more about the tumour microenvironment. *In vitro* 3D models can be constructed from components that are completely human derived, using scaffolds to try and replicate structures of the bone [165]. They are generally cost effective with a high-throughput ratio, but the majority do not yet have the complexity to replicate the multicellular interactions attained in osteosarcoma. *In vitro* models are also limited by the lack of published data showing combinations of osteosarcoma cells with other cells found in the bone and cartilage niche and tumour microenvironment. Without the interaction of these cells, we cannot effectively mimic the aetiology in a 3D model. Animal models are able to use the host for processes like angiogenesis and nutrient movement between the tumour and its microenvironment [166]. The continued development of *in vitro* 3D models may compensate for these issues in the future, but overall, these *in vitro* 3D models currently act as more of a bridge between 2D and *in vivo* animal models.

1.3.3 In Ovo Chorioallantoic Membrane Models

The Chorioallantoic membrane (CAM) is a dense vascular network that rapidly develops in a fertilised chicken egg, it is formed 4-5 days after fertilisation by the fusion of the chorion and the allantoic vesicle [166]. Its main role is as a respiratory organ for the embryo, storing waste products and absorbing calcium from the shell [166] (Figure 1-5). The use of the CAM to investigate tumour growth started back in the early 1900's, where Murphy (1913) grew rat sarcoma tumours in CAM models and transplanted them into adult chickens. Here he noted the tumour did not adapt to include avian cells, causing the tumour to be rejected from the adult

chickens [167]. This natural immunodeficiency of the embryo is a unique property of the CAM assay, which allows for in depth phenotypic analysis on the implanted tissue of interest, without the host avian cells rejecting or majorly altering the tissue [168].

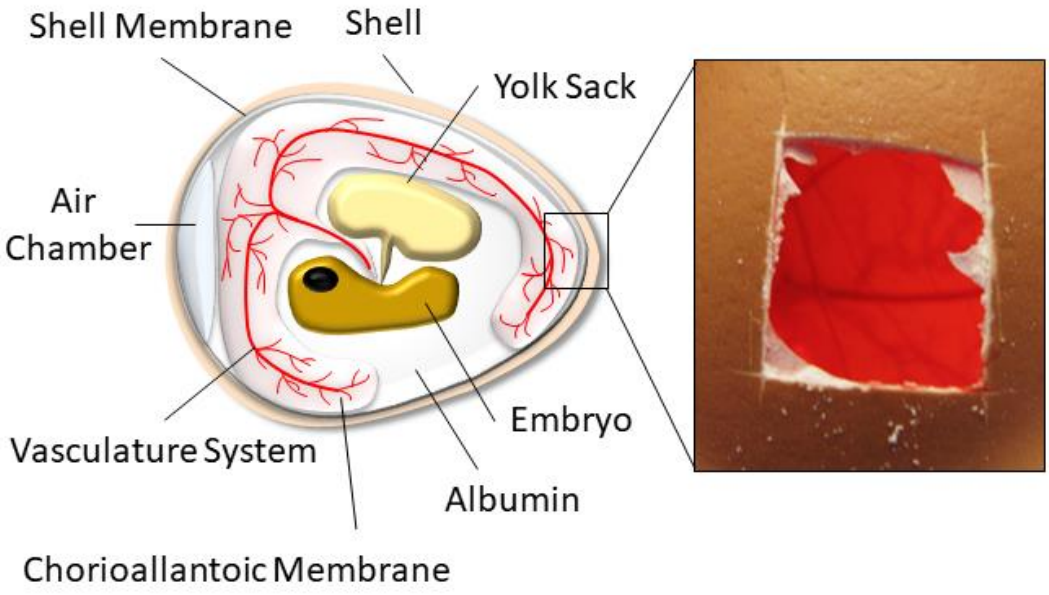

Figure 1-5 Structural composition of a chicken egg*. The CAM is a membrane that covers the inside of the eggshell, where it acts as a respiratory organ for the chick embryo. A window can be made in the shell and a scaffold or sample of interest placed on the CAM. Adapted from: Smith, H.L., et al., The Role of Pre-Clinical 3-Dimensional Models of Osteosarcoma. Int J Mol Sci, 2020. 21(15).*

One of the most important benefits of the CAM model over 2D methods is the ability to study angiogenesis. Angiogenesis promotes the generation of blood vessels, which is important in tumour development [169], thus precise monitoring with and without anti-angiogenic agents could lead to new targets for treating osteosarcoma [166]. Angiogenesis is also important in trying to accurately and robustly replicate the osteosarcoma microenvironment to characterise complete cellular interactions and signalling methods. Although osteosarcoma has not been widely studied in this model, there are many other cancer cell lines that have been studied in the CAM, with and without a support system for implantation, which can include collagen [170] and Matrigel [171] grafts, plastic rings [172] and sponges [173]. These implantation techniques have been used to look at invasion, metastasis, and drug development [170-173].

One of the few osteosarcoma experiments involving the CAM model was by Balke et al (2010) where they implanted eight different osteosarcoma cell lines into the CAM model to compare how the cell line affects tumour development and formation. Of the 8 cell lines only three

(MNNG-HOS, U2OS and Saos-2) formed solid, vascular tumours which were more than 2mm in size [166]. Unfortunately, none of the developed tumours showed osteoid formation that is normally found in the human disease, which could have resulted from a lack of mature bone cells or growth factors in the model. The low cost and ease of purchase allows for a high yield and quick turnover of CAM data, but there is only a short viable timespan of a CAM assay (up to 18 days, 2/3rd gestation). This timespan does not allow for long term studies, which could be key for osteosarcoma establishment.

Using the CAM model could be an effective method to study osteosarcoma. This model uses the blood vasculature of the chicken embryo for tumour growth and development [174], known to develop at a faster rate than other models. The lymphatic and vascular system is also present in mouse models, but compared with mouse models the CAM models are much more cost effective and easier to use [174-176]. As well as an inexpensive, easy to use tumour model, the CAM also allows researchers to look at cell-to-cell interactions and metastasis. Current studies of osteosarcoma are limited to cells in sponges or being implanted directly onto the CAM. Combining osteosarcoma cell lines with other cells in the microenvironment, most notably structural bone, could give a better insight into these processes and interactions. There are recent studies that have shown that bone regeneration is possible in the CAM model, Moreno-Jiménez et al (2018) successfully implanted bone cylinders onto the CAM resulting in bone growth, osteoid deposition, angiogenesis and the generation of mineralised tissue [177]. Further research that introduces osteosarcoma and pro-tumour immune cells into this bone regeneration model could gain a novel insight into effectively replicating the tumour microenvironment.

1.4 Summary

The main treatment methods for osteosarcoma patients remain a combination of surgery and chemotherapy, which has not changed since the late 1970s. The exception to this is the incorporation of the drug Mifamurtide, which has been shown to activate monocytes and macrophages to establish an inflammatory immune reaction, enabling phagocytosis of the remaining tumour cells. Unfortunately, systemic reviews are still comparing the effectiveness of this treatment, indicating an urgent need for more therapeutic targets and therapies to treat osteosarcoma patients. Further understanding of the complex tumour microenvironment is needed to develop new drugs and therapies. To achieve this goal research strategies have sought to develop both 2D and 3D models to mimic these cellular interactions. While there is currently limited research developing *in vitro* 3D models, including the use of scaffolds in osteosarcoma research, more work has been published regarding *in vivo* mouse models.

While osteosarcoma mouse models mimic the human tumour microenvironment in terms of vascularisation and immune response, the successful incorporation of osteosarcoma cells into bone remains a difficult method to establish and repeat. With subcutaneous osteosarcoma formation lacking the ability to form bone ectopically. The CAM model can also mimic vascularisation while being cheaper, less time consuming and less technically demanding. The CAM model has been used to study both cancer and bone regeneration using various biomaterials. This potentially makes it a better method for developing a 3D model to replicate cellular interactions of the human osteosarcoma microenvironment, as well as clinical response to drugs and therapies.

To date no study has yet described the use of human bone to develop a 3D multicellular model of osteosarcoma, with few researchers comparing the interactions of structural, stromal and immune cells. Thus, a human bone derived model would offer a more clinically relevant osteosarcoma microenvironment to examine cellular interactions. In addition, the use of the CAM assay as a surrogate blood supply would permit the study of osteosarcoma interactions in the context of angiogenesis, not found on other *in vitro* 3D models. This could have critical impact as it would provide a vascular 3D model, negating the use of mouse models, an ethical obligation in animal research (applying the 3Rs: replacement, reduction and refinement), while ultimately being used to test new drugs and therapies.

The ultimate aim of the project was to develop a 3D multicellular model of osteosarcoma, for preclinical research in cellular interactions of the tumour microenvironment. To achieve this, the study aimed to assess the interaction of three cell types; HBMSCs, macrophages and osteosarcoma cells, in a 3D model made from human living bone, collected from waste surgical material after total hip replacements. This was carried out using both long term culture methods with supplemented media, alongside the incubation on the CAM to establish vascularisation. To validate this model in its ability to replicate the human osteosarcoma microenvironment, both µCT analysis and histological analysis were carried out, assessing the level of bone formation and resorption as well as biological interactions.

1.5 Hypothesis

It is possible to engineer a functional human 3D model that mimics aspects of the osteosarcoma tumour microenvironment, including HBMSC and macrophage interactions that can be used to test new therapeutic approaches.

Research Objectives:

1. To characterise the functional interaction of human bone stromal cells and osteosarcoma cells in 2D culture models.
    - Compare the tri-lineage ability of HBMSCs from different skeletal locations of the human femur, including osteogenic, adipogenic and chondrogenic differentiation.
    - Compare the tri-lineage ability of different osteosarcoma cell lines.
    - Characterise the interaction of HBMSCs with an osteosarcoma cell line in a transwell assay.

2. To optimise the differentiation of monocyte-derived macrophages for incorporation in the 3D bone model.
    - Characterise macrophages differentiated from human bone marrow and PBMCs.
    - Characterise polarized macrophages differentiated from human bone marrow and PBMCs.
    - Compare differentiation and activation of osteoclasts derived from human bone marrow and PBMCs.

3. To develop the CAM assay as an *in ovo* 3D human bone model to investigate the role of cellular and extracellular matrix interaction in the development of osteosarcoma.
    - Optimise the production of 3D multicellular bone models for the CAM assay
    - Quantify structural changes, both bone formation and resorption, occurring in the bone model using µCT.
    - Quantify biological changes occurring in the bone model using histological methods.
    - Examine the potential of these models to test new drugs and therapies for the treatment of osteosarcoma.
    - Compare the resulting biological interactions in the 3D bone models against human osteosarcoma samples.

Chapter 2 Methodology

2.1 Ethical Approval

Ethical approval for using human leukocyte cones was obtained by the University Southampton Hospital NHS Foundation Trust from the East of Scotland Research Ethics Committee (REC reference 16/ES/0048). Informed patient consent was obtained in alignment with the Declaration of Helsinki.

Ethical approval for the use of bone marrow and femoral head samples were approved by an NHS Research ethics committee (NRES number: 18/NM/0231).

Human fetal tissue sent from the research bank of the Human Developmental Biology Resource (HDBR) at the University of Newcastle: age range from 9 to 18 post conception weeks (PCW). This is an ethically approved tissue bank. (REC reference: 18/NE/0290, IRAS project ID: 250012).

Ten osteosarcoma patient samples were taken at diagnosis after obtaining informed consent, and were processed by NHS Trust accredited pathology laboratories according to a standard protocol, before being deposited to the Human Tissue Act (HTA) licensed CCLG UK Tissue Bank for research use.

All egg CAM procedures were carried out in accordance with the guidelines and regulations stipulated in the Animals (Scientific Procedures) Act, UK 1986. The chick embryo CAM model was under Home Office Project license (P3E01C456).

2.2 Cell Culture

2.2.1 Cell Lines

Cancer cell lines Saos-2, MG63 (osteosarcoma) and SKBR3 (breast cancer), all obtained from the American Type Culture Collection (ATCC, US), were grown in basal media, see . Frozen cryo-vials, stored in liquid Nitrogen, were thawed in a 37^{o}C water bath and re-suspended in 10 ml of warm basal media. The cells were centrifuged at 161 g for 5 minutes, and the cell pellet was re-suspended in basal media. The cells were then seeded into a T25 or T75 flask (Corning, UK) and cultured in a humidified incubator at 37^{o}C with 5% CO_2. Cells were re-suspended in fresh media twice a week and seeded into flasks between $1x10^5$ to $6x10^5$ cells per ml.

Table 2-1. Media and Supplements

Name	Media	Supplements
Basal	αMEM	10% (v/v) fetal calf serum (FCS), 1% (v/v) P/S (100 U/ml Penicillin +100 µg/ml Streptomycin)
Osteogenic I	αMEM	10% (v/v) FCS+1% (v/v) P/S +100 µM ascorbate acid 2-phosphate (Sigma, UK) + 10 nM dexamethasone (Sigma, UK)
Osteogenic II	αMEM	10% (v/v) FCS +1% (v/v) P/S + 50 µM Ascorbic acid 2-phosphate + 10 nM Vitamin D3 (Sigma, UK)
Mineralisation	αMEM	10% (v/v) FCS +1% (v/v) P/S + 50 µM Ascorbic acid 2-phosphate + 10 nM Dexamethasone + 2 mM Beta-Glycerol phosphate (Sigma, UK)
Adipogenic	αMEM	10% (v/v) FCS +1% (v/v) P/S +100 mM Dexamethasone +0.5 mM IBMX (Sigma, UK) +3 µg/ml ITS solution (Sigma, UK) + 1 µM Rosiglitazone (Sigma, UK)
Chondrogenic	αMEM	1% (v/v) P/S +100 µl ascorbic acid 2-phosphate +10 ng/ml TGF-β3 (Peprotech, UK) +10 µg/ml ITS solution +10 nM Dexamethasone

2.2.2 Femoral Diaphysis and Epiphysis Isolation

Bone marrow from human femoral epiphysis (FE), and the femoral diaphysis (FD), were obtained from the University Southampton Hospital and Spire Southampton Hospital, from patients undergoing elective hip replacement surgery following informed consent (**Figure 2-1**). The tissue was stored for up to 5 days, at 4°C, before cell isolation. An 8 mm gouge and a pair of bone nibbler forceps were used to remove bone marrow fragments from the FE. For both the FE and FD the cells were removed from the bone using vigorous shaking. The cells were washed and filtered (70 µm filter, Fisher Scientific UK) in non-supplemented αMEM. The cell pellets were then re-suspended in 50 ml of in-house red cell lysis buffer (1 L of deionised water (dH_2O) plus 9.2 g NH_4CL and 1 g $KHCO_3$) and incubated for 5 minutes at room temperature. The cells were centrifuged at 161 g for 5 minutes then re-suspended in basal media (), and plated at a seeding density of between $2x10^5$ to $8x10^5$ cells per flask. The cells were cultured, in a humidified incubator at 37°C with 5% CO_2, balanced air, in T75 or T125 cell culture flasks for up to a week before the first media change. The cells were maintained in fresh media, replaced twice weekly, and passaged when they reached 80% confluency.

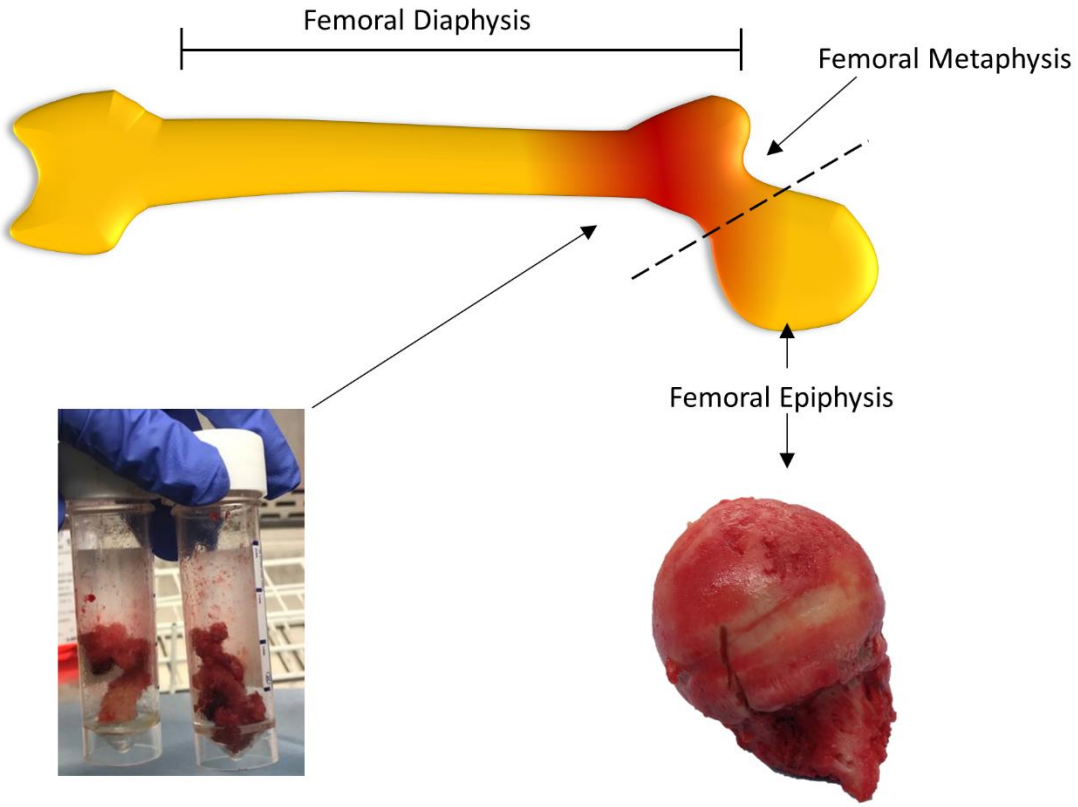

Figure 2-1. Bone marrow stromal cell isolation from the femoral epiphysis and the femoral diaphysis/metaphysis*. Bone marrow from the femoral metaphysis/ diaphysis was removed during surgery, and received alongside the femoral head. Bone marrow was removed from the femoral head using a gouge.*

2.2.3 Monolayer Cell Culture and Passaging

When cultured HBMSC cells reached 80% confluency, the media was removed and the flask washed with 1x PBS. Then 0.2 mg/ml of collagenase IV (Sigma, UK) was added to 1x PBS and the flask was incubated for 15 minutes, followed by a 5-8 minute incubation of 1x Trypsin/ Ethylenediaminetetraacetic acid (EDTA, 1700000 U/L trypsin 1:250 + 2g/L Versene, Lonza, Switzerland). The cells were seeded at a concentration of $3x10^5$ cells per ml. Cells were used up to passage 2.

2.2.4 Osteoblast Culture

Small bone explants from femoral diaphysis and epiphysis isolation were washed thoroughly with 1x PBS, then placed in a 6 well plate with 1-2 ml of basal media. After 7 to 14 days the bone explants were removed. When the remaining cells reached 50% confluency, they were passaged using 1x trypsin/EDTA to dissociate adherent cells. Media was changed every 2 to 3 days and following passages were carried out when the cells had reached 80% confluency.

2.2.5 Cell Spheroid Formation and Culture

Cells were seeded into inertGrade 96 well BRANDplates (Sigma, UK) between $5x10^4$ and $2x10^5$ cells per well. Cells were incubated for up to 4 days. Media was changed 2-3 days. To create a single cell suspension the pellets were incubated for up to 40 minutes in a thermal shaker, in a combination of collagenase, Liberase TL (Sigma, UK) or accutase (Sigma, UK).

2.2.6 Fetal Bone Marrow Isolation

The femur was isolated from the surrounding tissue, and the bone marrow was removed using repeated flushing and vigorous shaking in basal media. The cells were centrifuged at 161 g for 5 minutes, then re-suspended in 5 ml of basal media and seeded in a T25 flask. The cells were maintained in fresh media, replaced twice weekly, and passaged when they reached 80% confluency.

2.2.7 Alamar Blue Analysis

The proliferation of the osteosarcoma cell lines and potential primary cells of interest, including HBMSCs with and without Saos-2 co-culture, were analysed to optimise cell number for future assays. Alamar blue (ThermoFisher, US) is a reagent, which measures cell viability and proliferation via the reduction of the ingredient resazurin to resorufin, a fluorescent compound, after uptake from living cells. Alamar blue was diluted 10x in basal media and 100 µl was added to each well of a 96 well plate, 300 µl for a 24 well plate. The plates were incubated for an additional 1-3 hours before the fluorescence was measured at 560nm on a microplate reader (Promega Glomax).

2.2.8 Alkaline Phosphatase Assay

The level of alkaline phosphatase was analysed to look for early signs of osteogenic differentiation in the cells of interest. Cells were seeded in a 12 well plate between $1x10^4$ and $3x10^4$ cells per ml of basal media. When cells reached 70% confluency the basal media was removed and osteogenic I media was added (see). After seven days the cells were fixed in 95% (v/v) Ethanol, washed with 1x PBS and left to air dry. 300 µl of Alkaline Phosphatase Stain, a solution of 40 µl/ml Naphthol AS-MX phosphate (Sigma, UK) plus 0.24 mg/ml Fast Violet B Salts in 10 ml dH_2O, was added to each well and incubated between 10 (Saos-2) to 40 minutes (HBMSCs and MG63) at 37°C. The solution was removed after alkaline phosphatase staining appeared, wells were washed in dH_2O and the cells imaged on an inverted microscope (Zeiss Germany, Axiovert 200).

Unstained wells were lysed in CelLytic M (Sigma, UK) and stored at -20°C for further analysis. 5-10 µl of lysate was combined with 90-95 µl of substrate (40 mg phosphate substrate with 10 ml of

1.5 M Alkaline Buffer, Sigma UK, in 20 ml dH_2O), and incubated at 37°C for 5-60 minutes. The reaction was terminated with 1M NaOH, and the absorbance at 410 nm was read on a microplate reader (Promega, US, GloMax). The quantity of dsDNA was also determined for these samples; 5-10 µl of sample was combined with 90-95 µl of 1x Tris/EDTA buffer then stained with Pico Green (1:200, Thermofisher, US). The fluorescence was analysed (ex 480nm, em 520nm, sensitivity 90) on a microplate reader (Promega, US, Glomax).

2.2.9 Tri-lineage Osteogenic Differentiation

Later stage osteogenic differentiation, and early mineralisation of the HBMSCs and osteosarcoma cell lines were assessed by alizarin red (ARS) quantification and qPCR analysis (2.5.1) of *ALPL* and *COL1A1* genes. Alizarin red stains calcium deposited by the cells, and was imaged for localisation then quantified for absorbance. Cells were seeded in a 12 or 24 well plate between $1x10^4$ and $3x10^4$ cells per ml in 0.5-1 ml of basal media. When cells reached 70% confluency the basal media was removed and osteogenic II media was added (see). Media was changed every 2 to 3 days. On day 14 osteogenic II media was changed to mineralisation media (). To confirm differentiation on day 28 the cells were either lysed for qPCR analysis or stained for ARS. For ARS staining the cells were washed in 1x PBS and fixed in 4% PFA (40µg/ml, w/v) for 15 minutes. After washing three times in dH_2O, the cells were incubated at room temperature for 1 hour with 40 mM of ARS. Cells were washed five times in dH_2O and imaged on an inverted microscope (Zeiss, Germany, Axiovert 200). The level of ARS was quantified by analysing the absorbance at 405 nm, the stained cells were incubated in 10% (v/v) acetic acid for 30 minutes at room temperature, the cells were vortexed, heated to 85°C for 10 minutes and placed on ice for 5 minutes. Cells were centrifuged at 161g for 15 minutes and the supernatant was neutralized with 100 µl of 10% (v/v) ammonium hydroxide. Standards were created and the absorbance at 405 nm was measured on a microplate reader (Promega, US, Glomax).

2.2.10 Tri-Lineage Adipogenic Differentiation

The adipogenic differentiation of HBMSCs and osteosarcoma cell lines, was assessed by Oil Red O staining and qPCR analysis (2.5.1) of *FABP4* and *PPARγ* genes. Oil Red O stains lipid residues deposited by differentiated adipogenic cells. Cells were seeded in a 12 or 24 well plate between $1x10^4$ and $3x10^4$ cells per ml in 0.5-1 ml of basal media. When cells reached confluency, the basal media was removed and adipogenic media was added (). Media was changed every two to three days. To confirm differentiation, on day 14 the cells were either lysed for qPCR analysis or stained for Oil Red O; 1% w/v Oil Red O/isopropanol was diluted 3:2 in dH_2O. The resulting working solution was aliquoted onto the cells, which had been fixed in 4% (w/v) PFA for 15 minutes at room temperature and rinsed in 60% (v/v) isopropanol. After 15 minutes the working solution

was removed and the cells were rinsed three times in dH_2O before being imaged on an inverted microscope (Zeiss, Germany, Axiovert 200).

2.2.11 Tri-Lineage Chondrogenic Differentiation

Chondrogenic differentiation of HBMSCs and osteosarcoma cell lines were assessed by SRY-Box transcription factor 9 (SOX9) immunohistochemistry analysis (2.6.5), and by qPCR analysis (2.5.1) of *SOX9*, *COL2A1* and *ACAN* genes. Culturing cells detached and placed in 1.5ml Eppendorf tubes at a concentration of $5x10^5$ cells in 1ml of basal or chondrogenic medium (), and centrifuged at 400 g for 10 minutes. After centrifugation the tubes were placed into 50ml falcon tubes with filter lids taken from T175 flasks. The cell pellet was not re-suspended. The pellets were cultured for 28 days in a hypoxic environment at 37°C with 5% CO_2 and 5% O_2, with balanced air. Media was changed every two to three days. To confirm differentiation, on day 28 the cell pellets were either lysed for qPCR analysis or fixed in 4% (w/v) PFA for SOX9 histological analysis.

2.2.12 Transwell Assay

To assess whether the osteogenic differentiation ability and proliferation of primary cells were affected by Saos-2 osteosarcoma cells: HBMSCs, osteoblasts and fetal bone marrow were co-cultured with Saos-2 in a transwell assay. Culturing cells were seeded on to a 6 or 12 well plate at $3x10^4$ and $1.5x10^4$ cells respectively and incubated for 3-4 days in basal media. On day 3-4 the basal media was replaced, and a transwell was positioned into the well (Corning, US, 0.4 µm pore, polycarbonate). Saos-2 cells were seeded in the transwell at a density of $1x10^4$ or $2x10^4$ cells per well (12 and 6 well respectively) in basal media. The following day the media was changed in both compartments of the well into basal or osteogenic I media and incubated for up to 14 days, with media changes every 2-3 days. On the final day of culture, supernatant was removed and analysed for IL-6 (0), the cells were then analysed by alamar blue (2.2.7), and lysed for either qPCR analysis (2.5.1) or ALP biochemistry analysis (2.2.8), and stored at -80°/-20°C until needed.

2.2.13 PBMC Isolation

To isolate PBMCs, a blood leukocyte cone was diluted to 50 ml in PBS+ 2mM EDTA. 25 ml of diluted blood was layered onto 12.5 ml density gradient media (lymphoprep, Alere Ltd, UK) and centrifuged at 800 g for 20 minutes with the brake off. The cells layered at the interface were removed and washed in PBS+EDTA at 400 g for 10 minutes, then re-suspended and washed again at 300 g for 10 minutes. The cells were then washed again in αMEM+ 1% (v/v) P/S at 252 g for 5 minutes before being counted.

2.2.14 Macrophage Differentiation

PBMCs were isolated (2.2.13) and plated at a concentration of $1x10^7$ cells/ml, FD and FE cells were isolated (2.2.2) and plated at $2x10^7$ cells/ml in αMEM+1% (v/v) P/S + 1% (v/v) human AB serum (Sigma, UK). Cells were incubated for 2 hours at 37°C, before being washed twice in 1x PBS then incubated in basal media overnight. The following day 100 ng/ml of M-CSF (in-house) was added to the culturing cells and incubated for 7 days. The cells were fed every 2-3 days in basal media + 100 ng/ml M-CSF. On day 7 cells were either detached by incubation in 1x PBS on ice for 15 minutes, for flow cytometry analysis, or incubated for 48 hours in skewing media (Table 2-2) before flow cytometry analysis (Becton Dickinson, US, FACS Canto II).

Table 2-2. Polarising agents for macrophage skewing

Condition	*Polarisation agents*
M0	*100 ng/mL M-CSF*
M1	*100 ng/mL M-CSF + 50 ng/mL LPS (Peprotech) + 2 ng/mL recombinant human (rh) interferon gamma (IFNγ, Peprotech)*
M2	*100 ng/mL M-CSF + 10 ng/mL rh IL-4 (Peprotech) + 10 ng/mL rh IL-13 (Peprotech)*

2.2.15 CD14+ Magnetic Isolation

To separate monocytes from other cells in the PBMC and human bone marrow populations magnetic cell sorting was used to isolate the CD14+ cells. This was carried out using either the Miltenyi (Germany) CD14 MicroBeads Isolation kit, or StemCell (Canada) EasySep CD14+ selection kit, both processes were performed using the manufacturer's protocol. Briefly, for the Miltenyi kit, cells were re-suspended in 80 µl isolation buffer per $1x10^7$ cells. 20 µl of CD14 MicroBeads per $1x10^7$ cells were added to the solution, incubated on ice for 15 minutes, washed and then isolated using a LS Column (Miltenyi, Germany). Buffer = 1x PBS + 5 µg/ml (w/v) bovine serum albumin (BSA) + 2mM EDTA. For the StemCell kit, $1x10^8$ cells were re-suspended in 1 ml basal media and 100 µl/ml of selection cocktail was added to the cells and incubated for 10 minutes at room temperature. 100 µl/ml of RapidSpheres were then added to the cells and incubated for a further 3 minutes. 1.5 ml of basal media was added to the cell solution and the tube was placed into the magnet and incubated for 3 minutes before the supernatant was removed. The remaining cells were washed and incubated in the magnet twice before cells were removed and counted. The resulting CD14+ cells were plated at a concentration of $1x10^6$ cells per ml in αMEM+1% (v/v) P/S + 1% (v/v) human ab serum and incubated at 37°C for 2 hours. After 2 hours the wells were washed twice in 1x PBS, and incubated in basal media overnight. The following day 100 ng/ml M-CSF were

added to the cells, which were incubated for 7 days. Basal media + M-CSF was replaced every two to three days. On day 7, the cells were detached by incubation in PBS on ice for 15 minutes and stained for flow cytometry (Becton Dickinson, US, FACS Canto II).

2.2.16 Phagocytosis Assay

CD14+ cells isolated from PBMCs and human bone marrow were cultured with 100 ng/ml M-CSF for 7 days. On day 7 the cells were detached by incubation on ice for 15 minutes, and re-plated on a 96 well plate at $2x10^5$ cells/well. The cells were incubated for a further 48 hours with 100 ng/ml M-CSF, washed with PBS then incubated with or without $1.2x10^6$ 3 µM BSA Beads for 1 hour. The cells were washed again with PBS, then placed on ice for 15 minutes to detach the cells, and analysed by flow cytometry (Becton Dickinson, US, FACS Canto II). The 3µM beads were labelled with AF488 BSA prior to use by incubating at 4°C for 1 hour, then washed with PBS. The final stock concentration was 1.65 $x10^{10}$ beads per ml, the beads were diluted to a ratio of 25 beads per macrophage as a working concentration, and this was previously established as the lowest saturation value.

2.2.17 Osteoclast Differentiation

PBMCs and human bone marrow cells were isolated (2.2.13 and 2.2.2), then either processed through magnetic cell sorting for CD14+ cells (2.2.15), or directly seeded in a 24 well plate at a range of dilutions. The cells were incubated for 2 hours at 37°C, before being washed twice in PBS then incubated in basal media overnight. The following day the media was changed into osteoclast differentiation media: basal media+ 50 ng/ml RANKL (R&D Systems, US) + 30 ng/ml M-CSF. The cells were incubated for a further 14 days, with media changes every 2 to three days. On day 14 the cells were fixed in 4% (w/v) PFA for 15 minutes, and stored in 1x PBS for Tartrate-resistant acid phosphatase (TRAP) staining (2.6.6).

To quantify the activation of osteoclasts; slices of cortical bone were cut from the femoral neck of patient samples using an isomet saw (Buehler, US) at a thickness of between 1-2 mm. The cortical slices were placed into a 96 well plate and non-sorted HBMSCs and PBMCs were seeded onto them at a concentration of $1x10^5$ cells per well and incubated as above. After 14 days incubation the cortical slices were fixed in 4% (w/v) PFA and a TRAP stain (2.6.6) was performed to visualise the osteoclasts. Following this staining the cortical slices were placed in a sonicating water bath (Ultrawave, UK, 220 V, 50 Hz) for 10 minutes to remove the cells and then stained for toluidine blue (2.6.7) to measure pit formation.

2.2.18 Effect of Mifamurtide on HBMSC and Osteosarcoma Cell Lines

Reconstituted Mifamurtide that was surplus to clinical use, was acquired from the Southampton General Hospital and stored at 4°C for up to 72 hours. Cells were seeded between $3x10^4$ and $4x10^4$ cells per well in a 48 well plate and cultured overnight. The following day Mifamurtide was added to the wells in a 2-fold dilution starting at 32 µM (0.8 µg/ml), and cultured for a further 7 days, with media/ Mifamurtide changes every 2-3 days. At day 7 the media was removed, and the wells were washed 3x in 1x PBS before being lysed in 100 µl CellLytic M for ALP biochemical analysis (2.2.8).

2.3 Flow Cytometry

Adherent MDMs and hBMDMs were detached by incubating with ice-cold 1x PBS for 15 minutes, centrifuged at 252 g for 5 minutes and then re-suspended in 1x PBS. The cells were stained for 15 minutes at room temperature in the dark, with a panel of antibodies to cell surface markers (Table 2-3). After incubation the cells were either centrifuged and re-suspended in FACS buffer (1x PBS+ 5 µg/ml (w/v) BSA+ 0.1% (v/v) Azide) before being analysed by flow cytometry (Becton Dickinson, US, FACS CantoII), or fixed in 500 µl fixation medium (00-5523, ThermoFisher, US) for 30 minutes. The cells were then washed in 10x permeabilisation medium (00-5523, ThermoFisher, US) and stained with a CD68 intracellular antibody for 30 minutes at room temperature in the dark. After incubation the cells were centrifuged and re-suspended in FACS buffer before being analysed on a BD Canto. UltraComp eBeads (ThermoFisher, US) were stained using the membrane antibody protocol for compensation controls. Flow cytometry data was analysed using FlowJo software (Becton Dickinson, US).

Table 2-3. Flow Cytometry Antibodies

Antibody	Fluorochrome		Isotype		Company
HLA-DR	PerCpCy5.5	Monoclonal	Mouse IgG2a	Membrane	Biolegend, 307629
CD271	PE	Monoclonal	Mouse IgG1	Membrane	Biolegend, 345105
CD34	APC Cy7	Monoclonal	Mouse IgG2a	Membrane	Biolegend, 343613
CD14	APC	Monoclonal	Mouse IgG1	Membrane	Biolegend, 367117
	PE	Monoclonal	Mouse IgG1	Membrane	Biolegend, 367103
CD11b	Pacific Blue	Monoclonal	Rat IgG2b	Membrane	Biolegend, 101224

CD38	APC Cy7	Monoclonal	Mouse IgG1	Membrane	Biolegend, 356615
	PE	Monoclonal	Mouse IgG1	Membrane	Biolegend, 356604
CD40	APC	Monoclonal	Mouse IgG1	Membrane	Biolegend, 334309
	APC Cy7	Monoclonal	Mouse IgG1	Membrane	Biolegend, 334324
Rat 1gG2b	Pacific Blue	Monoclonal		Isotype control	Biolegend, 400627
Mouse IgG2a	PerCPCy5.5	Monoclonal		Isotype control	Biolegend, 400257
	APC Cy7	Monoclonal		Isotype control	Biolegend, 400229
Mouse IgG1	PE	Monoclonal		Isotype control	Biolegend, 400112
	APC	Monoclonal		Isotype control	Biolegend, 400122
	APC Cy7	Monoclonal		Isotype control	Biolegend, 400127
CD68	FITC	Monoclonal	Mouse IgG2a	Intracellular	ThermoFisher, 11-0689-42

2.3.1 Propidium Iodide Staining

To assess the viability of cells after spheroid culture, the resulting single cell suspensions were analysed by Propidium Iodide (PI). Cells were processed into a single cell suspension via the incubation of collagenase or Liberase TL, and re-suspended in media. Then 10 µl of PI solution per 100 µl of media was added to the cell suspension, and incubated at room temperature in the dark for 15 minutes. After 15 minutes the cells were analysed immediately, without washing, on a Becton Dickinson (US), FACS Canto II.

2.4 Bone Core Model

2.4.1 Femoral Epiphysis Bone Cores

An OsteoPower2 drill (Osteomed, UK) with a hole saw drill bit was used to create 8 mm sized cores in FE samples; a partial defect was then drilled, using twist drill bit, through the centre of the cartilage layer (**Figure 2-2**A). All bone cores were produced under sterile conditions. The cores were either rinsed in αMEM media, or made acellular by incubation in hydrogen peroxide (30%

w/w, Sigma, UK) for 48 hours before being washed three changes of 1x PBS (minimum 6 hour incubations). The bone cores were then cultured in 3 ml of basal media for up to 30 days, or inserted onto the CAM (**Figure 2-2**B). The cores were cultured with a combination of cells seeded between $1x10^5$ - $5x10^5$ cells, which were re-suspended in a 11 µg/ml (w/v) Alginate (Sigma, UK) + 20 µg/ml (w/v) Gelatine (Sigma, UK) solution at 20 µl per core, which was inserted into the defect area. After incubation the cores were fixed with 4% (w/v) paraformaldehyde (PFA) for 24-72 hours, then decalcified. Micro computed tomography (µCT) images were taken of all cores before and after incubation.

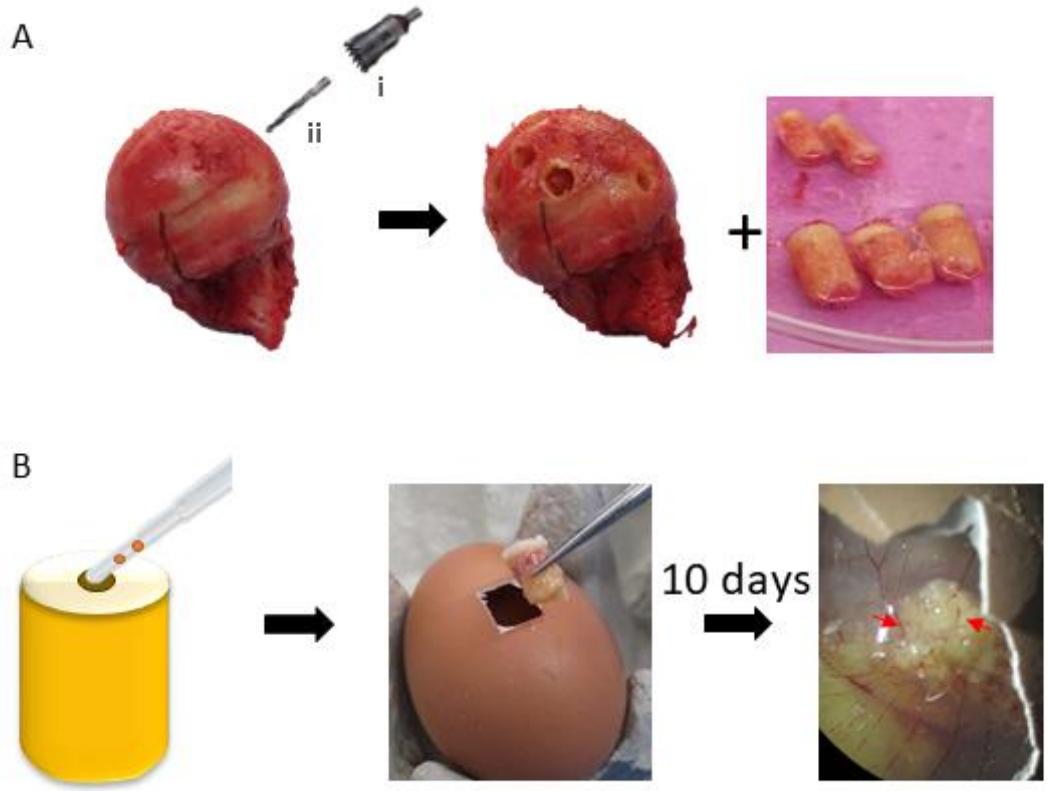

Figure 2-2. A schematic representation of the bone core isolation and implantation on the CAM. *(A) A hole saw (i) and twist (ii) drill bit were used to drill 8 mm bone cores from the femoral epiphysis. (B) Cell pellets were transferred into the centre defect of the bone core, before being implanted onto the CAM surface; the eggs were then incubated for 10 days. Red arrows denote areas of vascularisation in the bone cores.*

2.4.2 Femoral Epiphysis Bone Slices

To generate bone slices, femoral heads were placed in hydrogen peroxide (30% w/w, Sigma, UK) for a minimum of 48 hours before being cut into ~5mm slices using an isomet saw with a diamond wafering blade (Buehler, US). The sections were placed into 30% hydrogen peroxide until 72 hours before use. The bone slices were then washed in 1x PBS for 24 hours, then incubated in 10% (v/v)

antibiotic antimycotic solution (stock= 1,000 units penicillin +1 mg streptomycin + 2.5 µg amphotericin B per ml) for 1 hour followed by 1% (v/v) antibiotic antimycotic solution overnight. The following day the bone slices were washed in 1xPBS before being used in culture. The bone slices were seeded with a combination of cells between $1x10^5$ - $5x10^5$ cells, which were re-suspended in a 11 µg/ml (w/v) Alginate + 20 µg/ml (w/v) Gelatine solution, at 20 µl per slice (**Figure 2-3**). After incubation the bone slices were fixed with 4% (w/v) PFA for 24-72 hours, then decalcified. Micro-CT images were taken of all cores before and after incubation, using a Skyscan 1176 µCT machine (Bruker, Belgium)

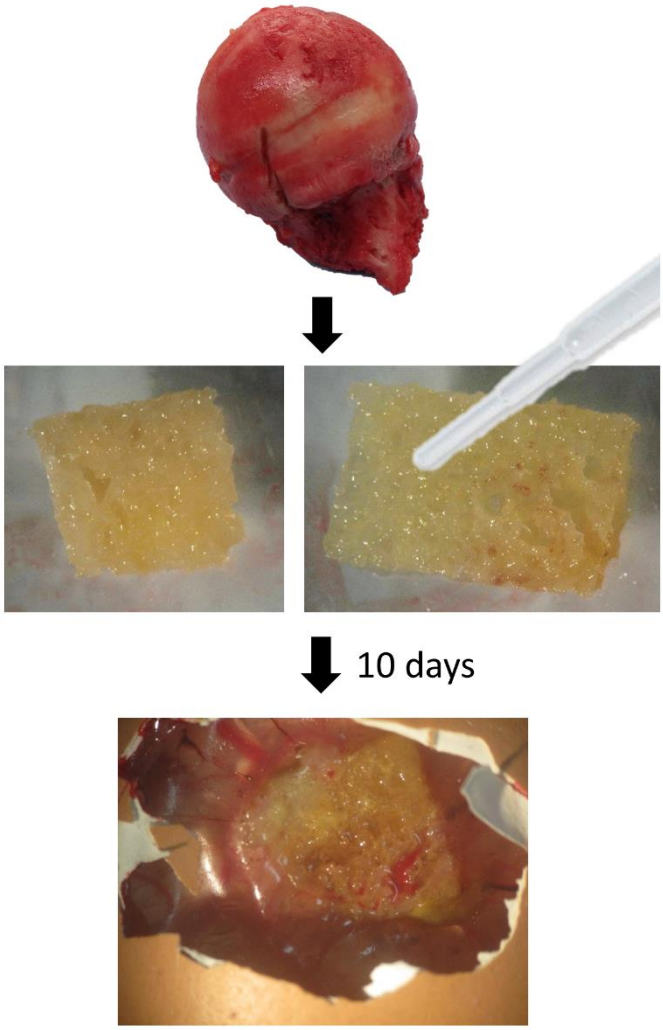

Figure 2-3 A schematic representation of bone slice isolation and implantation into the CAM assay*. Slices of trabecular bone were sectioned from the femoral head using an isomet saw, and made acellular with 30% hydrogen peroxide. Cells were seeded directly onto the bone slice before being implanted on the CAM surface; the eggs were then incubated for 10 days.*

2.4.3 Chorioallantoic membrane

Fertilised wild type chicken eggs were obtained from Henry Stewart & Co, Norfolk, England. The eggs were placed in an incubator (Hatchmaster, Brinsea, UK), and incubated for 7-8 days at 37°C in a 60% humidified atmosphere, with rotation every hour. At day 7-8 a 1 cm^2 window was cut in the eggshell using a scalpel, and the implant was placed on the membrane. Parafilm had been previously sterilised in 70% (v/v) Ethanol for more than 10 minutes, then washed in 1x PBS for 15 minutes before being used to seal the window. The parafilm was fixed in place using autoclave tape. The eggs were returned to the incubator and incubated for a further 10-11 days without rotation. After 10-11 days the chicks were killed humanely using a schedule 1 method according to Home Office regulations, and the bone core removed.

2.5 Molecular Biology

2.5.1 qPCR

RNA extraction was performed on pre-lysed samples stored at -80°C, using the ReliaPrep RNA Cell Miniprep System (Promega, US). This was carried out according to manufacturer's protocol. The resulting RNA was measured using a spectrophotometer (Nanodrop 100 V3.8.1, ThermoFisher Scientific, US), and stored at -80°C.

The RNA was then reverse transcribed using a TaqMan Kit (Applied Biosystems, US) with either a 20 µl or 40 µl total reaction volume. The RNA was processed using a Verriti 96-well Thermal Cycler (ThermoFisher Scientific, US) using the following protocol: 10 minutes at 25°C, 30 minutes at 48°C then 5 minutes at 95°C. The resulting cDNA samples were stored at -20°C.

Gene expression was then analysed by qPCR (Table 2-4), with a GoTaq qPCR Master Mix (Promega, US). This master mix consisted of 10 µl Power Sybr Green MM, 0.75 µl of 5 µM forward primer, 0.75 µl of 5 µM reverse Primer (Sigma UK, 100 µM stock), and 7.5 µl nuclease free water per well. 18 µl of the master mix was combined with 2 µl of cDNA, and qPCR was performed in a 7500 Real-Time PCR system (Applied Biosystems, US), then analysed using Applied Biosystems 7500 System SDS Software v2.0.5.

All primers were designed and characterised by previous postdoctoral researchers and PhD students in the Bone and Joint Laboratory group, supported by published literature. Before use all the primers were tested for their efficiency; cDNA concentration was plated in a serial dilution then mixed with the GoTaq qPCR master mix, before being analysed. The resulting CT values were plotted and a standard curve fitted, which was then used to calculate the resulting efficiency. The

efficiency for each primer was used in the analysis of the raw CT values for each qPCR experiment. A list of the primer efficiencies can be found in (**Appendix 1**).

Table 2-4. Primer Sequences for qPCR Analysis

	Gene Name	Protein	Ref	Forward 5'-3'	Reverse 5'3'
Housekeeping Genes	*ACTB*	βActin	[178]	GGCATCCTCACCCTGAAGTA	AGGTGTGGTGCCAGATTTTC
Adipogenic Genes	*PPARγ*		[179]	GGGCGATCTTGACAGGAAAG	GGGGGGTGATGTGTTTGAACTTG
	FABP4		[179]	TAGATGGGGGTGTCCTGGTA	CGCATTCCACCACCAGTT
Osteogenic Genes	*ALPL*	ALP	[178]	GGAACTCCTGACCCTTGACC	TCCTGTTCAGCTCGTACTGC
	COL1A1	Collagen type I α1	[178]	GAGTGCTGTCCCGTCTGC	TTTCTTGGTCGGTGGGTG
Chondrogenic Genes	*SOX9*		[180]	CCCTTCAACCTCCCACACTA	TGGTGGTCGGTGTAGTCGTA
	COL2A1	Collagen, type II α1	[180]	CCTGGTCCCCCTGGTCTTGG	CATCAAATCCTCCAGCCATC
	ACAN	Aggrecan	[179]	GACGGCTTCCACCAGTGT	GTCTCCATAGCAGCCTTCC
Other Genes	*HIF1A*	HIF 1α	[181]	GTTTACTAAAGGACAAGTCACC	TTCTGTTTGTTGAAGGGAG
	MKI67	Ki67	[182]	GGTCTGTTATTGATGAGCCTGTA	CAGTTGACTTCCTTCCATTCTG
	SP7	Osterix	[180]	ATGGGCTCCTTTCACCTG	GGGAAAAGGGAGGGTAATC

2.5.2 ELISA

An IL-6 ELISA assay was carried out on supernatant samples stored at -80°C. The assay was carried out following manufacturers protocol (ThermoFisher US, 88-7066-86); briefly, 96 well flat bottom plates were incubated overnight at 4°C with the capture antibody (diluted 250x in 1x PBS). All following steps were carried out at room temperature. The following day the plates were washed and incubated for 1 hour in the blocking reagent (ELISA Diluent, ThermoFisher US). 100 µl of

samples were added to the appropriate wells in a serial dilution (up to 1:50) and incubated for a further 2 hours followed by a 1 hour incubation in the detection antibody (diluted 250x in ELISA Diluent), a 30 minute incubation in Streptavidin HRP and a final 5 minute incubation in tetramethylbenzidine (TMB) substrate solution. The reaction was stopped by adding 2N H_2SO_4 directly to the TMB solution. The plate was then analysed immediately on a microplate reader (Promega US, Glomax), absorbance 450 nm. Washing occurred between all steps using an ELISA Washer.

2.6 Histology

2.6.1 Decalcification

Four different decalcification methods were compared for preservation of structural integrity of bone cores and slices (Table 2-5). All solutions were replaced every 5 days if needed, with a minimum of 5 ml per bone core/slice. After decalcification all cores/slices were rinsed in 1x PBS before embedding. Prior to the EDTA-glycerol solution was added to the cores they were incubated for 24 hours in 5% (v/v) glycerol, 10% (v/v) glycerol then 15% (v/v) glycerol, all in 1x PBS. After decalcification, the EDTA-glycerol cores were then incubated for 24 hours in the following solutions, all in 1x PBS: 150 µg/ml (w/v) sucrose+ 15% (v/v) glycerol, 200 µg/ml (w/v) sucrose +10% (v/v) glycerol, 200 µg/ml (w/v) sucrose + 5% (v/v) glycerol, 200 µg/ml (w/v) sucrose, 100 µg/ml (w/v) sucrose, 50 µg/ml (w/v) sucrose then 1x (v/v) PBS alone.

Table 2-5. Decalcification Solutions

Name	Solution	Decalcification Time
Formic Acid	10% (v/v) formic acid (Sigma) in deionised H_2O	~72 to 168 hours
Krajian	100 g/L sodium citrate dehydrate (Sigma) + 250 ml/L formic acid in deionised H_2O	~72 to 168 hours
TCA	6% (v/v) trichloroacetic acid (Sigma) in deionised H_2O	~72 to 168 hours
EDTA-glycerol	145 g/L EDTA + 12.5 g/L sodium hydroxide (ThermoFisher) +15% (v/v) Glycerol (Sigma) in deionised H_2O, pH 7.3	~14 days

2.6.2 Paraffin Embedding

Cell pellets and bone core samples were embedded in paraffin following one-hour incubations in increasing percentages of ethanol, starting at 50% (v/v), 90% (v/v) then 2x 100% (v/v) followed by 2x histoclear (SLS, UK). The samples were then placed in molten paraffin in a vacuum oven (Heraeus, Germany, Vacutherm) for 2x 1-hour incubations, before being embedded in paraffin. 5-10 µm sections were cut using a microtome and transferred onto Super-Frost Plus microscope slides (MENZEL-GLÄSER, Germany).

2.6.3 OCT Embedding

After decalcification bone cores were covered in optimal cutting temperature (OCT) embedding medium (Cellpath, UK) and placed in a vacuum for 15 to 20 minutes. The cores were then removed from vacuum, topped up with OCT and placed in isopentane (Sigma, UK) on dry ice. Once frozen samples were stored at -20 °C short term and -80 °C long term. 10 µm sections were cut using a cryostat (Leica CM1850) and transferred onto TOMO® adhesive microscope slides (CellPath, UK).

2.6.4 Haematoxylin and Eosin (H+E) Staining

Paraffin slides were warmed to room temperature before being hydrated through a series of histoclear (2x 7 minutes) and Ethanol (2 minutes at 100% (v/v) x2, 90% (v/v) and 50% (v/v)) before being washed in a running water bath. OCT slides were warmed to room temperature, then rehydrated in a running water bath prior to staining. Haematoxylin (Weigert's, solution A and B in equal measures) was added to each slide and incubated in the dark for 10 minutes, before being washed in a running water bath for 5 minutes. The slides were dipped in 1% (v/v) HCL in 70% (v/v) Ethanol five times, to remove excess haematoxylin from the cytoplasm, and then rinsed in a running water bath for a further 5 minutes. 1% (w/v) Eosin Y (Sigma, UK) was added to each section and left to stain for 10 minutes. The slides were washed for 2 minutes then dehydrated for 30 seconds in 90% (v/v) Ethanol, 100% (v/v) x2 and histoclear x2, before being mounted in DPX (Fisher Scientific, US).

2.6.5 Immunohistochemistry

Paraffin slides were warmed to room temperature before being hydrated through a series of histoclear (2x 7 minutes) and Ethanol (2 minutes at 100% (v/v) x2, 90% (v/v) and 50% (v/v)) before being washed in a running water bath. OCT slides incubated in acetone for 10 minutes, at 4°C, allowed to air dry and rehydrated in 1x PBS for 10 minutes. The slides were either immersed in EDTA or Citrate antigen retrieval buffer pre-warmed to 90°C (Table 2-6), and incubated at 90°C for 20 minutes, before cold water was run over the slides until cool. EDTA: 0.37 g EDTA in 1 L H_2O +

0.5 ml Tween-20, pH8. Citrate: 3g Sodium Citrate in 1L H_2O, adjust pH6 with acetic acid. ImmPRESS Horse anti-Rabbit and ImmPRESS Horse anti-mouse polymer staining kits (Vector Laboratories, US) were used for staining following the manufacturers protocol; all wash steps used 1x PBS unless otherwise specified. Briefly, after antigen retrieval endogenous peroxidase activity was blocked using BLOXALL blocking solution (Vector Laboratories, US) for 10 minutes, washed and slides were incubated in 2.5% (v/v) normal horse serum for 20 minutes. Primary antibodies were diluted to appropriate concentrations (Table 2-6) and incubated for 2 hours at room temperature. After washing the sections were incubated with the appropriate ImmPRESS reagent for 30 minutes, and washed again. For anti-rabbit antibodies the slides were then incubated in ImmPACT DAB EqV working solution for 2-10 minutes, while anti-mouse antibodies were incubated in ImmPACT Vector Red Diluent for 20-30 minutes until desired stain develops. The slides were then washed in a running water bath and counterstained with Light Green before being dehydrated through increasing concentrations of ethanol (30 seconds at 50% (v/v), 90% (v/v) 100% (v/v) x2) and histoclear (30 seconds x2) before being mounted in DPX.

Table 2-6. Antibodies for immunohistochemistry

Antibody	Species	Antigen Retrieval	Dilution	Company
CD68	Mouse	EDTA	1:200	Agilent, US, M087601-2
RANK	Mouse	EDTA	1:500	Novus Biologicals, US, NBP2-24702
CD105	Rabbit	Citrate	1:100	Abcam, UK, ab231774
SOX9	Rabbit	Citrate	1:200	Merck, Germany, AB5535

2.6.6 Tartrate-Resistant Acid Phosphatase Staining

To stain osteoclasts, previously fixed wells were rinsed in 1x PBS. 1 ml of pre-warmed TRAP staining solution was added to each well and incubated at 37°C for 30 minutes (or until control developed). The solution was removed and the wells rinsed in deionised H_2O. The wells were counterstained in light green (1 minute) then washed in H_2O, and imaged immediately on an inverted microscope (Zeiss, Germany, Axiovert 200). TRAP staining solution: 200 ml basic incubation medium +1 ml napthol AS-MX solution + 120 mg FAST red violet LB salt (Sigma, UK). Basic incubation medium: 9.2 g sodium acetate, anhydrous (Sigma, UK) + 11.4g L-(+) Tartaric Acid (Sigma, UK) + 2.8 ml Glacial Acetic Acid (Sigma, UK) + 1 L deionised H_2O, pH 4.7-5. Napthol AS-MX

solution: 20 mg Napthol AS-MX phosphate (Sigma, UK) + 1 ml Ethylene Glycol Monoethyl Ether (Sigma, UK).

2.6.7 Toluidine Blue

Toluidine blue was used to analyse the cortical bone slices for pit resorption by osteoclasts. A droplet (~20 µl) of toluidine was placed onto a petri dish. The bone slice was carefully placed onto the droplet, without being submerged, and incubated for 4 minutes before being rinsed in dH_2O. After air drying the bone slices were imaged on an inverted microscope (Axiovert 200, Zeiss, Germany). Toluidine Blue = 1 g sodium borate (Sigma, UK) in 100 ml dH2O + 1 g toluidine blue (Sigma, UK). Solution was left to stand overnight before being filtered and stored at room temperature.

2.6.8 Alkaline Phosphatase Staining

Paraffin slides were warmed to room temperature before being hydrated through a series of histoclear (2x 7 minutes) and Ethanol (2 minutes at 100% (v/v) x2, 90% (v/v) and 50% (v/v)) and washed in a running water bath. Slides were then submerged in Activating buffer and incubated at room temperature overnight. The following day the slides were removed from the activating buffer then submerged in AS-B1/fast red solution and incubated at 37°C for 1 hour. The slides were then washed in a running water bath before being stained with Light Green (1 minute) and Alcian blue (2 minutes). The slides were then mounted in hydromount (National Diagnostics, US). Activating buffer: 75 ml of 1.8g Tris + 1.74g maleic acid (Sigma, UK) in H_2O combined with 81 ml of 0.65g Sodium hydroxide in H_2O, plus 144 ml H_20 and 0.6g Magnesium chloride (Sigma, UK). AS-B1/ fast red solution: 25 mg Napthol AS-B1 Phosphate (Sigma, UK) + 10 ml Dimethyl Formide + 10 ml H_2O (pH 8), was combined with 180 ml of 4.36 g Tris in H_2O (pH 8.3) then diluted with 300 ml H_2O. Immediately prior to staining 1 mg/ml of Fast red TR salt (Sigma) was added to AS-B1 solution and filtered.

2.6.9 Multiplex Immunohistochemistry Staining

Multiplex analysis is the staining of multiple antibodies on the same tissue section, allowing for the ability to analyse overlapping markers of interest. Multiplex staining of 10 osteosarcoma patients (Table 2-7) was carried out using a Dako (AS4) staining machine, all optimisation and multiplex staining steps were carried out by the Research Histology department, University Southampton Hospital. The antibodies were first optimised for concentration and antigen retrieval. An osteosarcoma tissue section was then stained and de-stained with the same primary antibody (Table 2-8) up to 8 times to determine the order of antibodies for the final multiplex staining.

Table 2-7. Gender and Age of Osteosarcoma Samples

Gender	Age
Male	9 months
Male	5 years
Female	6 years
Male	11 years
Female	12 years
Female	13 years
Female	13 years
Male	14 years
Male	16 years
Female	17 years

In the multiplex staining the osteosarcoma sample were first stained with CD31-DAB, which was not de-stained for alignment purposes. Antigen retrieval was performed, then the section was stained for a primary antibody of interest with an AEC red aqueous substrate. The section was then mounted using Glycergel mounting medium (Dako, UK) before being scanned at high resolution using an Axioscan (Zeiss, Germany). The coverslips were removed by soaking in hot water before the section was de-stained (50% (v/v) alcohol, 2 min; 100% (v/v) alcohol, 2 min; 100% (v/v) xylene, 2 min; 100% (v/v) alcohol, 2 min; and 50% (v/v) alcohol, 2 min) and antigen retrieval was performed for the next primary antibody. Antigen retrieval was performed with either a target retrieval solution at pH 9 or pH 6.2 (Dako, UK), washing steps were performed using the Wash Buffer reagent (Dako, UK).

Table 2-8. Antibodies for Multiplex Immunohistochemistry Staining

Antibody	Species	Company	Antigen Retrieval	Dilution
RANK	Mouse	Novus Biologicals, US, NBP2-24702	pH 9	1:200
CD105	Rabbit	Abcam, UK, ab231774	pH 9	1:100
Osteocalcin/ BGLAP	Rabbit	Booster Biological Technology, US, PB9088	pH 6.1	1:500
HIF1α	Rabbit	Abcam, UK, ab51608	pH 6.1	1:100
Phospho-STAT3	Rabbit	Cell Signalling Technology, US, 9145S	pH 6.1	1:100
STAT3	Mouse	Cell Signalling Technology, US, 9139S	pH 9	1:300
VEGF	Mouse	Agilent, US, M727329-8	pH 9	1:50
CD68	Mouse	Dako, UK, IR613	pH 9	Ready-To-Use
CD163	Mouse	Leica, Germany, NCL-L-CD163	pH 6.1	1:250
CD32B	Rabbit	Abcam, UK, ab45143	pH 9	1:3000

2.7 Imaging

2.7.1 Microscopy

Brightfield and fluorescent imaging was obtained using a Zeiss axiovert 200 microscope with Axiovision Software (Carl Zeiss Ltd, Germany). Images were taken using either the axioCam MR (monochrome) or the AxioCam HR (colour) cameras. Multiplex staining was imaged using a Zeiss AxioScan (Carl Zeiss Ltd, Germany).

2.7.2 Micro-CT Scanning

Bone core and bone slices were imaged using Bruker micro CT (Skyscan 1176) scanner at day 0, before cells were added, and at the end of culture (up to day 30). Cores were scanned in low density 1.5 ml Eppendorf tubes using the following settings: average voxel size 18 µm, X-ray

source 45 kV, 556 µA, Al 0.2mm filter, rotation step 0.70° and exposure time 496 ms. The results were analysed using NRecon, DataViewer and CTAn (all Bruker, Belgium).

2.7.3 NRecon

The raw µCT data files were reconstructed using the NRecon software. Settings included: misalignment compensation (-2), ring artefact reduction (9) and beam-hardening correction (40%). The reconstructed files were then further analysed in DataViewer.

2.7.4 DataViewer

Using DataViewer the pre and post scans for each bone core were aligned under 3D registration. By overlapping the two images, areas of non-registered bone are shown black if present in the pre-image but not the post, and white when present in the post image but not the pre; aligned bone is represented in grey. Both the pre and post cores in their aligned forms were saved and imported into CTAn for further analysis.

2.7.5 CTAn

The pre and post data sets were then loaded individually into CTAn software, where data was produced based on the pixel of grayscale value between 70 to 255. A region of interest was centred over the defect area with approximately 1 mm of edging into the core and analysed for both pre and post images.

2.8 Statistics

All experimental data was analysed using GraphPad Prism version 9.2 software. Results were expressed as mean +/- SD. Significance was assessed using either the one-way ANOVA (>2 groups) with Tukey's post hoc test, or an unpaired T Test statistical analysis, depending on the number of groups. The statistical test used is stated on each figure. Values of $p \leq 0.05$ were considered significant. Significance presented as *<0.05, ** <0.01, ***<0.001, ****<0.0001.

Chapter 3 Functional Characterisation of HBMSCs from Differing Locations of the Femur in Comparison to Osteosarcoma Cell Lines

3.1 Introduction

The tumour microenvironment of most cancers, including osteosarcoma, involves complicated interactions and signalling of many different cell types. The limited understanding of these interactions presents a challenge for the development of new and effective treatments, with very few novel therapies in clinical trials showing efficacy [46, 50]. The overall aim of this thesis was to develop a novel 3D multicellular model of osteosarcoma, enabling the study of these interactions in a human bone environment. Initially, it was important to assess cellular characterisation and interactions in 2D assays. This allowed for the determination of the most appropriate cell types that accurately represented the tumour microenvironment.

The skeletal location of HBMSCs, assessed by various imaging techniques, has shown there are variations in cellular phenotype, where different locations indicated differing levels of haematopoietic and adipogenic cells [183]. While the role of 'red' and 'yellow' bone marrow has been explored with regards to haematopoiesis, there are limited reports exploring their cellular characteristics, particularly in the ability to differentiate down the tri-lineage pathway, into osteoblasts, adipocytes and chondrocytes. The osteosarcoma tumour is known to produce osteoid in the microenvironment, and this production can be used to differentiate osteosarcoma from other bone tumours [184]. This suggests that the HBMSCs in the tumour microenvironment have a high osteogenic differentiation ability, resulting in an increased number of osteoblasts. Variations found in the differentiation ability of HBMSCs from differing skeletal locations could have an impact on the development of a 3D bone model. To quantify these differences *in vitro*, HBMSCs isolated from the FE and FD of donors who underwent elective hip replacement surgery, were assessed for osteogenic, adipogenic and chondrogenic potential, and compared with two osteosarcoma cell lines Saos-2 and MG63. Saos-2 and MG63 are both immortalised cell lines from osteosarcoma patients, but studies have shown they have different characteristics [185].

The microenvironment has been shown in many cancers to be manipulated by the tumour, which may release various signals to inhibit a productive immune response, as well as to manipulate the stromal architecture for its continued growth and development [106, 109]. To test this theory the level of osteogenic potential was analysed from HBMSCs and osteoblasts co-cultured with the

Saos-2 osteosarcoma cell line. Following this, human fetal bone marrow assays were also assessed, as these cells have been shown to have a high proportion of progenitor cells [186] akin to adolescent bone marrow. This potentially made this source more relevant than HBMSCs obtained from older patients undergoing hip replacement surgery. By co-culturing human fetal bone marrow with Saos-2 osteosarcoma cells, their response in releasing signals for bone formation or resorption was investigated.

Although cellular composition is an important factor when developing a 3D model, the structure and architecture of the tumour microenvironment also plays a large role. Many studies have shown differences between cells grown in a 2D and 3D environment [152]. One method of comparing 2D and 3D assays is through the generation of spheroids, which are 3D cell pellets. By inserting multi-cellular spheroids into the 3D bone model cellular interactions could be primed, while also limiting cell loss from the porous bone structure during insertion. Cells in the bone core model were initially inserted as spheroids to ensure the majority of cells remained within the bone during implantation, as such the spheroids were first characterised to optimise the level of proliferation and differentiation that occurred within the model.

3.2 Results

3.2.1 Examining the Proliferation of HBMSC and Osteosarcoma Cell Lines

A selection of cells were initially quantified for their potential use in developing the 3D bone model of osteosarcoma. These cells included HBMSCs from both the FD and FE regions; one of the main components of the bone microenvironment, two osteosarcoma cell lines Saos-2 and MG63; which were initially immortalised from osteosarcoma patients but have unique characteristics from each other, osteoblasts; the main cells involved in bone development, and fetal bone marrow; which have been previously classified as having high levels of progenitor cells. All these cell types have varying functionality and growth rates, so for direct comparison in 2D experiments, differences in cell proliferation were determined. The cells were cultured at various concentrations in basal media for 24 hours before being assessed using alamar blue (2.2.7). The alamar blue reagent is reduced to resorufin upon being taken up by living cells, a red compound fluorescent at 560nm, thus the number of viable cells was quantified by the level of fluorescence emitted. Figure 3-1 shows the proliferation of (A) FD and FE HBMSCs from donors F66 and F13, (B) two osteosarcoma cell lines Saos-2 and MG63, (C) fetal bone marrow from a 12PCW sample, and (D) osteoblasts from donor F66 (2.2.4) alongside fetal osteoblasts from a 9PCW sample. Figure 3-1A demonstrates the variability of donor samples, where both FD and FE cells from donor F13 showed a higher level of cell viability after 24 hours compared with donor F66. Figure 3-1B shows

MG63 cells had a higher number of viable cells than Saos-2 cells, and consequently increased level of proliferation. In contrast to cells in A and B, the alamar blue of fetal bone marrow cells in Figure 3-1C were still increasing exponentially until the highest cell concentration, without reaching a plateau. This was also seen in the fetal osteoblast cells in Figure 3-1D, which also did not reach plateau by the top cell concentration. In contrast osteoblasts from donor F66 had a similar curve to the HBMSCs, starting to plateau by $2.5x10^5$ cells. Using this data, in later assays the different cell types were seeded at varying concentrations in order for them to reach confluency at similar time points.

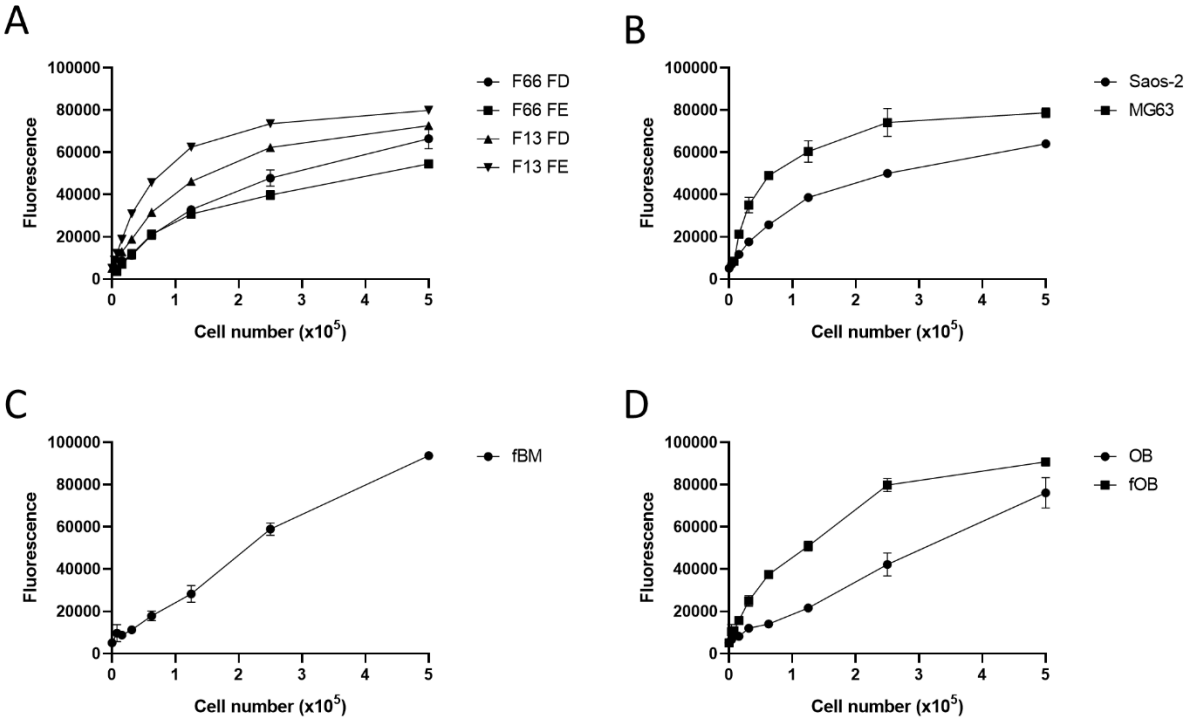

Figure 3-1. Proliferation of cells after a 24 hour incubation in basal media*. HBMSCs from two donors F66 and F13, (B) Osteosarcoma cell lines Saos-2 and MG63, (C) fetal bone marrow from a 12PCW sample, and (D) osteoblasts from donor F66 alongside fetal osteoblasts from a 9PCW sample, were seeded in decreasing concentrations and cultured for 24 hours before a 2 hour incubation with alamar blue. Fluorescence was read at 560 nm. Results presented as mean +/- SD.*

3.2.2 Early Osteogenic Potential of HBMSCs and Osteosarcoma Cell Lines

To assess the ability of osteosarcoma cell lines and HBMSCs to differentiate down the osteogenic pathway, they were cultured in Osteogenic I media (Table 2-1) for 7 days before the level of ALP, an early marker for osteogenic differentiation, was analysed (2.2.8). Figure 3-2A are representative images depicting ALP staining of the osteosarcoma cell lines Saos-2 and MG63. The Saos-2 cell line showed high levels of ALP staining in both basal and osteogenic I media, indicating

early osteogenic differentiation, while in contrast the MG63 cells had no ALP staining in either condition. ALP specific activity was calculated by dividing the level of ALP by the DNA concentration, to determine whether an increase of ALP was due to an increased cell number or to an increased level of differentiation (Figure 3-2B). There was a high level of ALP and specific activity in both types of media for the Saos-2 cells, although it tended to be higher in the osteogenic I media. This could be a result of the increased DNA concentration, which was statistically significant between the basal and osteogenic I cultured Saos-2 cells, suggesting the rise in ALP was due to an increase in cell number. As was observed with the imaging, the MG63 cells showed very low levels of ALP and specific activity, and consequently no osteogenic differentiation.

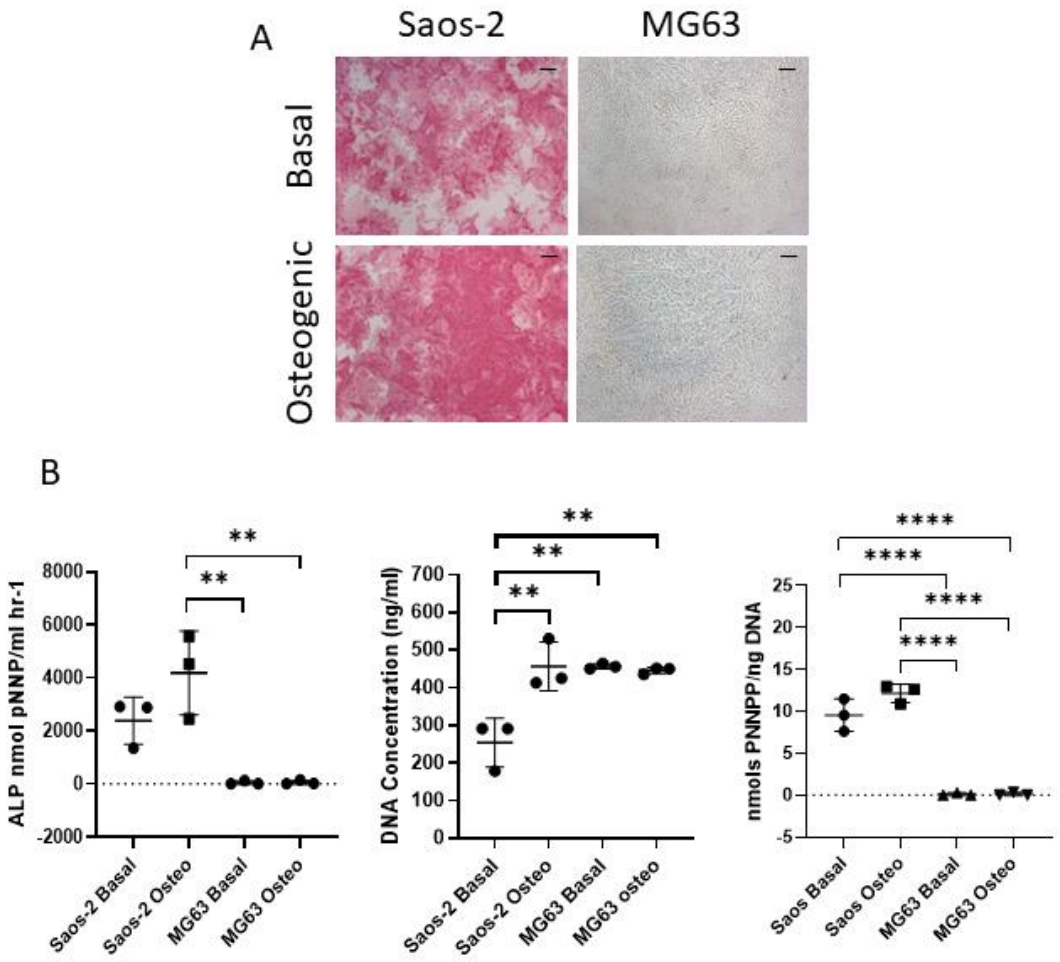

Figure 3-2. Early osteogenic differentiation of osteosarcoma cell lines. *(A) ALP staining (pink/red) of two osteosarcoma cell lines, Saos-2 and MG63, after culture in basal or osteogenic media for 7 days, demonstrating osteogenic differentiation. Scale Bar= 100 µm. (B) ALP analysis, DNA concentration and ALP specific activity of Saos-2 and MG63 cells. N=3 each with three technical replicates. Results presented as mean +/- SD, statistics analysed using a one-way ANOVA, significance presented as ** <0.01, ****<0.0001.*

HBMSCs were also analysed for ALP expression (2.2.8). Figure 3-3A showed representative images of ALP staining of FD and FE cells from donor F90. The images demonstrated an increased amount of ALP staining in the FD cells compared with FE, with comparable results across multiple donor samples (n=5, age range 13-90). Subsequently, HBMSCs were also analysed for ALP signalling, DNA concentration and specific activity (Figure 3-3B to D). The data showed 3 out of 5 donors have a significant increase in the level of ALP, for both FE and FD cells, when cultured in osteogenic I media compared with basal media. This increase was also seen in the DNA concentration between basal and osteogenic cultured HBMSCs. The basal vs osteogenic specific activity of the FD and FE cells (Figure 3-3D) demonstrated that the majority of samples have a lower or similar signal when cultured in osteogenic media than basal, with one donor showing a significant decrease in ALP specific activity for both FD and FE. When comparing FD and FE expression in osteogenic I media, both ALP and specific activity showed a decreasing trend in the FE cells compared with FD, which was statistically significant in two of the donor samples. Overall, these results show that osteogenic differentiation could be induced in three of the cell cultures, Saos-2, FD and FE, but the level of ALP was variable.

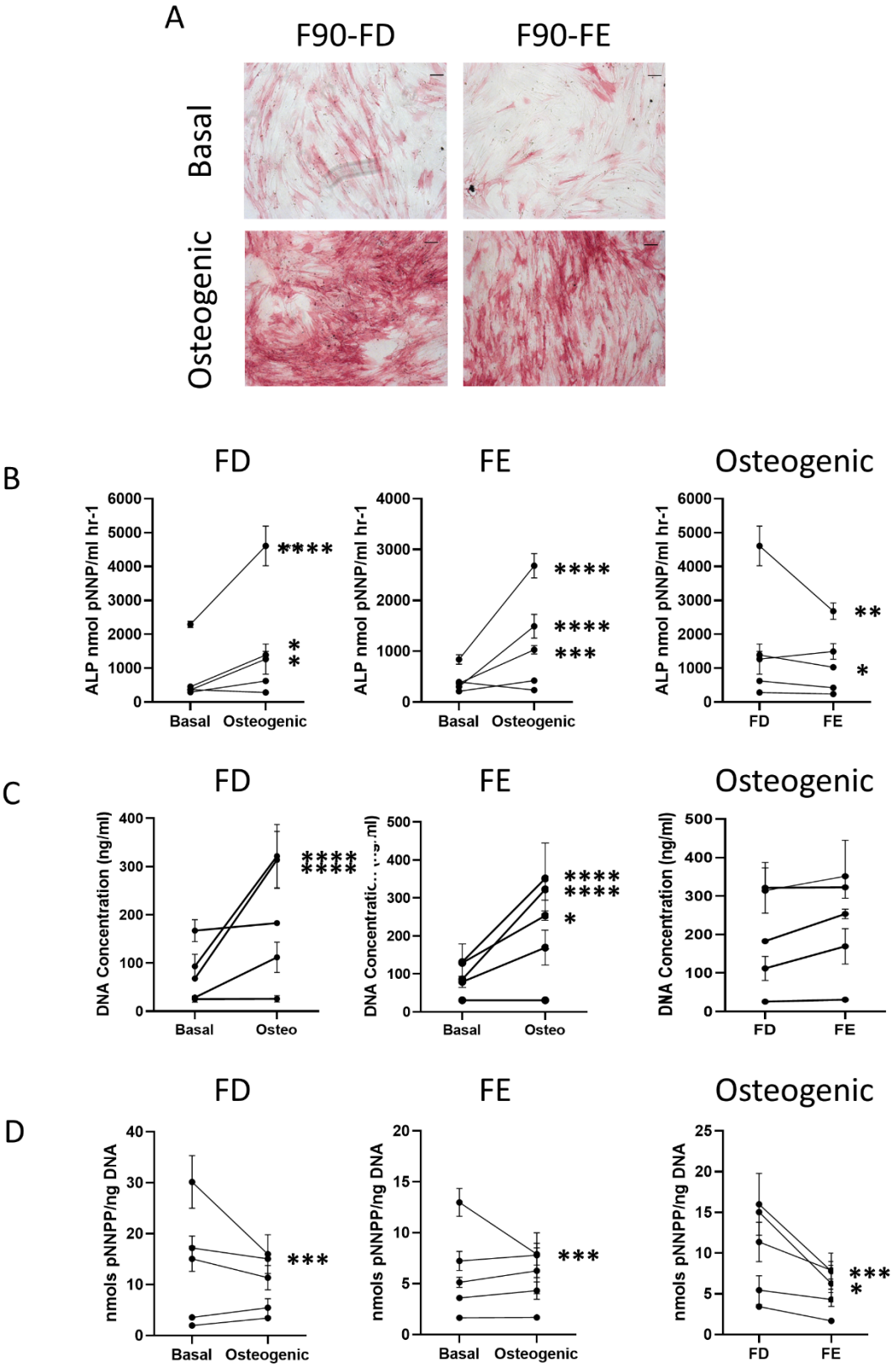

Figure 3-3. Early osteogenic differentiation of HBMSCs*. (A) ALP staining (pink/red) of FD and FE HBMSC, cultured for 7 days in basal or osteogenic media, demonstrating early osteogenic differentiation. Scale Bar= 100 µm. (B) ALP analysis, (C) DNA concentration and (D) ALP specific activity of FD and FE HBMSCs. N=5 each with three technical replicates. Results presented as mean*

*+/- SD, statistics analysed using a one-way ANOVA, significance presented as *<0.05, ** <0.01, ***<0.001, ****<0.0001.*

3.2.3 Osteogenic Differentiation and Mineralisation

The ability of HBMSCs and osteosarcoma cell lines to undergo mature osteogenic differentiation and mineralisation were investigated. Cells were cultured in osteogenic II media (Table 2-1) for 14 days, and then for a further 14 days in mineralisation media. At day 28, the cells were stained with ARS, which stains areas of calcium deposits red (2.2.9). Figure 3-4A illustrated differences in the level of osteogenic differentiation of the FD and FE cells, where the FD cells had a higher concentration of ARS stain, suggesting more mature osteogenic differentiation compared with the FE cells. The ARS staining of the osteosarcoma cell lines also presented distinct differences, where the MG63 cells were negative for ARS, while the Saos-2 cells showed a high level of staining. The level of ARS was then quantified (2.2.9), demonstrating a higher concentration in Saos-2 cells than MG63 over three independent experiments (Figure 3-4B). While the basal HBMSCs both demonstrated no ARS staining, the osteogenic FD cells showed a significantly higher concentration of ARS than the corresponding osteogenic FE cells in three donor samples (Figure 3-4D), indicating an increase in osteogenic differentiation.

To further confirm osteogenic differentiation, gene expression for two osteogenic markers, *ALPL* and *COL1A1*, were determined by qPCR (2.5.1). *ALPL* is the gene for ALP, an early marker of osteogenic differentiation, while Collagen I (*COL1A1*) is an extracellular protein expressed during all stages of osteoblast differentiation [187]. In Figure 3-4C, the Saos-2 samples expressed significantly higher levels of *ALPL* in osteogenic media compared with basal, where MG63 cells showed little to no *ALPL* expression. Saos-2 cells also showed a significant increase in the expression of *COL1A1* in osteogenic media compared with basal, while MG63 cells demonstrated a higher level of *COL1A1* when cultured in basal media compared with osteogenic. Figure 3-4E shows the level of *ALPL* and *COL1A1* expression from five different HBMSC donors. While there was a high level of variability between the different donor samples, there was a significant increase in the level of *ALPL* in the FE cells cultured in osteogenic media compared with basal. This trend was also seen in the FD cells, although it was not significant. The expression of *COL1A1* in the HBMSCs were similar between basal and osteogenic conditions, although there was a slight increase in the osteogenic conditions for both FD and FE cells compared with the basal. When comparing the osteogenic cultured FD and FE cells, there was an increased trend of *ALPL* expression in the FE compared with the FD, this was reversed in the *COL1A1* data, suggesting the FD cells reached a more mature osteogenic differentiation than the FE cells.

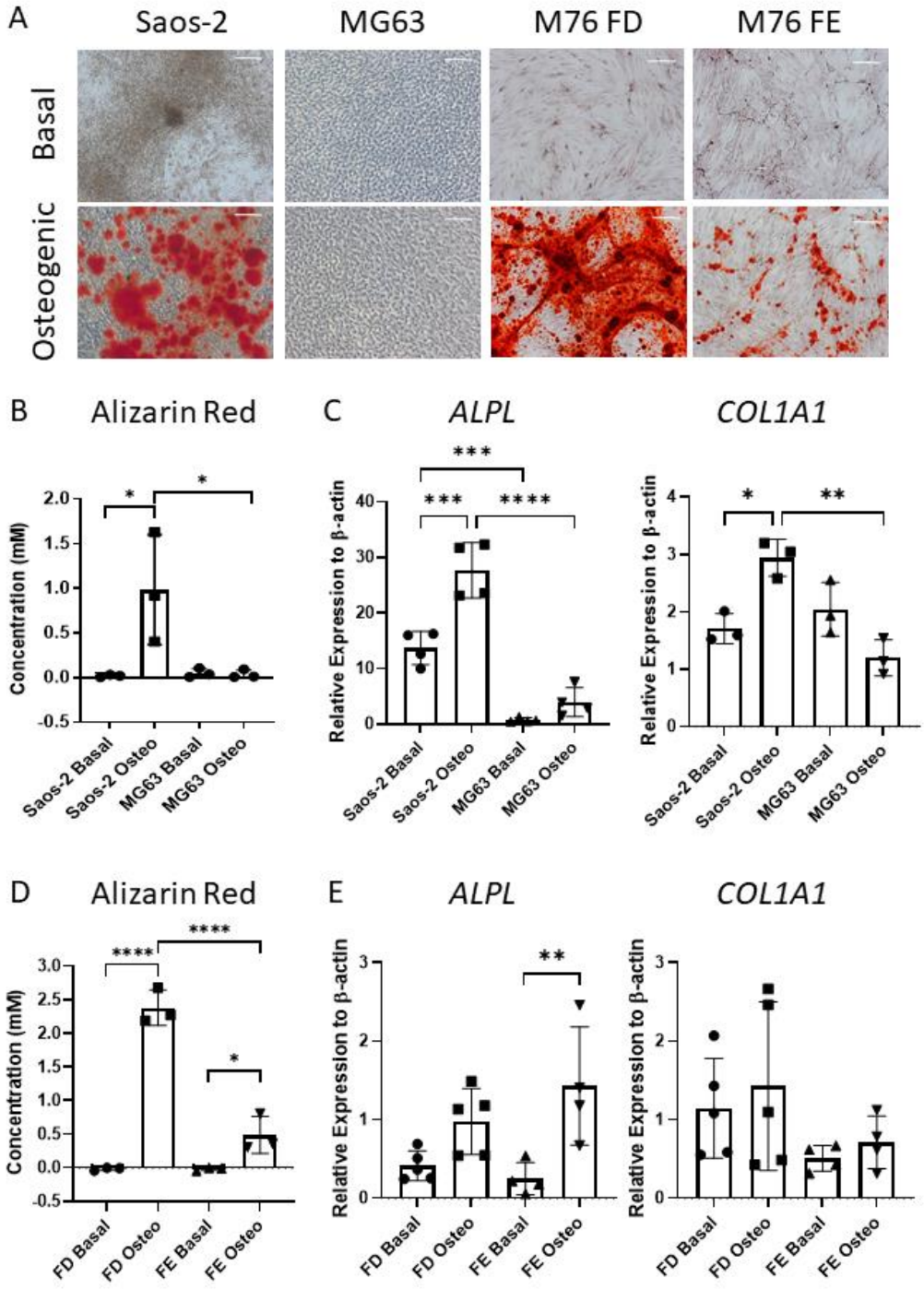

Figure 3-4. Osteogenic differentiation and mineralisation of HBMSCs and osteosarcoma cell lines. *FD and FE HBMSCs as well as Saos-2 and MG63 osteosarcoma cell lines, were cultured in basal or Osteogenic II and Mineralisation media for 28 days. (A) Alizarin red stains areas of mineralisation red, demonstrating osteogenic differentiation. Scale bar= 100 µm. Alizarin Red quantification was performed of (B) osteosarcoma cell lines and (D) HBMSCs, absorbance analysed at 405nm. Gene expression analysis of* ALPL *and* COL1A1 *as a relative expression to β-Actin for (C) osteosarcoma cell lines and (E) HBMSCs was performed by qPCR. N=3-5 each with three technical replicates. Results presented as mean +/- SD. Significance determined using a one-way ANOVA, significance presented as *<0.05, ** <0.01, ***<0.001, ****<0.0001.*

3.2.4 Adipogenic Differentiation

Alongside osteogenic differentiation, the production of adipocytes is another tri-lineage differentiation pathway. To analyse the HBMSC and osteosarcoma cell lines for adipogenic potential the cells were cultured in adipogenic media (Table 2-1) for 14 days. The cells were then subsequently stained with Oil Red O, which stains lipid droplets red, demonstrating adipogenic differentiation (2.2.10). The resulting Oil Red O lipid stain and qPCR data showed distinctive differences between both the cell lines and the HMBSCs. As shown in Figure 3-5A, both FD and FE cells differentiated into adipogenic cells with comparable morphology and similar levels of staining. In contrast, the majority of Saos-2 cells had low Oil Red O staining, while the MG63 cells had a strong Oil Red O staining, which was equally distributed across the well.

Further experiments using q-PCR (2.5.1) to analyse the HBMSCs and osteosarcoma cell lines for two markers of adipocyte differentiation, peroxisome proliferator-activated receptor γ (*PPARγ*) and fatty acid binding protein 4 (*FABP4*), supported the Oil Red O staining. The gene *PPARγ* is the main regulator of adipogenic differentiation, while *FABP4* is expressed in mature adipocytes [188]. The PPARγ and FABP4 gene expression of the basal cultured cells were too low to be analysed, for both osteosarcoma cell lines and HBMSCs, but the expression of the adipogenic cultured cells was compared. Figure 3-5B demonstrated higher expression of both *FABP4* and *PPARγ* in the MG63 cells compared with the Saos-2, although the expression for both genes was lower than for the HBMSCs. Five HBMSC donors were analysed for the gene expression of *FABP4* and *PPARγ.* For three out of five donors there was a higher level of *PPARγ* expression in the FE cells compared with the FD, where two of these donors showed a significantly higher expression. The remaining two donors demonstrated very similar low levels of *PPARγ* in both FD and FE cells. In contrast the FE cells showed a lower level of *FABP4* expression compared with FD, although this was only significant in one of the donor samples (F52). In all cell types qPCR expression does not necessarily correlate directly to the levels of Oil Red O staining.

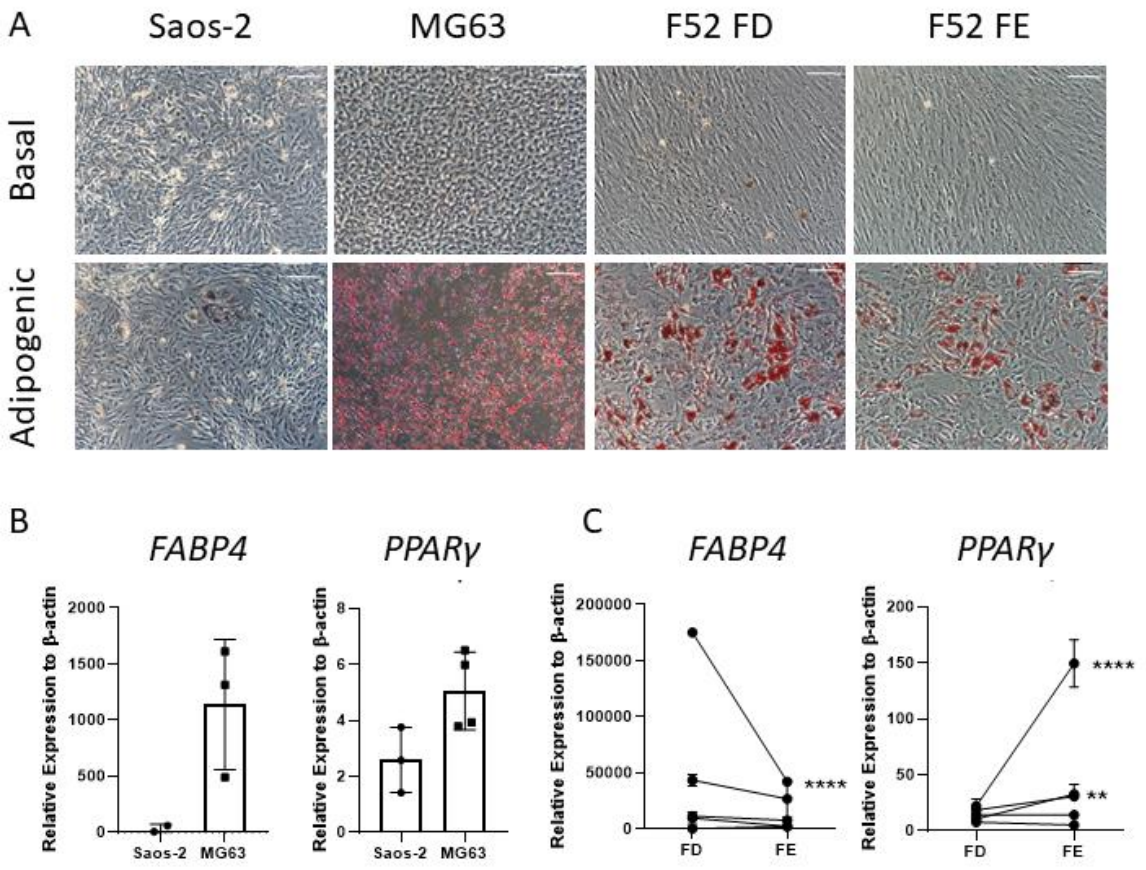

Figure 3-5. Adipogenic differentiation of HBMSCs and osteosarcoma cell lines*. FD and FE HBMSCs as well as Saos-2 and MG63 osteosarcoma cell lines, were cultured in basal or Adipogenic media for 14 days. (A) Adipogenic cells release lipid droplets which are stained by the Oil Red O (red). Scale bar = 100 µm. (B) Gene expression analysis of* FABP4 *and* PPARγ *as a relative expression to β-Actin for osteosarcoma cell lines was performed by qPCR, N=3 each with three technical replicates. Results presented as mean +/- SD, significance determined using a student's T test. (C) Gene expression analysis of* FABP4 *and* PPARγ *in HBMSCs was performed by qPCR, N=5 each with three technical replicates. Results presented as mean +/- SD, significance determined using a one-way ANOVA. For both statistical analysis significance presented as ** <0.01, ****<0.0001.*

3.2.5 Chondrogenic Differentiation

The final tri-lineage differentiation pathway is the ability to produce chondrocytes. To determine this, HBMSCs and osteosarcoma cell lines were formed into pellets and cultured in chondrogenic media (Table 2-1) for 28 days. Chondrocytes are routinely generated in spheroid culture as monolayer culture has been shown to decrease chondrogenic potential [189]. The pellets were then either fixed, embedded in paraffin, sectioned and stained for SOX9 (2.2.11), or lysed for

qPCR analysis (2.5.1). SOX9 is a transcription factor that is expressed in chondrocytes and is involved in early cartilage development [190]. Figure 3-6A are representative images of SOX9 staining, the Saos-2 osteosarcoma cell line showed no SOX9 staining, while the MG63 cells and the HBMSCs showed an increased level of SOX9 staining in the chondrogenic cultured pellets compared with the basal. Gene expression of three markers of chondrogenic differentiation, *COL2A1, SOX9*, and *ACAN* was determined by qPCR. Collagen II (*COL2A1*) is one of the major components of the cartilage matrix and has been found to regulate chondrocyte metabolism, differentiation and proliferation [191]. Aggrecan (*ACAN*) is present in articular cartilage, and is import in the structure and function of the cartilage [192]. Figure 3-6B showed the MG63 chondrogenic pellets had a significant increase in *SOX9* expression compared with the MG63 basal control and also to the Saos-2 chondrogenic pellets. Similar to the images in Figure 3-6A the level of *SOX9* in the Saos-2 cells was very low. In contrast to the *SOX9* expression, *COL2A1* was significantly increased in the Saos-2 chondrogenic pellets compared with both the Saos-2 basal control and the MG63 chondrogenic pellets. *ACAN* expression was similar in both Saos-2 and MG63 chondrogenic pellets, and for both cell lines there was an increase in the chondrogenic pellet compared with the basal control. Figure 3-6C showed the gene expression in the HBMSCs, where there was an increase in all three genes in the FD chondrogenic pellets compared with the FE chondrogenic pellets, although this was only significant for *ACAN*. While a clear increase could be seen in all genes for FD chondrogenic pellets compared with the FD basal control, there was no difference in the FE chondrogenic pellets compared to the FE basal control. This suggested that the FD chondrogenic pellet culture had resulted in a more mature chondrogenic phenotype than the FE chondrogenic pellet cultures.

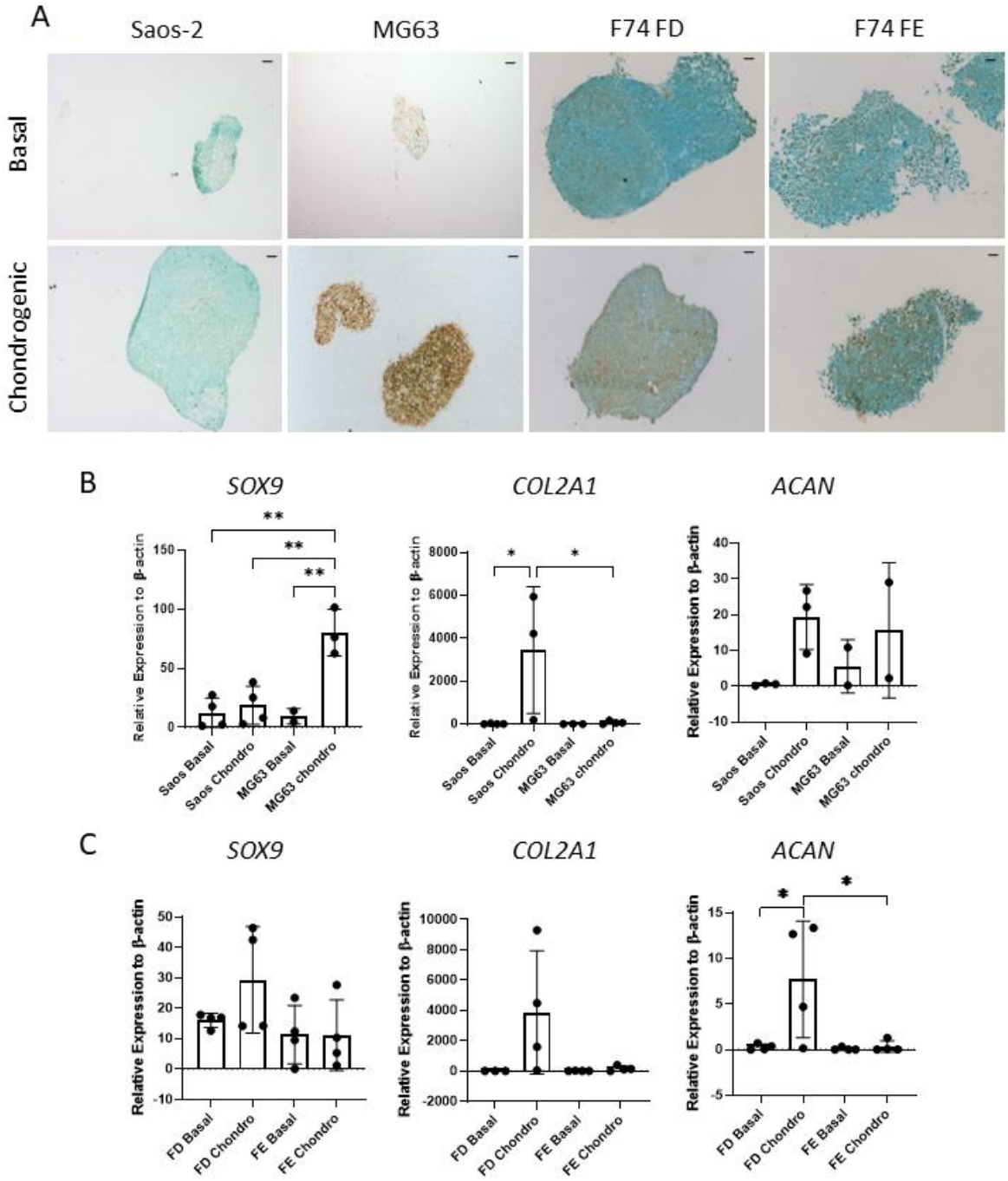

Figure 3-6. Chondrogenic differentiation of HBMSCs and osteosarcoma cell lines*. A pellet culture of FD and FE HBMSCs as well as Saos-2 and MG63 osteosarcoma cell lines, were cultured in basal or chondrogenic media for 28 days. (A) SOX9 staining of basal and chondrogenic cultured cell pellets. SOX9 stained brown, proteoglycans stained blue with alcian blue, Scale bar = 100 µm. Gene expression analysis of* SOX9*, Aggrecan (*ACAN*) and Collagen II (*COL2A1*) as a relative expression to β-Actin were performed by qPCR for (B) osteosarcoma cell lines Saos-2 and MG63 (N=3), and (C) FD and FE HBMSCs (N=4). Results presented as relative expression to β-actin +/- SD, significance determined using a one-way ANOVA, significance presented as *<0.05 and ** <0.01.*

3.2.6 Examining HBMSC differentiation when co-cultured with Saos-2 Osteosarcoma cells

Ectopic bone formation is common in osteosarcoma patients, which could be a result of an increase in osteoblasts present in the tumour microenvironment regulated by the cancer cells. To quantify whether osteosarcoma cells have an effect on the osteogenic potential of stromal cells, HBMSCs and the Saos-2 osteosarcoma cell line were co-cultured using transwells in basal and osteogenic I media for 7 and 14 days (2.2.12). The supernatant was analysed for IL-6 expression (2.5.2), as it is a regulator of the osteoblast/ osteoclast activation pathway, as well as being secreted by stromal cells to enhance migration and metastasis of tumours [79]. The cells were then lysed for either ALP analysis (2.2.8) or qPCR analysis (2.5.1). Figure 3-7 shows the level of ALP, DNA concentration and specific activity of the FD and FE cells cultured in basal media after 7 (B) and 14 (C) days. Transwells with the same HBMSC on both the bottom and in the insert were used as a control to determine whether any differences seen were a result of the Saos-2 cells, or an increase in cell number. Although there was a high level of donor variability, with donor F79 having a high level of DNA concentration at both 7 and 14 days suggesting an increased cell number, there was no difference in either ALP expression or specific activity between both FD and FE cells cultured with and without Saos-2 cells. There was also no difference in ALP expression and specific activity when HBMSCs were cultured in osteogenic media with and without Saos-2 cells in Figure 3-8, after 7 (B) and 14 (C) days.

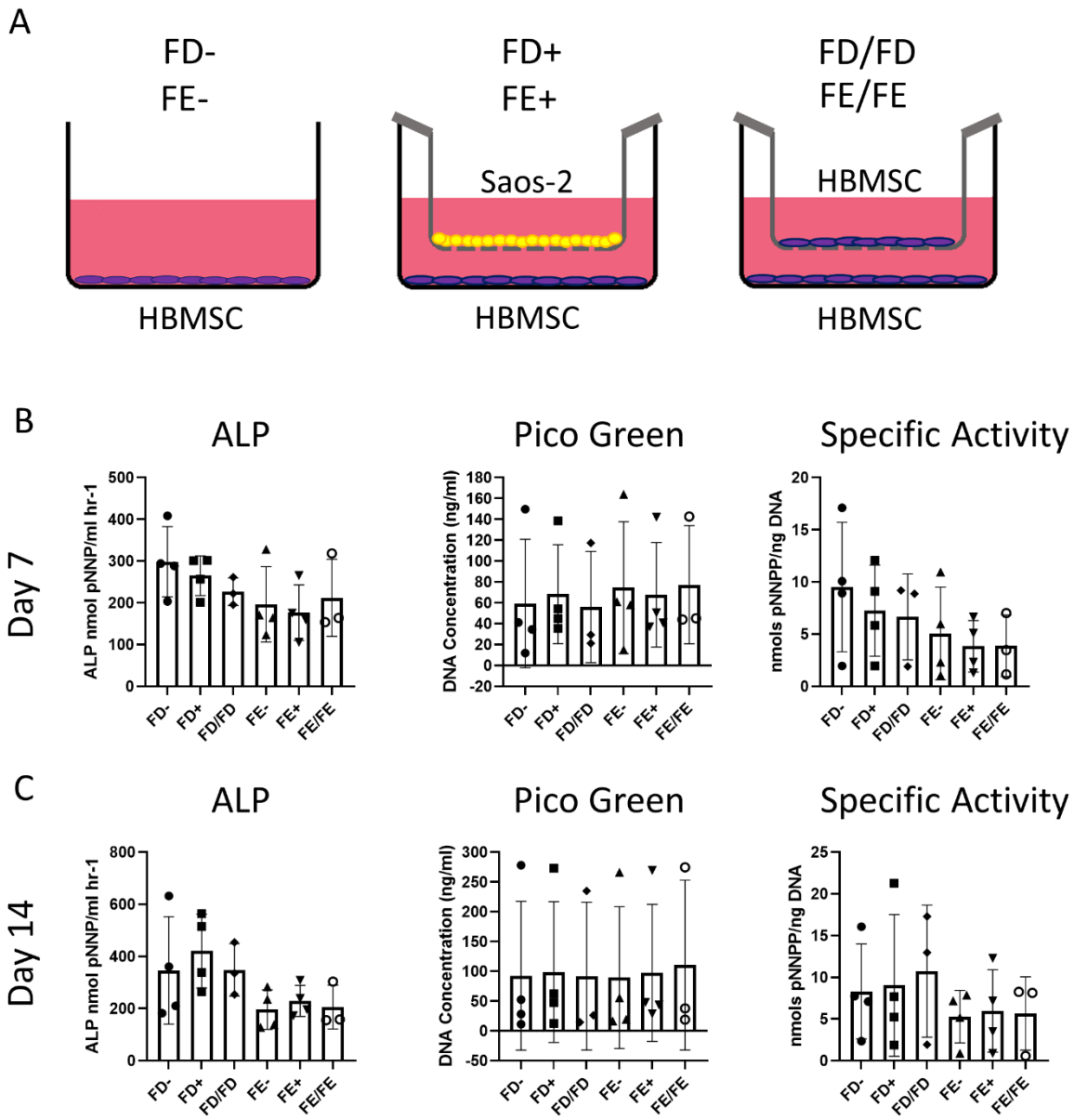

Figure 3-7. Early osteogenic differentiation of HBMSCs co-cultured with Saos-2 cells in basal media. *(A) A schematic of the transwell assay. ALP analysis, DNA concentration and ALP specific activity after (B) 7 days or (C) 14 days in basal media. N=4 each with three technical replicates. Results presented as mean +/- SD, statistics analysed using a one-way ANOVA, no significance found.*

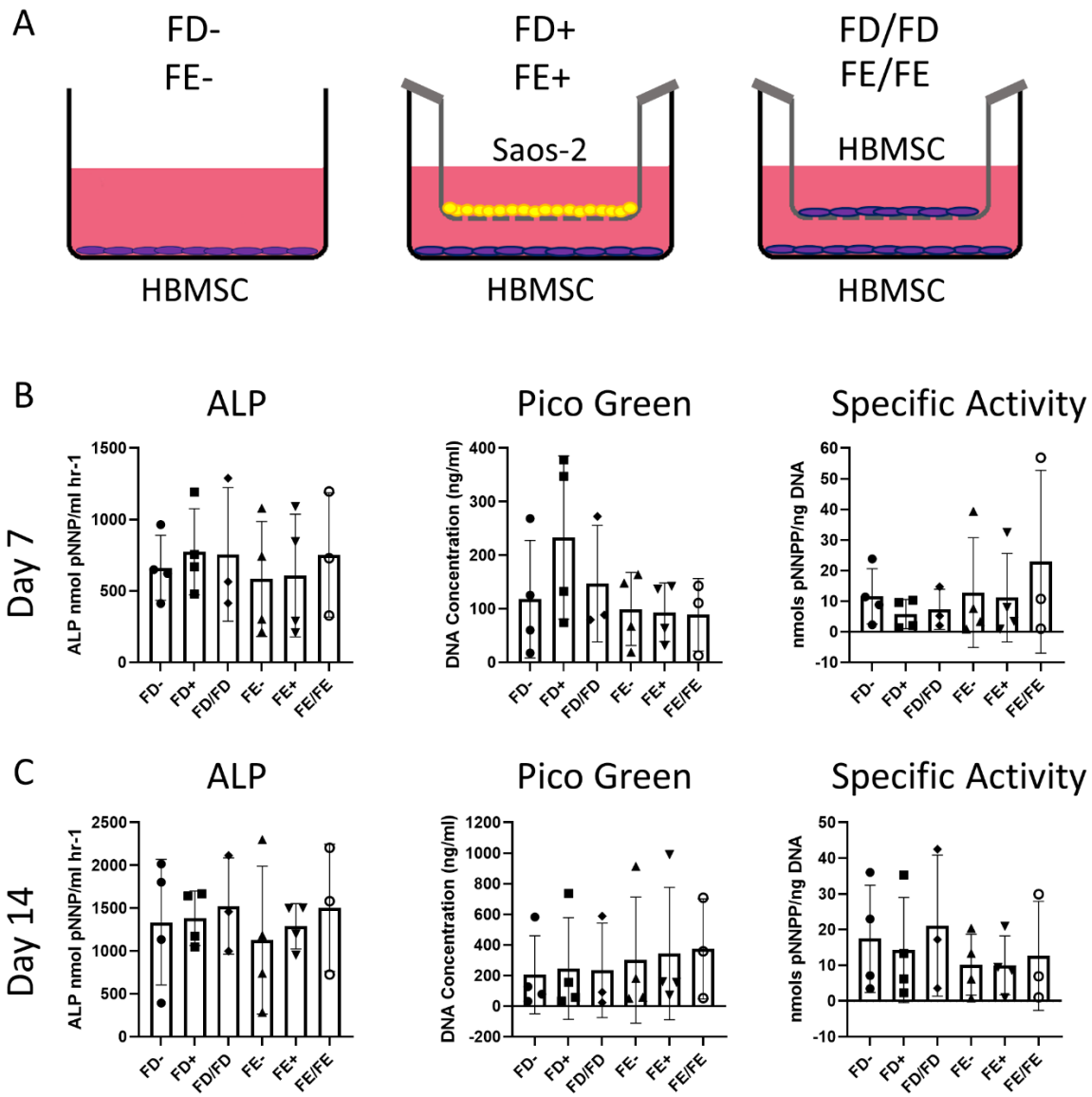

Figure 3-8. Early osteogenic differentiation of HBMSCs co-cultured with Saos-2 cells in osteogenic media*. (A) A schematic of the transwell assay. ALP analysis, DNA concentration and ALP specific activity after (B) 7 days or (C) 14 days in osteogenic media. N=4 each with three technical replicates. Results presented as mean +/- SD, statistics analysed using a one-way ANOVA, no significance found.*

The cells were further analysed by qPCR analysis at day 7 (Figure 3-9), after culture in both basal (A) and osteogenic (B) media. There was no difference in expression of *ALPL,* HIF1α *(HIF1A)*; a marker of hypoxia, Ki67 *(MKI67)*; a proliferation marker, or Osterix (*SP7);* a mature osteogenic marker, when FD and FE HBMSCs were cultured with and without Saos-2 cells. This was true for both basal and osteogenic media. One of the three donor samples, F13, showed a markedly higher expression of all four genes tested compared with the other two donor samples,

suggesting there was large donor variability when culturing cells in these 2D assays. Figure 3-10 illustrated the gene expression for HBMSCs cultured with and without Saos-2 cells in (A) basal or (B) osteogenic media for 14 days. Similar to Figure 3-9, there was no difference in gene expression for the cells cultured in basal media. This was also the case for the majority of data generated from the osteogenic cultured cells, with exceptions for *ALPL* and *HIF1A*. Although not significant *HIF1A* expression showed a higher trend when FD cells were co-cultured with Saos-2, and *ALPL* expression was lower in both FD and FE cells cultured with Saos-2 cells compared with FD and FE cells cultured alone.

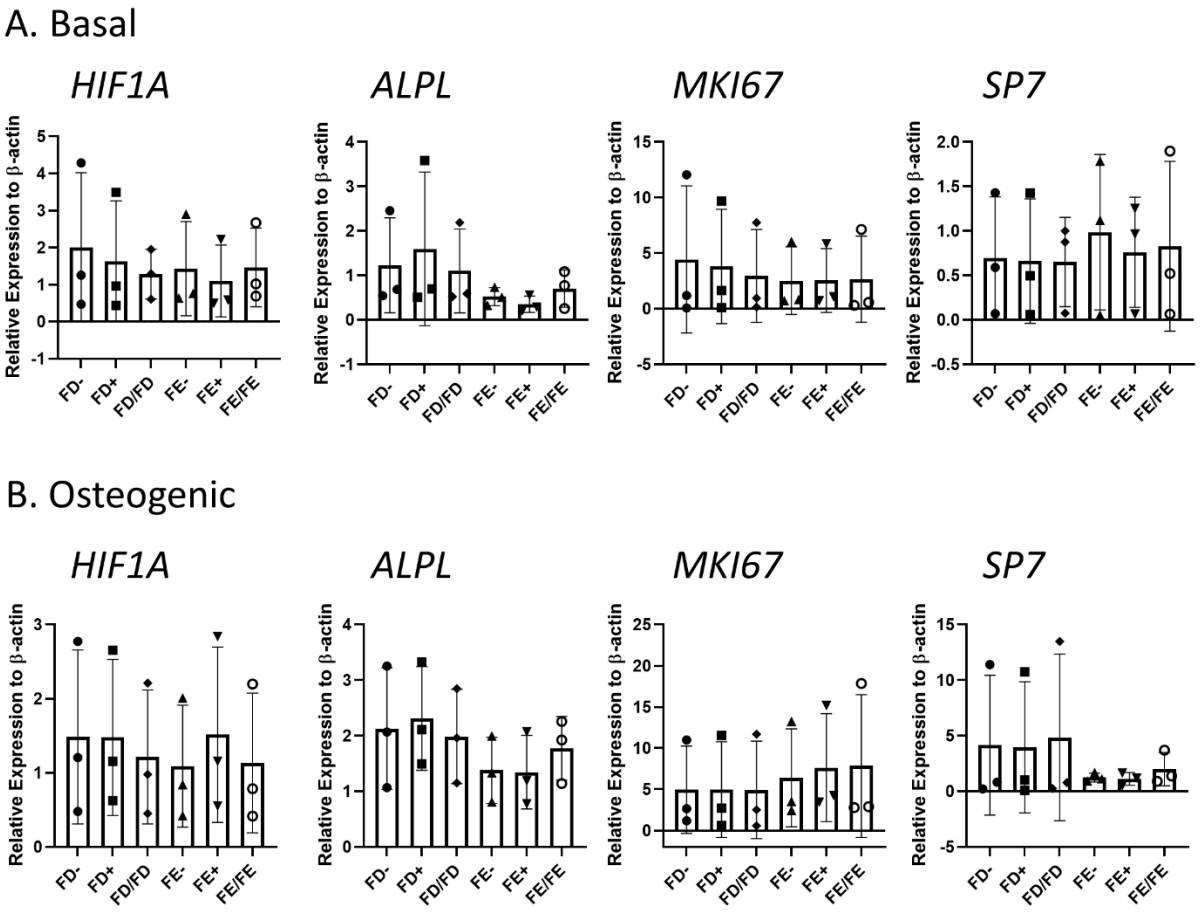

Figure 3-9. Gene expression analysis of HBMSCs co-cultured with Saos-2 cells for 7 days*. Gene expression analysis of* HIF1A, ALPL, MKI67 *and* SP7 *as a relative expression to β-Actin, after a 7 day incubation in (A) Basal or (B) osteogenic media, performed by qPCR. N=3 each with three technical replicates. Results presented as mean +/- SD. Statistics analysed using a one-way ANOVA, no significance found.*

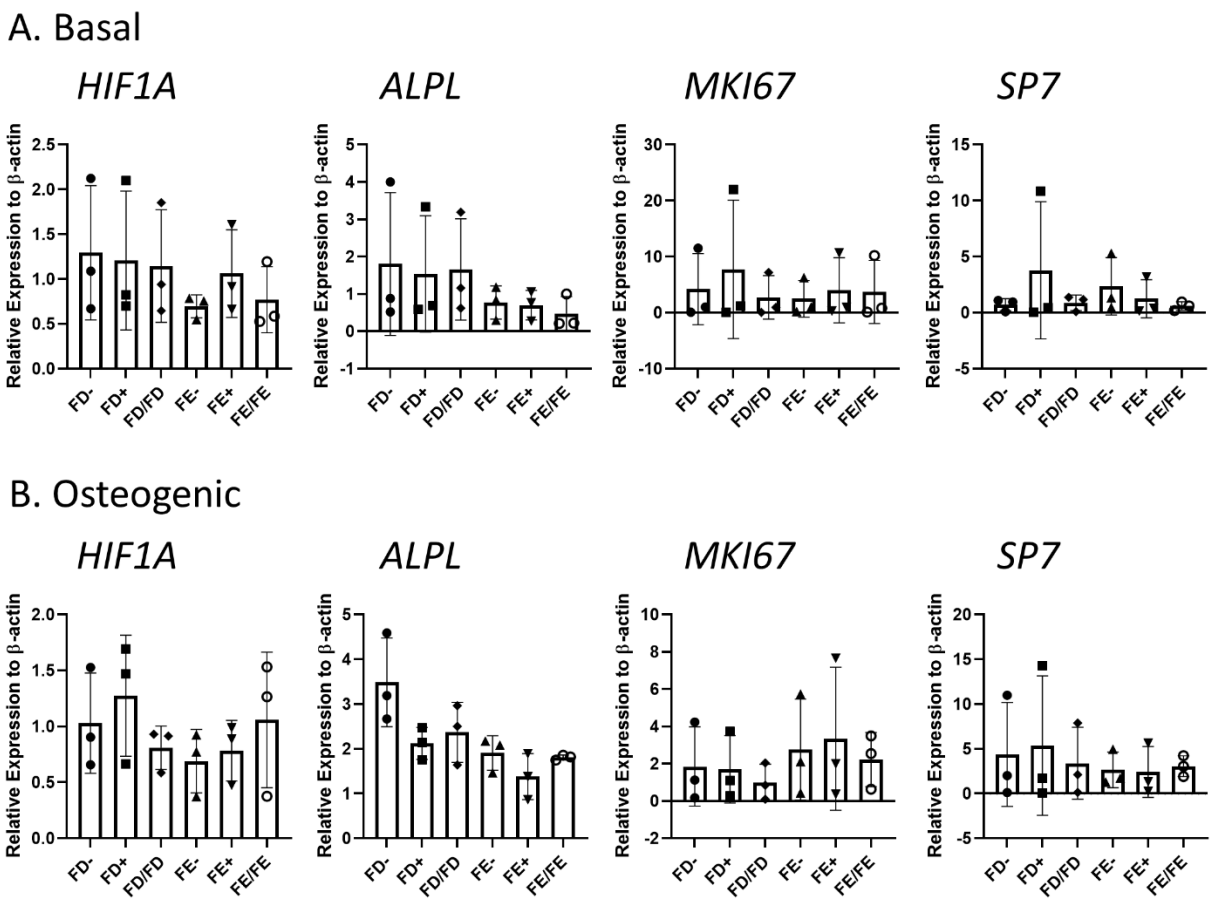

Figure 3-10. Gene expression analysis of HBMSCs co-cultured with Saos-2 cells for 14 days*. Gene expression analysis of* HIF1A, ALPL, MKI67 *and* SP7 *as a relative expression to β-Actin, after 14 days incubation in (A) Basal or (B) osteogenic media, performed by qPCR. N=3 each with three technical replicates. Results presented as relative expression to β-Actin +/- SD. Statistics analysed using a one-way ANOVA, no significance found.*

IL-6 has been shown to be involved in the osteosarcoma microenvironment, where it has been found to be upregulated in the presence of cancer. IL-6 expression was analysed from the supernatant of the transwells. Figure 3-11 showed the secretion of IL-6 after 7 and 14 days of culture in basal and osteogenic media, normalised to media only controls. As expected, based on the ALP and gene expression data, there was a large donor variability in the secretion of IL-6, particularly in the osteogenic media cultured cells. Although a small increase of IL-6 secretion can be seen at day 14, for both FD and FE cells cultured with Saos-2 cells in basal media compared to their respective controls, this was not significant, furthermore there was no difference in IL-6 secretion for all other cell conditions. Finally, the level of proliferation of the FD and FE cells cultured in the transwell assay was tested at day 7 and 14, for both basal and osteogenic conditions (Figure 3-12). Similarly, to previous transwell data, there was no difference in the

proliferation of the HBMSCs when cultured with and without Saos-2 cells in all four conditions, with a high level of donor variability.

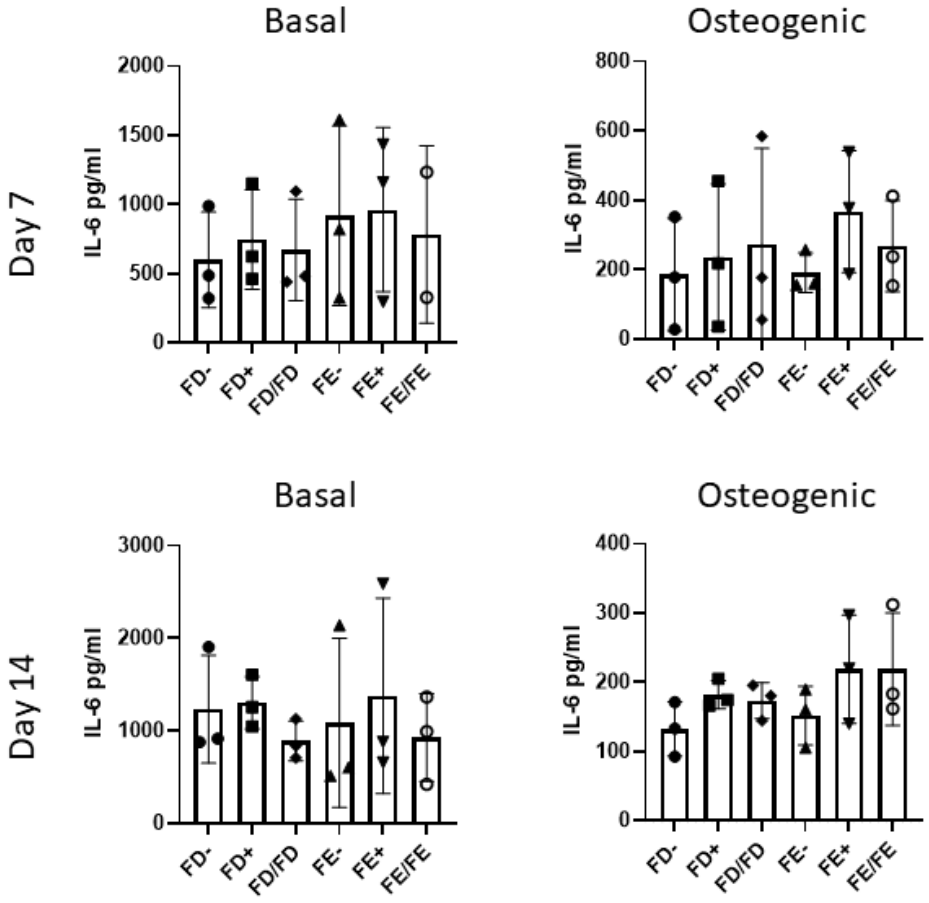

Figure 3-11. IL-6 activity of HBMSCs co-cultured with Saos-2 cells*. The concentration of IL-6 was determined via an ELISA assay at day 7 and 14, after incubation in basal and osteogenic media. Media only controls were used as a control to normalise data. N=3 each with three technical replicates. Results presented as mean +/- SD, statistics analysed using a one-way ANOVA, no significance found.*

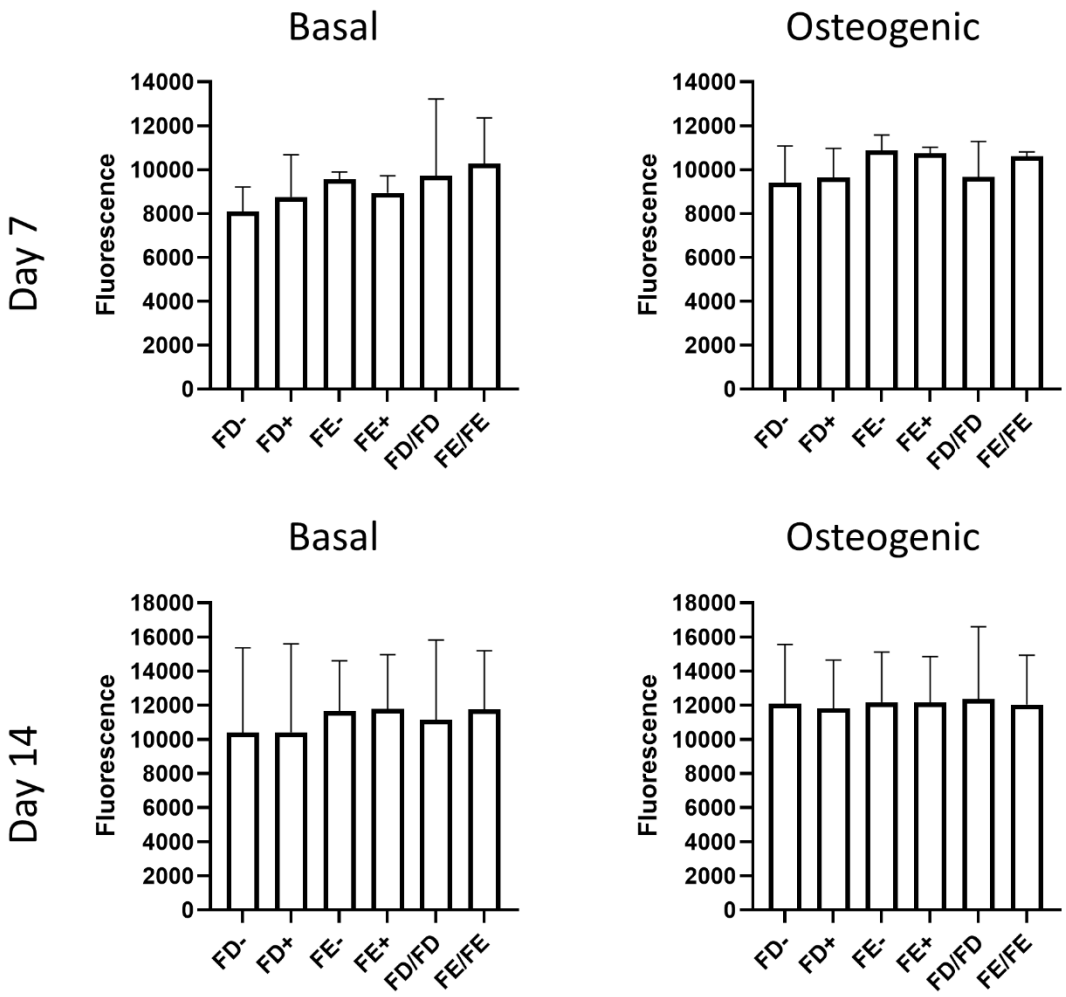

Figure 3-12. Proliferation of HBMSCs co-cultured with Saos-2 cells*. The proliferation of the HBMSCs was determined by a 2 hour incubation with alamar blue at day 7 and 14, after incubation in basal and osteogenic media. Fluorescence was read at 560 nm. N=2 each with three technical replicates. Results presented as mean +/- SD, statistics analysed using a one-way ANOVA, no significance found.*

3.2.7 The Effect of Mifamurtide on HBMSCs and Osteosarcoma Cell lines Saos-2 and MG63

The drug Mifamurtide is used to treat patients with osteosarcoma, and is the main treatment given with post-operative chemotherapy. There have been several studies looking at the effect Mifamurtide has on macrophages in patients with osteosarcoma [193, 194], but very few have focussed on other cell types found in the tumour microenvironment. To assess whether Mifamurtide has any effect on the cell proliferation of HBMSCs; FD and FE cells were cultured with increasing concentrations of Mifamurtide for 24 hours, before the level of proliferation was assessed by alamar blue (2.2.7). Literature indicated Mifamurtide (not in the liposomal formulation) have been used at high concentrations of 100 µM [195] on macrophages and MG63

cells. This was not possible with the Mifamurtide used in these experiments (in liposomal formulation). The drug was reconstituted at 1.6 µg/ml, which equated to 64.6 µM. The top concentration used in these experiments was 32.3 µM (0.8 µg/ml), which allowed for a 1:1 Mifamurtide to basal media ratio. Figure 3-13 showed Mifamurtide had no effect on the proliferation of both FD and FE cells at four different cell concentrations. The cell concentrations were chosen as they represented the initial exponential growth phase as found in Figure 3-1.

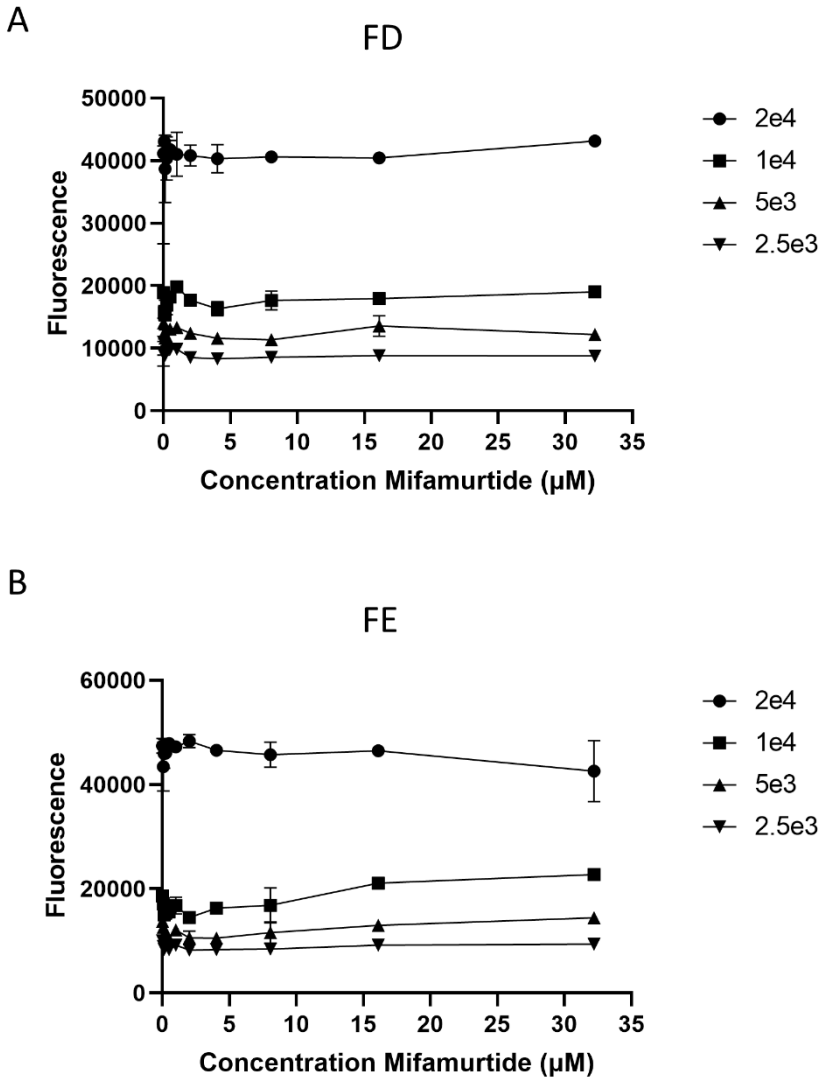

Figure 3-13. Proliferation of HBMSCs after 24 hour incubation with Mifamurtide*. (A) FD and (B) FE HBMSCs were seeded at four cell densities and cultured with increasing concentrations of Mifamurtide for 24 hours, before a 2 hour incubation in alamar blue. Fluorescence was read at 560 nm. N=1, with three technical replicates. Results presented as mean +/- SD.*

FD and FE cells were then cultured with a range of Mifamurtide concentrations for 7 days before being lysed for ALP analysis (2.2.8). Figure 3-14 showed the level of ALP expression was first

enhanced then inhibited by increasing concentrations of Mifamurtide. The peak of the curve differed between FD and FE cells, where FD reached its peak at around 4 µM, while FE started decreasing after 2 µM of Mifamurtide. In contrast, there was a similar level of DNA concentration for both FD and FE at all concentrations except for the highest concentration, which showed a decrease in DNA concentration. This suggested Mifamurtide had no effect on cell proliferation until 32.3 µM. The FE cells had only a small increase in specific activity as the level of Mifamurtide increased, although a small peak can be seen at 2 µM. In comparison the FD cells showed an increase up to 4 µM, before the specific activity started to decrease, following a similar pattern to the ALP data, suggesting low levels of Mifamurtide can increase the osteogenic potential of FD cells.

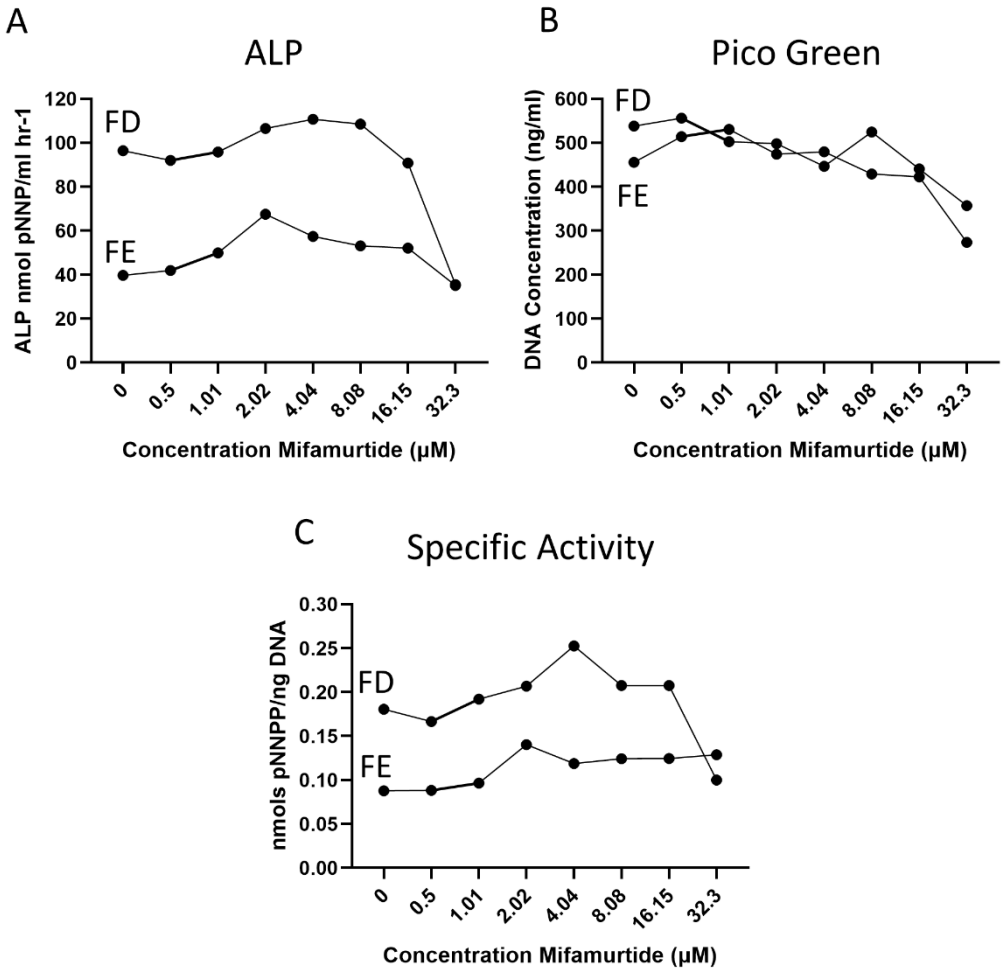

Figure 3-14. Early osteogenic differentiation of HBMSCs after incubation with Mifamurtide*. (A) ALP analysis, (B) DNA concentration and (C) ALP specific activity after 7 days in basal media supplemented with increasing concentrations of Mifamurtide. N=1 with three technical replicates. Results presented as mean.*

After HBMSCs demonstrated an increase in ALP at lower concentrations of Mifamurtide, the osteosarcoma cell lines Saos-2 and MG63 were also cultured with Mifamurtide for 7 days before they were analysed for ALP expression (Figure 3-15). Increasing concentrations of Mifamurtide on Saos-2 cells showed very little effect on the expression of ALP specific activity until the highest concentration of 32.3 µM (0.8 µg/ml), which was lower than the basal control. In contrast, the increased concentration of Mifamurtide correlated with a small increase in ALP expression and specific activity for the MG63 cells, although overall it was still very low, suggesting no osteogenic differentiation occurred.

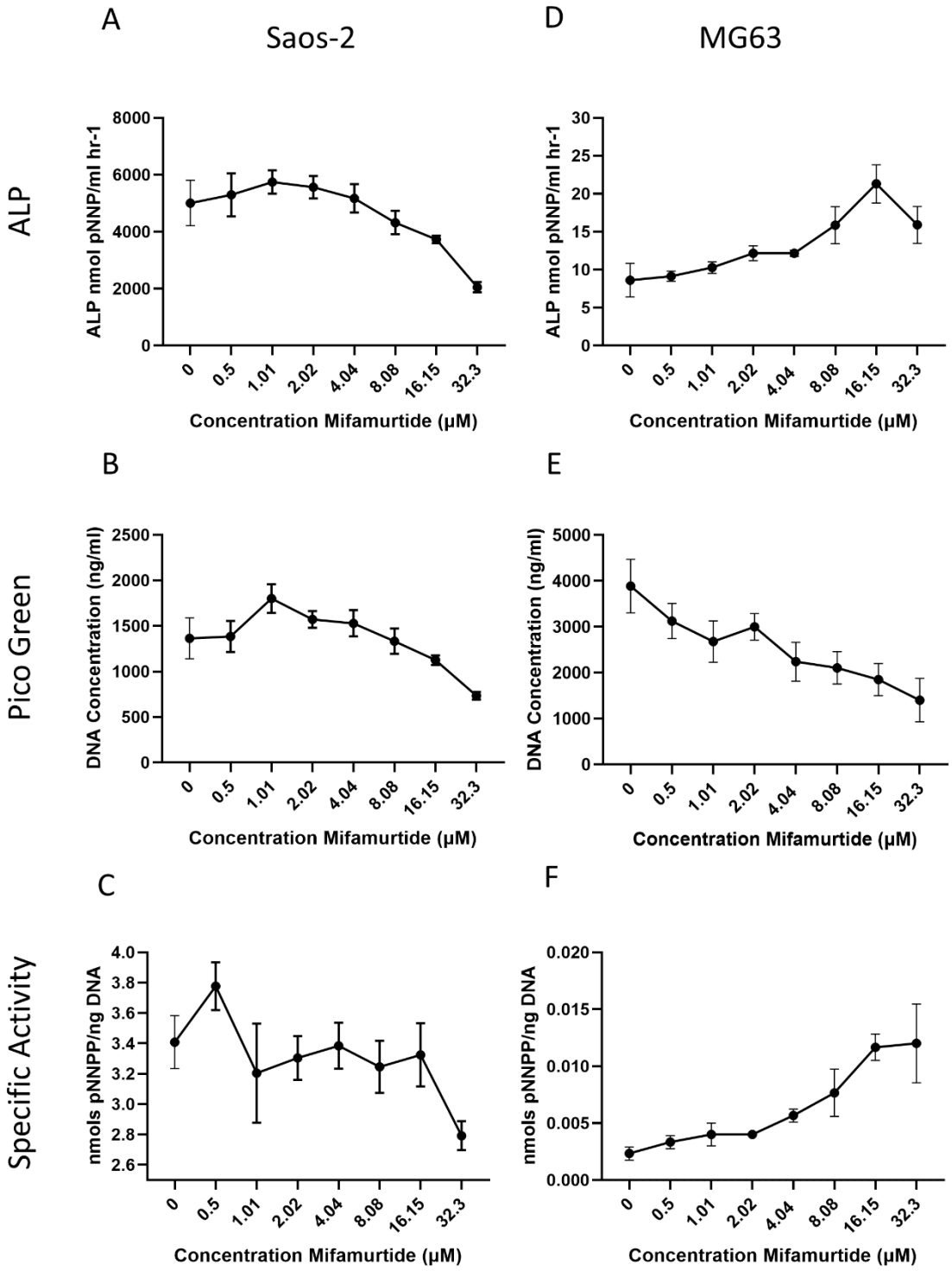

Figure 3-15. Early osteogenic differentiation of osteosarcoma cell lines after incubation with Mifamurtide*. (A) ALP analysis, (B) DNA concentration and (C) ALP specific activity of Saos-2 cells, alongside the (D) ALP analysis, (E) DNA concentration and (F) ALP specific activity of MG63 cells. Cells were cultured for 7 days in basal media supplemented with increasing concentrations of Mifamurtide. N=1 with three technical replicates. Results presented as mean +/- SD.*

3.2.8 Osteoblast Phenotype after Co-Culture with Saos-2 Cells

Evidence has suggested osteoblasts are important in the osteosarcoma tumour microenvironment, which often involves unexplained bone remodelling as a result of cytokine expression by tumour cells [62]. To investigate the effects of Saos-2 cells on the characterisation of osteoblasts, a transwell system was used to culture human osteoblasts in the presence (OB+) or absence (OB-) of Saos-2 cells. The cells were cultured in basal media for 7 and 14 days (2.2.12). The resulting supernatant from the co-cultured cells was analysed for IL-6 expression (2.5.2), while the cells were either lysed for ALP (2.2.8) or qPCR analysis (2.5.1). Figure 3-16A showed similar ALP and specific activity at day 7 regardless of the presence of Saos-2 cells. However, at day 14 (Figure 3-16B) there was a decreased trend in ALP, DNA concentration and specific activity when co-cultured with Saos-2 cells.

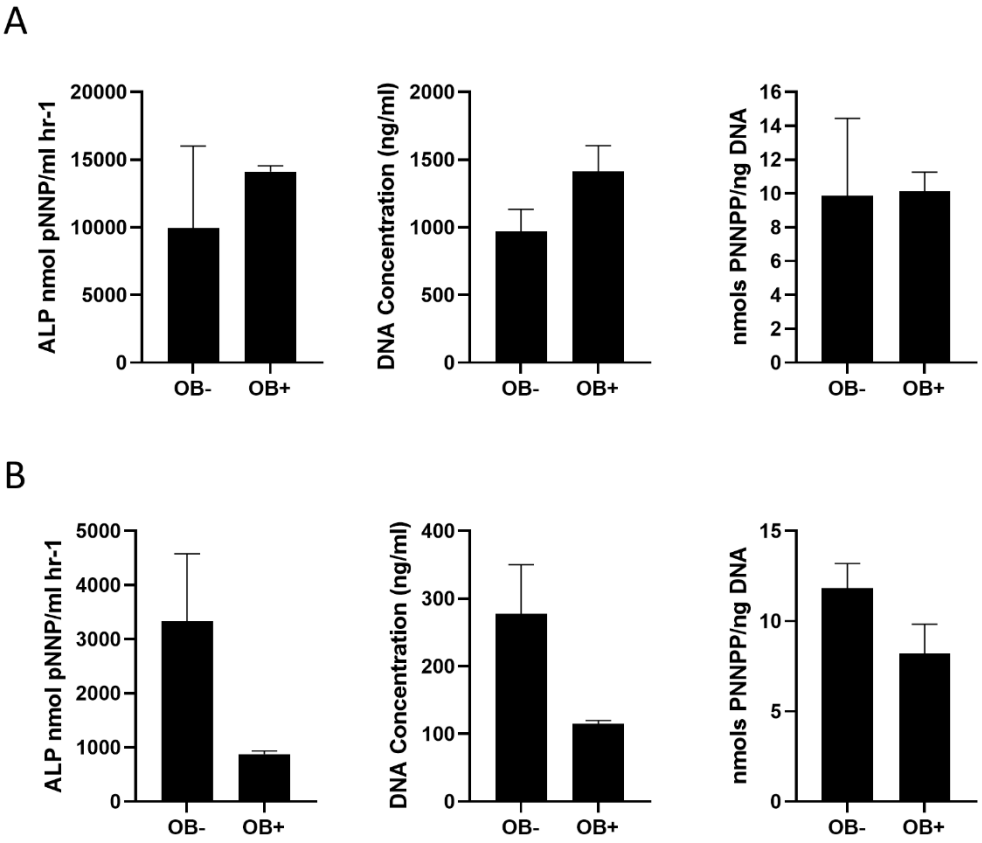

Figure 3-16. Early osteogenic activity of osteoblasts co-cultured with Saos-2 cells*. ALP analysis, DNA concentration and ALP specific activity after (A) 7 days or (B) 14 days in basal media. N=1 with three technical replicates. Results presented as mean +/- SD, statistics analysed using student T test, no significance found.*

The IL-6 expression for both day 7 and day 14 also showed a downward trend when co-cultured with Saos-2 cells (Figure 3-17A), which was significant at day 14. Similarly, the qPCR analysis of these cells at day 7 (Figure 3-17B) demonstrated decreased expression of *ALPL, HIF1A* and *SP7*, when osteoblasts were co-cultured with Saos-2 cells. This decrease in expression was significant in *HIF1A*. There was also an increase in *MKI67* expression when the osteoblasts were cultured with Saos-2 cells, suggesting an increase in proliferation.

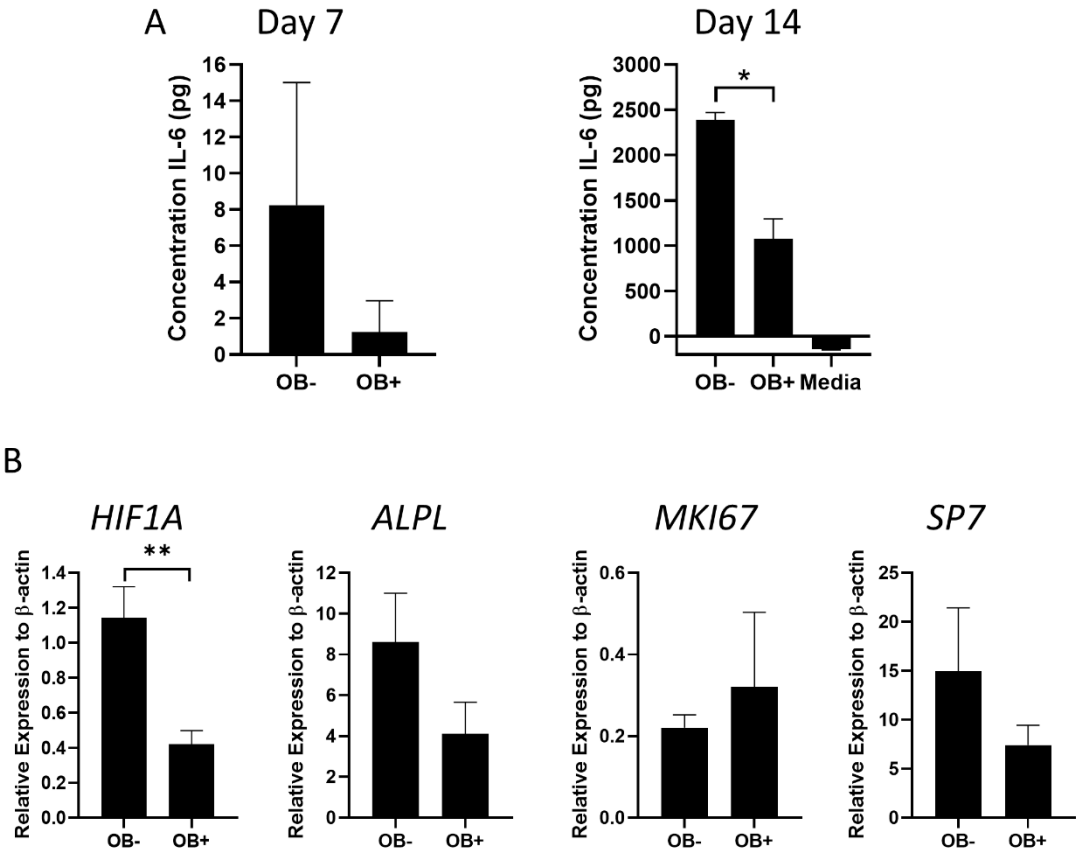

Figure 3-17. IL-6 and gene expression analysis of osteoblasts co-cultured with Saos-2 cells*. (A) The concentration of IL-6 determined via an ELISA assay at day 7 and 14 of incubation in basal media. (B) Gene expression analysis of* HIF1A, ALPL, MKI67 *and as a relative expression to β-Actin, was performed by qPCR. N=1 with three technical replicates. Results presented as mean +/- SD. Statistics analysed using student T test, significance presented as *<0.05, ** <0.01.*

3.2.9 Fetal Bone Marrow Differentiation when Co-cultured with Saos-2 Cells

The first peak of incidence in osteosarcoma patients is around adolescence, while the human bone marrow samples received were from donors above the age of 50. The difference in age and disease, most donors had osteoarthritis or osteoporosis, could have impacted the similarity of the bone marrow environment during development of the 3D bone model. Fetal bone marrow

contains a high level of progenitor cells [186], which could be more relevant to adolescent bone marrow than the older donors. To test this proposition, fetal bone marrow and the Saos-2 osteosarcoma cell line were co-cultured using transwells in basal media for 10 days (2.2.12). The supernatant was analysed for IL-6 expression (2.5.2), while the cells were either lysed for ALP analysis (2.2.8) or qPCR analysis (2.5.1). Figure 3-18A showed there was no difference in ALP expression, DNA concentration or specific activity when co-cultured with and without Saos-2 cells. In contrast, Figure 3-18B illustrated there was a significant decrease in IL-6 expression when fetal bone marrow was co-cultured with Saos-2 cells. This pattern was replicated in *ALPL* gene expression although the relative expression was very low, and also in *HIF1A* (Figure 3-18C), where there was a significant decrease in the *HIF1A* expression. In contrast, there was an increase in *MKI67* expression when fetal bone marrow cells were co-cultured with Saos-2 cells. Suggesting that while the level of proliferation increased when fetal bone marrow cells were co-cultured with Saos-2 cells, the levels of osteogenic differentiation and hypoxia decreased.

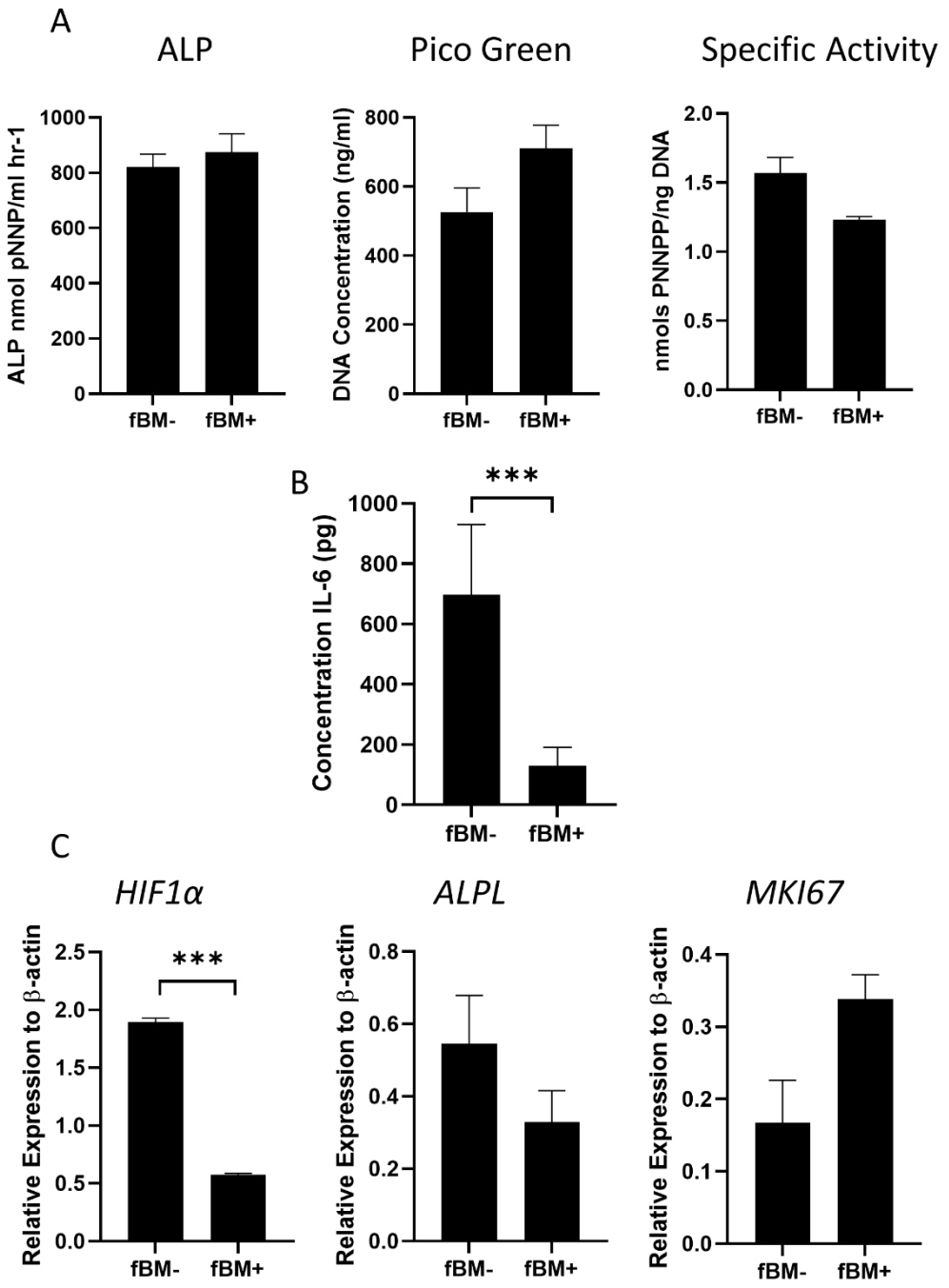

Figure 3-18. Analysis of fetal bone marrow cells co-cultured with Saos-2 cells*. (A) ALP analysis, DNA concentration and ALP specific activity of fetal bone marrow cells co-cultured with Saos-2 after 10 days in basal media. (B) The concentration of IL-6 determined via and ELISA assay. (C) Gene expression analysis of* HIF1A, ALPL *and* MKI67 *as a relative expression to β-Actin, was performed by qPCR. N=1 with three technical replicates, Results presented as mean +/- SD. Statistics analysed using a T test, significance presented as ***<0.001.*

3.2.10 Osteogenic Differentiation of Cell Spheroids

Previous research has shown phenotypic differences between cells in a 3D and 2D culture, including through the generation of cell spheroids [152]. The generation of cell spheroids could give better indication of the cell integration and communication found in cancer patients, and as such initial 3D bone model experiments used Saos-2 spheroids to imitate the osteosarcoma tumour. To determine phenotypic differences of HBMSCs and osteosarcoma cell lines in a 3D cell spheroid, the spheroids were cultured for 4, 7 and 14 days in basal media (2.2.5) before being fixed, embedded in paraffin and stained for ALP (2.6.8). Figure 3-19 and Figure 3-21 demonstrated representative images of these cells; ALP is stained pink/brown, cytoplasm is stained with fast green and proteoglycans/cartilage is stained blue with Alcian blue. In Figure 3-19 both FD and FE cell pellets showed no ALP expression at all three time points, in contrast to 2D cell culture (see 3.2.2). The MG63 spheroids also showed no ALP staining at all three time points, but this was similar to the 2D data in 3.2.2. Saos-2 cells did not express ALP in spheroid formation until day 7, but by day 14 the ALP expression covered the entirety of the spheroid. Interestingly, a 4-day 2D culture of Saos-2 cells showed a high level of ALP expression and specific activity (Figure 3-20) when cultured in basal and osteogenic I media, suggesting the formation of spheroids initially inhibited the expression of ALP. Osteoblast and fetal bone marrow cell spheroids were also histologically analysed for the presence of ALP after culture for 4, 7 and 14 days (Figure 3-21). Osteoblasts had a strong ALP staining at day four, which was lost by day 7 but started returning by day 14. In contrast, fetal bone marrow spheroids showed no ALP staining at any time point, similar to data shown in 3.2.9.

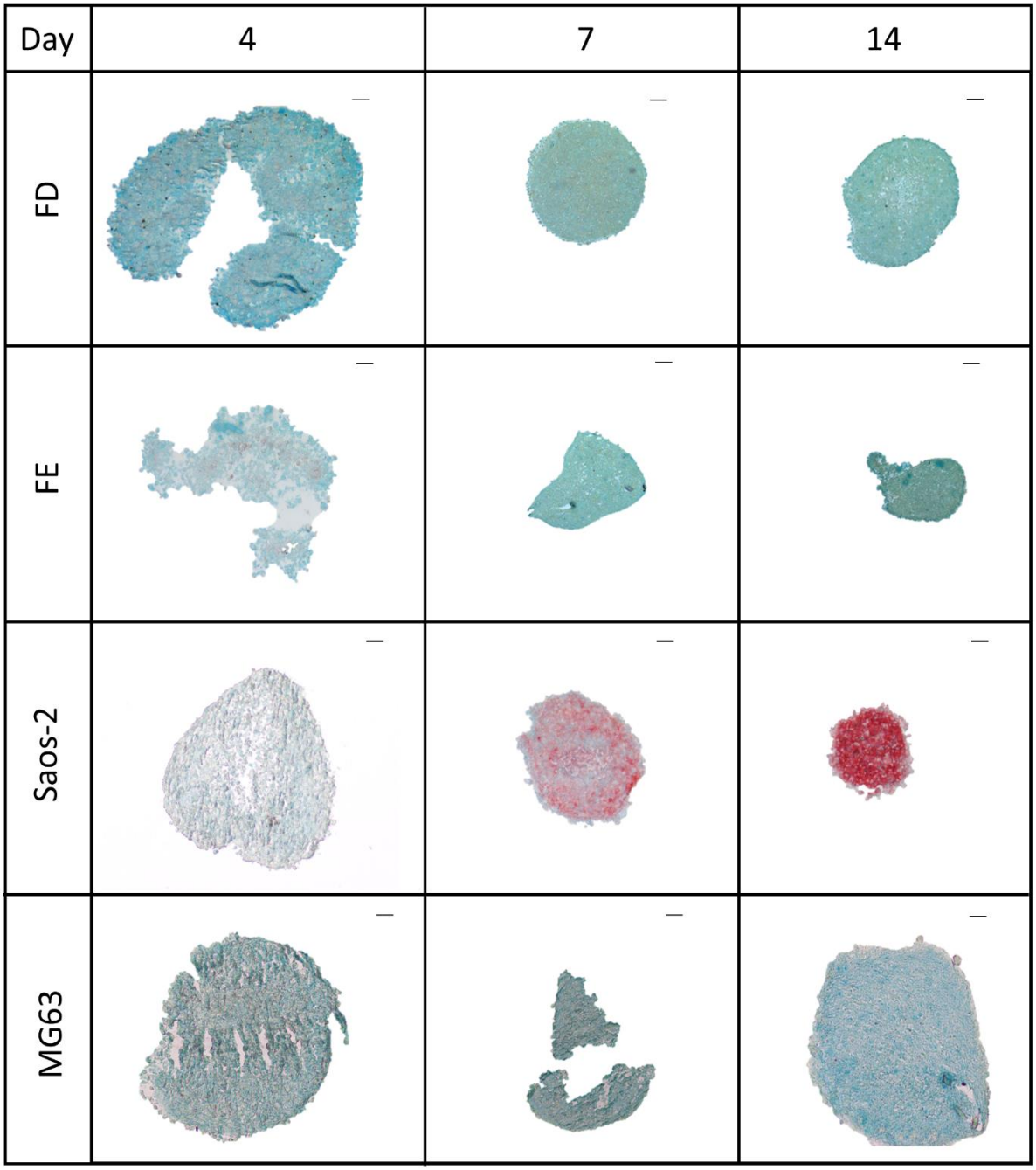

Figure 3-19. Early osteogenic differentiation of HBMSC and osteosarcoma cell line spheroids. *HBMSCs, FD and FE, and osteosarcoma cell lines, Saos-2 and MG63, were cultured as spheroids in basal media for up to 14 days before being embedded in paraffin. The sections were stained for ALP (red/brown), cytoplasm stained by light green, and proteoglycans/cartilage stained with Alcian blue. Images are representative of N=2 with four technical replicates, scale bar= 100 µm.*

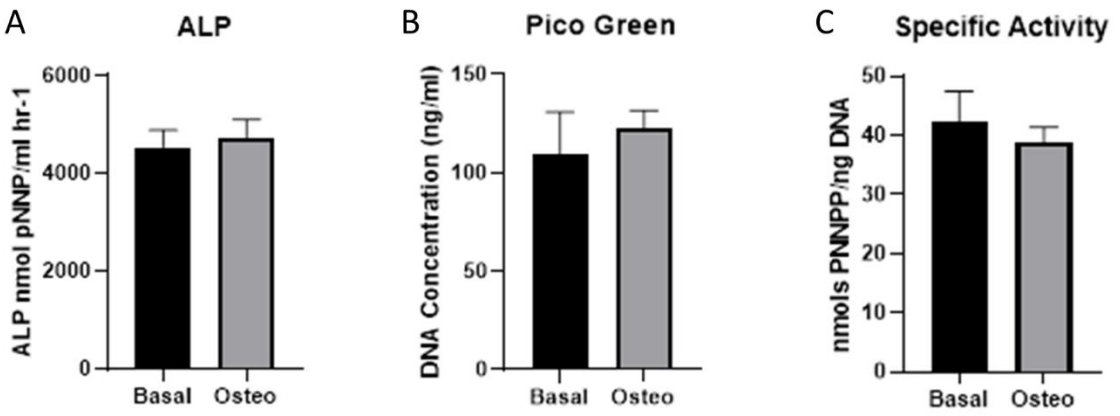

***Figure 3-20. Early osteogenic differentiation of Saos-2 cells**. The ALP analysis, (B) DNA concentration, and (C) ALP specific activity of Saos-2 cells after a 3 day culture in basal and osteogenic I media. N=1 with three technical replicates. Results presented as mean +/- SD, statistics analysed using a T test, no significance found.*

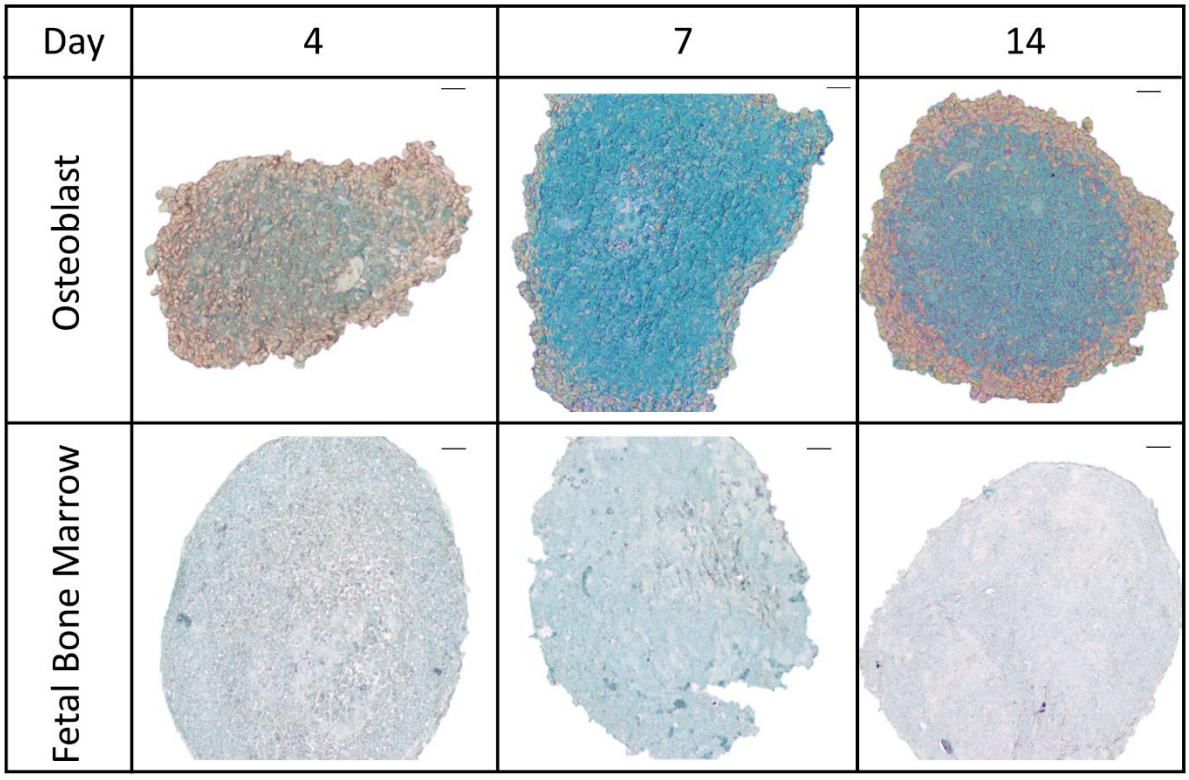

***Figure 3-21. Early osteogenic differentiation in spheroid culture**. Osteoblasts and fetal bone marrow spheroids were cultured in basal media for up to 14 days before being embedded in paraffin. The sections were stained for ALP (red/brown), cytoplasm stained with light green, and proteoglycans/cartilage stained with Alcian blue. Images are representative of N=2 with four technical replicates, scale bar= 100µm.*

3.2.11 Characterising HBMSC and Saos-2 Cell Spheroids

The phenotype of cell spheroids were further analysed by flow cytometry in comparison to 2D cultured cells, initially for stromal cell markers. Saos-2 cells and HBMSCs were cultured in low adherent 96 well plates to form spheroids. After four days they were dissociated into single cell suspension by enzymatic digest using a combination of accutase and collagenase. Figure 3-22 are representative flow cytometry plots comparing Saos-2 cells that had been dissociated with accutase (A) or accutase plus collagenase (B). There was a high level of cell death after dissociation by both accutase and accutase plus collagenase, with the 'live' population not exceeding 25% (gated on the FSC vs SSC plot), lower than the average of 80-90% viability expected of 2D harvested cells. PI staining (2.3.1) was then used to more accurately determine the percentage of live cells, PI binds to DNA but is impermeable through the cell membrane, thus only dead cells are stained positive by PI. Subsequent PI staining of these 'live' gated populations showed less cell death in the accutase only treated spheroids, with 72% of the population PI negative, compared with only 59% of the accutase plus collagenase treated cell spheroids.

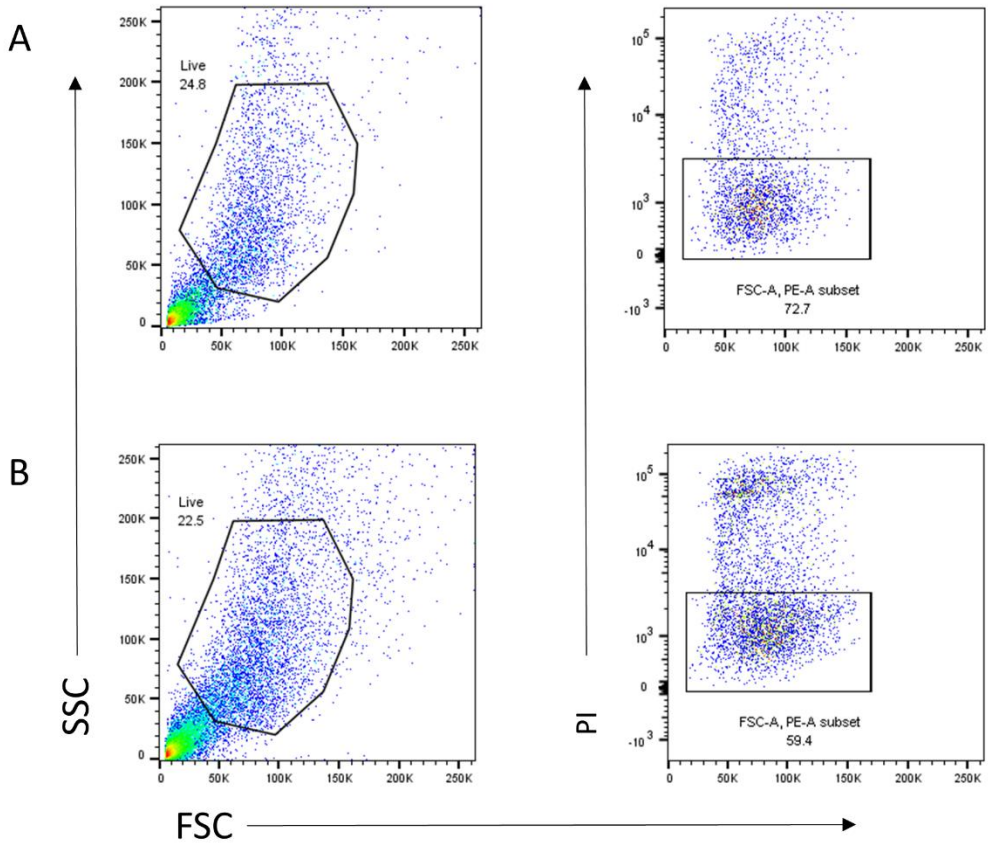

Figure 3-22. Representative flow cytometry data of Saos-2 spheroid cell isolation*. A single cell suspension was isolated from spheroids cultured for 4 days in basal media, using (A) accutase and (B) accutase and collagenase. Pellets were incubated for up to 40 minutes in a thermal shaker. Live cells from the FSC vs SSC plots were gated for PI staining, PI stains dead cells.*

To understand whether an increased cell density resulted in rising levels of cellular necrosis, and consequently more cell death, HBMSCs were plated at varying densities and cultured for four days (2.2.5) before being dissociated in a combination of accutase and liberase TL (Figure 3-23). Liberase TL was used as it contained a mixture of collagenases and protease aimed to enhance cell dissociation. In the FE samples (Figure 3-23B), the lower the initial cell number the clearer the live population was. This pattern was also seen in the FD spheroids, although to a lesser extent. For both cell cultures, dissociation occurred quicker in the two lowest cell densities, only 20 minutes in a thermal shaker, compared with the three higher cell densities, which were stopped after 40 minutes in a thermal shaker. Therefore, to increase cell yield after dissociation, smaller spheroids of below $1.25x10^4$ should be used. As cell viability was a problem when trying to create a single cell suspension, we attempted to dissociate the cells by incubating them on standard 48-well cell culture plates, to allow the cells to migrate from the spheroid and adhere to the bottom of the well. Figure 3-24 showed representative images of Saos-2 cells migrating from the cell spheroid

after 7 days culture in a 48 well plate, but a large number of cells still remain in spheroid form, which also resulted in a large number of dead cells when forming a single cell suspension.

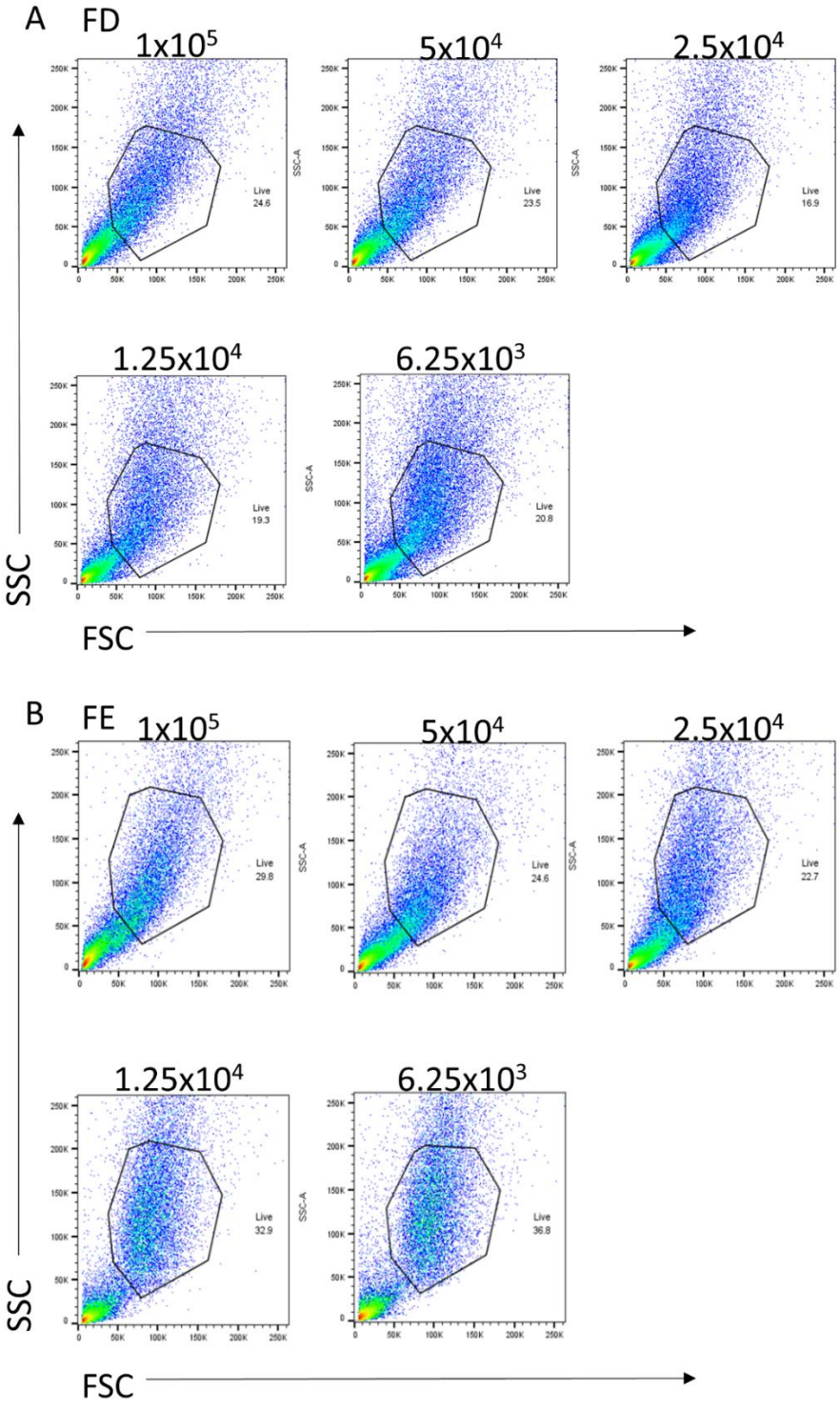

Figure 3-23. Representative flow cytometry data of HBMSC spheroid isolation after 4 days*. (A) FD and (B) FE cells were seeded into cells spheroids at different densities and cultured for 4 days in basal media. The spheroids were then isolated using a combination of Accutase and Liberase TL for up to 40 minutes in a thermal shaker. The number of live cells was determined using the FSC vs SCS flow cytometry gate.*

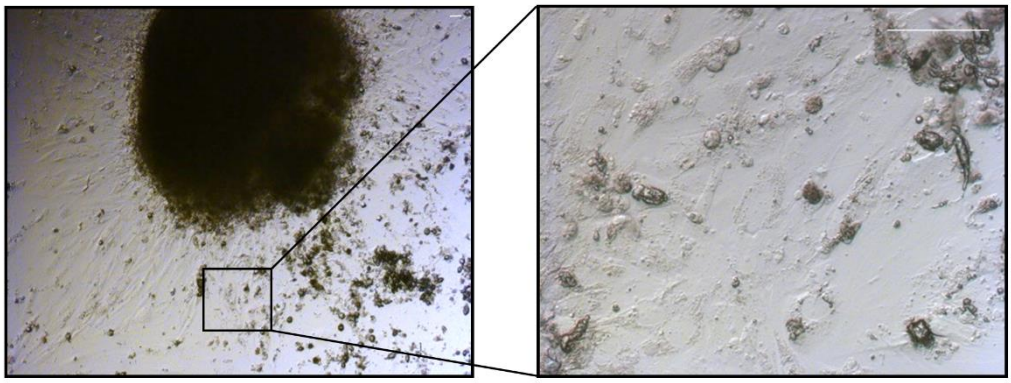

Figure 3-24. Images of cell migration from a Saos-2 cell spheroid*. A Saos-2 cell spheroid was cultured for 4 days before being transferred to a standard 48 well plate. Images taken at 7 days after transfer. Images are representative of N=1 with five technical replicates. Scale bar= 100 µm.*

3.3 Discussion

The osteosarcoma microenvironment encompasses many different cellular interactions. A range of cell types including; HBMSCs, osteosarcoma cell lines, osteoblasts and fetal bone marrow cells, were analysed and quantified, to determine the final selection of cells used to establish a 3D multicellular bone model of osteosarcoma. Key findings:

- Osteosarcoma cell lines had differing tri-lineage differentiation potential.
- HBMSCs taken from different locations in the femur showed distinct characteristics.
- Co-culturing various bone and stromal cells with Saos-2 cells did not affect their osteogenic differentiation.

Two osteosarcoma cell lines, Saos-2 and MG63, were characterised alongside HBMSCs from different skeletal locations, to establish if there were phenotypic differences between stromal cells obtained from different anatomical areas within the femur. Differences in proliferation of various cell types (Figure 3-1) were important in optimising the setup of 2D in vitro assays. This meant different cell seeding densities were used so confluency of each cell type was reached at the same time point for comparability. While there was little difference found between FD and FE HBMSCs from the same donor, the level of proliferation of the MG63 osteosarcoma cell line was higher compared with the Saos-2. This suggested that for 2D assays, MG63 cells needed to be seeded at a lower density than Saos-2 to be comparable. An optimal seeding density for all the cells analysed in Figure 3-1 was sought, in order to limit the cells from reaching confluency too quickly and consequently starting to detach from the plate before reaching the end time point.

Osteosarcoma cell lines and HBMSCs were cultured in media supplemented with osteogenic, adipogenic and chondrogenic differentiation components, before being analysed with histological staining and qPCR gene expression profiling. ALP is an early marker of osteogenic differentiation [196] that is downregulated during bone mineralisation. ALP analysis and staining revealed osteogenic differentiation of Saos-2 cells cultured in both the basal and osteogenic media (**Figure 3-2**). In contrast, MG63 cells demonstrated very low levels of osteogenic differentiation. These results reflected data found in the literature [197, 198], which suggested that the high levels of ALP in Saos-2 cells correlates with osteosarcoma metastatic potential and active bone metabolism. The presence of a high level of ALP in Saos-2 cells reflects the expression in osteosarcoma patients, where high levels of serum ALP have been linked to a poorer prognosis [199, 200]. Hence it is important to understand the level of ALP already present in the HBMSCs.

There are distinguishable cellular characteristics between the bone marrow compositions in different areas of the femur: for example, the FD region has more active haematopoietic tissue, while the FE region has a higher percentage of adipocytes [201]. ALP analysis of these cells performed here revealed osteogenic differentiation occurred in both cell types, with a trend towards increased differentiation in FD cells, although donor variability in differentiation potential was clear (Figure 3-3). The increased cell number in the osteogenic I cultured HBMSCs, denoted by the increase in DNA concentration, may be skewed by the heterogenous cell population or indicate a loss of ALP activity as the cells mineralise. To investigate this, ARS staining and qPCR analysis was assessed looking at mineralisation potential. ARS staining revealed a later stage osteogenic phenotype in three of the cell cultures, FD, FE and Saos-2 (**Figure 3-4**). Concentration analysis of this stain was higher in FD cells than FE (three out of five donors), while Saos-2 cells demonstrated a significant increase in ARS over the Saos-2 basal control and also MG63 osteogenic cultured cells. Expression profiles of ALP genes revealed low levels of *ALPL* for all cell types, with the exception of Saos-2 cells. As ALP is an early marker of osteogenic differentiation it starts to decline as more mature osteoblasts start forming [202], which could explain the decrease of *ALPL* in the HBMSC samples. Collagen I is an extracellular protein expressed during all stages of osteoblast differentiation [187], thus the gene expression of *COL1A1* positively correlates with osteogenic differentiation, found in the Saos-2 and HBMSCs. Interestingly the level of *COL1A1* is higher in FD cells than FE, in contrast to the *ALPL* data, suggesting that the FD cells have reached a more mature osteogenic differentiation.

Osteosarcoma cell lines and HBMSCs were also compared for their ability to differentiate into adipogenic and chondrogenic cells. Oil Red O staining revealed an adipogenic phenotype in all cell cultures after 14 days, although Saos-2 cells showed a decreased level of differentiation compared with the other three cell cultures (**Figure 3-5**). Gene expression analysis were

determined for two adipogenic genes, *FABP4* and *PPARγ*. *PPARγ* is the main regulator of adipogenic differentiation, transcribing genes expressed in mature adipocytes including *FABP4* [188]. It has also been suggested than *PPARγ* can act as a tumour suppressor gene [188], while in contrast *FABP4* may have a role in tumorigenesis [203]. Expression profiles of these genes also suggest variable adipogenic differentiation occurred between the cell types. The high level of Oil Red O staining for the MG63 cells, does correlate with an increase in *FABP4* and *PPARγ*, but the level of expression for both of these genes are lower than for the HBMSCs. The data generated cannot confirm the potential roles of *FABP4* and *PPARγ* in tumorigenesis or as a tumour suppressor gene, and it also suggests that the high level of lipid deposited by the MG63 cells may be due to another biological process rather than adipogenic differentiation. Literature has shown MG63 cells deposit high levels of collagen III [204], which has been linked with adipogenesis [205]. For three out of five donors, FE cells had an increased level of *PPARγ* compared with FD cells, with a corresponding decreased level of *FABP4*, suggesting the FD cells are further down the adipocyte differentiation pathway with more mature adipocytes, while FE cells are still in the earlier stages of adipogenic differentiation. This further supports the hypothesis that HBMSCs have different characteristics depending on skeletal location.

Chondrogenic differentiation was determined by SOX9 staining alongside qPCR analysis of three genes *COL2A1, ACAN* and *SOX9 (***Figure 3-6***)*. While SOX9 staining and gene expression, an early marker of chondrogenic differentiation, was very low in Saos-2 chondrogenic pellets, the level of *COL2A1* and *ACAN* was increased, suggesting that the Saos-2 pellets were in the later stages of chondrogenic differentiation. In contrast MG63 cells showed increased levels of *SOX9* and *ACAN*, but a very low expression of *COL2A1*, which is a mature chondrogenic marker, suggesting MG63 chondrogenic pellets were in the earlier stages of chondrogenic differentiation. Three out of four donor samples tested showed an increase in *SOX9, COL2A1* and *ACAN* gene expression in the FD compared with the FE chondrogenic pellets, further corroborated by an increased SOX9 staining. This data also supports the hypothesis that HBMSCs have different characteristics depending on skeletal location.

To assess cellular changes in HBMSCs in the presence of osteosarcoma, HBMSCs were then co-cultured with Saos-2 cells in transwell experiments, before being analysed for protein expression and qPCR gene profiling (3.2.6). ALP expression at both day 7 and 14 when cultured in either basal or osteogenic media, showed no change when HBMSCs were co-cultured with Saos-2. As mentioned previously, high levels of serum ALP have been linked to a poorer prognosis in osteosarcoma patients [199, 200]. This alongside the spontaneous bone formation, which is a hallmark of osteosarcoma, would suggest that the co-culture of HBMSCs with Saos-2 would result in an increase of osteogenic differentiation. As this was not found, it could suggest that the

exchange of cytokines and signals between the cells in these type of transwell assays were not enough for a shift in HBMSC function, and that either direct contact is needed between the cells, or a third cell type is needed for the osteosarcoma cell line to indirectly affect the differentiation ability of HBMSCs. Alternatively, immortalised cell lines do show differences in phenotype and native functions compared with primary cells [206], and so primary tumour cells could be needed to engage the osteogenic function in HBMSCs.

A panel of gene expression markers were chosen for qPCR analysis of these transwell assays to test the hypothesis that the signalling from Saos-2 cells resulted in increased osteogenic differentiation of HBMSCs. These genes included two osteogenic markers *ALPL* and *SP7* (osterix), which is an osteoblast transcription factor, important in skeletal formation [207]. It also included *MKI67*, a marker of proliferation that when expressed on solid tumour cells is correlated with poor prognosis [208]. As well as *HIF1A,* a nuclear transcription factor that is upregulated in hypoxic conditions, which has been linked to both tumour and HBMSCs microenvironments [209, 210]. This theory that the HBMSCs need either direct contact with Saos-2 cells or another cell type for indirect targeting, was supported by the qPCR data generated from these transwell assays, which similarly to the ALP analysis do not show differences in HBMSCs cultured with and without Saos-2 cells. Any small differences found were negated by the HBMSC transwell control, suggesting it was the increase in cell number which affected the gene expression of HBMSCs not the presence of Saos-2 cells. The supernatant from the transwell culture experiments were also analysed for secretion of IL-6. IL-6 is a pro-inflammatory cytokine, which has been shown to affect both bone formation and osteoclast bone resorption pathways [55], and although the role of IL-6 is unclear, it has been positively correlated with osteogenic differentiation [211]. There are small increases in IL-6 expression in the day 14 basal cultured cells, and the day 7 osteogenic cultured FE cells, when HBMSCs are cultured with Saos-2 compared with the HBMSC controls. Unfortunately, due to the large donor variation between samples this data could not determine that the Saos-2 cells are having any effect on the HBMSCs.

Mifamurtide is the most common treatment of osteosarcoma following surgery and chemotherapy, but there are few studies looking at the effect of this drug on cell types other than macrophages. By culturing HBMSCs and osteosarcoma cell lines with different concentrations of Mifamurtide we have found that there was a small dose dependant effect on the HBMSCs, although this has a negative impact with the highest concentration of Mifamurtide (**Figure 3-14** and **Figure 3-15**). Compared with other studies, the top concentration of Mifamurtide used in these experiments was lower than the standard concentration used in literature [195]. As excess Mifamurtide from osteosarcoma patients was being used, the formulation isn't optimised for cell culture as it was reconstituted in sodium chloride. This could suggest that the decrease in ALP and

DNA concentration seen at the top concentration could be due to the limited amount of nutrients in the well instead of the effect of the drug. To test this a higher concentration of stock Mifamurtide would have to be acquired.

Osteoblast function has been shown to be affected in the osteosarcoma tumour microenvironment, inhibition of osteoblasts leads to expression of osteoclast signalling cytokines, and consequently bone resorption [54]. To characterise the effect osteosarcoma cells have on osteoblasts, they were co-cultured with Saos-2 cells in a transwell assay for 7 and 14 days, and the expression of ALP, IL-6 and qPCR analysis was acquired (**Figure 3-16** and **Figure 3-17**). Although there was no difference at day 7, at day 14 there was a downward trend in both ALP and specific activity when the cells were in co-culture. This data could suggest that either osteogenic differentiation was being slowed or suppressed by the presence of Saos-2 cells, or that the cells were further along the differentiation pathway and had stopped producing ALP. This was initially supported by the decrease in *ALPL* gene expression in the co-culture, but *SP7*, another osteogenic marker produced later in the pathway, also decreased, indicating that it was more likely a suppression/ or slowing of osteogenic differentiation. Two other genes, *MKI67* and *HIF1A* also showed a downward trend in expression when co-cultured with Saos-2 cells, resulting in a decrease in proliferation and hypoxic factors, although this was only significant in *HIF1A*. At both day 7 and 14 the level of IL-6 decreased in the transwell culture, meaning there was less activation of osteoblasts in the co-culture wells. Unfortunately, a transwell control using osteoblasts on both the bottom of the plate and in the transwell was not included, which would tell us whether any changes seen were because of the increase in cell number or because of the presence of Saos-2 cells. Only one transwell experiment combining osteoblasts with Saos-2 cells was performed, this was due to the difficulties in expanding osteoblasts from bone fragments to a sufficient number without having contaminating stromal cells in the culture. Due to this it was decided not to include additional osteoblasts in the 3D model.

Transwell co-culture experiments were also conducted with fetal bone marrow and Saos-2 cells, in basal media, to assess whether a high level of progenitor cells can affect tumour bone marrow interaction (**Figure 3-18**). There was no effect on the expression of ALP and specific activity on fetal bone marrow cells when they were co-cultured with Saos-2, but a decrease was found in IL-6 secretion, *ALPL* and *HIF1α* gene expression. Combined with the increase in *MKI67* expression when cultured with Saos-2 cells, which determined that level of cell proliferation increased, the data suggested that there was an inhibition of osteogenic differentiation. The fetal bone marrow cultures were also analysed for *SP7* gene expression but had extremely low levels in all conditions and could consequently not be quantified. The lack of *SP7* expression and the low level of *ALPL* gene expression means that even without the co-culture of Saos-2 cells, the fetal bone marrow

has low levels of osteogenic differentiation. Although the data was only from one experiment, osteogenic potential is important in replicating the osteosarcoma tumour microenvironment, as such it was determined that HBMSCs from older donor samples were more appropriate than fetal bone marrow cells for culture in the 3D bone model.

Alongside the proliferation assays, the different cell types were cultured as spheroids before being histologically analysed for ALP expression (**Figure 3-19** and **Figure 3-21**). This allowed for the distribution of ALP to be analysed alongside the structural organisation of the spheroid. MG63 cells didn't express ALP at any time point, supporting the 2D data. Interestingly, although as a 2D culture Saos-2 cells showed a high level of ALP expression at early time points, by culturing these cells in a spheroid format the level of ALP expression was initially lost, most likely while the cells are proliferating, and was then regained over 14 days. Low levels of ALP expression can be seen on the FD and FE HBMSCs, which doesn't change over the three time points, similar to the low level of ALP expression in the 2D assay when the cells were cultured in basal media. Osteoblasts in spheroid culture initially expressed a large amount of ALP, which was lost by day 7 most likely where the spheroid concentrates on cell growth, but ALP expression started to return at day 14. In contrast fetal bone marrow showed no ALP expression in spheroid culture up to 14 days, which correlates with the transwell data, suggesting fetal bone marrow cells are not initially focussed down the differentiation pathway. The spheroid ALP analysis does show evidence that cells in a 3D spheroid have different characteristics to 2D cell cultures, particularly the Saos-2 pellets which showed a steady increase of ALP expression up to 14 days in culture, whereas in Figure 3-2 and Figure 3-20 Saos-2 cells showed a steady level of ALP expression at day 3, 7 and 14, when cultured in basal media.

To further assess potential changes in phenotype of the cell spheroids, both Saos-2 and HBMSCs spheroids were isolated into a single cell suspension for flow cytometry analysis. While the data was not shown, the use of Trypsin/EDTA and PBS/EDTA were initially used prior to combinations of accutase, liberase and collagenase, where they all resulted in high levels of cell death. Even using very small cell numbers that give distinct live cell populations in flow cytometry analysis (**Figure 3-23**), only resulted in a live cell population of around 35% in FE cells. Consequently, unspecific staining was likely to affect the phenotyping of key markers of interest, reducing the validity of using this method to analyse spheroids. Finally, the ability of the Saos-2 cells to migrate from the cell spheroid was tested, as a potential new method to create a single cell suspension. After 7 days from being transferred into a standard 48 well plate there was evidence that cells had begun migrating from the spheroid, but the size of the cell spheroid was still large. This information combined with the different characteristics from the ALP staining, and the lack of viable cells when dissociated into a single cell suspension, resulted in cell spheroids no longer

being used for the 3D bone model. Although this method allowed all cells inserted to remain within the model initially, it wasn't optimal for cell migration and interaction with the bone structure.

The final selection of cells introduced into the 3D bone model were established by the 2D characterisation assays. Osteoblasts and fetal bone marrow cells were not carried forward after initial experiments due to the lack of cell number for the osteoblasts and low levels of ALP expression by the fetal bone marrow cells. HBMSCs from two different locations in the femur showed distinct characteristics; with FD cells having higher levels of osteogenic differentiation at both early and late time points, an increased ability to differentiate into chondrocytes, and a more mature adipocyte differentiation compared with FE cells. They also had a higher level of ALP expression when treated with Mifamurtide. As osteogenic ability is important in the osteosarcoma environment, FD cells were used as the source of HBMSCs in the development of the 3D bone model, additionally to the HBMSCs already present in the bone core. The two osteosarcoma cell lines also showed distinctly different characteristics, with Saos-2 cells expressing high levels of osteogenic differentiation and later stage chondrogenic differentiation, but low levels of adipogenic differentiation. In contrast, the MG63 cells had high levels of lipid secretion, although not necessarily adipogenic differentiation due to the low expression of adipogenic genes, high levels of early stage chondrogenic differentiation, but no osteogenic differentiation. As with the HBMSCs osteogenic ability is important for the development of the 3D bone model, as such Saos-2 cells were chosen as the osteosarcoma cell line to be integrated.

Chapter 4 Differentiation of Monocyte-Derived Macrophages and Osteoclasts from bone marrow and PBMCs

4.1 Introduction

Macrophages are functionally diverse cells, which are important for both an effective immune response as well as tissue maintenance and homeostasis. They have also been shown to play key roles in the development of a range of cancers including osteosarcoma, and can be actively recruited into the tumour microenvironment [92, 93]. Macrophages can be characterised under a spectrum of polarisation, with the extremes labelled as having an M1-like and M2-like phenotype. Interestingly there have been links found between increases in overall macrophage infiltration in patients with metastatic osteosarcoma compared with non-metastatic [95], although there were conflicting data on how this was linked to polarisation. Some research suggested these macrophages were polarised towards an M2-like phenotype [101], and other data showed no difference in polarisation [95]. Further research has also shown a higher level of M1-like macrophages in non-metastatic patients [212]. The importance of macrophages in the osteosarcoma microenvironment is also supported by the apparent therapeutic benefits of Mifamurtide, an osteosarcoma drug, which is reported to target and activate monocytes and macrophages in the tumour microenvironment [25]. While a combination of neoadjuvant chemotherapy and surgical resection of the tumour is still the main treatment protocol for osteosarcoma patients, comparative analysis have shown that the three year event free survival increased to between 65-92% when patients were also treated with Mifamurtide [22, 33, 35]. Mifamurtide is now a standard of care in many countries in addition to chemotherapy and surgery. The 3D bone model developed here will be used to test osteosarcoma drugs and therapies, as such macrophages are one of the key cell types to be included in this model.

Primary human macrophages *in vitro* are generally isolated and differentiated from PBMCs [213, 214], while in mouse studies, macrophages are routinely generated from bone marrow instead of blood [215, 216]. In both of these cases, this was mainly due to availability and volume of tissue, but there is little data characterising differences between macrophages derived from human PBMCs and human bone marrow. What data is published focuses on specific diseases, for example how the replication of the Hepatitis E Virus compared in human monocyte-derived macrophages (MDMs) and human bone marrow-derived macrophages (hBMDMs) [217]. With access to both PBMC from leukocyte cones and bone marrow from patients undergoing hip

replacement surgery, comparative experiments were performed looking at the differentiation of macrophages from these sources. Data in Chapter 3 showed that the skeletal location of bone marrow affected the corresponding HBMSC characterisation. To test whether skeletal location affects the phenotype of macrophages, multiple studies were carried which compared hBMDMs derived from FD and FE bone marrow alongside MDMs derived from PBMCs.

Osteoclasts are important bone resorption cells that differentiate from a monocyte/macrophage haematopoietic lineage, and are critically involved in bone remodelling [54]. As uncoordinated bone growth and resorption is prevalent in osteosarcoma patients, the generation of osteoclasts may be directly affected by the tumour, and have an important role in the tumour microenvironment [61]. Reports have rarely directly compared the differentiation of osteoclasts from PBMCs [218] and from bone marrow [219]. One of the few studies that did compare osteoclast differentiation from peripheral blood and bone marrow was published in 1989 [220], and found that bone marrow derived osteoclasts were functionally active, while peripheral blood osteoclasts were not. Osteoclast differentiation protocols have adapted since then and it has also been found that there were no differences in bone resorption activity after differentiation from bone marrow and PBMCs [221]. To compare these findings, the functional differences in osteoclasts derived from human PBMCs and human bone marrow were assessed. These cells were isolated and the level of differentiation and activation was compared. This chapter assessed the function of macrophages and osteoclasts derived from PBMCs and human bone marrow cells, to determine the appropriate method and cell source for inclusion in the 3D bone core model.

4.2 Results

4.2.1 Phenotyping MDMs Derived from a Heterogeneous PBMC or Bone Marrow Population

Macrophages have different characteristics based on both their location and role in either an immune response or in tissue maintenance [88]. As macrophages were one of the main cell types to be introduced into the 3D bone model, it was important to determine whether there were phenotypic differences found between macrophages derived from bone marrow (hBMDMs) and those derived from PBMCs (MDMs). As previous assays have shown bone marrow have different characteristics based on skeletal location, this was also assessed for the differentiation of hBMDMs, which could have affected future experiments. To determine the phenotype of MDMs and hBMDMs, cell suspensions were isolated from PBMC leukocyte cones (2.2.13) and bone marrow samples (2.2.2), the heterogenous populations were plated, incubated for 2 hours and then washed to allow the monocytes to adhere to the plastic. The cells were then cultured with M-CSF for 7 days to compare macrophage differentiation. **Figure 4-1** are representative images of MDMs derived from PBMCs and hBMDMs derived from FD and FE cells after being cultured for 7

days. There was similar cellular morphology between the three cell sources, although the MDMs showed a higher level of confluence than the hBMDMs. This was true for the majority of assays performed, even though the hBMDMs were plated at double the MDM cell concentration. The lower confluency of the hBMDMs could have been due to the higher level of adherent stromal cells, including fibroblasts, found in the bone marrow population, which have been shown to contaminate the hBMDM differentiation process [222]. These cells were seen growing in small colonies highlighted by white arrows in **Figure 4-1**B.

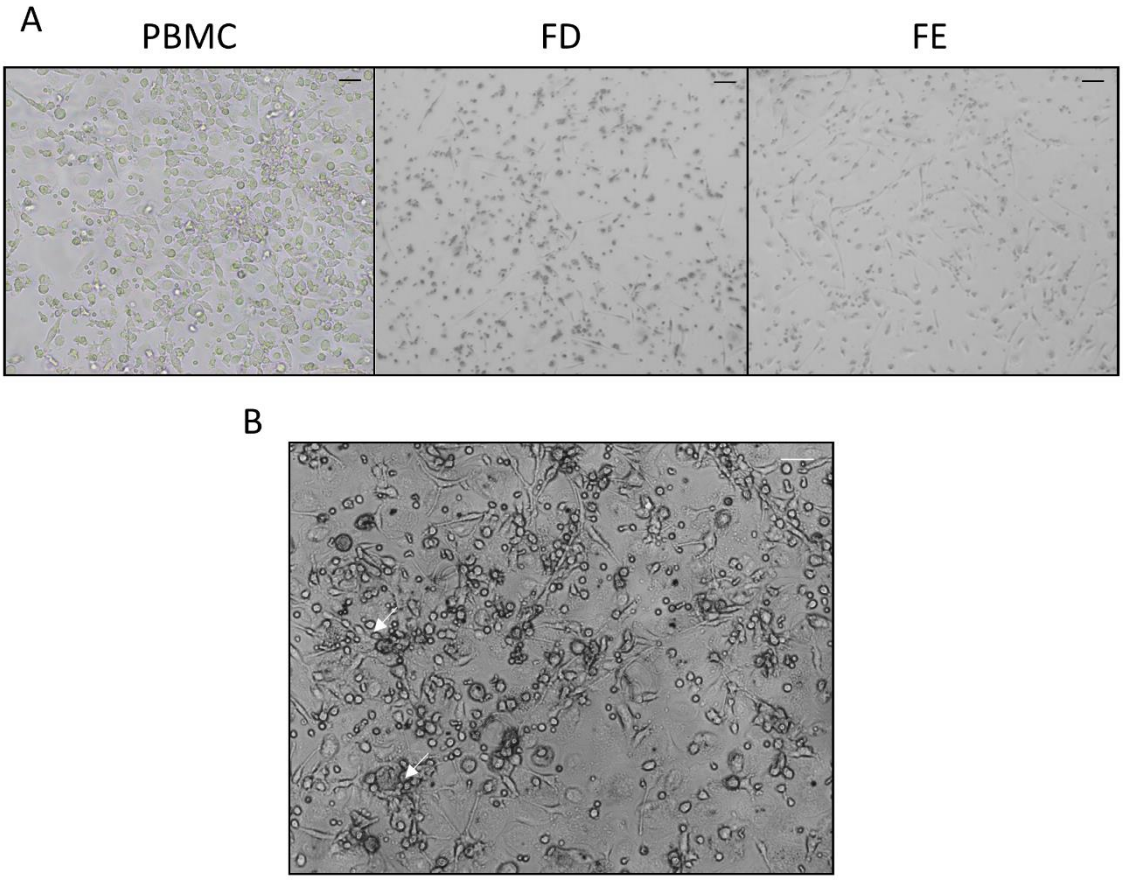

Figure 4-1. Representative images of MDMs from a heterogenous population*. (A) Images of MDMs generated from PBMCs, and hBMDMs generated from FD and FE bone marrow cells. Cells were cultured for 7 days with M-CSF. (B) An image of FD derived hBMDMs indicating areas of stromal cell proliferation, highlighted by the white arrows. Scale bar= 100 µm.*

After 7 days the cells were dissociated into a single cell suspension and analysed for a panel of macrophage markers by flow cytometry (2.3). **Figure 4-2** shows a representative gating strategy for characterising MDMs. Dead cells (FSC vs SSC) and doublets (FSC-H vs FSC-A) were excluded from analysis (**Figure 4-2**A). Non-specific binding was eliminated from the analysis by using isotype controls, which allowed the percentage positive stain to be determined (**Figure 4-2**B and

C). The intensity of the antibody fluorescence was also compared by analysing the geometric mean.

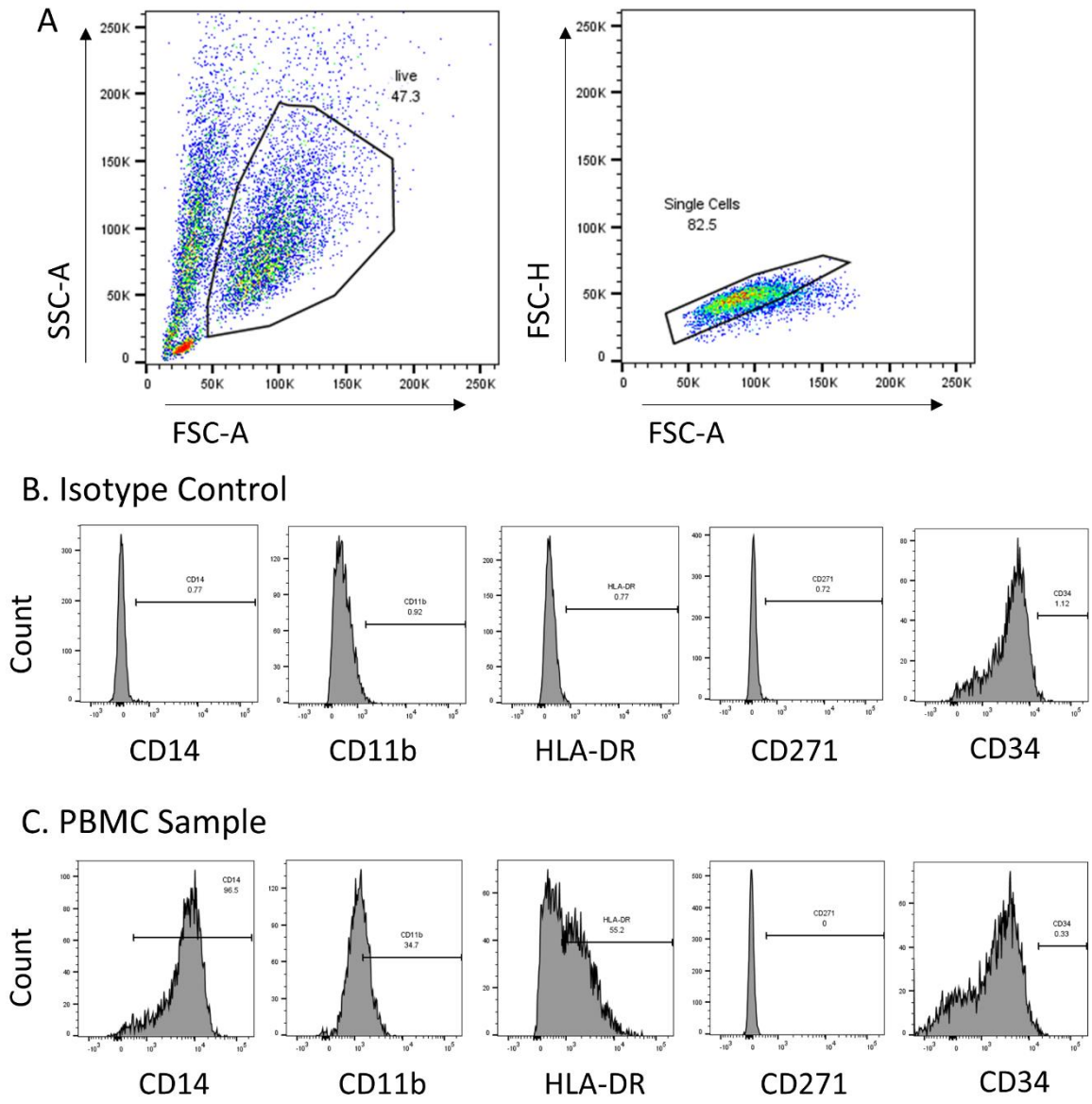

Figure 4-2. A representative flow cytometry gating strategy for characterising MDMs*. PBMCs were cultured for 7 days in basal media + M-CSF, and analysed by flow cytometry for CD14, CD68, HLA-DR, CD11b, CD34 and CD271 expression. (A) Illustrates the gating strategy for the live and single cells, (B) isotype controls were then used to set the gates for the (C) samples analysed.*

Figure 4-3 showed the percentage positive cells and geometric mean of CD14, CD11b, and HLA-DR, as well as a hematopoietic stem cell marker CD34 and a stromal marker CD271. Geometric mean calculates fluorescence intensity for each marker of interest. Due to the low yield of cells from the FE cell suspensions, only one sample had enough cells for flow cytometry analysis, as such statistical significance was not assessed. There was a higher percentage of CD14 % positive MDMs (A) compared with both the FD and FE hBMDMs, this pattern was also seen in the CD14

geometric mean. There was a reduction in both the percentage of CD11b (B) and HLA-DR (C) expression in the hBMDMs compared with the MDMs, which was also seen for the CD11b geometric mean of PBMC MDMs vs FD hBMDMs. Large patient variations were found in both the MDM and hBMDMs samples. All samples were negative for CD34 (D) and CD271 (E).

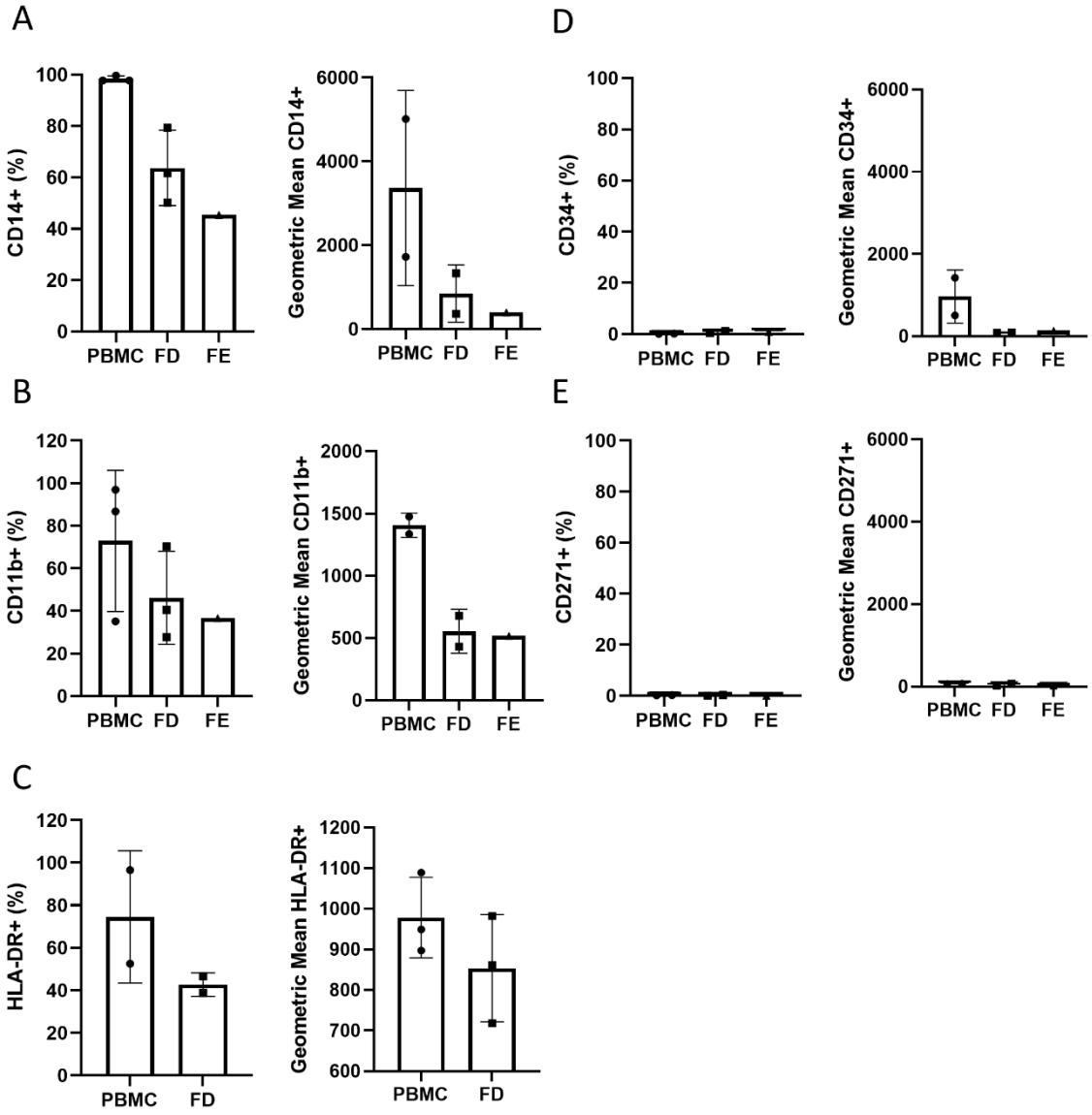

Figure 4-3. Phenotyping of MDMs differentiated from a heterogenous population. Bone marrow cells and PBMCs were isolated and cultured for 7 days in basal media + M-CSF. The cells were then analysed by flow cytometry for the percentage and geometric mean of (A) CD14, (B) CD11b, (C) HLA-DR, (D) CD34, and (E) CD127. N=1-3 each with three technical replicates. Results presented as mean +/- SD, Statistical significance was not determined due to low biological replicate numbers.

4.2.2 Polarisation of MDMS Derived from Heterogenous PBMC and Bone Marrow Populations

Macrophages can be characterised based on their function, which is linked to polarisation. To determine whether MDMs and hBMDMs could be polarised into a M1-like and M2-like phenotypes, heterogenous cell populations were isolated following standard protocols (2.2.2 and 2.2.13), and the cells cultured with M-CSF for 7 days. The MDMs and hBMDMs were then polarised into a M1-like phenotype, by culturing with lipopolysaccharide (LPS) and interferon γ (IFNγ), or M2-like phenotype, by culturing with IL-4 and IL-13, for a further 48 hours. M-CSF alone was used as a M0-like control. **Figure 4-4** are representative images of MDMs and hBMDMs cultured in the different polarisation conditions. The M1-like differentiation process resulted in a lower confluency of cells compared with the M0 and M2-like macrophages. Unfortunately, a high number of dead cells affected the images taken, this was likely due to high seeding densities or non-adherent cells that were not removed during the wash steps. The FD and FE hBMDMs also showed low levels of stromal cell contamination.

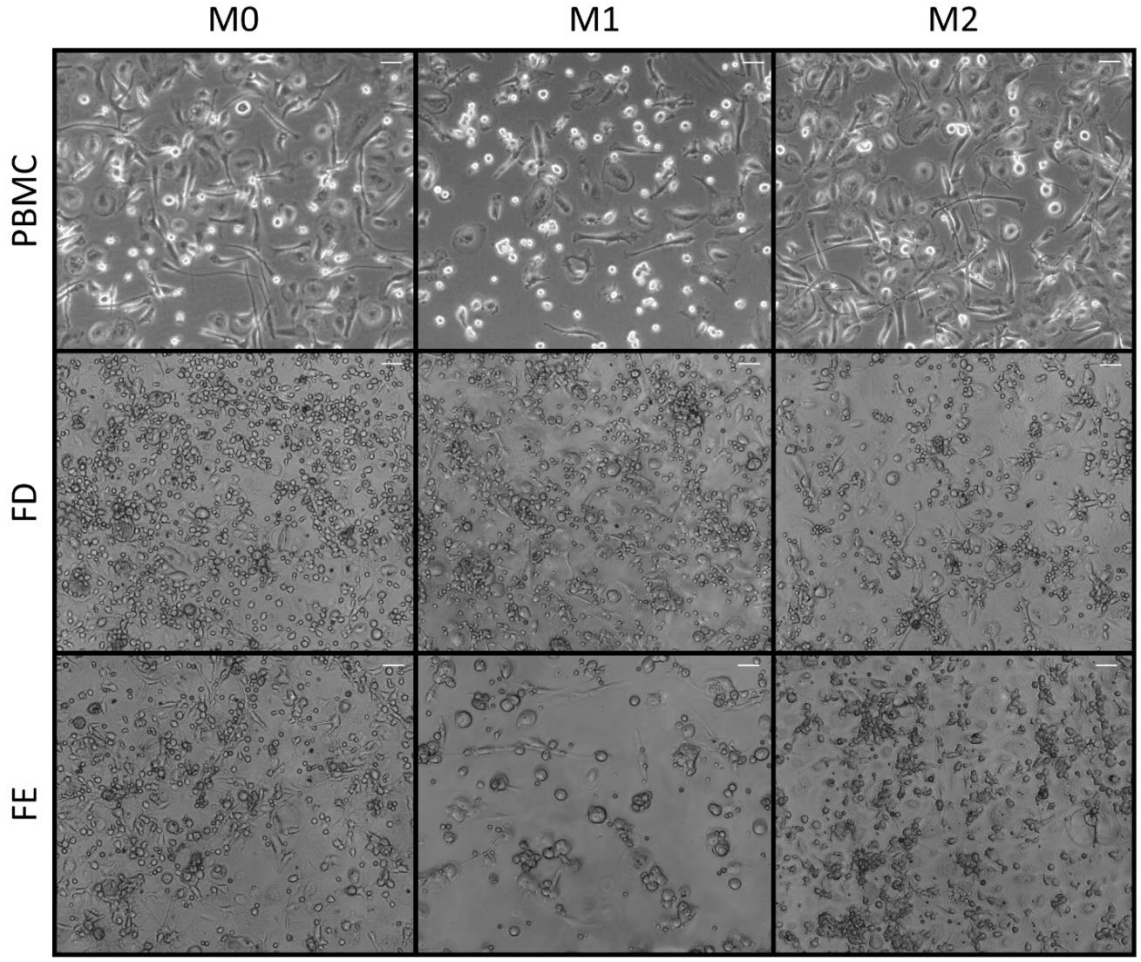

Figure 4-4. Representative images of polarised macrophages differentiated from a heterogenous cell population*. MDMs generated from PBMCs, and hBMDMs generated from FD and FE bone marrow cells after culture with M-CSF for seven days, followed by 48 hour incubation in polarisation media for an M0-like, M1-like and M2-like phenotype. Scale bar= 100 µm.*

After 9 days the MDMs and hBMDMs were dissociated into single cell suspensions and analysed by flow cytometry for a panel of macrophage markers (2.3). **Figure 4-5** shows the percentage of positive MDMs or hBMDMs expressing CD14, CD68, CD40, CD38 and CD11b. The expression of CD14 (A) was lower in the majority of hBMDM FD and FE samples compared with the corresponding PBMC MDMs, which was significant between the M1-like polarised cells. The expression of CD14 (A) was very similar between the M0, M1 and M2-like cells from each source, where both FD and FE hBMDMs showed a higher expression in the M0-like hBMDMs compared with the M1-like and M2-like hBMDMs. The CD68 (B) expression showed a similar trend, with a significant difference between the PBMC M1 and M2-like MDMs compared with the FD M1 and M2-like hBMDMs. The FD hBMDMs also showed a trend towards a lower level of expression compared with the FE hBMDMs across all three polarisation conditions, which was significant between the M1-like hBMDMs.

There was a reduced expression of CD40 (C) and CD38 (D) in the FD and FE M1-like hBMDMs compared to the PBMC M1-like MDMs. The M1-like polarised cells also had a higher expression of CD40 and CD38 compared with M0 and M2-like MDMs and hBMDMs from the same source, which was significant in PBMC and FE samples. This suggested that the M1-like MDMs and hBMDMs showed higher expression of M1-like macrophage markers compared with the M0 and M2-like cells, although stromal cell contamination could have limited the overall expression of these macrophage markers in the hBMDM assays, particularly in the FD hBMDMs. The expression of CD11b (E), a M2-like marker, was reduced in the hBMDM FD and FE samples compared with the PBMC MDMs, although there was large variation between the donors. There was also a lower CD11b expression in M1-like MDMs/hBMDMs compared with M0 and M2-like MDMs/hBMDMs from the same source, but none of these trends were significant. This could suggest that the M0-like MDMs and hBMDMs were already primed towards an M2-like phenotype.

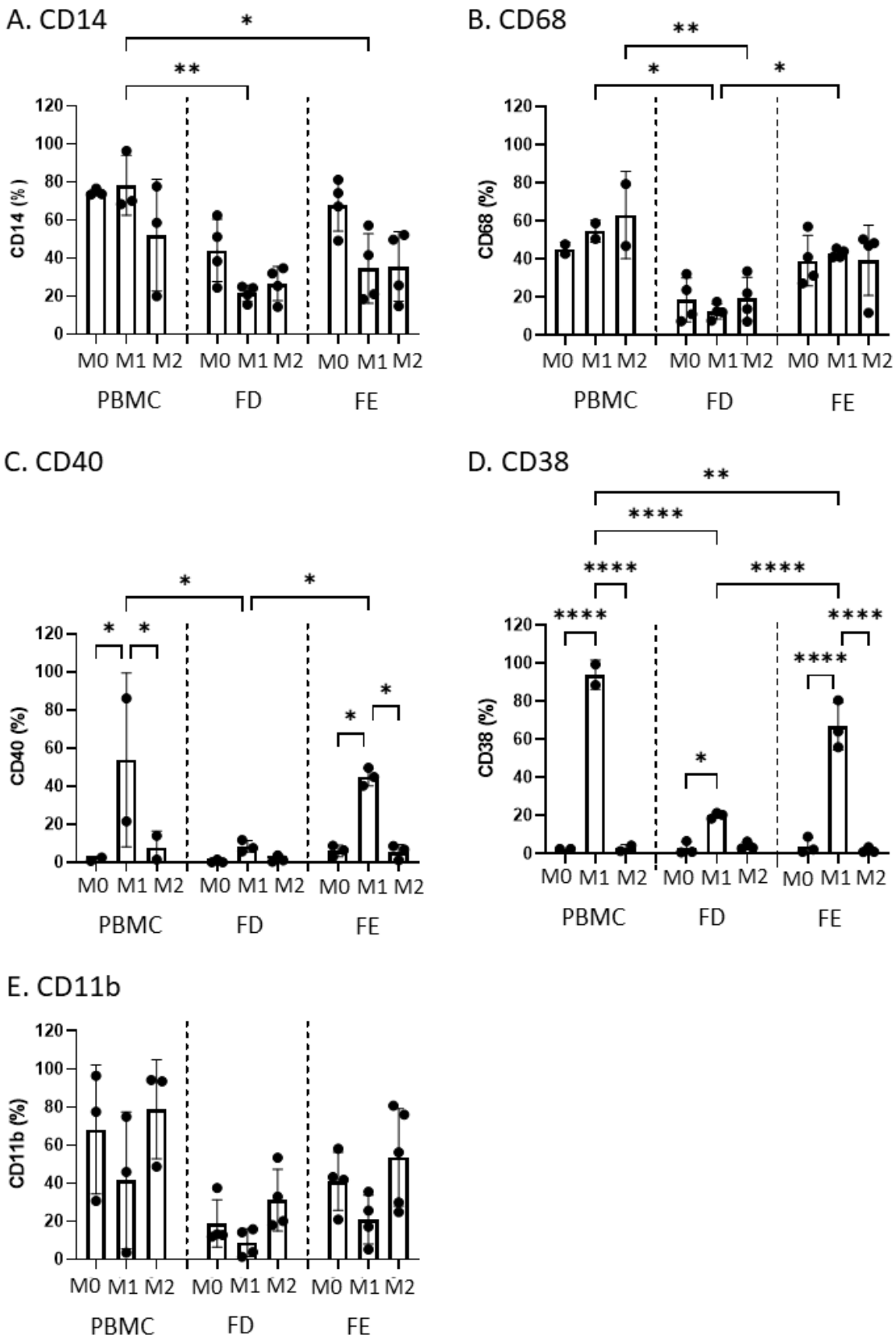

Figure 4-5. Phenotyping of polarised macrophages differentiated from a heterogenous population. *PBMCs and bone marrow cells were isolated and cultured for 7 days in basal media + M-CSF, then for a further 48 hours in polarisation media. They were then analysed by flow cytometry for the percentage of (A) CD14, (B) CD68, (C) CD40, (D) CD38, and (E) CD11b expression.*

*N=2-4 each with three technical replicates. Results presented as mean +/- SD, statistics determined using a one-way ANOVA, significance represented as *<0.05, ** <0.01, ***<0.001.*

Figure 4-6 shows the CD14, CD68, CD40, CD38 and CD11b geometric mean of the polarised MDMs/ hBMDMs. Significant differences in CD14 geometric mean were found between the three cell sources, but they changed depending on the polarisation condition. While PBMC derived MDMs always showed an increased level of CD14 (A) geometric mean compared with FD hBMDMs in all three polarisation conditions, the geometric mean of the FE hBMDMs varied. M0-like hBMDMs showed a significantly higher CD14 geometric mean in the FE hBMDMs compared with the FD hBMDMs, this trend was also seen compared with the PBMC MDMs. PBMC MDMs and FD hBMDMs also showed very similar levels of CD14 across the three polarisation conditions, whereas the FE cells illustrated a significantly higher geometric mean in the M0-like hBMDMs compared with the M1 and M2-like hBMDMs. This data suggested that the FD hBMDMs possibly had a higher contamination of stromal cells, limiting the expression of CD14 in the total population, this could also be true of the M1 and M2-like FE hBMDMs, which showed a lower expression than the MDMs. In contrast the CD68 (B) geometric mean showed a similar pattern between all three polarisation conditions from each cell source, with similar levels in PBMC MDMs and FD hBMDMs, with a slight rise in the FE hBMDMs.

CD40 (C) geometric mean was significantly increased in M1-like PBMC derived MDMs compared to both the FD and FE M1-like hBMDMs. The CD40 geometric mean of the FE M1-like hBMDMs were also significantly higher than the FD M1-like hBMDMs. The M1-like polarised cells also indicated a higher CD40 geometric mean compared to the M0 and M2-like polarised cells of the same source, this was significant in the PBMC MDMs and FE hBMDMs. The CD38 (D) geometric mean was lower in the FD hBMDMs compared to the corresponding PBMC MDMs and FE hBMDMs, which also suggested there was a potential contamination of stromal cells. When analysed between the three polarisation conditions of each cell source the CD38 (D) geometric mean was higher in M1-like polarised cells compared with M0 and M2-like polarised cells from the same source, which was significant for the FE hBMDMs. A reduced trend of the CD11b (E) geometric mean was shown in the FD hBMDMs compared to the corresponding PBMC MDMs and FE hBMDMs. The expression of CD11b was also lower in M1-like MDMs/hBMDMs compared with M0 and M2-like MDMs/hBMDMs from the same cell source. Similarly to the percentage of CD11b positive cells, there is also a large variation of CD11b geometric mean between the different donors, which could potentially suggest some cells were already polarised towards an M2-like phenotype prior to the addition of polarising cytokines.

As expected, the phenotype data generated showed the M1-like MDMs and hBMDMs from all three cell sources had higher levels of CD38 and CD40, M1-like macrophage markers, than M0 and M2-like MDMs and hBMDMs. The M2-like MDMs and hBMDMs also showed higher levels of CD11b expression, a M2-like macrophage marker, than the M1-like cells but showed similar levels to the M0-like cells, supporting the contention that the M0-like MDMs and hBMDMs were already polarised towards an M2-like phenotype.

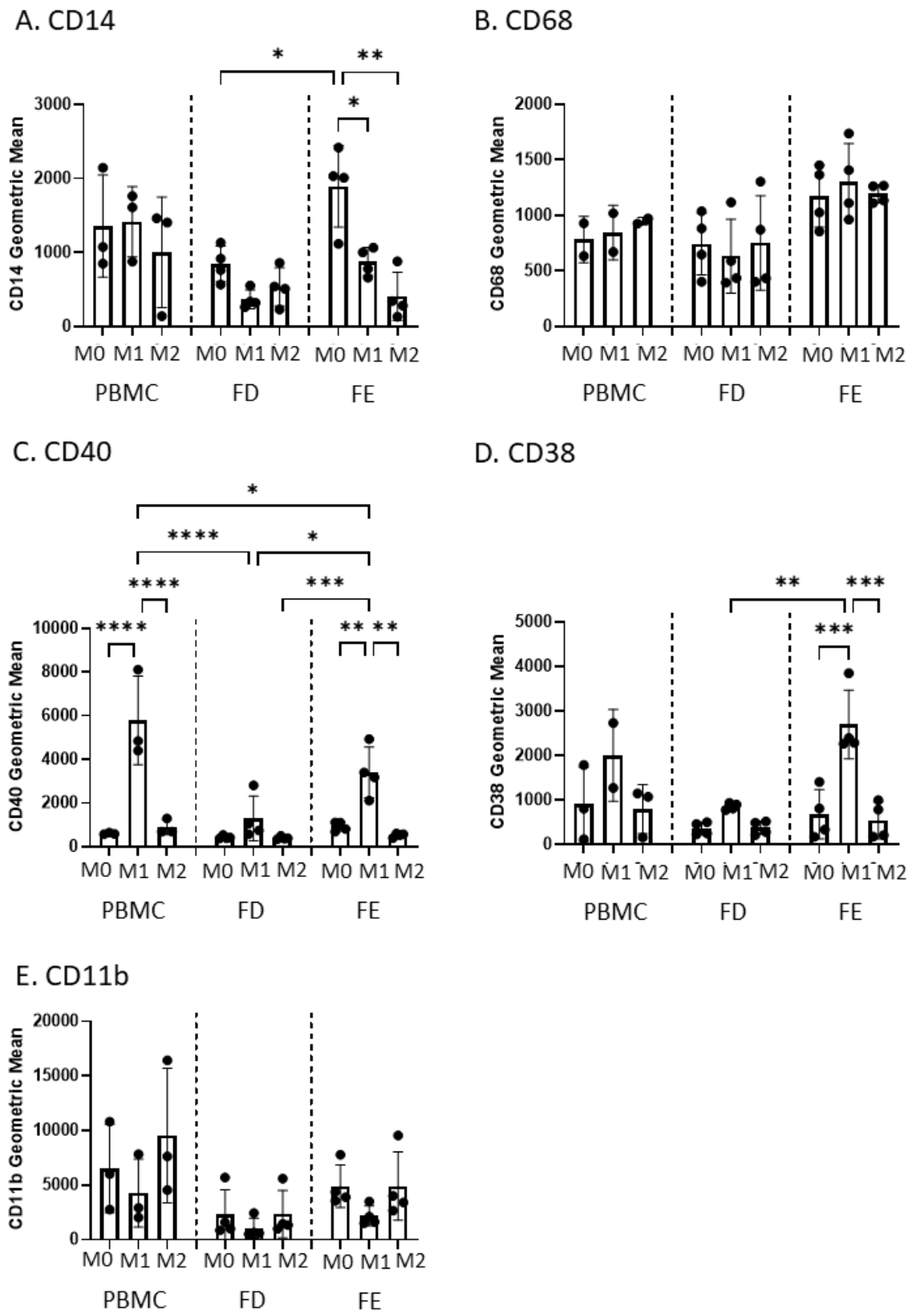

Figure 4-6. Geometric means of polarised macrophages differentiated from a heterogenous population*. Isolated PBMCs and bone marrow cells were cultured for 7 days in basal media + M-CSF, followed by 48 hours in polarisation media. They were then analysed for the geometric mean of (A) CD14, (B) CD68, (C) CD40, (D) CD38, and (E) CD11b, by flow cytometry. N=2-4 each with*

*three technical replicates. Results presented as mean +/- SD, statistics determined using a one-way ANOVA, significance represented as *<0.05, ** <0.01, ***<0.001, ****<0.0001.*

4.2.3 Characterising MDMs Derived from CD14+ Isolated PBMCs and Bone Marrow

The phenotypic expression of MDMs generated from a heterogenous population of cells showed distinct differences when originating from PBMCs or bone marrow cells. It was then assessed whether this was a result of the differentiation of macrophages from these cell sources, or whether it was a result of stromal cell contamination and low monocyte population in the bone marrow samples. To analyse this CD14+ cells were isolated from PBMCs and bone marrow cells using a magnetic isolation kit (2.2.15) before being cultured with M-CSF for 7 days. **Figure 4-7** are representative images of MDMs differentiated for 7 days, which showed similar morphology and confluency between PBMSCs derived MDMs, FD hBMDMs and FE hBMDMs, with no evidence of stromal cell contamination.

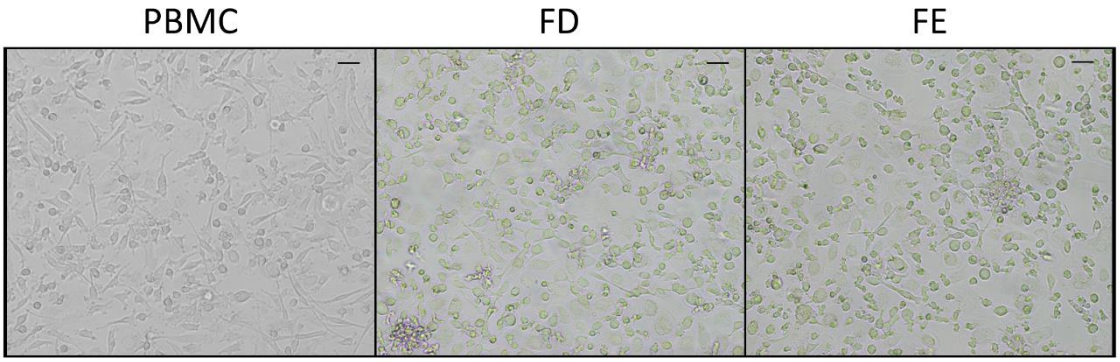

Figure 4-7. Representative images of MDMs and hBMDMs differentiated from CD14+ isolated cells*. CD14+ PBMCs and bone marrow cells were isolated and cultured with M-CSF for 7 days. Scale bar= 100 µm.*

After a 7-day incubation the cells were analysed for a panel of macrophage markers by flow cytometry (2.3). **Figure 4-8** are representative images of the gating strategy used for characterising MDMs. Live cells were gated on the FSC vs SSC, with doublets being excluded in the FSC-H vs FSC-A plot (**Figure 4-8**A). The gates for the markers of interest were placed using isotype controls to eliminate non-specific binding before being used to determine the percentage and geometric means of the markers of interest (**Figure 4-8**B and C).

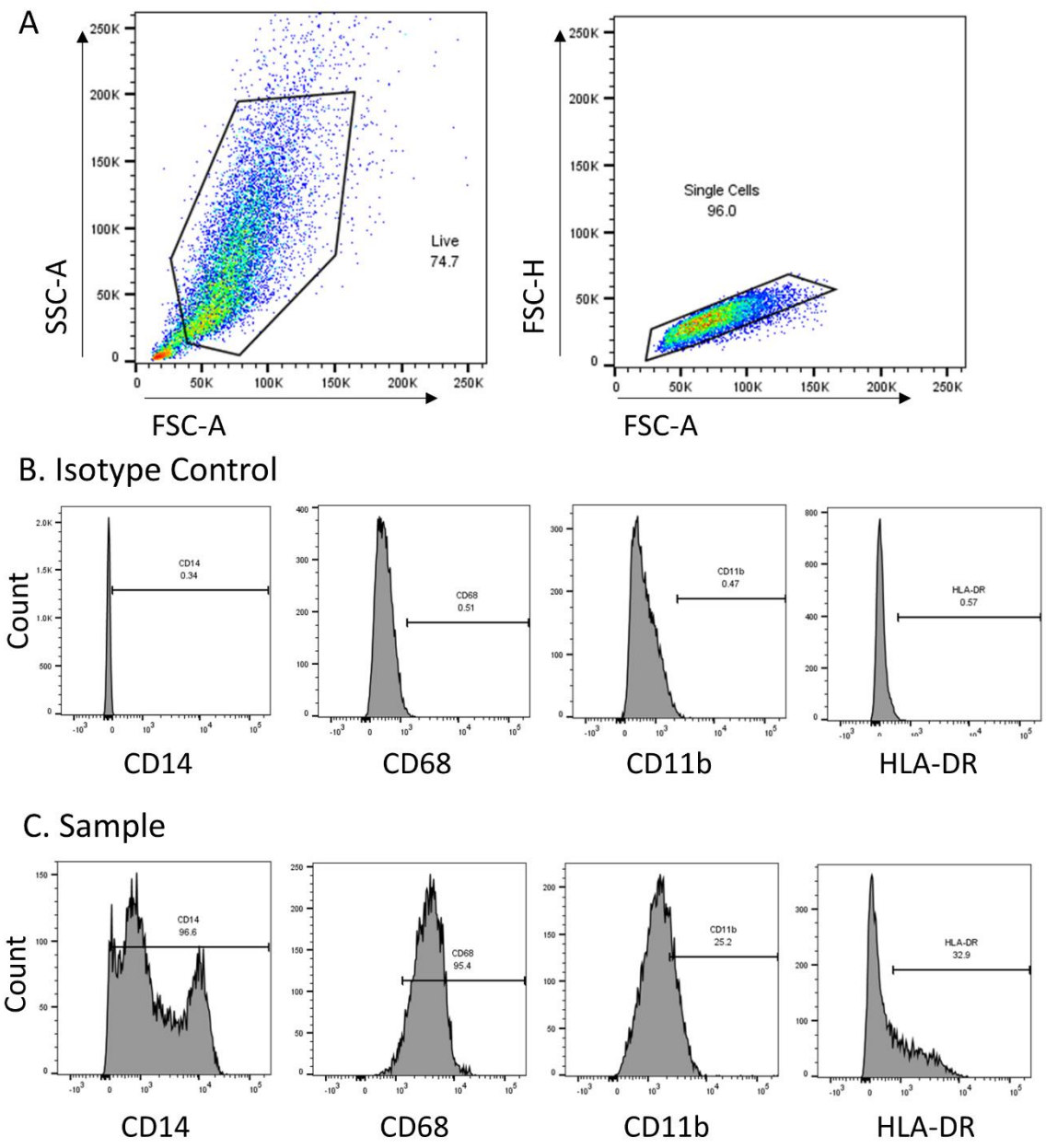

Figure 4-8. A representative flow cytometry gating strategy for characterising macrophages*. CD14+ bone marrow cells and PBMCs were isolated and cultured for 7 days in basal media + M-CSF, before being analysed for CD14, CD68, HLA-DR, CD11b, and CD68 expression by flow cytometry. (A) Illustrates the gating strategy to isolate the live and single cells, (B) isotype controls were then used to set the gates for the (C) samples analysed.*

Figure 4-9 shows the percentage positive cells and geometric mean for four macrophage markers, CD14 (A), CD11b (B), HLA-DR (C), and CD68 (D) as well as a stem cell marker CD34 (E) and a stromal marker CD271 (F). The PBMC derived MDMs and FD and FE derived hBMDMs showed similar levels of all macrophage marker expressions as well as geometric means. For the majority of markers analysed the different patient samples showed similar levels of expression, with the exception of CD11b. For PBMC MDMs, FD hBMDMs and FE hBMDMs the percentage CD11b

expression could be split into two groups, donors with a high (>60%) or low (<60%) CD11b expression, this suggested there may be some level of macrophage activation that occurred in the 'high' donor samples. This distinction wasn't as clear in the CD11b geometric mean, but the samples did show a large range compared with the other markers analysed. All three cell sources were also negative for CD34 and CD271 expression, suggesting there was no stem cell or stromal cell contamination.

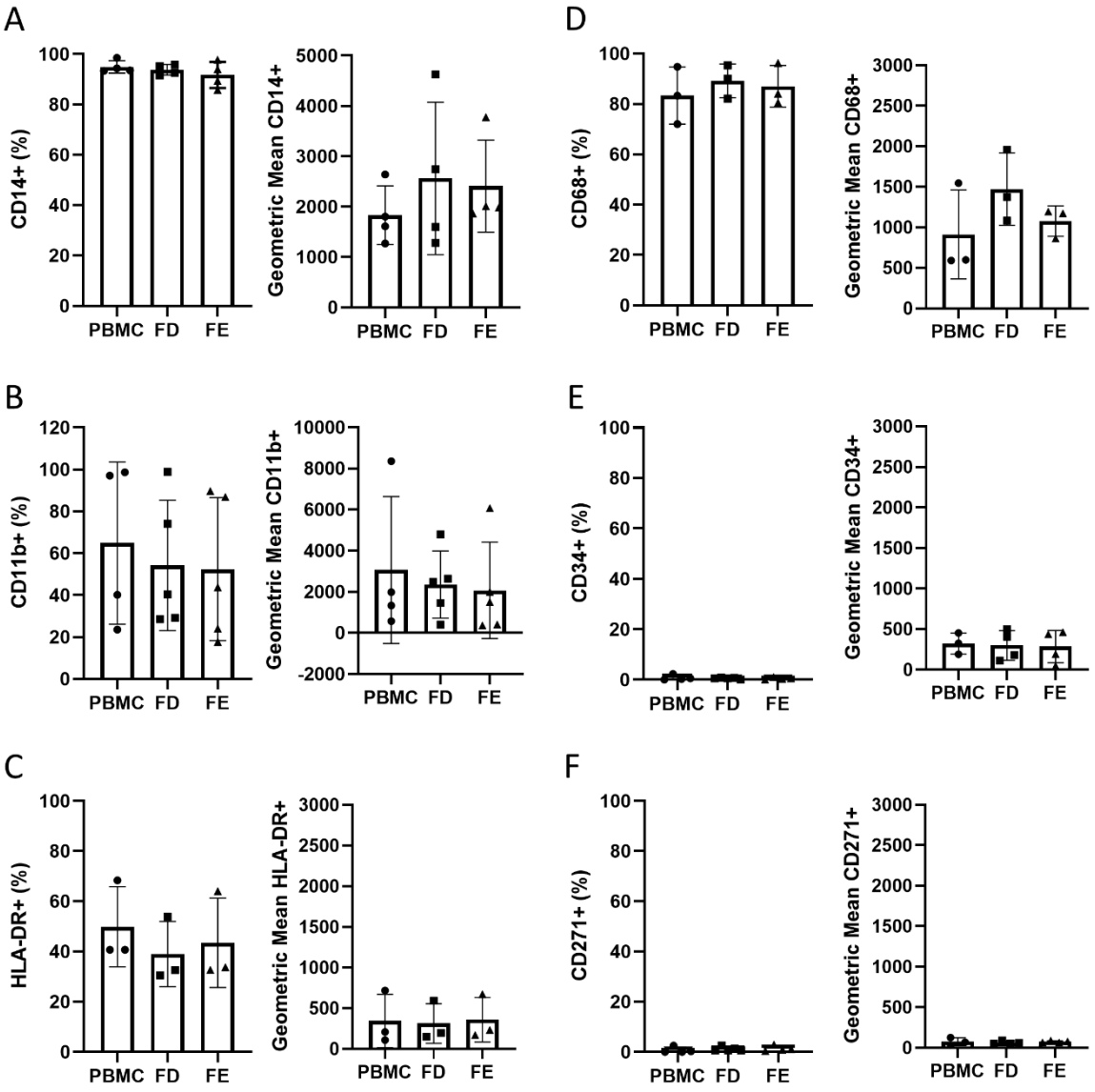

Figure 4-9. Phenotyping of macrophages differentiated after CD14+ isolation*. CD14+ bone marrow and PBMCs were isolated and cultured for 7 days in basal media + M-CSF, and analysed for the percentage and geometric mean of (A) CD14, (B) CD11b, (C) HLA-DR, (D) CD68, (E) CD34 and (F) CD127 by flow cytometry. N=3-4, each with three technical replicates. Results presented as mean +/- SD, statistics determined using a one-way ANOVA, no significance determined.*

4.2.4 Isolating CD14+ cells for MDM Polarisation into M1-like and M2-like phenotypes

Polarisation of the heterogenous MDMs and hBMDMs showed distinct differences in the expression of CD38, CD40 and CD11b markers when isolated from PBMCs, FD or FE bone marrow cells. It was assessed whether this was a direct result of the differentiation of MDMs/hBMDMs from these cell sources, or whether it was a result of stromal cell contamination and low monocyte population in the bone marrow samples. To do this CD14+ FD, FE and PBMC cells were isolated, using either the Miltenyi or StemCell kits (2.2.15), and cultured with M-CSF for 7 days; they were then polarised into a M1-like phenotype, by culturing with LPS and IFNγ, or M2-like phenotype, by culturing with IL-4 and IL-13, for a further 48 hours (2.2.14). M-CSF alone was used as M0-like control. **Figure 4-10** are representative images of M0, M1 and M2 like MDMs/hBMDMs. The M1-like differentiation process resulted in a lower confluency of cells than the M0 and M2-like macrophages.

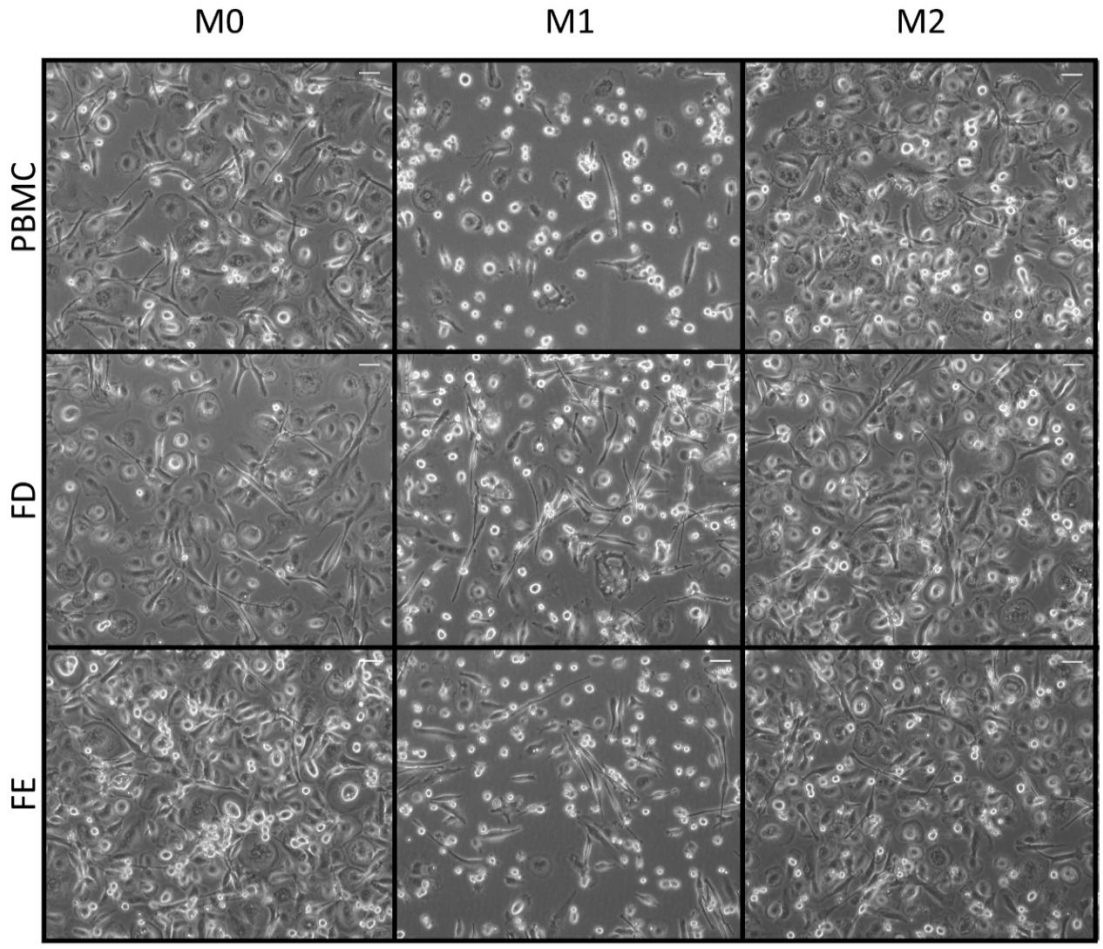

Figure 4-10. Representative images of polarised MDMs and hBMDMs differentiated from CD14+ isolated cells*. CD14+ PBMCs, FD and FE bone marrow cells were isolated and cultured in M-CSF for 7 days. The cells were then cultured in polarisation media for a further 48 hours to differentiate into M0-like, M1-like and M2-like MDMs and hBMDMs. Scale bar= 100 µm.*

After a 9-day culture the cells were dissociated into single cell suspensions and analysed by flow cytometry for a panel of macrophage markers as before (2.3). **Figure 4-11** shows the percentage of positive cells for CD14, CD68, CD40, CD38 and CD11b expression. The expression of CD14 (A) and CD68 (B) were very similar between the PBMC derived MDMs, FD hBMDMs and FE hBMDMs, in all three polarisation conditions. The CD40 (C) percentage expression showed a higher trend in PBMC MDMs compared with the FD and FE hBMDMs for all three corresponding polarised conditions. CD40 expression was also higher in the M1-like polarised cells compared to the M0 and M2-like polarised cells from the same source. CD38 (D) expression was similar between the corresponding polarised cells between each source, but showed an increased level of expression in the M1-like polarised cells compared to the M0 and M2-like polarised cells of the same source.

CD11b (E) positive cells also showed a higher level of expression in the PBMC MDMs compared with the FD and FE hBMDMs for all corresponding polarised conditions. The CD11b expression was also lower in the M1-like polarised cells for each cell source, while there was only a slight increase in the M2-like MDMs compared with the M0-like MDMs. This suggested that the combination of LPS and IFNγ cytokines resulted in expression of an M1-like phenotype including an increase the percentage of CD38 and CD40 positive cells, while lowering the percentage of CD11b, an M2-like phenotypic marker. Similarly to previous data, the percentage of CD11b was high in the M0-like MDMs and hBMDMs, suggesting these cells may have been already polarised towards an M2-like phenotype possibly due to an already activated immune system prior to donating blood or bone marrow, which may affect these assays.

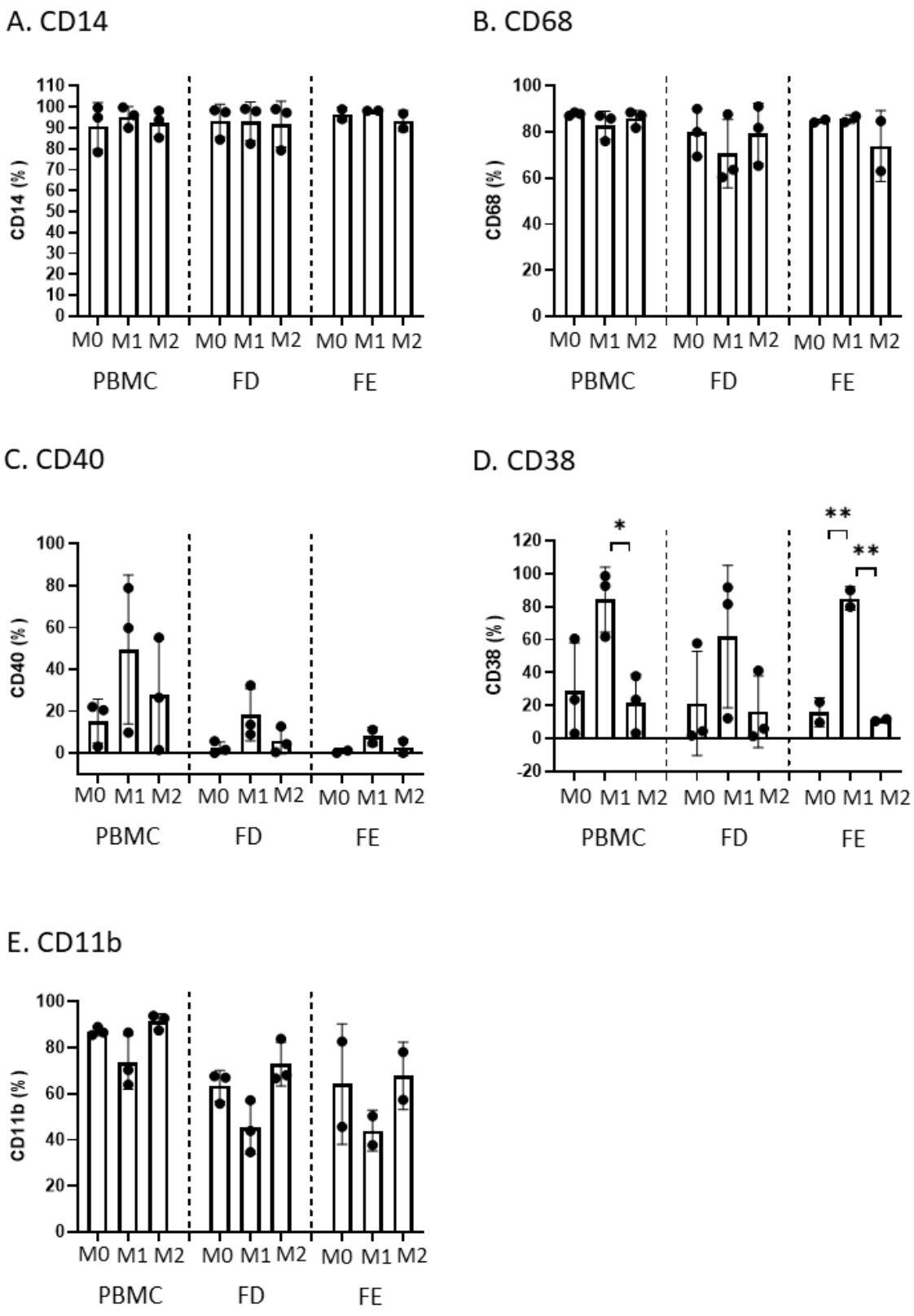

Figure 4-11. Phenotype of polarised MDMs and hBMDMs differentiated from CD14+ isolated cells*. CD14+ bone marrow and PBMCs were isolated and cultured for 7 days in basal media + M-CSF, then cultured for 48 hours in polarisation media. The cells were analysed for the percentage (A) CD14, (B) CD68, (C) CD40, (D) CD38, and (E) CD11b, by flow cytometry. N=2-3, each with three*

*technical replicates. Results presented as mean +/- SD, statistics determined using a one-way ANOVA, significance represented as *<0.05, ** <0.01.*

Figure 4-12 shows the geometric mean for CD14, CD68, CD40, CD38 and CD11b expression of the PBMC derived MDMs, FD hBMDMs and the FE hBMDMs. There were no differences in the geometric mean of CD14 (A) between the corresponding polarised PBMC MDMs, FD hBMDMs and FE hBMDMs from the different cell sources. The expression of CD14 also showed a higher trend in the M1-like polarised cells compared to the M0 and M2-like polarised cells of the same source. Similarly, there were few differences between the geometric mean of CD68 (B) from both the different cells sources and polarisation conditions. CD40 (C) geometric mean also showed similar expression between the corresponding polarisation conditions of the different cell sources, but the M1-like polarised cells had a higher level of expression compared to the M0 and M2-like polarised cells from the same source. The M0 and M2-like CD38 (D) expression was very low for all cell sources, which also indicated similar CD38 geometric mean between the M1-like polarised cells between each cell source.

In contrast the PBMC MDMs showed a higher CD11b (E) geometric mean for all three polarised conditions compared with the corresponding FD hBMDMs and FE hBMDMs, although this was only significant in the M2-like PBMC MDMs and FD hBMDMs. There was also significantly higher geometric mean for the CD11b+ M2-like MDMs compared with the M1-like MDMs, and this trend was also seen in the FD and FE hBMDMs. The data from **Figure 4-11** and **Figure 4-12** shows as expected, M1-like polarised cells had an increase in CD38 and CD40 expression, while M2-like polarised cells showed an increase in CD11b. There was also similar expression of all markers between the corresponding polarised conditions from the three cells sources, suggesting isolating the cells for CD14 prior to differentiation negates the differences found in the heterogenous populations.

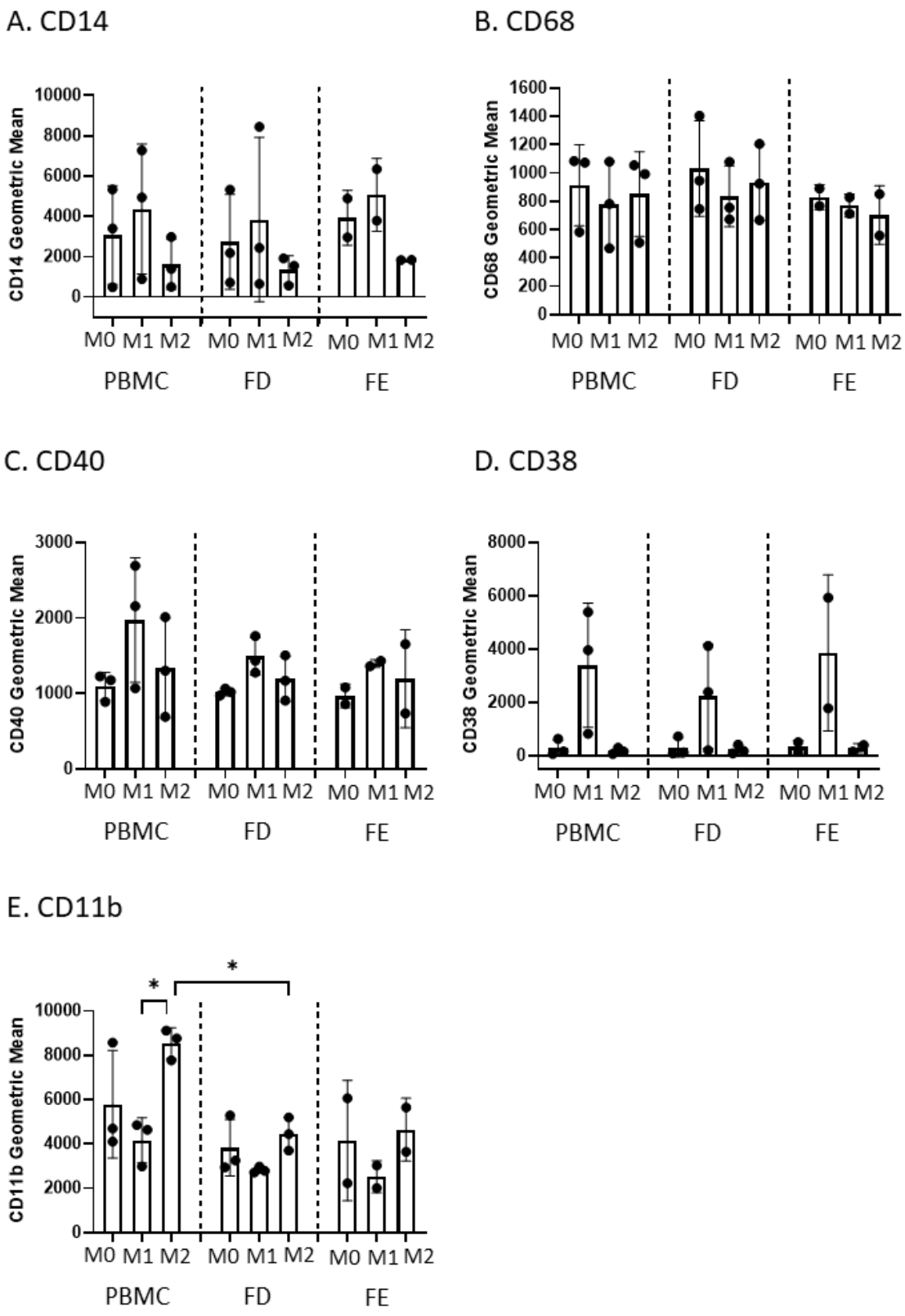

Figure 4-12. Phenotype of polarised MDMs and hBMDMs differentiated from CD14+ isolated cells*. CD14+ PBMC and bone marrow cells were isolated and cultured for 7 days in basal media + M-CSF, followed by 48 hours in polarisation media. The geometric mean of (A) CD14, (B) CD68, (C) CD40, (D) CD38, and (E) CD11b, was analysed by flow cytometry. N=2-3, each with three technical*

*replicates. Results presented as mean +/- SD, statistics determined using a one-way ANOVA, significance represented as *<0.05.*

4.2.5 Phagocytosis of PBMC derived MDMs and Bone Marrow derived hBMDMs

The MDMs and hBMDMs generated from a heterogenous population of cells and from isolated CD14+ cells showed a very similar phenotype, but there were differences in CD11b expression between different donors. To determine whether skeletal location or original source of the MDMs and hBMDMs affected the activation of these cells, the level of Fc independent phagocytosis was assessed. PBMC derived MDMs and bone marrow derived hBMDMs were isolated and cultured with M-CSF for 7 days before being re-plated and cultured for a further 48 hours in M-CSF. Then 3µM BSA-FITC coated beads were introduced into the MDMs and hBMDMs cultures, and incubated for a further 1 hour (2.2.16). Figure 4-13 demonstrates the flow cytometry gating strategy for PBMCs (A) and bone marrow (B). Live cells were gated on the FSC vs SSC, with doublets being excluded in the FSC-H vs FSC-A plot.

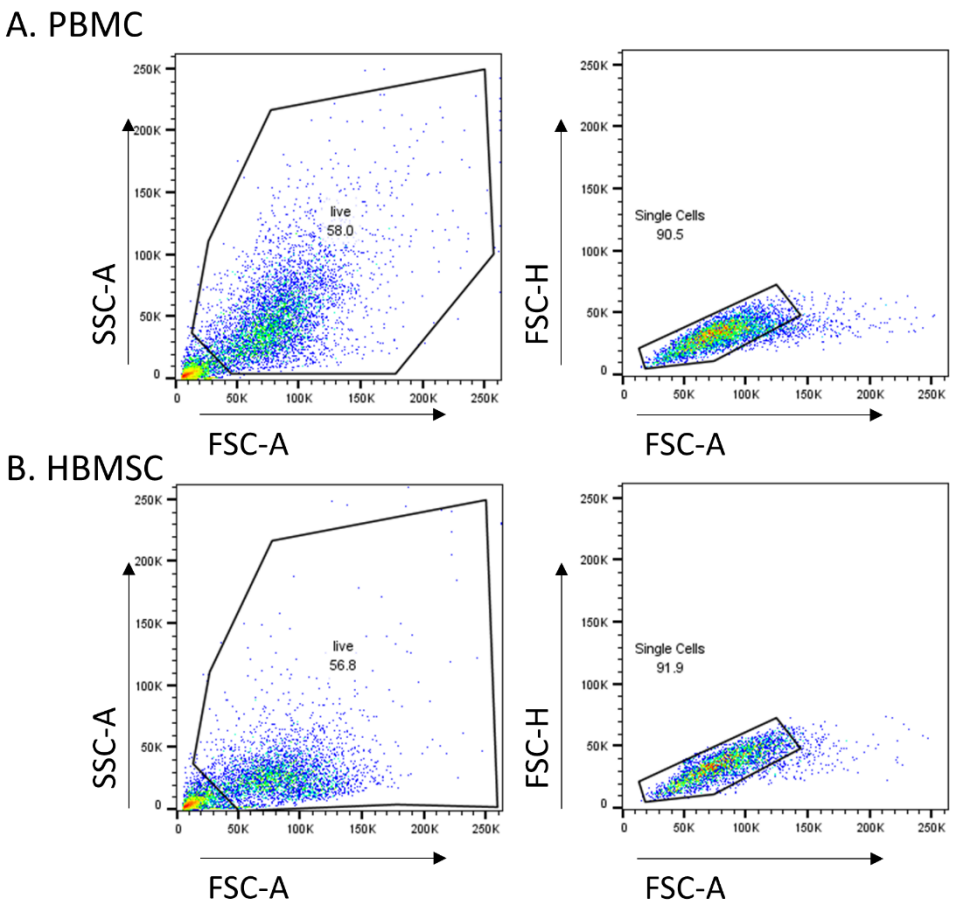

Figure 4-13. Flow cytometry gating strategy for a MDM and hBMDM phagocytosis assay*. Heterogenous human bone marrow cells and PBMCs were isolated and cultured for 7 days in basal media + M-CSF, then re-plated and cultured for a further 48 hours. BSA-FITC beads were co-cultured with the MDMs for one hour before being analysed by flow cytometry. (A) Shows representative images of the live and single cell gating strategy for PBMC MDMs and (B) shows representative images of the live and single cell gating strategy for bone marrow hBMDMs.*

The percentage of FITC positive cells were determined by analysing MDMs and hBMDMs cultured without the beads as a negative control. When FITC labelled beads had been phagocytosed by the macrophages the level of FITC should have increased, which was clearly seen in Figure 4-14A for both MDMs and hBMDMs. These cells were differentiated from a heterogenous population. Figure 4-14B also showed the percentage and geometric mean of FITC, where there were clear increases for both PBMC MDMs and FE hBMDMs. Unfortunately, in this assay there was a large number of dead cells in the FD hBMDM condition, likely due to problems detaching the cells during re-plating, which meant the FD hBMDMs were not analysed. As a large number of cells were needed for a phagocytosis assay, the conditions were only analysed in duplicate when cultured with the beads and as a single well without, as such statistical analysis could not be performed, but the data suggested there was a similar level of phagocytosis occurring between

the MDMs and FE hBMDMs. This assay was set up and analysed by Emma Teal, Cancer Sciences, University of Southampton.

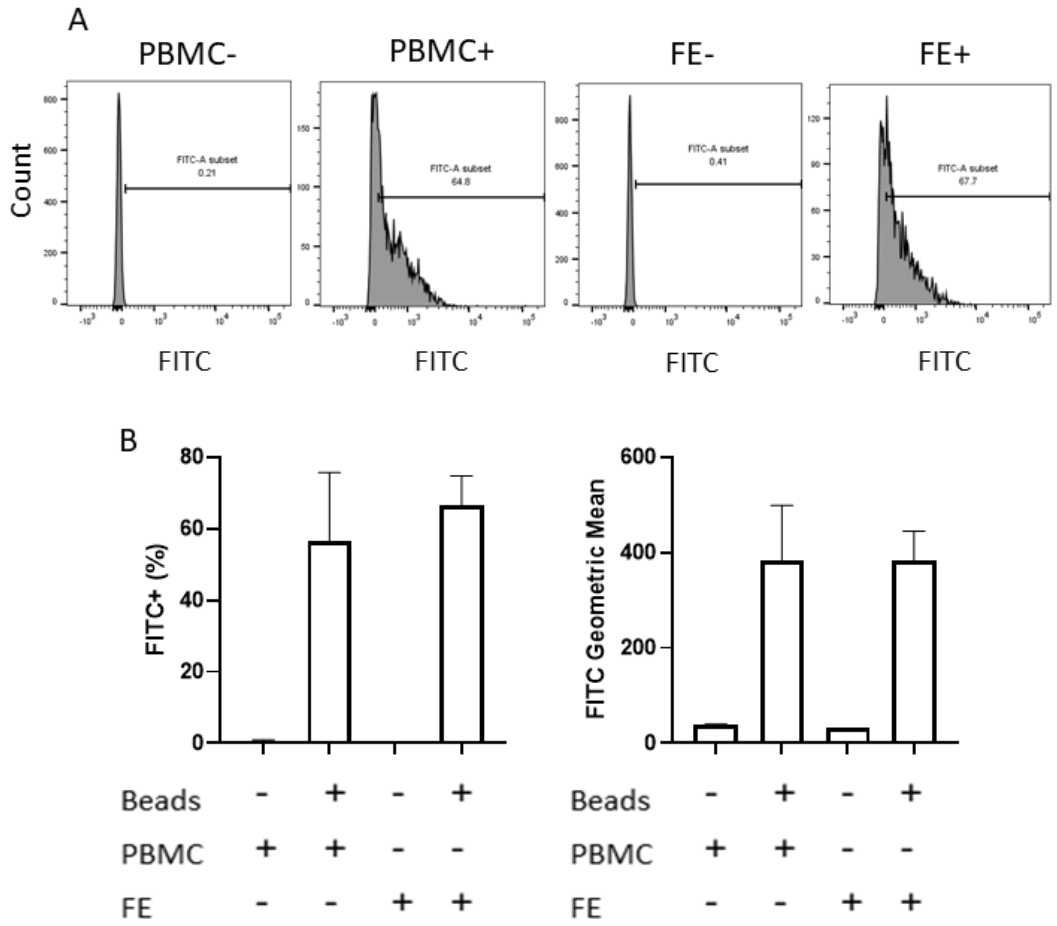

Figure 4-14. Phagocytosis of macrophages generated from heterogenous PBMCs and FE bone marrow. *Phagocytosis of the macrophages was measured by the increase in BSA-FITC beads taken up by the MDMs and hBMDMs. (A) Representative images showing the gating strategy for the FITC+ MDMs and hBMDMs. Macrophages cultured without BSA-FITC beads were used as a negative control. (B) The percentage and geometric mean of FITC+ MDMs and hBMDMs. N=1, with one or two technical replicates. Results presented as mean +/- SD, Results not analysed for significance due to low sample number.*

To reduce contamination of stromal cells in the hBMDM cultures, CD14+ cells were isolated from PBMC and bone marrow samples, differentiated using M-CSF before being re-plated and incubated with 3µM BSA labelled beads. Figure 4-15 are representative images of MDMs from two PBMC samples (A) and hBMDMs from two bone marrow samples (B). Both of the hBMDMs were less confluent than the PBMC2 differentiated MDMs, and the M49 hBMDMs were less confluent than the PBMC1 MDMs. Although lower in cell number there were clearly still live cells in the bone marrow samples, which indicated phagocytosis could occur.

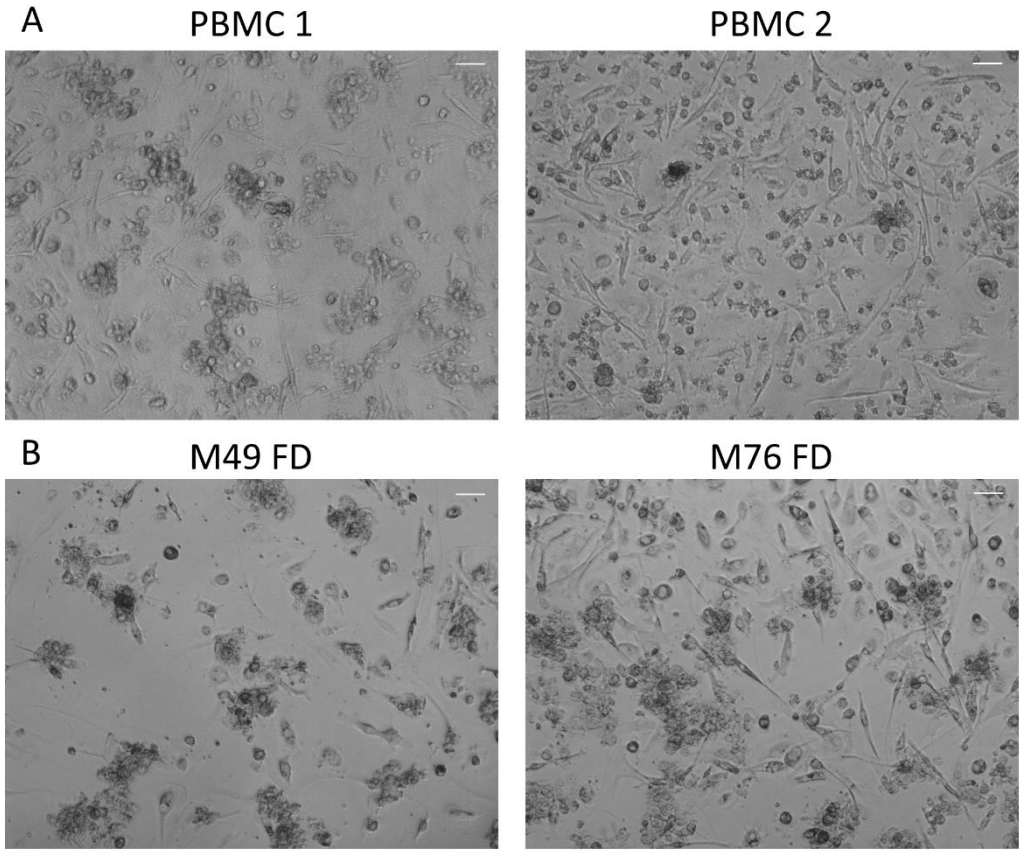

***Figure 4-15. Representative images of macrophages differentiated from CD14+ isolated cells**. Images of CD14+ (A) MDMs and (B) hBMDMs were taken after the cells were cultured for seven days with M-CSF, then re-plated and cultured for a further 48 hours in M-CSF. Scale bar= 100 µm.*

CD14+ isolated PBMCs and bone marrow cells were isolated and cultured as above with 3µM BSA-FITC coated beads (2.2.16). The percentage of FITC positive cells were determined by analysing MDMs and hBMDMs cultured without the beads as a negative control (Figure 4-16A). Figure 4-16B shows the percentage and geometric mean for the PBMC derived MDMs and FD derived hBMDMs, cultured with and without the beads. The BSA-FITC beads alone were also analysed as a positive control. The PBMC samples showed a clear increase in both the percentage and geometric mean of FITC when cultured with the beads, indicating a high level of phagocytosis. In contrast there was no increase in FITC signal when the FD hBMDMs were cultured with the BSA-FITC beads, suggesting phagocytosis had not occurred. As only one independent experiment was analysed for this assay the lack of phagocytosis in the FD hBMDMs was likely due to human error, and would need to be repeated to determine if CD14+ hBMDMs could actively phagocytose the BSA-FITC beads.

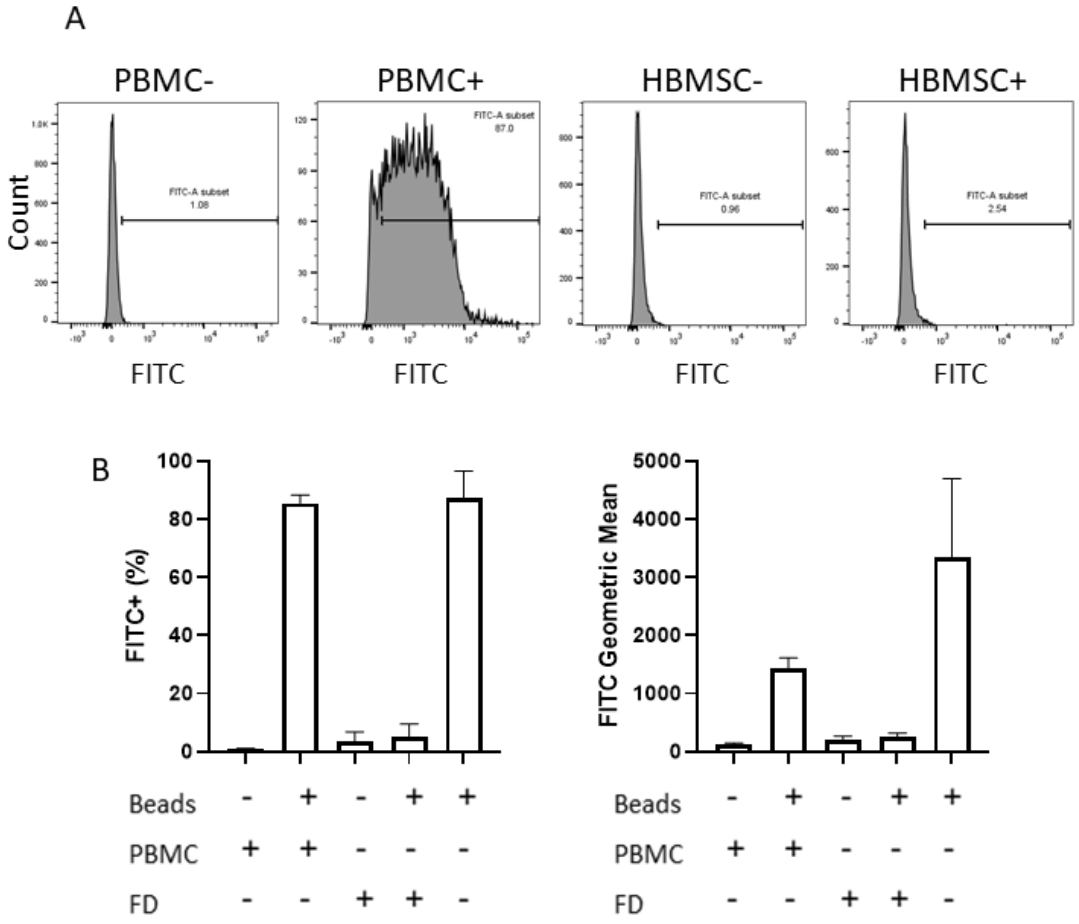

Figure 4-16. Phagocytosis of macrophages generated from a CD14 isolated PBMC and FD cell populations*. Phagocytosis of the macrophages was measured by the increase in BSA-FITC beads taken up by the cells. (A) are representative images showing the gating strategy for the MDMs/hBMDMs cultured with the beads (PBMC+/FD+). Cells cultured without BSA-FITC beads (PBMC-/ FD-) were used as a negative control. (B) The percentage and geometric mean of FITC+ MDMs/ hBMDMs. N=2, with two technical replicates. Results presented as mean +/- SD, Results not analysed for significance due to low sample number.*

4.2.6 Differentiating Osteoclasts from PBMCs and Bone Marrow Cells

Osteoclasts differentiate from the same lineage as macrophages, and are the main regulator of bone resorption [54]. These cells are also likely to be already present in the human bone samples used for the 3D bone model. Due to similarities in phenotypic and functional characteristics found in MDMs differentiated from PBMC and hBMDMs differentiated from bone marrow, phenotypic differences in the differentiation of osteoclasts was also assessed. To compare the generation of osteoclasts, PBMCs and bone marrow cells were isolated and plated at varying concentrations in a 48 well plate. The cells were incubated for 14 days in M-CSF + RANKL (2.2.17), then fixed and analysed by staining for TRAP (**Figure 4-17**), osteoclasts are stained pink/purple. **Figure 4-17**A showed more osteoclasts were present in the high cell number plated at $4x10^6$ cells per ml in both

FD and FE cells, but there was no osteoclast differentiation from PBMCs plated at the same density. Osteoclast differentiation from PBMCs occurred at higher cell density than bone marrow, at around $1x10^7$ cells per ml. TRAP staining of the PBMC derived osteoclasts plated at a density of $1x10^7$ cells per ml illustrated a higher number of osteoclasts compared with those plated at $2x10^7$ cells per ml. This suggested a cell density above $1x10^7$ cells per ml could limit osteoclast differentiation, possibly due to a higher number of dead cells.

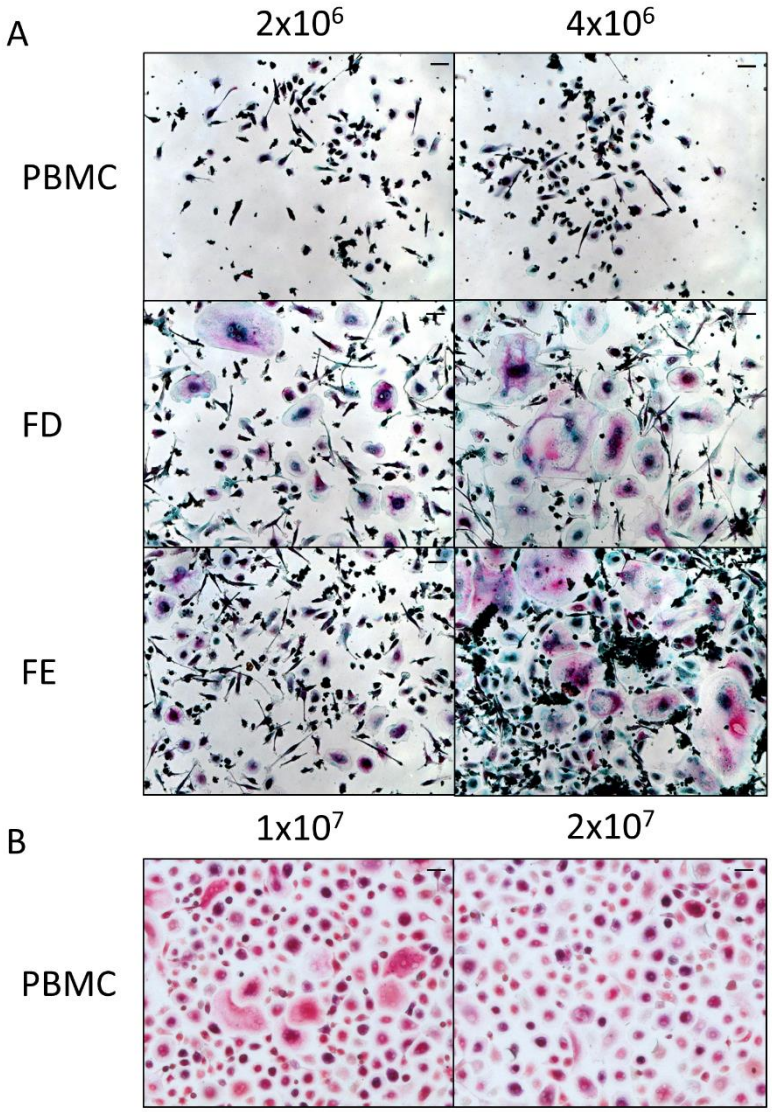

Figure 4-17. Differentiation of osteoclasts from PBMCs and bone marrow cells. *(A) PBMC, FD and FE cells were isolated and plated at $4x10^6$ and $2x10^6$ cells per well, with (B) PBMCs also plated at $1x10^7$ and $2x10^7$ cells per well. The cells were then incubated for 14 days in basal media + M-CSF + RANKL. After 14 days the cells were fixed then stained using the TRAP protocol. Osteoclasts stained red/ purple. Images are representative of N=1 with three technical repeats. Scale bar= 100µm.*

Due to the high discrepancy in cell number needed to differentiate osteoclasts from a heterogenous population, CD14+ PBMCs and bone marrow cells were isolated and cultured in osteoclast differentiation media (2.2.17). To do this, CD14+ isolated PBMC and FD cells were plated at varying concentrations and incubated for 14 days in M-CSF + RANKL, before being fixed and analysed by TRAP staining (**Figure 4-18**). While osteoclast differentiation occurred at all cell concentrations, a clear increase in osteoclast differentiation could be seen in the two higher concentrations of CD14+ PBMCs compared with the CD14+ FD cells, where they created very large multinucleated osteoclasts.

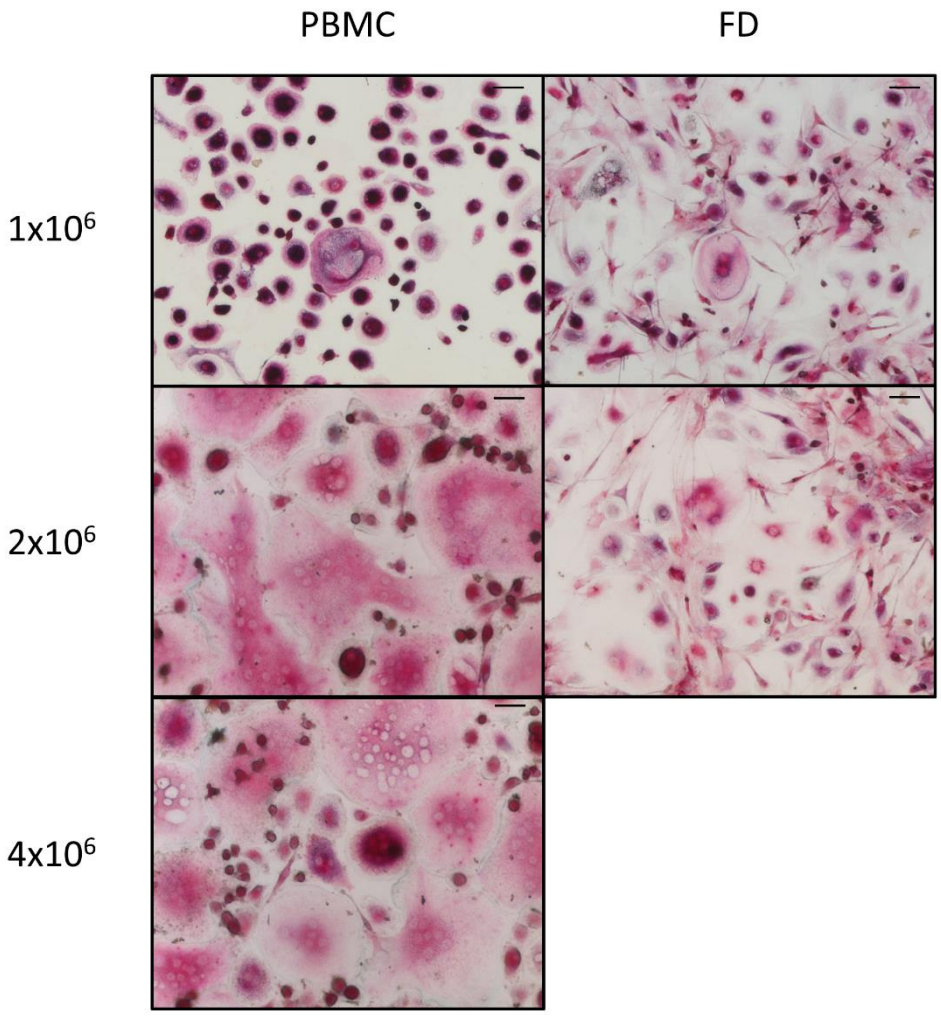

Figure 4-18. Differentiation of osteoclasts from CD14+ isolated PBMCs and bone marrow cells. *(A) CD14+ PBMC and FD cells were isolated and plated at 1x10^6, 2x10^6, and 4x10^6 cells per well, before being incubated for 14 days in basal media + M-CSF + RANKL. After 14 days the cells were fixed then stained using the TRAP protocol. Osteoclasts stained red/ purple. Images are representative of N=1 with three technical repeats. Scale bar= 100µm.*

4.2.7 Activation of Osteoclasts

Previous data showed that osteoclasts could be derived from both PBMCs and bone marrow cells. There was a particularly high level of differentiation from CD14 isolated PBMCs, but the TRAP staining could not assess whether these osteoclasts were activated and could resorb bone. To assess this a pilot study was set up to determine whether cortical bone slices could be used to look at bone resorption using a pit assay (2.2.17, 2.6.7). Isolated PBMCs were cultured for 14 days in M-CSF + RANKL, on cortical bone slices that were drilled from the femoral neck of a patient who had undergone hip replacement surgery, before being fixed and stained for TRAP. Cortical slices were incubated without cells as a control, osteoclasts were stained pink/purple and nuclei were stained black. **Figure 4-19**A are representative images of TRAP staining from PBMC derived osteoclasts. There was a clear coverage of PBMC derived osteoclasts over the cortical bone, but the bone itself was not as flat as initially determined without the use of a microscope, which resulted in some slices being unusable for this assay. Following TRAP staining the bone slices were sonicated to remove the cells, before being stained with toluidine blue (**Figure 4-19**B). Darker areas of stain indicated pits where the bone had been resorbed by the osteoclasts. Areas of bone resorption indicated that the osteoclasts were active and could be used to compare the activation between PBMC and bone marrow derived osteoclasts. Further assays would need to be completed to determine whether cortical slices would be a robust method to analyse osteoclast activation.

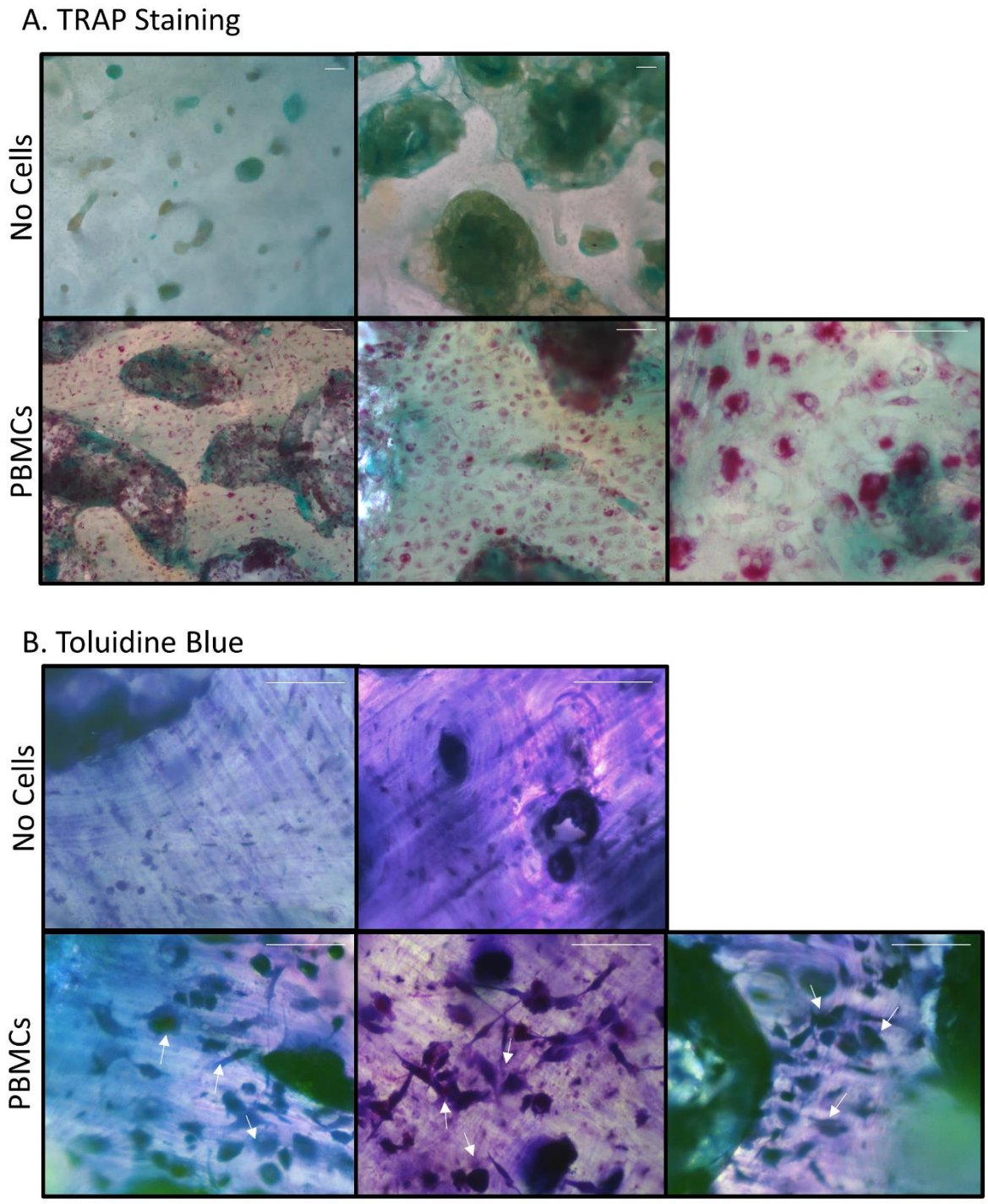

Figure 4-19. Activation of osteoclasts from CD14+ isolated PBMCs*. CD14+ PBMCs were isolated and incubated on cortical bone slices for 14 days in basal media + M-CSF + RANKL. After 14 days the cells were fixed then stained using the TRAP protocol (A), images were taken at various objectives. Osteoclasts stained red/ purple. (B) Toluidine Blue staining of cortical bone slice after osteoclasts were removed by sonication, areas of resorption are stained darker blue, represented by white arrows. Images are representative of N=1 with three technical replicates. Scale bar= 100µm.*

4.3 Discussion

These studies were designed to compare macrophage and osteoclast differentiation ability from PBMCs and bone marrow isolated cells. The 3D multicellular model consisted of human bone cores drilled from the femoral epiphysis; as such macrophages derived from the bone marrow (hBMDMs) could be more appropriate in this model than PBMCs (MDMs). Key findings:

- After CD14 isolation macrophages derived from PBMCs and bone marrow showed similar phenotypes.
- The derived macrophages from PBMCs and bone marrow also showed similar characteristics after polarisation towards an m1-like and M2-like phenotype.
- Osteoclasts can be differentiated from both PBMCs and human bone marrow cells.

Analysis of the PBMC and bone marrow derived cells showed the percentage of CD14 positive MDMs was significantly higher compared with the FD hBMDMs and FE hBMDMs when plating from a heterogenous population, with differences also found in CD11b and HLA-DR expression. These differences were negated after isolating CD14+ cells before macrophage differentiation. The similarity in macrophage marker expression from the three cell sources after CD14 isolation, demonstrated that the presence of stromal cells were contaminating the flow cytometry analysis of the heterogenous cell populations, and was most likely causing the differences between the MDMs and hBMDMs. Interestingly these stromal cells did not show an increase in CD271, a stromal/ mesenchymal stem cell marker [223], which questions the validity of using this antibody to check for the presence of contaminating cells. MDM assays which showed a large population of stromal cells (roughly more than 40%) were discarded before analysis, this reduced the overall number of assay repeats for the hBMDMs.

In the CD14+ isolated MDMs and hBMDMs there were large donor variations in the expression of CD11b from all three cell sources. CD11b is an M2-like macrophage marker, these cells are known to secrete anti-inflammatory cytokines, and are involved in wound healing and tissue repair [224]. This could suggest that some patient samples were already primed towards this M2-like phenotype. Previous studies have suggested a strong link between the M1-like pro-inflammatory macrophages in osteoarthritis and osteoporosis patients. These are the two most common diseases of patients undergoing hip replacement surgery, with chronic inflammation a direct contributor to the aetiology of osteoporosis and osteoarthritis [225]. More recent studies have also linked M2-like macrophage polarisation with osteogenic differentiation and mineralisation [226, 227]. It has been hypothesised that modulation to favour M2-like macrophages could be an effective treatment strategy for these diseases [228]. This suggests that macrophages from osteoporosis and osteoarthritis samples are more likely to be polarised towards an M1-like

phenotype, and thus have a lower expression of CD11b. While this could be the reason of the 'low' level of CD11b in some patient samples, this was not the case for the PBMCs. More recently a study has hypothesised that there could be a correlation between an increased M2-like phenotype with extended cell culture, particularly in the presence of biomaterials, suggesting that *in vitro* culture may polarise macrophages towards an M2-like phenotype [229]. While the macrophage assays in this thesis were all standardised to a 7/9 day culture, other factors like confluence of the cultures may play a role in activating these cells towards a M2-like phenotype.

The MDMs generated were also polarised with LPS and IFNγ to generate a M1-like phenotype [230], and IL-4 and IL-13 for a M2-like phenotype [230]. Using these cytokines, previous studies have shown M1-like MDMs upregulate CD38 [231] and CD40 [232], while M2-like macrophages upregulate CD11b expression [233]. Polarised macrophages from heterogenous populations showed that FD hBMDMs had the lowest expression for all standard and polarised macrophage markers, while PBMCs generally had the highest expression of all macrophage markers. This did not affect their ability to differentiate down the M1 and M2-like phenotypes, suggesting contaminations of stromal cells in the culture was lowering the overall macrophage marker expression. This contention was supported by the similarity of macrophage markers in the CD14 isolated cell cultures, although higher expression could be seen in CD40 and CD11b PBMC MDMs verses the FD and FE hBMDMs. Previously it was shown that PBMC MDMs were more confluent than bone marrow hBMDM populations, and the increase in CD11b expression could support the contention that confluency could be linked to a default M2-like phenotype, although more experiments would be needed to test this hypothesis clearly.

Phagocytic ability of macrophages is important as it is the main role of all macrophages of various phenotypes. Thus, the phagocytic ability of PBMC derived MDMs and bone marrow derived hBMDMs was compared. An initial experiment was performed using MDMs differentiated from an heterogenous population, but due to the high number of cells needed there were not enough FD MDMs to analyse, as such only PBMCs and FE MDMs were compared. The MDMs showed very similar phagocytic ability from both the PBMCs and the FE cells, but this was a very hard assay to replicate as contaminating stromal cells in further assays meant phagocytosis could not be analysed. To overcome this, the phagocytic ability of CD14 isolated PBMC MDMs and FD hBMDMs was also analysed. FE hBMDMs were not analysed due to a limiting number of samples. Interestingly and unexpectedly the FD hBMDMs showed no phagocytic capacity. While images taken before flow cytometry analysis suggested that there were living macrophages in the FD cultures, which was confirmed by a clear FSC vs SSC population albeit a lower density than the PBMCs, there was no uptake of the BSA-FITC labelled beads. As this was only from one experiment it was possible that an error during the setup of the assay meant no phagocytosis

occurred. Further experiments will need to be performed to confirm the phagocytic ability of the bone marrow compared with the PBMC generated MDMs.

Osteosarcoma patients have uncontrolled bone regulation leading to not just abnormal bone formation but also areas of bone resorption. Bone resorption is regulated by osteoclasts, these cells share a progenitor cell ancestor with macrophages [234], and in a healthy body work alongside osteoblasts for bone growth and maintenance. In a later results chapter (Chapter 5) µCT analysis was used to determine whether bone growth or resorption occurred in the 3D bone models. Bone cores with activated osteoclasts were used as a positive control for bone resorption, as such culture conditions were optimised for osteoclast differentiation, including whether PBMCs or bone marrow cells resulted in a higher number of activated osteoclasts. It has been shown that osteoclasts can be generated from both bone marrow and PBMCs heterogenous populations (**Figure 4-17**), although different cell concentrations were needed. While CD14+ PBMCs showed the highest level of osteoclast differentiation (**Figure 4-18**), bone marrow suspensions had a clear increase in osteoclast differentiation compared with PBMCs when plated from a heterogenous population. These cells were taken from patient's most likely suffering from osteoarthritis or osteoporosis, which have both been shown to upregulate osteoclasts [235]. A pilot study was also performed to test whether these osteoclasts were actively resorbing bone, which showed it was possible to perform pit experiments on cortical bone slices, but further optimisation needs to be undertaken to make this assay more robust. Due to the limiting data on osteoclast activation, these cells were not added to the final 3D bone model, but due to the nature of the bone cores used, activity of osteoclasts already present in the models will be assessed in Chapter 6.

Overall, any differences in MDM phenotype, between PBMC derived MDMs and hBMDMs from both FD and FE, were mostly negated when CD14+ cells were isolated before differentiation. This suggested that either MDMs or hBMDMs could be used as a suitable cell source to introduce macrophages into the 3D bone model. Further preliminary studies showed mixed results for the phagocytic ability of hBMDM, which suggested further analysis would be needed to confirm whether the hBMDMs would be appropriate for this model. PBMCs also generated a much larger number of macrophages from one leukocyte cone compared to one bone marrow sample. Combining this data together PBMC derived MDMs were chosen to be used as the source of macrophages in the 3D bone model.

Chapter 5 Micro Computed Tomography Analysis of a 3D Multi-Cellular Model of Osteosarcoma

5.1 Introduction

A greater understanding of cellular interactions in the osteosarcoma tumour microenvironment will allow for the development of more effective drugs and therapies. Consequently, although the generation of a 3D multicellular model was complex, it could lead to unique insights into osteosarcoma. Previous research has produced many different 3D models for cancer, including the integration of cancer cells into scaffolds. These have been made with various biological and synthetic components [156, 165], but human bone has yet to be used as the structural component for a 3D model of osteosarcoma.

The CAM is a dense vascular network present in a fertilised chicken egg, and functions by transporting nutrients and waste as the chick develops [166]. Many studies have used this membrane to implant a substance of interest, including scaffolds or cells, to visualise and study vascularisation. The CAM model was also used to allow blood vessels to integrate into bone, with literature showing successful bone growth and remodelling can occur in human bone cylinders [177]. The CAM model has been used in cancer research for many years, as vascularisation is an important factor in researching tumour growth and initiation, while the immunosuppressive nature of the fertilised chicken egg limits the effect of tissue rejection which may be found in other models.

To develop a 3D multi-cellular model, human bone, taken from the femoral head of patients who have undergone hip replacement surgery, was combined with the three cell types of interest determined in Chapter 3 Chapter 4 namely HBMSCs, Saos-2 osteosarcoma cells and MDMs. The 3D bone model was then implanted on the CAM, to allow for growth and vascularisation. One of the methods of diagnosing osteosarcoma over other bone cancers is the presence of spontaneous and disorganised bone growth [236], as such it was important to determine whether there were early signs of bone formation occurring in the 3D bone model through the use of µCT. This imaging technique has been invaluable in researching bone microarchitecture as well as scaffold-bone interactions *in vivo*, as it is both non-destructive and non-invasive [237-239]. This allowed for the opportunity to combine multiple analysis from one bone core and to perform serial assessments, to gain a better understanding of the 3D bone model.

Overall, there were a number of culture conditions as well as the size and shape of the bone fragments that needed to be compared to develop the 3D multicellular bone core model, these included:

1. Whether the ability of bone growth or resorption was affected by the culture method, either in a long-term culture or incubation on the CAM.
2. Whether acellular bone cores, which could be stored for longer, showed similar affects to standard bone cores.
3. Whether the use of bone slices, which had a lower initial bone volume, could improve the ability for the cells to produce osteoid.
4. Finally, whether the 3D bone model could be used to assess drug and therapies.

5.2 Results

5.2.1 Development of the CAM Model

The CAM model was first optimised to determine whether vascularisation could integrate into the 3D bone model. Thus, 7 days after fertilisation windows were made on the chicken eggs, as described in (2.4.3), and either an 8 mm bone core (2.4.1) or approximately 5 mm bone slice (2.4.2) was placed onto the CAM membrane (2.4.3). The windows were sealed and the eggs incubated for a further 10 days. On day 17 after fertilisation the bone cores were removed from the eggs and the chicks humanely killed. At the end of the incubation period blood vessels were shown to be integrating into a representative bone core (**Figure 5-1**A). The presence of blood vessels was also seen in histological staining of the bone core; **Figure 5-1**B shows a representative H+E image indicating the presence of a blood vessel in the bone marrow of the core.

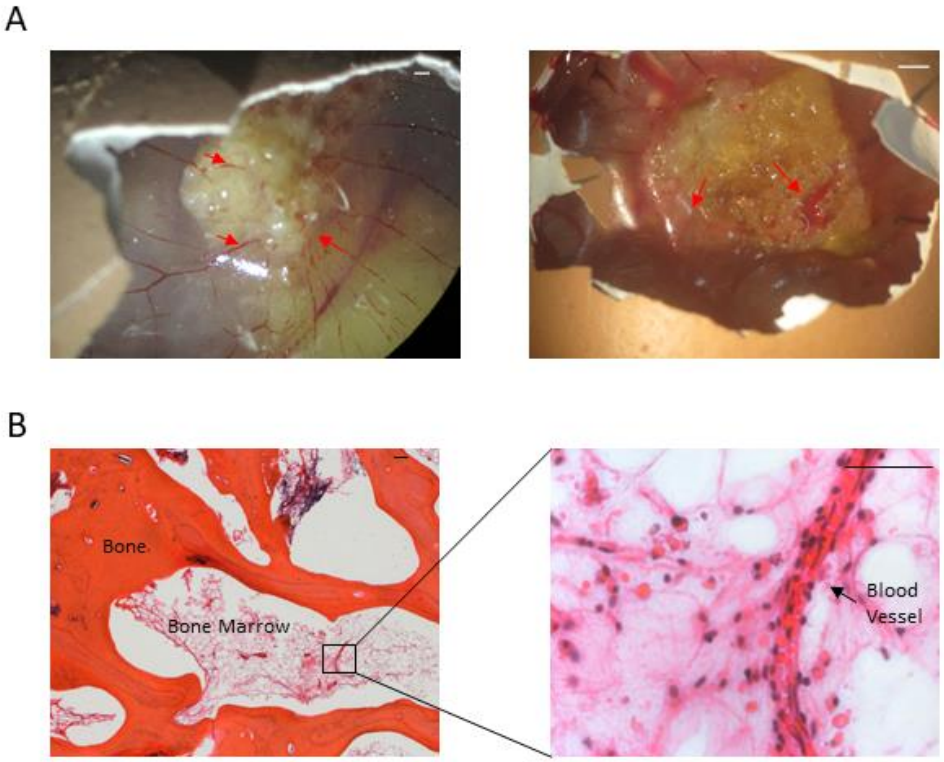

Figure 5-1. Vascularisation of bone cores incubated on the CAM*. (A) An image of a bone core and bone slice after incubation on the CAM, red arrows show areas of angiogenesis. Scale bar = 1 mm. (B) H+E staining of a bone core section, showing vascularisation through the internalisation of blood vessels. Scale bar = 100µm.*

5.2.2 Optimising the Quantification of Bone Cores using Micro-CT Analysis

To assess whether bone formation or resorption had occurred within the bone cores and slices, µCT images (2.7.2) were taken of the bone cores before and after incubation in either long term culture (37°C 5% CO_2 for up to 30 days) or incubated for 10 days on the CAM. These images were reconstructed, overlaid, and quantitatively analysed to compare bone formation and resorption (2.7.2 to 2.7.5). **Figure 5-2** illustrates the process used to align the µCT images, where **Figure 5-2**A and D showed a 2D section of the bone core taken before incubation (pre) and Figure 5-2B and E taken after incubation (post). When these images were overlaid (**Figure 5-2**C and F) they showed areas of bone misalignment (indicated by yellow circle), areas of bone loss (red); where bone was present in the pre image but not in the post, and areas of bone formation (blue); where bone was present in the post image but not the pre.

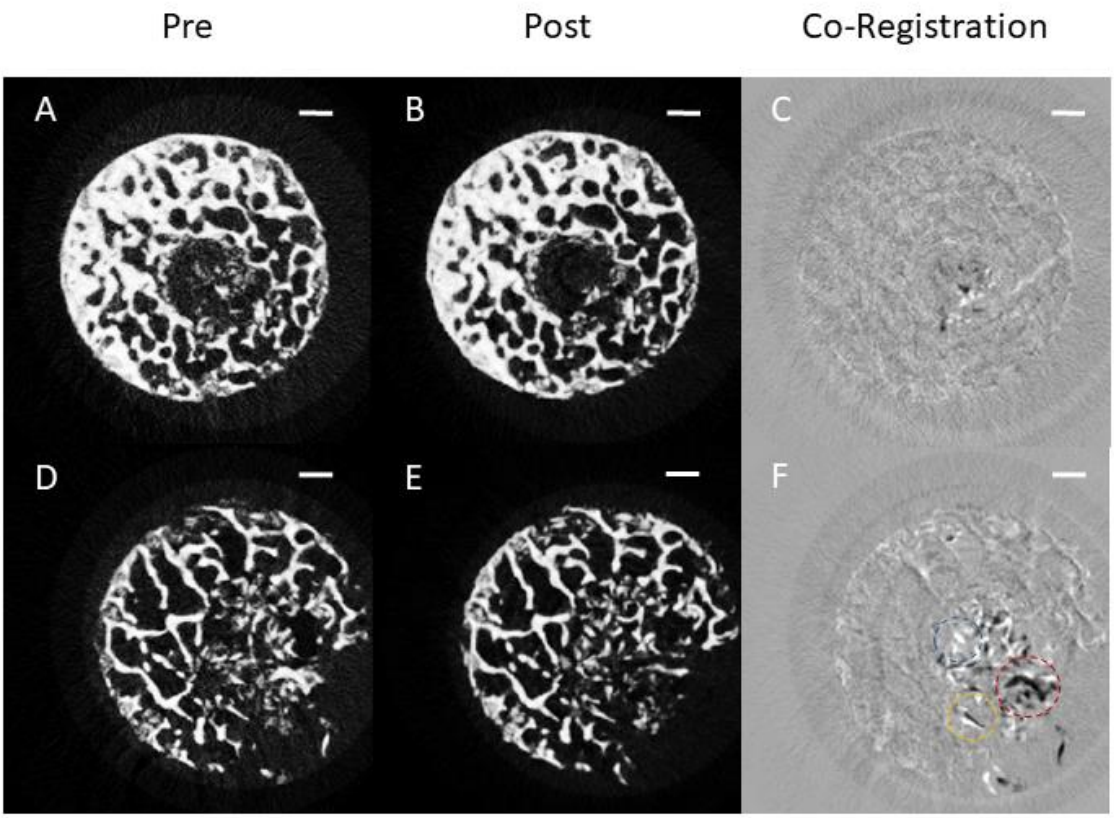

Figure 5-2. Reconstructed µCT images of a bone core at two different planes*. (A) and (D) are representative images taken before CAM incubation, (B) and (E) are images of the same core taken after a 10 day CAM incubation. (C) and (F) are the pre and post images overlaid showing areas of bone misalignment (yellow), bone loss (red) and bone gain (blue). All following µCT analysis was produced using this reconstruction method. Scale bar= 1 mm.*

Once correctly aligned these tiff images could be reconstructed into a 3D image. **Figure 5-3** are representative images of a bone core pre (A) and post (B) incubation. **Figure 5-3**C also shows the bone fragments present in the pre images but not in the post (bone loss or resorption) suggesting there was bone loss around the outside of the bone core, likely due to damage during handling of the bone cores. **Figure 5-3**D indicates the bone fragments present in the post bone core that were not in the pre (i.e. new bone formation), indicating areas of bone growth around the centre of the bone core. In all experiments, both the whole bone core and a region of interest (ROI), taken approximately 1 mm around the bone defect, were analysed for bone and trabecular data. Fold change was calculated by dividing the post data by the pre data of each bone core. In all experiments the control was bone cores or slices incubated without additional cells unless stated otherwise.

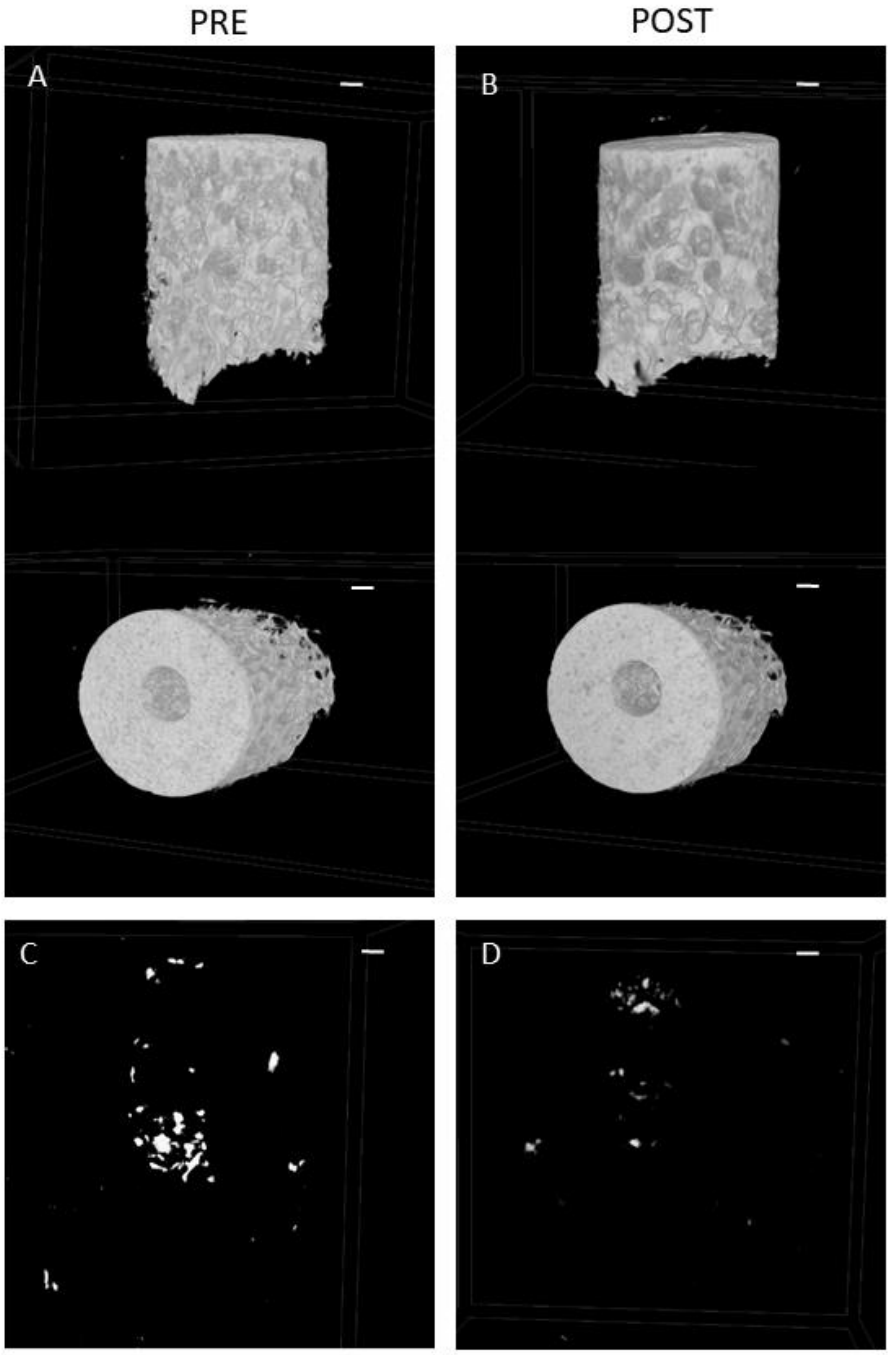

Figure 5-3. Reconstructed µCT images of a bone core*. Representative µCT images were taken (A) before incubation in the CAM assay (pre), and (B) after incubation in the CAM assay (post). The post images were overlaid on the pre-images, and the overlapped areas were removed, resulting in areas of bone loss (C). Conversely the pre-images were overlaid on the post images and areas of overlap were removed, resulting in areas of bone formation (D). Images are representative of N=3 with three technical replicates. Scale bar = 1 mm.*

To determine if any structural changes were taking place in the bone cores, quantitative analysis was carried out based on the minimum set of variables [240] including percentage bone volume, trabecular number, trabecular thickness and trabecular separation, as well as bone surface to

volume ratio. For these parameters an increase in bone volume, trabecular number and trabecular thickness as well as a decrease in trabecular separation and bone surface to volume ratio are correlated with an increase in bone volume. TBPf was also important in analysing data as it compares the connectivity of trabecular bone by describing the bone as convex or concave, this meant more concave surfaces were representative of a connected spongy lattice, while more convex surfaces represented a badly connected lattice [241]. Decreases in TBPf indicated the presence of bone growth, while increases were linked with bone loss. Connectivity density was also assessed; the amount of connected bone divided by the total volume of the sample, alongside the Euler number; which computes the number of marrow cavities completely surrounded by bone, alongside the number of objects, and calculates the number of connections that need to be broken to split the bone structure into two parts [240]. For both connectivity density and Euler number, an increase suggested bone growth had occurred, while a decrease indicated bone loss.

Figure 5-4 represents the µCT analysis for bone cores cultured with and without Saos-2 spheroids, in basal (A) or osteogenic I (B) media for 30 days, at 37°C 5% CO_2. In these experiments there was no difference between the bone cores with and without Saos-2 cells, with the exception of the trabecular pattern factor (TBPf) and Euler number (**Figure 5-4**). In **Figure 5-4**A the TBPf of the whole bone core remained similar between the control and Saos-2 cells, but the ROI showed an increased trend when cultured with Saos-2 cells, suggesting early signs of bone loss. In contrast, **Figure 5-4**B demonstrated the opposite for the whole bone core analysis, with a significant decrease in TBPf when the bone cores were cultured with Saos-2 cells compared with the control (**Figure 5-4**C), suggesting signs of osteoid production, although this difference was not seen in the ROI. The Euler number for **Figure 5-4**A showed a very similar pattern to the TBPf, showing an increased trend with Saos-2 cells in the whole core and ROI. In **Figure 5-4**B the Euler number was very similar in the ROI, but was lower in the whole bone analysis with Saos-2 cells compared with the control, suggesting that that the level of connectivity increased slightly on the outside edges of the control bone core.

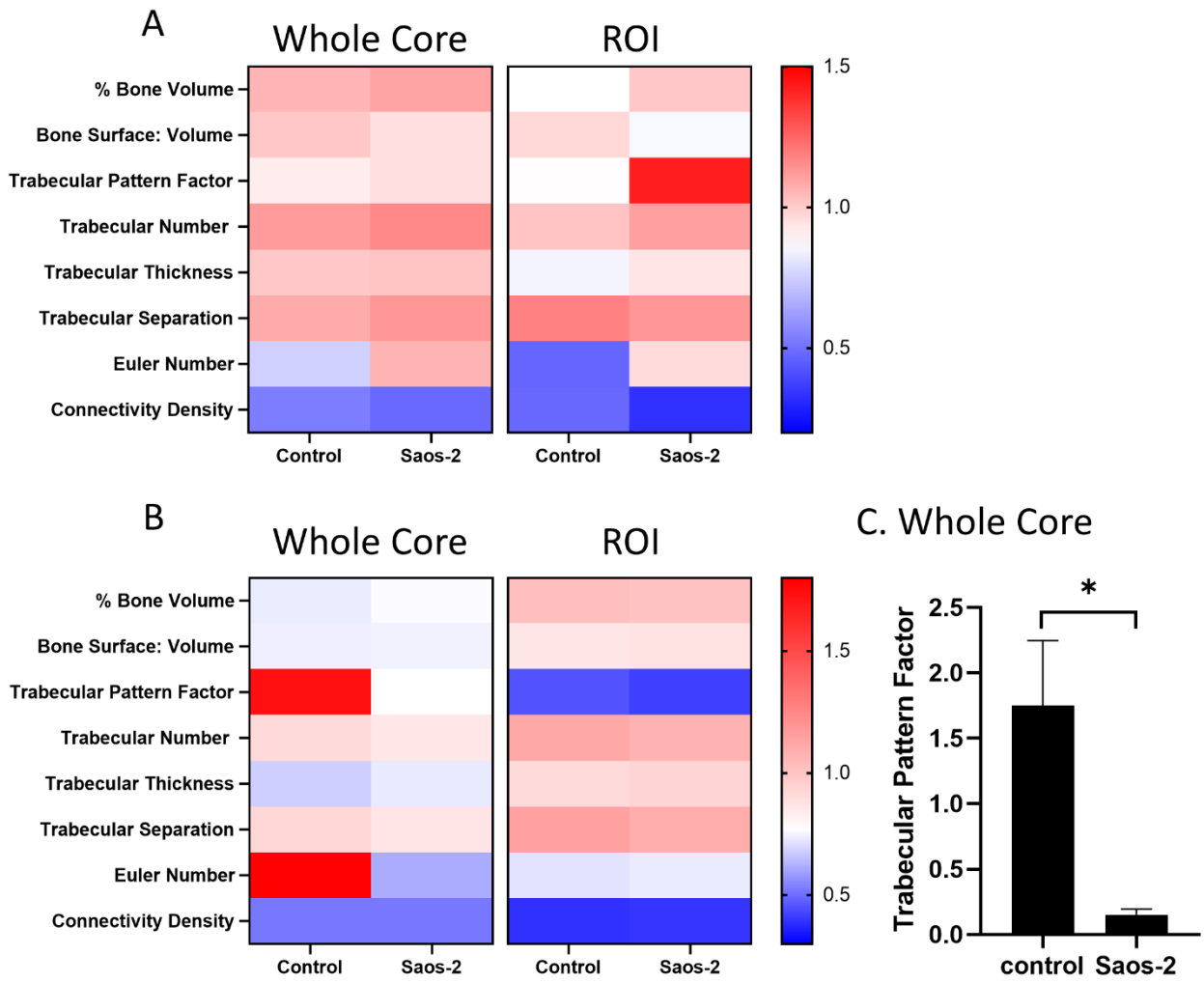

Figure 5-4. Quantitative µCT analysis of bone cores cultured in basal or osteogenic media*. Bone cores were cultured with and without Saos-2 cells in (A) Basal or (B) osteogenic media for 30 days, with µCT images taken before and after incubation. Analysis was performed on the whole bone core and a ROI approximately 1mm around the defect area. Heat maps represent the fold change, of percentage bone volume, bone surface to volume ratio, trabecular pattern factor, trabecular thickness, trabecular number, trabecular separation, Euler number and connectivity density. Data presented as mean. (C) The trabecular pattern factor from while core cultured in osteogenic media. N=1 with three technical replicates. Data presented as mean +/- SD, statistics determined using a one-way ANOVA, significance represented as *<0.05.*

5.2.3 Quantifying the Bone Formation and Resorption of Bone Cores incubated on the CAM

Further µCT analysis was carried out on bone cores before and after a 10-day incubation on the CAM (2.4.1 and 2.4.3). The bone cores were implanted with and without a combination of Saos-2, HBMSC and SKBR3 cells. **Figure 5-5**A combined the µCT analysis of bone cores cultured with or

without Saos-2 cells. Analysis of these two experiments showed more differences between the Saos-2 and control cores were found in the ROI compared with whole bone analysis. In the ROI, there were marked trends in the trabecular separation and Euler number. The decrease in trabecular separation and increase in Euler number in the Saos-2 bone cores compared against the control, suggested that although bone volume had not changed, osteoid production may have occurred in the presence of Saos-2 cells. This could have resulted in a decreased separation between trabecular bones, which consequently meant more connections were needed to be broken before the core could be split into two, resulting in a higher Euler number.

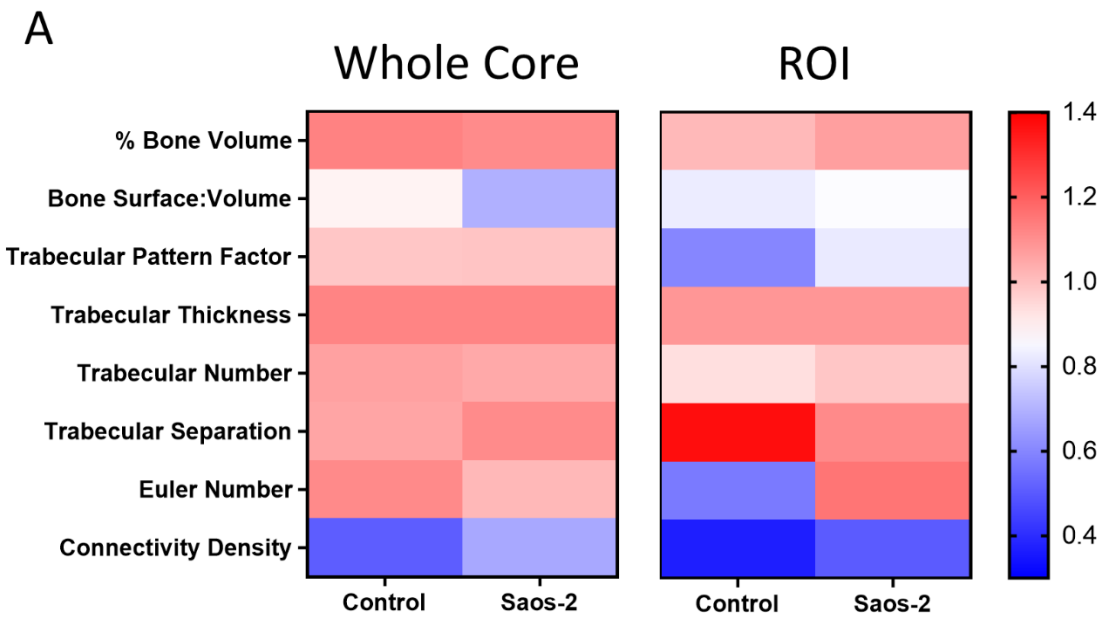

Figure 5-5. Quantitative µCT analysis of Saos-2 bone cores cultured on the CAM*. Bone cores were cultured with and without Saos-2 cells for 10 days on the CAM, with µCT images taken before and after incubation. Analysis was performed on the whole bone core and a ROI approximately 1mm around the defect area. Heat maps represent the fold change, of percentage bone volume, bone surface to volume ratio, trabecular pattern factor, trabecular thickness, trabecular number, trabecular separation, Euler number and connectivity density. N=2 with 14 technical replicates. Data presented as mean, statistics determined using a one-way ANOVA, no significance found.*

As previous experiments showed little bone formation or regression when bone cores were co-cultured with Saos-2 cells, other cell types were implanted in the bone cores including, FD and FE HBMSCs as well as a breast cancer cell line SKBR3 (**Figure 5-6**). As a breast cancer cell line, SKBR3 was used as an additional control alongside the empty control. This could determine whether any changes found between the HBMSC/ Saos-2 bone cores and the empty control were a result of bone growth/ resorption, or due to the presence of metabolically active cells. To try and stimulate

osteogenic differentiation and mineralisation of the bone cores, they were cultured in osteogenic I media (Table 2-1) for 5 days before implanting on the CAM. Whole bone core analysis showed all cell lines had a marked increase in TBPf compared with the control, particularly the cores cultured with FD cells. FD bone cores also showed a small increase in trabecular separation compared with the other cell types. Saos-2 and SKBR3 bone cores showed a slightly higher percentage bone volume compared with the other cell types, and a significantly higher level of trabecular thickness compared with the control, but were very similar in all other analyses. Further trends between the cell lines were also seen in the TBPf analysis of the ROI, where control and FE bone cores were higher than FD, Saos-2 and SKBR3 cores. The FD bone cores also showed a higher Euler number compared with the other cell types, suggesting there could have been production of osteoid but the level of mineralisation across the ROI had not been affected.

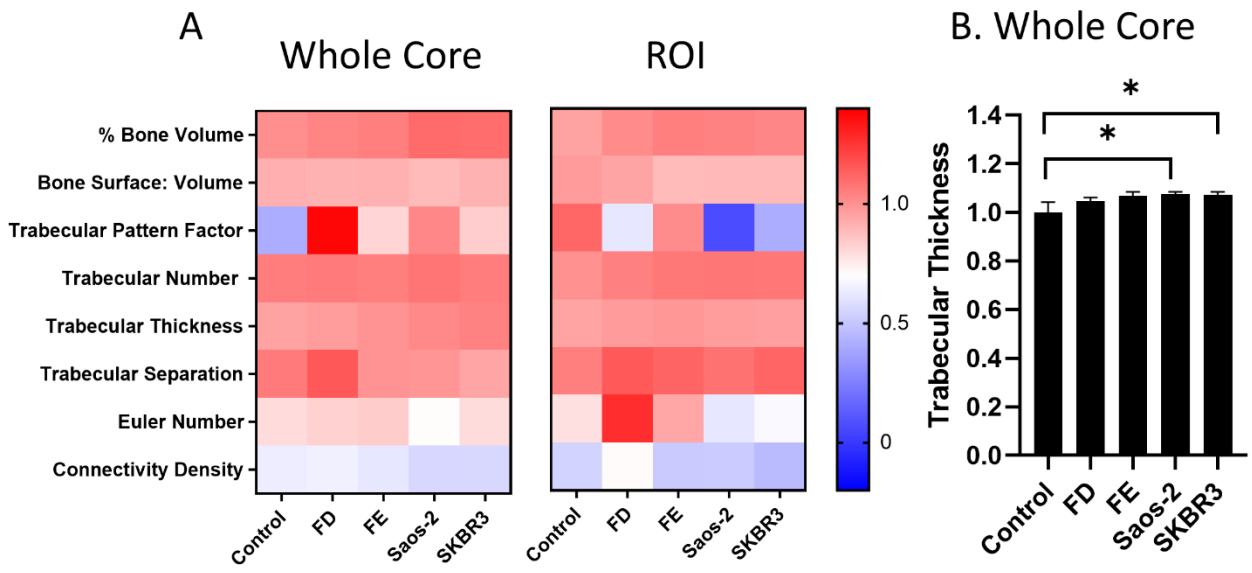

Figure 5-6. Quantitative µCT analysis of bone cores cultured on the CAM*. Bone cores were cultured in osteogenic media for 5 days with and without FD, FE, Saos-2 or SKBR3 cells before being implanted on the CAM for 10 days, µCT images were taken before and after incubation. Analysis was performed on the whole bone core and a ROI approximately 1mm around the defect area. (A) Heat maps represent the fold change, of percentage bone volume, bone surface to volume ratio, trabecular pattern factor, trabecular thickness, trabecular number, trabecular separation, Euler number and connectivity density. Data presented as mean. (B) The trabecular thickness of the whole bone core analysis. N=1 with three technical replicates. Data presented as mean +/- SD, statistics determined using a one-way ANOVA, significance represented as *<0.05.*

In previous experiments when bone cores were extracted from the femoral epiphysis, the original bone marrow cells were kept within the core, with isolation of the cores taking place up to 5 days after removal of the femoral epiphysis from the patient. Due to the necessity for a longer storage period of the bone cores before use, acellular bone cores were incubated in the CAM and assessed for bone formation or resorption (2.4.1). Using acellular bone cores also negated any variations in the cellular composition of the bone cores found from different patients. These cores were inserted with a combination of HBMSCs (mix of FD and FE) with or without Saos-2 and SKBR3 cells and implanted on the CAM for 10 days. As with previous data both the whole bone and a ROI were analysed (**Figure 5-7**). The HBMSC only group had the lowest TBPf and Euler number in the whole bone analysis, whereas the HBMSCs+ SKBR3 had the highest trabecular separation. In the ROI the control cores showed the lowest fold-change of TBPf and Euler number, while the HBMSC showed a decrease in trabecular number. Overall, there was little change in bone formation when bone cores were incubated with HBMSCs, Saos-2 or SKBR3, which was similar to data analysed from the cellular bone cores.

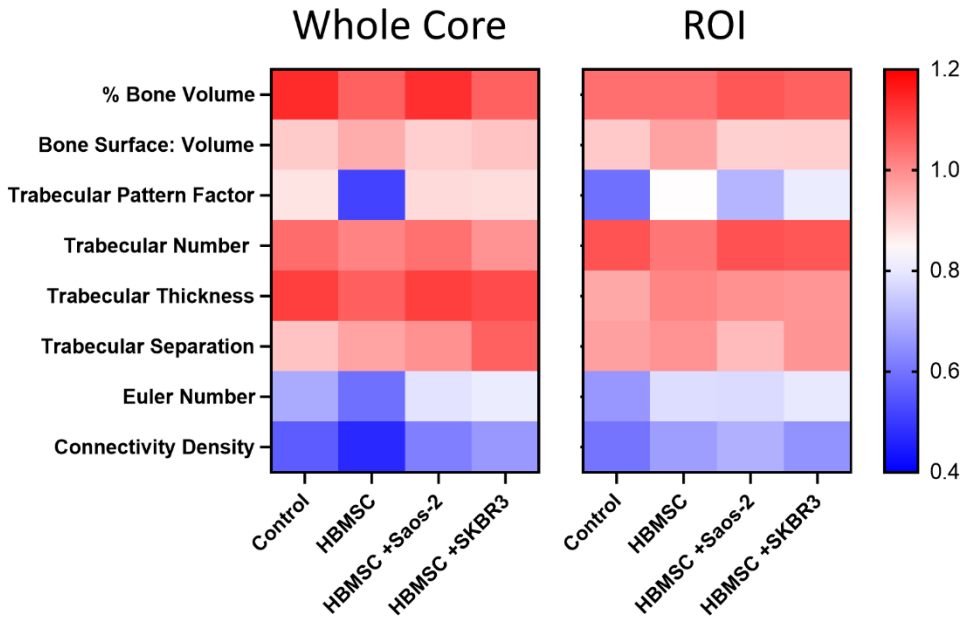

Figure 5-7. Quantitative µCT analysis of acellular bone cores cultured on the CAM*. Acellular bone cores were inserted with and without HBMSC, Saos-2 or SKBR3 cells before being implanted on the CAM for 10 days, µCT images were taken before and after incubation. Analysis was performed on the whole bone core and a ROI approximately 1mm around the defect area. (A) Heat maps represent the fold change, of percentage bone volume, bone surface to volume ratio, trabecular pattern factor, trabecular thickness, trabecular number, trabecular separation, Euler number and connectivity density. N=1 with four technical replicates. Data presented as mean, statistics determined using a one-way ANOVA, no significant differences found.*

5.2.4 Assessing the Structural Effect of MDMs in Bone Cores Implanted onto the CAM

In Chapter 4, MDMs were phenotypically assessed for introduction into the 3D bone model. As such MDMs were differentiated from PBMCs for 7 days (2.2.14) before being inserted into the bone model and implanted on the CAM (2.4.3). This experiment was performed on acellular bone cores because of availability (**Figure 5-8**). In both the whole bone and ROI there was very little difference found between the MDM and control bone cores, but in the ROI the combination of MDM+Saos-2 showed an increased trend in Euler number compared with the MDM and control. The PBMC derived MDMs were then skewed into M1-like or M2-like phenotype before being cultured on the CAM. Interestingly in the whole bone core there was a significant decrease in bone surface to volume ratio between the control and M1 bone cores (**Figure 5-8**C), which also showed a corresponding decrease in connectivity density (**Figure 5-8**D), suggesting a thickening or increase in existing trabecular bone, although there was only a small increase in trabecular thickness. This pattern was also seen in the ROI although to a lesser extent, which was not significant. A difference was also seen in the TBPf for the ROI, with a decrease in all MDM samples compared with the control, significant in the M0 samples (**Figure 5-8**E), suggesting an increase in the level of connections between trabecular bone.

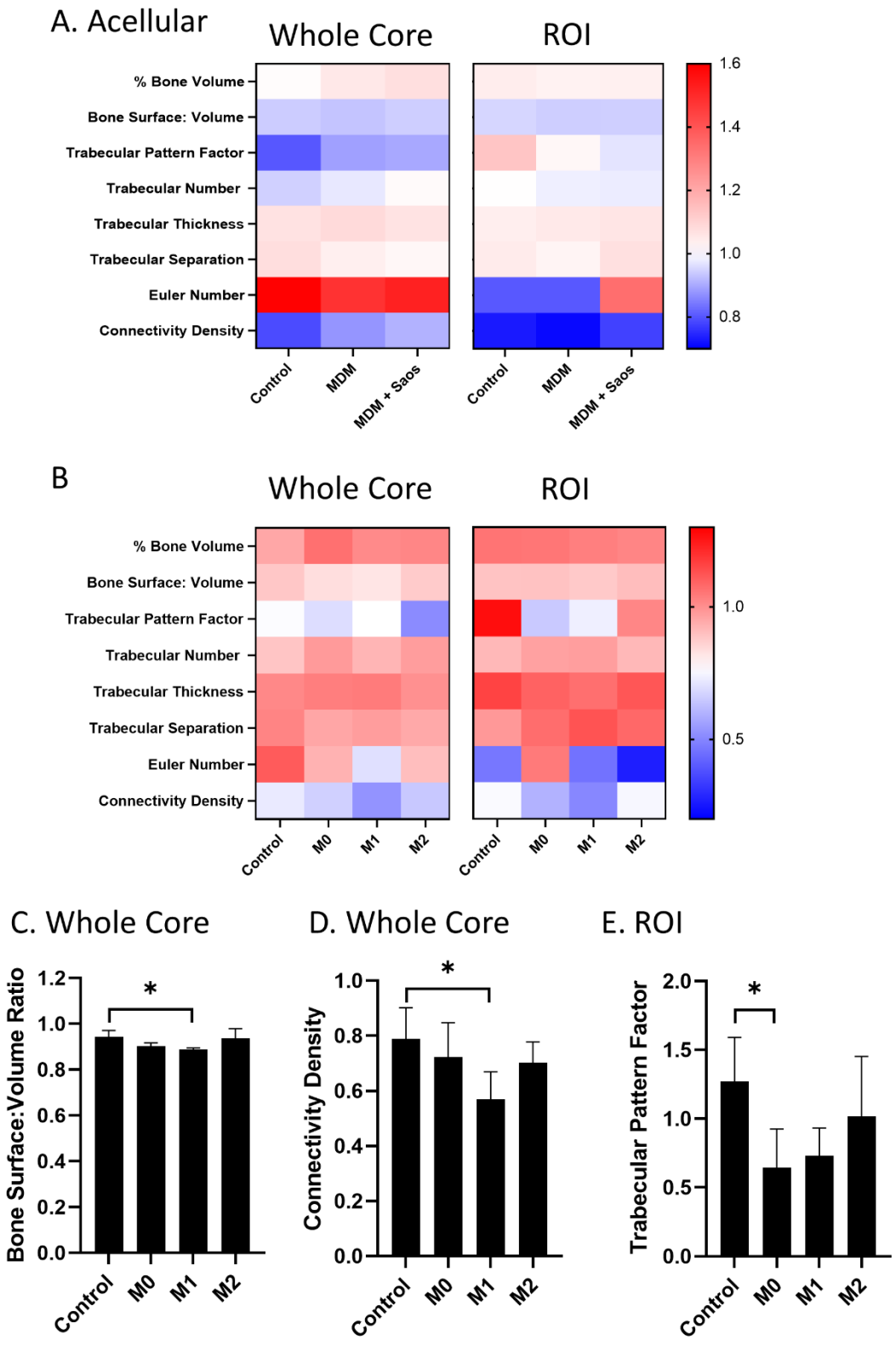

Figure 5-8. Quantitative µCT analysis of MDM bone cores cultured on the CAM. *(A) Acellular bone cores were inserted with and without MDMs and Saos-2 cells before being implanted on the CAM for 10 days. (B) Polarised MDMs were inserted into standard bone cores and implanted on the CAM for 10 days. Micro-CT images were taken before and after incubation. Analysis was performed on the whole bone core and a ROI approximately 1mm around the defect area. Heat*

*maps represent the fold change, of percentage bone volume, bone surface to volume ratio, trabecular pattern factor, trabecular thickness, trabecular number, trabecular separation, Euler number and connectivity density. Data presented as mean. (C) The bone surface: volume ration of the whole bone core, (D) the connectivity density of the whole bone core and (E) the trabecular pattern factor of the ROI. N=1 with 4 to 7 technical replicates. Data presented as mean +/- SD, statistics determined using a one-way ANOVA, significance represented as *<0.05.*

5.2.5 Quantifying Bone Formation and Resorption of Bone Cores inserted with a Combination of Saos-2, HBMSC and MDMs

Chapter 3 and Chapter 4 determined that the combination of FD HBMSCs, Saos-2 and MDMs were to be used as the final composition inserted into the 3D bone model, as these three cell types allowed for a potential insight into the osteosarcoma microenvironment. The cells were inserted into the bone cores before being incubated at 37°C 5% CO_2 for 20 days. The same number of Saos-2 and MDMs were introduced to each core, with half the number of FD cells due to low confluency. There was no difference in µCT analysis for the whole bone core, with the exception of Euler number, which showed a significant increase in the triple combination bone cores compared with the control (**Figure 5-9**B). This increase in Euler number was also seen in the ROI although it was not significant (**Figure 5-9**C). There was also little difference in the other µCT analysis for the ROI, with the exception of trabecular separation, which showed a decreased trend in the triple combination bone cores compared with the control. A higher Euler number combined with a lower trabecular separation could suggest early signs of osteoid formation.

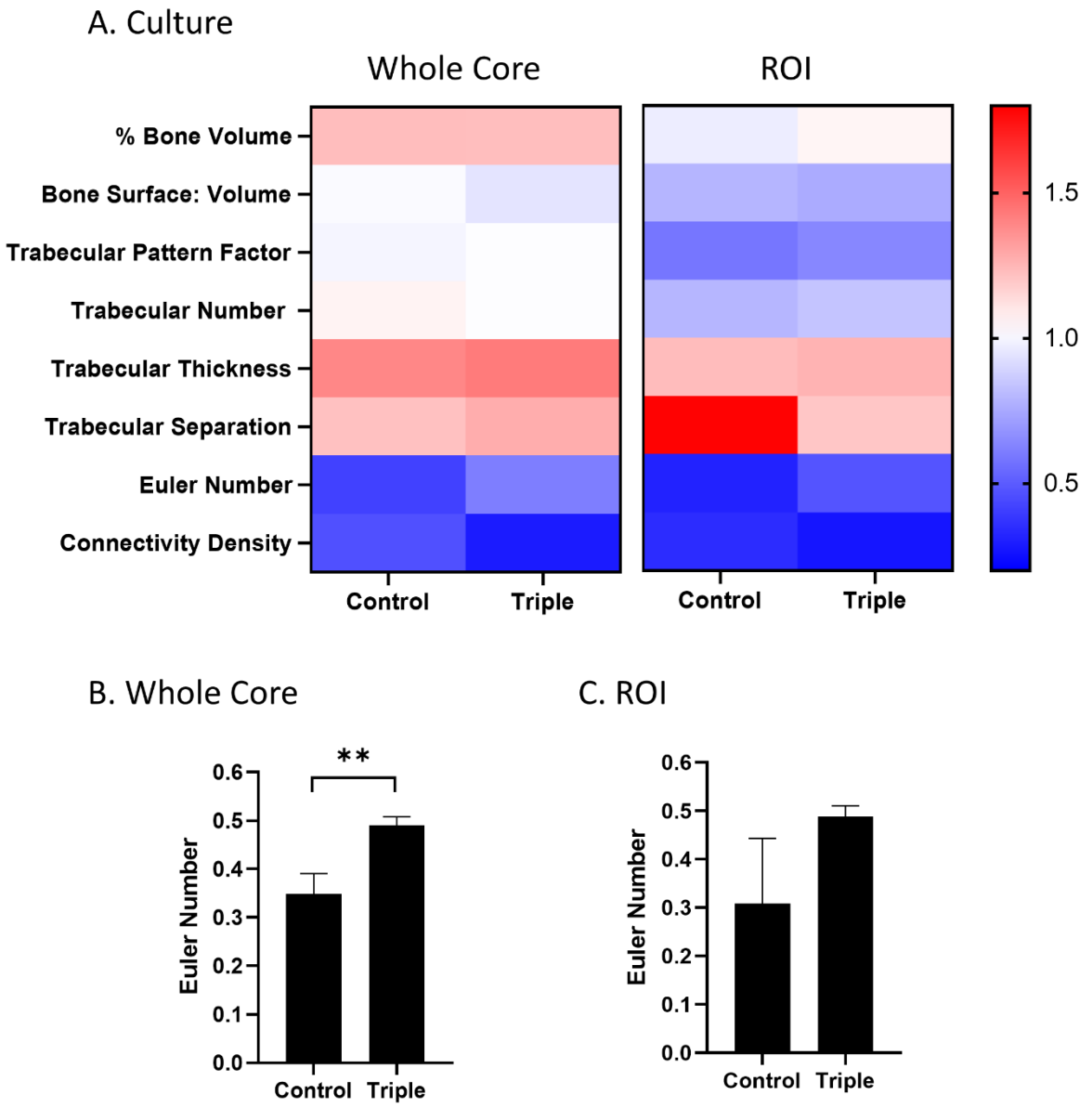

Figure 5-9. Quantitative µCT analysis of triple combination bone cores cultured in basal media. *Bone cores were inserted with and without a combination of HBMSC, MDMs and Saos-2 cells (Triple) before being incubated in basal media for 20 days, µCT images were taken before and after incubation. Analysis was performed on the whole bone core and a ROI approximately 1mm around the defect area. (A) Heat maps represent the fold change, of percentage bone volume, bone surface to volume ratio, trabecular pattern factor, trabecular thickness, trabecular number, trabecular separation, Euler number and connectivity density. Data presented as mean. The Euler Number of the (B) whole bone core and (C) ROI. N=1 with five technical replicates. Data presented as mean +/- SD, statistics determined using a one-way ANOVA, significance represented as ** <0.01.*

The three cell types of interest were then inserted separately or as a combination into bone cores before being incubated on the CAM (**Figure 5-10**). Interestingly in the whole core analysis, all cores cultured with cells showed an increase in percentage bone volume. The bone cores cultured with Saos-2 cells also showed the highest level of bone surface volume ratio and TBPf, as well as the lowest trabecular thickness. This was a significant increase in TBPf (**Figure 5-10**B) and a significant decrease in trabecular thickness (**Figure 5-10**C) compared with the triple combinations. This suggested that there was an increase in the strength of the trabecular connections when the three cell types were combined, compared with each cell type individually and the control cores. This pattern was also seen in the ROI, where the triple combination cores showed the lowest level of TBPf compared with the other cores, and the Saos-2 cores had the lowest trabecular thickness, although it was not significant. Conversely, there was also conflicting data showing the Saos-2 cores had a significant increase in trabecular number compared with both the control and the triple combination cores (**Figure 5-10**D) in the ROI, with a similar pattern in the whole bone analysis, suggesting trabecular formation had increased. While there was conflicting data, any differences determined when culturing Saos-2 cells, which showed a decrease in trabecular thickness and separation but an increase in trabecular number, was negated by the HBMSCs and MDMs when combined in the triple combination cores.

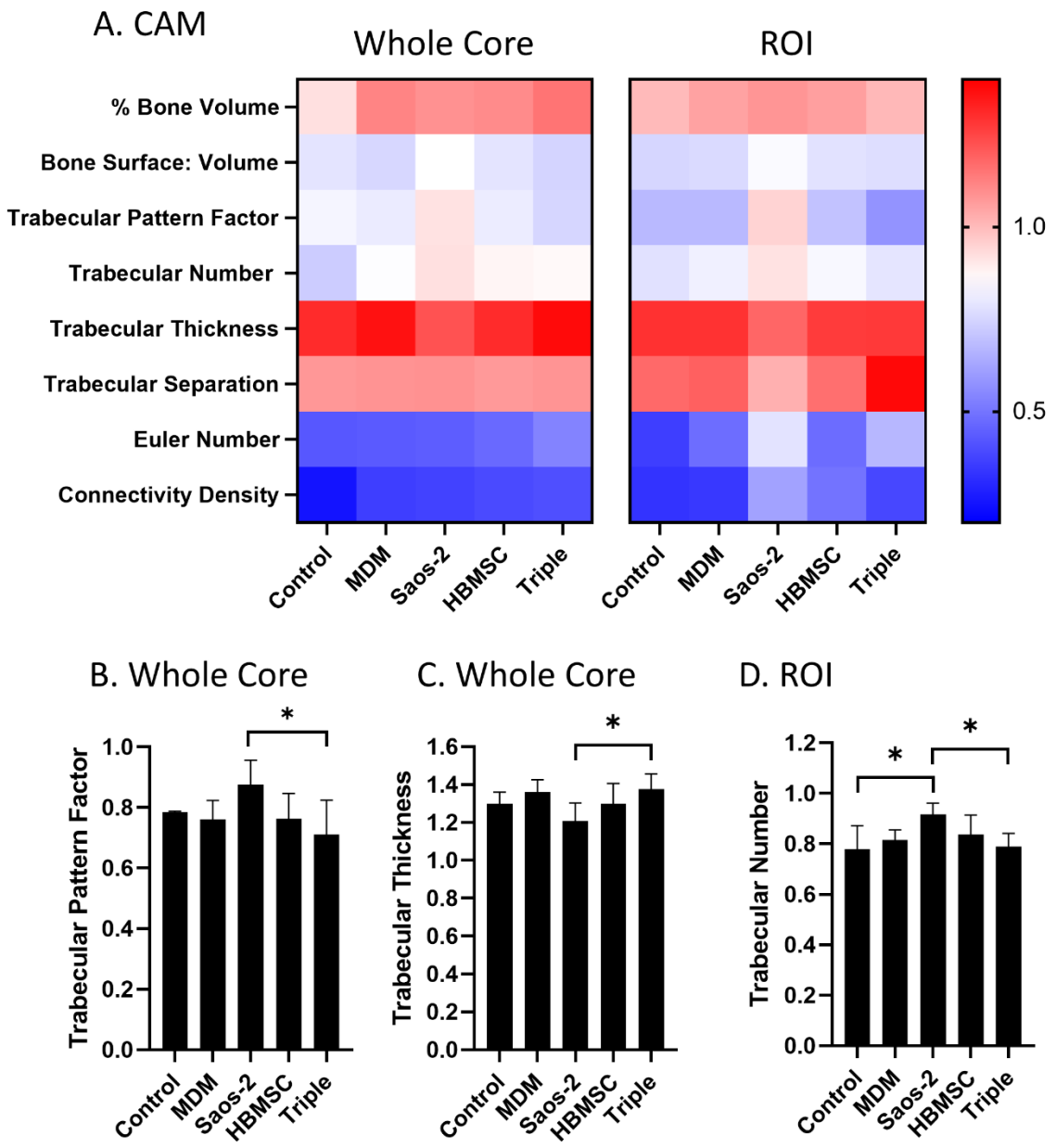

Figure 5-10. Quantitative µCT analysis of triple combination bone cores cultured on the CAM. *Bone cores were inserted with and without a combination of HBMSC, MDMs and Saos-2 cells before being implanted on the CAM for 10 days, µCT images were taken before and after incubation. Analysis was performed on the whole bone core and a ROI approximately 1mm around the defect area. (A) Heat maps represent the fold change, of percentage bone volume, bone surface to volume ratio, trabecular pattern factor, trabecular thickness, trabecular number, trabecular separation, Euler number and connectivity density. Data presented as mean. (B) The Trabecular pattern factor of the whole bone core, (C) the trabecular thickness of the whole bone core, and (D) the trabecular number of the ROI. N=1 with five technical replicates. Data presented as mean +/- SD, statistics determined using a one-way ANOVA, significance represented as *<0.05.*

5.2.6 Assessing the effect of Mifamurtide on the 3D Bone Core Model

Mifamurtide is given concurrently with chemotherapy post-operatively to patients in the UK [242]. As the ultimate success of this 3D bone core model will be determined by the testing of new therapies, a pilot study was used to demonstrate whether it was feasible to assess the effects of Mifamurtide using the model. To do this bone cores which contained a combination of the three cell types of interest were either cultured for 5 days in Mifamurtide before implantation in the CAM (Mif Pre) or for 5 days after removal from the CAM (Mif Post). Empty bone cores were incubated in Mifamurtide before implantation as an additional control. Mifamurtide was diluted to a 1:10 with basal media, for a final concentration of 0.16 µg/ml (6.4 µM), based on HBMSC and Saos-2 2D analysis (3.2.6 and 3.2.7). Interestingly in the whole bone analysis, the standard control cores showed a significant decrease in percentage bone volume compared with all the other conditions, with the exception of Triple+ Mif Pre (**Figure 5-11**B). The control also showed a decreased trend in trabecular number and an increase in trabecular separation compared with the other conditions. The control-Mif bone cores also showed an increase in TBPf compared with the other conditions (**Figure 5-11**C), although this was only significant in the triple and triple-Mif Pre bone cores. Small differences were also seen in the triple bone cores compared with the triple+ Mif Pre and triple +Mif Post bone cores although there was little consistency between the different µCT analyses.

The ROI data showed significant differences between the triple Mif Post cores compared with the other conditions (**Figure 5-11**D), with the exception of the Mifamurtide control, which also showed an increased trend in trabecular thickness. This suggests there may have been an increase in osteoid growth and mineralisation when the triple combination was cultured in Mifamurtide after incubation in the CAM, this was supported by small increases in Euler number and connectivity density. The TBPf also showed large differences in the five conditions, although large standard deviations mean it was not significant, with the triple combination having the lowest TBPf, while triple +Mif Pre had the highest, suggesting incubating the triple combination in Mifamurtide before incubation on the CAM resulted in poorer and weaker trabecular connections.

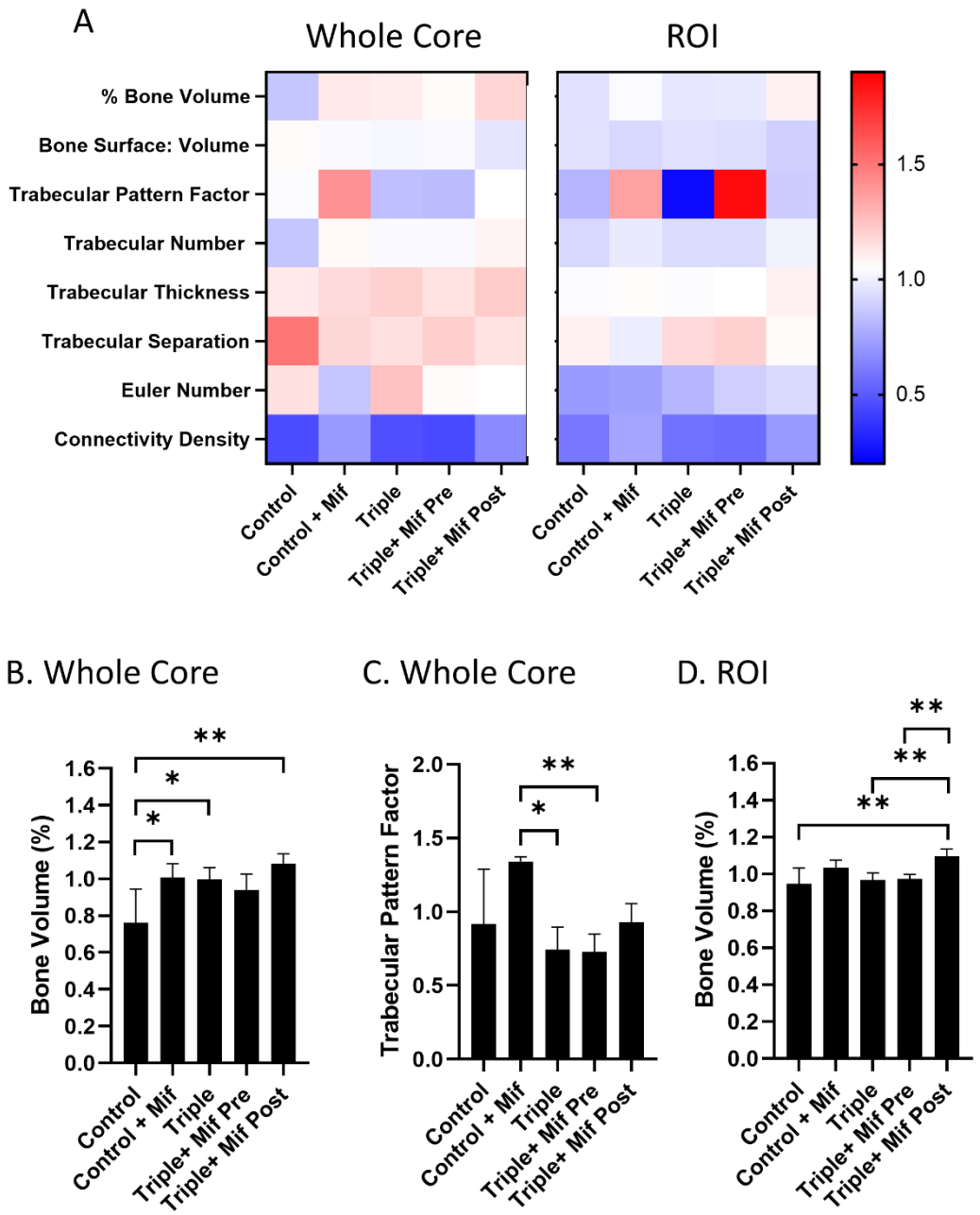

Figure 5-11 Quantitative µCT analysis of bone cores cultured with Mifamurtide. *Bone cores were inserted with and without a combination of HBMSC, MDMs and Saos-2 cells (triple) before being implanted on the CAM for 10 days. Mifamurtide was either added to culture 5 days before implantation or for 5 days after implantation, µCT images were taken before and after incubation. Analysis was performed on the whole bone core and a ROI approximately 1mm around the defect area. (A) Heat maps represent the fold change, of percentage bone volume, bone surface to volume ratio, trabecular pattern factor, trabecular thickness, trabecular number, trabecular separation, Euler number and connectivity density. Data presented as mean. (B) The percentage bone volume of the whole bone core, (C) the trabecular pattern factor of the whole bone core, and (D) the percentage bone volume of the ROI. N=1 with five technical replicates. Data presented as*

*mean +/- SD, statistics determined using a one-way ANOVA, significance represented as *<0.05, ** <0.01.*

5.2.7 Determining Positive and Negative Controls for µCT Analysis of Bone Cores

The majority of data produced when bone cores were analysed by µCT involved very small changes, as such methods determining whether the bone cores are consistently producing osteoid or undergoing bone resorption needed to be optimised. To support this, bone remodelling was attempted through the use of different supplemented media, both in culture and in the CAM (Table 2-1). Bone cores were implanted with FD HBMSCs and incubated in basal, mineralisation or osteoclast media for either 20 days (**Figure 5-12**A), or for 7 days before being implanted on the CAM (**Figure 5-12**B). The bone cores incubated for 20 days showed small increases in percentage bone volume, trabecular number and trabecular thickness compared with the basal incubated cores, which did indicate early signs of bone formation, although this was not significant. Unfortunately, the cores incubated in osteoclast media also showed small increases in percentage bone volume and trabecular number, which suggested bone resorption was not occurring under these conditions. Alternatively, both bone formation and bone resorption are closely mediated during bone regulation, as such bone resorption may have been induced but the resulting growth factors and signals released from the resorbed bone may have also increased bone formation. The bone cores incubated on the CAM demonstrated even fewer differences in µCT analysis compared to long-term culture, where both mineralisation and osteoclast media incubated cores only showed a decrease in TBPf, with an increase in trabecular separation. Consequently, the combination of HBMSCs with osteoclast media did not effectively activate the differentiation of osteoclasts for bone resorption, as such a new approach is needed. It also suggested that there was a small amount of osteoid production occurring after a longer incubation in mineralisation media, but these were very small differences not statistically significant. To try and enhance the level of bone formation occurring in the bone cores, culturing human osteoblasts (2.2.4) were inserted into the bone cores and incubated on the CAM for 10 days (**Figure 5-12**C). Compared to the control, the osteoblasts cultured bone cores showed a higher fold change in percentage bone volume, trabecular number, trabecular thickness and Euler number, with a corresponding lower fold change in bone surface to volume ratio, TBPf and trabecular separation. All of these data together suggested there was a low-level rate of bone formation occurring, although none of these were statistically significant.

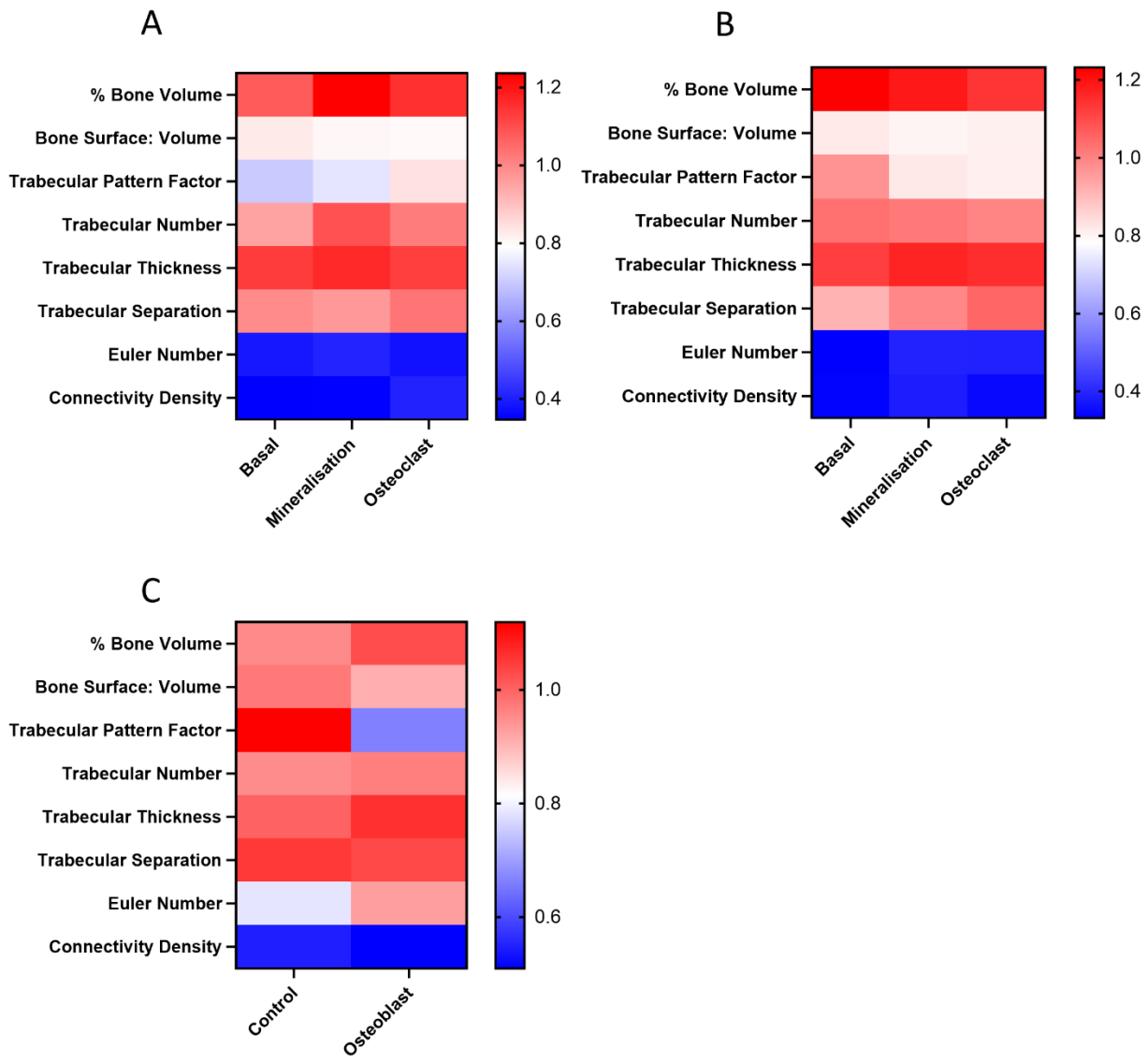

Figure 5-12. Quantitative µCT analysis of bone cores generated for positive bone formation and resorption controls. *HBMSCs were inserted into bone cores and either (A) cultured for 20 days in basal, mineralisation or osteoclast media, or (B) cultured for 7 days in basal, mineralisation or osteoclast media before being implanted on the CAM for 10 days. (C) Osteoblasts were inserted into bone cores and cultured in the CAM for 10 says. Micro-CT images were taken before and after incubation. Analysis was performed on the whole bone core and a ROI approximately 1mm around the defect area. Heat maps represent the fold change, of percentage bone volume, bone surface to volume ratio, trabecular pattern factor, trabecular thickness, trabecular number, trabecular separation, Euler number and connectivity density. N=1 with two to three technical replicates. Data presented as mean, statistics determined using a one-way ANOVA, no significance found.*

5.2.8 Quantifying Bone Formation and Resorption of 3D Bone Slices

The design of the bone cores enabled easy access to insert cells into the model, as well as fitting in sterile micro tubes for µCT imaging. Unfortunately, the cores themselves were quite large, at 8 mm in diameter. To determine whether the size of the bone core affected the ability for bone formation or resorption, approximately 5mm square bone slices were designed, which were made acellular as they needed to be cut in a non-sterile environment (2.4.2). A combination of HBMSCs and Saos-2 cells were placed onto the bone slices, and they were either incubated in culture for 28 days (**Figure 5-13**A) or inserted into the CAM assay (**Figure 5-13**B). **Figure 5-13**A showed conflicting results for the HBMSC bone cores, with decreased percentage bone volume and trabecular thickness, suggesting a low level of bone resorption occurring, but alternative increases in trabecular number, bone surface to volume ratio and a decrease in trabecular separation, which suggested low levels of bone formation. This conflicting data could be seen in both the Saos-2 and combined HBMSC+ Saos-2 cores, which overall suggested there was no bone formation or bone resorption occurring. Alternatively, in the CAM incubated bone cores (**Figure 5-13**B), there were fewer conflicting results, suggesting small levels of bone formation occurring in both the HBMSC and HBMSC+ Saos-2 bone cores compared with the control, with increases in percentage bone volume, trabecular number, trabecular thickness and a decrease in trabecular separation. Interestingly, the Saos-2 bone cores illustrated low levels of bone resorption, with decreases in percentage bone volume, trabecular number, trabecular thickness and an increase in trabecular separation. This suggested the presence of the HBMSCs was overcoming the bone resorption effect of the Saos-2 cells, and even potentially inducing low levels of osteoid production when HBMSC and Saos-2 were combined.

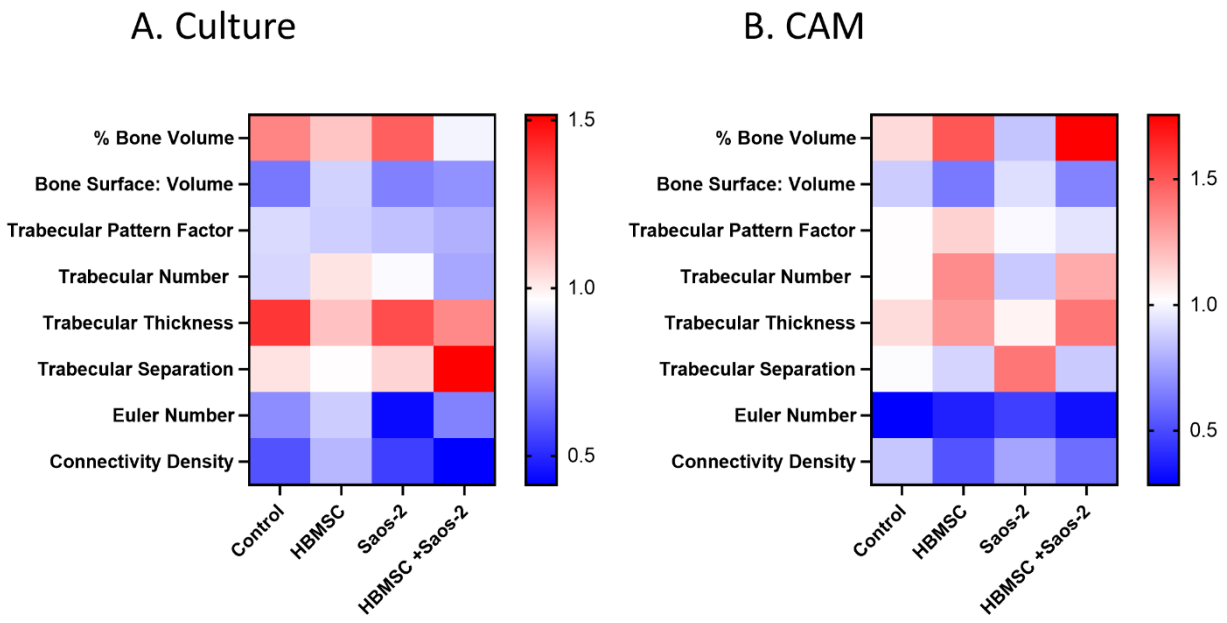

Figure 5-13. Quantitative µCT analysis of bone slices*. HBMSCs and Saos-2 cells were inserted onto bone slices and either (A) cultured for 28 days in basal media or (B) for 10 days on the CAM, µCT images were taken before and after incubation. Analysis was performed on the whole bone core and a ROI approximately 1mm around the defect area. Heat maps represent the fold change, of percentage bone volume, bone surface to volume ratio, trabecular pattern factor, trabecular thickness, trabecular number, trabecular separation, Euler number and connectivity density. N=1 with four technical replicates. Data presented as mean, statistics determined using a one-way ANOVA, no significance found.*

Following the introduction of HBMSC and Saos-2 cells into the bone slices, the third cell type of interest, MDMs, were also inserted into the model. The MDMs were differentiated (2.2.14) and inserted onto bone slices either on their own or in combination with Saos-2 cells, and cultured in both basal or osteoclast media for 20 days (**Figure 5-14**A). Both basal incubated MDM and MDM+ Saos-2 showed a lower connectivity density compared with the control slices, which was significant for the MDM+Saos-2. They also both demonstrated an increase in Euler number, which combined with the connectivity density suggested a change in the trabecular connections. This conflicts with an increase in TBPf, which suggested a decrease in connectivity. There was even less change in the osteoclast media incubated bone slices, with only very few differences in the MDM cultured bone cores compared with the control. MDMs were also introduced onto the CAM (**Figure 5-14**B), which illustrated potential early signs of bone formation, with a decrease in TBPf from both the MDM and the MDM+Saos-2 slices compared with control, as well as an increase in Euler number and connectivity density.

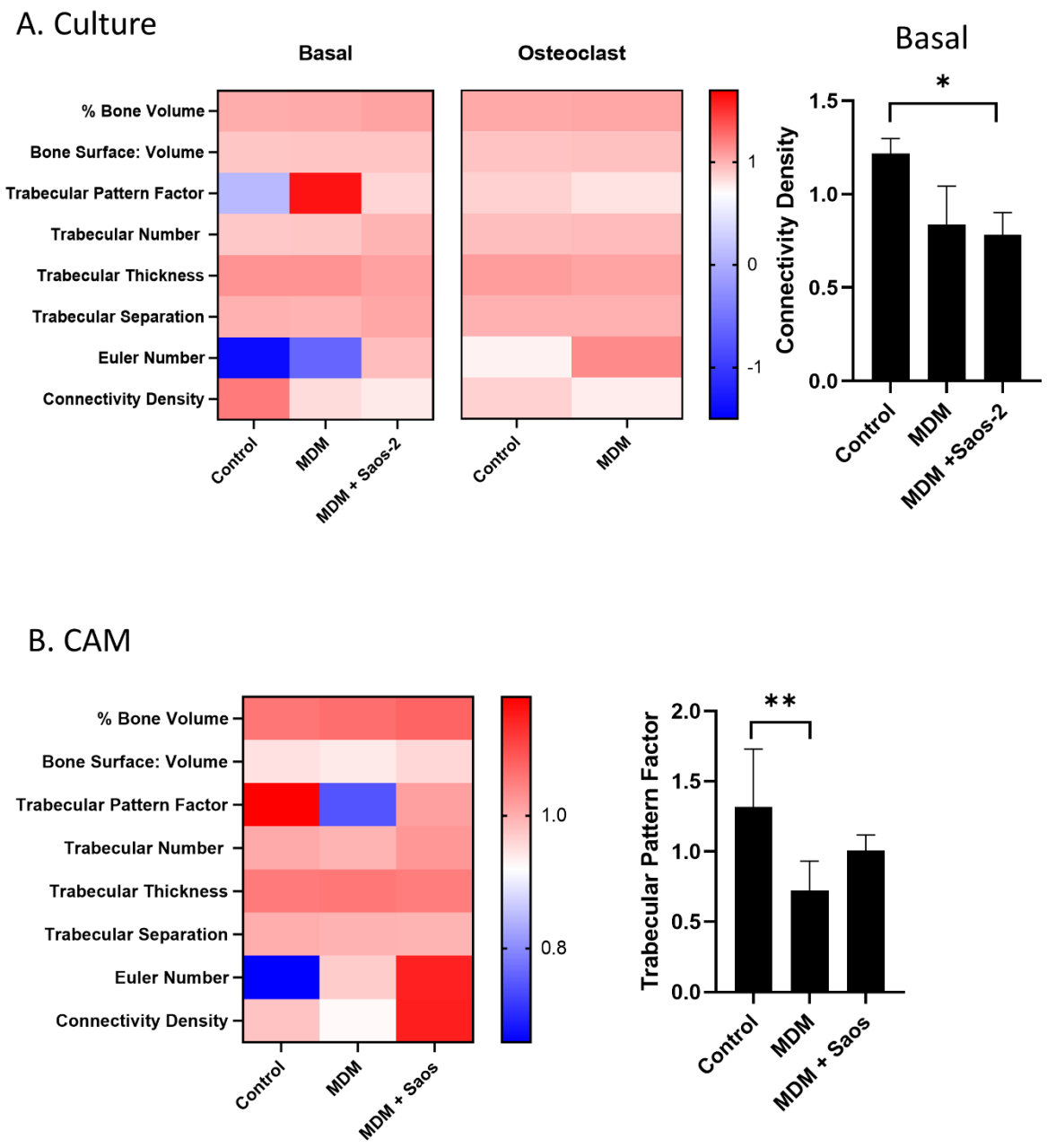

Figure 5-14. Quantitative µCT analysis of MDM bone slices. *MDM and Saos-2 cells were inserted onto bone slices and either (A) cultured for 20 days in basal or osteoclast media, or (B) for 10 days on the CAM, µCT images were taken before and after incubation. Analysis was performed on the whole bone core and a ROI approximately 1mm around the defect area. Heat maps represent the fold change, of percentage bone volume, bone surface to volume ratio, trabecular pattern factor, trabecular thickness, trabecular number, trabecular separation, Euler number and connectivity density. Data presented as mean. (A) Also shows the connectivity density of the basal incubated slices, while (B) also shows the trabecular pattern factor of the CAM cultures slices. N=1 with three to seven technical replicates. Data presented as mean +/- SD, statistics determined using a one-way ANOVA, significance represented as *<0.05, ** <0.01.*

5.2.9 Quantifying Bone Formation and Resorption of Bone Slices inserted with a Combination of Saos-2, HBMSC and MDMs

The final three cell types to be combined and analysed in the 3D bone model were FD HBMSCs, Saos-2 cells and MDMs, determined in Chapter 3 and Chapter 4. The Saos-2 and MDMs were seeded on to the bone slices at the same cell number, with HBMSCs inserted at half the cell number to replicate the bone core experiment. They were then either incubated for 20 days in basal media or inserted onto the CAM. **Figure 5-15**A shows the µCT analysis for the bone slices cultured for 20 days. Compared to the control, the triple combination slices showed small decreases in percentage bone volume, trabecular number and Euler number, as well as increases in TBPf and trabecular separation, which all suggest bone loss. Interestingly, the opposite was found in the bone slices cultured in the CAM assay (**Figure 5-15**B), which compared with the control, showed statistically significant increases in bone volume, Euler number and connectivity density (**Figure 5-15**C), as well as an increased trend in trabecular number, and trabecular thickness. This combined with the decrease seen in the TBPf, suggested early stages of bone growth had occurred.

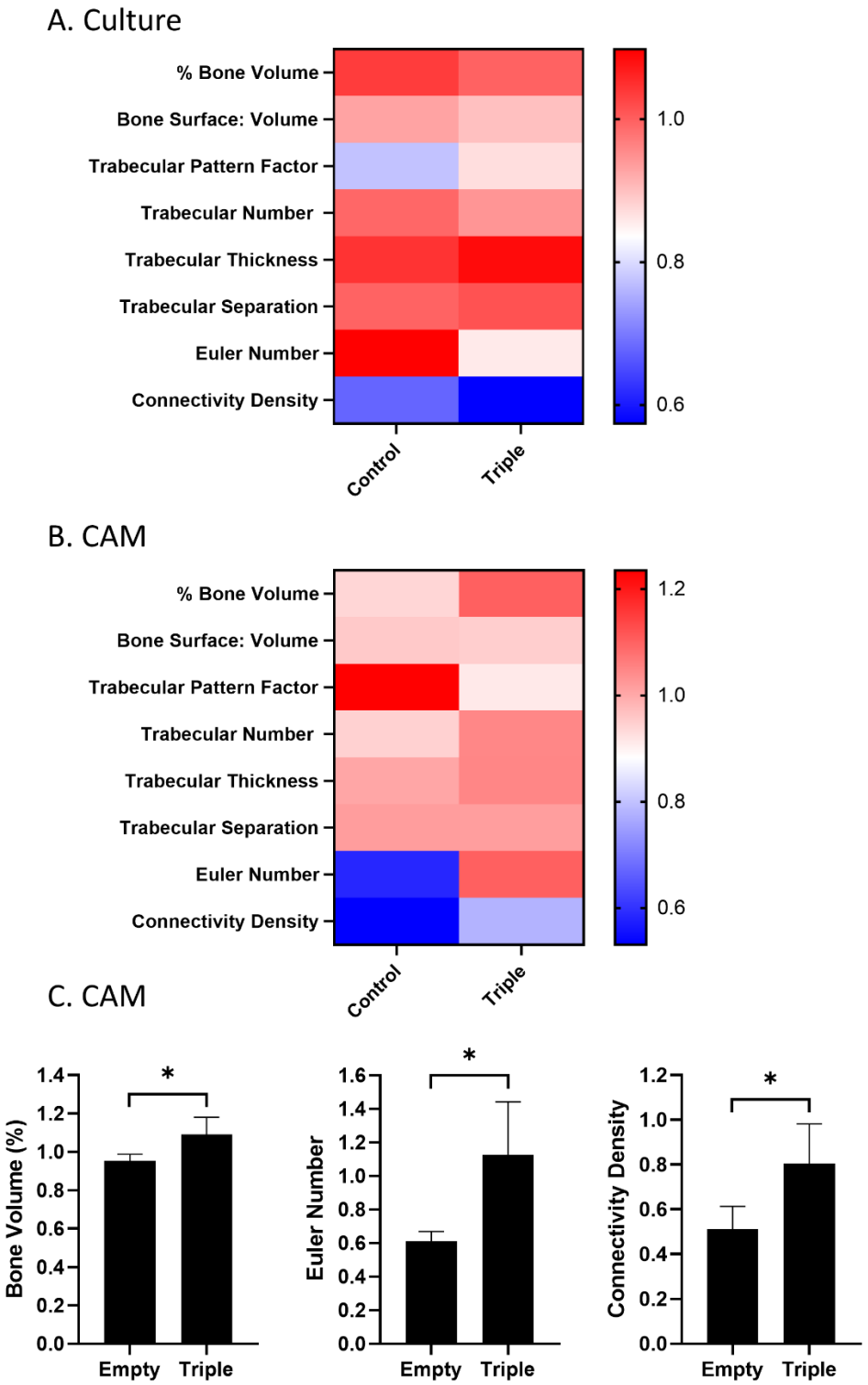

Figure 5-15. Quantitative µCT analysis of triple combination bone slices. *HBMSCs, MDM and Saos-2 cells (triple) were inserted onto bone slices and either (A) cultured for 20 days in basal or media, or (B) for 10 days on the CAM, µCT images were taken before and after incubation. Analysis was performed on the whole bone core and a ROI approximately 1mm around the defect area. Heat maps represent the fold change, of percentage bone volume, bone surface to volume ratio, trabecular pattern factor, trabecular thickness, trabecular number, trabecular separation,*

*Euler number and connectivity density. Data presented as mean. (C) The percentage bone volume, Euler number and connectivity density of the CAM incubated slices. N=1 with five technical replicates. Data presented as mean +/- SD, statistics determined using a one-way ANOVA, significance represented as *<0.05.*

5.2.10 Determining Positive and Negative Controls for µCT Analysis of Bone Slices

For the bone core model there was some success in forcing bone growth via the incubation of osteoblasts, but it was important to determine whether the lower volume of bone to cell ratio found in the bone slice model, could show larger differences in bone growth and resorption. To do this, HBMSCs were first inserted onto the bone slices (2.4.2) and incubated in basal or mineralisation media for either 28 days, or for 7 days before being incubated in the CAM assay. **Figure 5-16**A, demonstrates that the bone slices cultured for 20 days in mineralisation media showed conflicting results, with a decrease in percentage bone volume and trabecular thickness suggesting bone loss, but an increase in trabecular number and a small decrease in trabecular separation suggesting bone formation. Overall, the conflicting data suggested there was no real bone formation or resorption occurring. In contrast, the CAM incubated bone slices showed a clear trend towards bone growth, with a higher percentage bone volume, trabecular number, trabecular thickness, and Euler Number, alongside lower bone surface to volume ratio and trabecular separation compared with the control. As a positive control for bone resorption, MDMs were inserted onto bone slices and incubated in basal or osteoclast media for 7 days before being cultured on the CAM (**Figure 5-16**B). Unfortunately, while there did seem to be a reduction in trabecular thickness, suggesting bone loss, there was also increases in percentage bone volume, and Euler number as well as decreases in TBPf which suggested bone growth. As such the combination of MDMs with osteoclast media were not an effective positive control for bone resorption analysed by µCT.

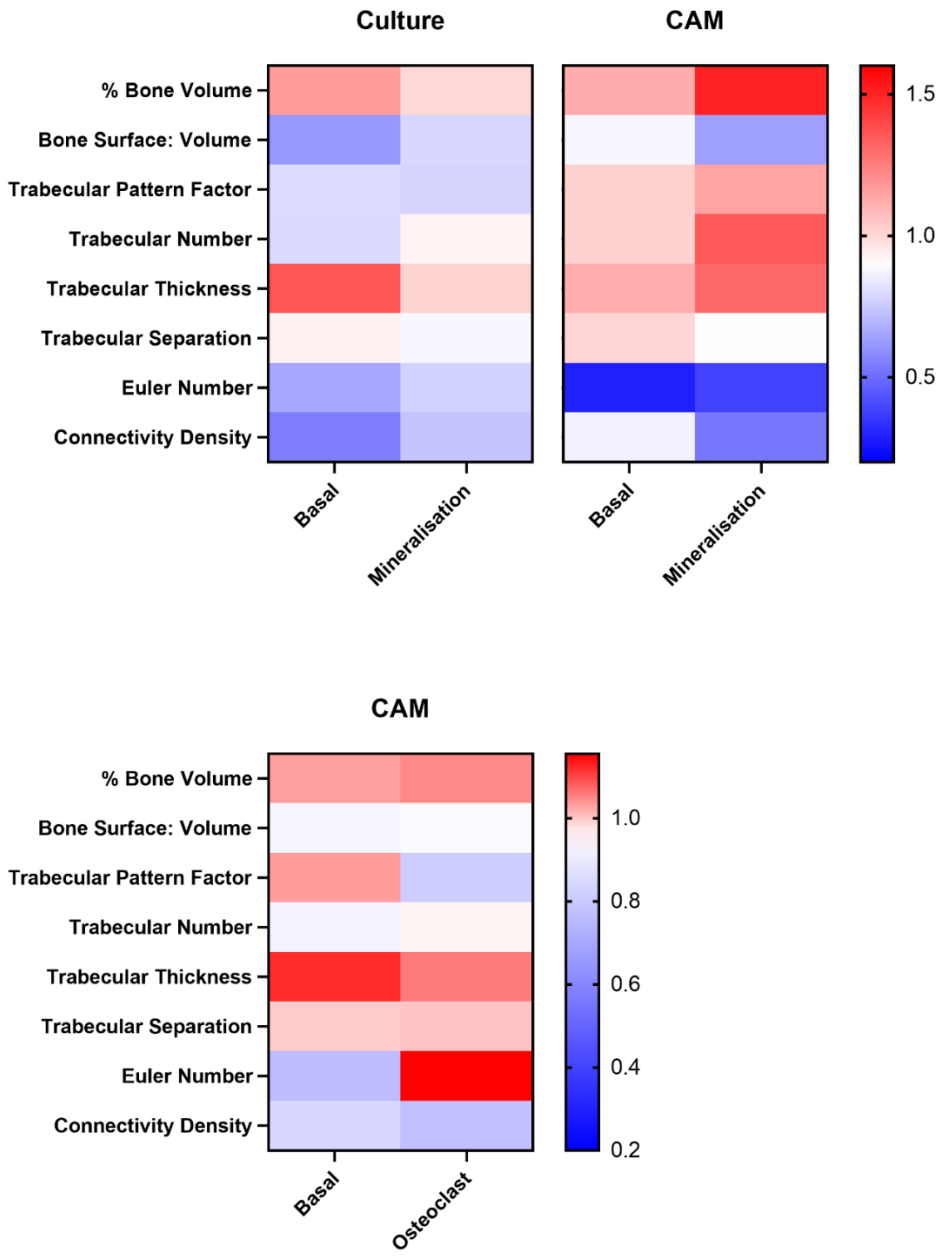

Figure 5-16. Quantitative µCT analysis of bone slices generated for positive bone formation and resorption controls*. HBMSCs were inserted into bone slices and either (A) cultured for 20 days in basal, mineralisation or osteoclast media, or (B) cultured for 7 days in basal, mineralisation or osteoclast media before being implanted on the CAM for 10 days. (C) MDMs were inserted into bone cores and cultured in osteoclast media for 7 days before being implanted on the CAM for 10 days. Micro-CT images were taken before and after incubation. Analysis was performed on the whole bone core and a ROI approximately 1mm around the defect area. Heat maps represent the fold change, of percentage bone volume, bone surface to volume ratio, trabecular pattern factor, trabecular thickness, trabecular number, trabecular separation, Euler number and connectivity density. N=1 with three to five technical replicates. Data presented as mean, statistics determined using a one-way ANOVA, no significance found.*

5.3 Discussion

Induction of blood vessels into the bone cores when cultured on the CAM, can be important in establishing a successful 3D model. This integration allowed for growth of the bone and potentially the cells which had been inserted inside the core. Figure 5-1 illustrated that there was successful incubation of the bone cores on the CAM, showing areas of vascularisation within the egg, which was important for successful establishment of the 3D model. Key findings:

- Incubation of bone on the CAM resulted in vascularisation.
- Micro-CT data showed few differences in bone formation or bone resorption, when the bone core and bone slice models were incubated on the CAM or in long term culture.

Analysis of the bone cores by µCT was the first method used to quantifying the success of the 3D model. In patients, one of the features of osteosarcoma is the production of osteoid, the initiation of excess bone formation by the tumour, which can be detected in µCT images taken of the affected area [236]. As well as osteoid formation [62], a large proportion of osteosarcoma patients demonstrate excess bone resorption occurring in the surrounding bone, which could be a result of an increase in osteoclast numbers and resorptive activity mediated by the tumour [243, 244]. Micro-CT analysis was used before and after the incubation of bone cores to see whether this bone production/resorption can be replicated. Representative images of the bone cores before and after CAM incubation were shown in Figure 5-3 A and B (respectively), with the bone loss (Figure 5-3C) and bone gain (Figure 5-3D) also shown from this core. Analysis was carried out on the whole bone core as well as a region of interest taken approximately 1 mm around the centre defect.

Culturing bone cores long-term and on the CAM both have advantages and disadvantages. Culturing long-term allowed for the introduction of various cytokines and growth proteins to skew the development of the model in different directions, for example incubating in mineralisation media to enhance bone growth, and incubation in osteoclast media to enhance bone resorption. In contrast, the length of time available to prime bone cores using conditioned media before insertion onto the CAM was limited. Alternatively, the CAM did introduce vascularisation into the bone core model, which was not possible in any *in vitro* method. Vascularisation was important in mimicking the human osteosarcoma microenvironment, as well as being a more efficient method of introducing nutrients to the cells. Interestingly, long term culture experiments with the bone cores showed very little change in bone growth. Some data from these cultures did suggest early increases in bone growth, but this was not always supported by other parameters of µCT analysis. This was true of both the Saos-2 experiments and the triple-cell combination assay. In contrast the CAM models did show more supporting analysis suggesting bone growth was occurring,

although this changed between the different experiments. For example, early Saos-2 experiments suggested an increase in osteoid formation compared with the control, whereas later experiments comparing the triple-cell combinations suggest Saos-2 cells induce low levels of bone resorption. This was similar in the bone slice experiments, where those cultured long term generally showed low levels of bone resorption, for both the MDM and triple combination experiments, whereas in the CAM there was an overall increase in osteoid formation in the HBMSC, MDM and triple experiments. The differences between the long-term culture and the CAM experiments, although small, are important in developing the model, and suggested that for inducing stronger bone formation the CAM was the more appropriate method.

Acellular bone cores were introduced as a potential alternative to the standard bone cores, as they could be stored for longer. Two acellular CAM experiments were performed, looking at all the cell types of interest. For both of these experiments, they showed very similar analysis compared to the appropriate standard CAM core assays, but there was little change in bone formation as well as conflicting results for both experiments, which limits the comparability. What was most evident during the setup of the assays was that the lack of cellular material found between the trabecular bone in the acellular bone cores, which resulted in fewer cells remaining in the defect area, and instead washing into the cell culture plastic before implantation. While the benefit of using acellular cores means they were more standardised between different patients, a new method of containing the cells would need to be optimised. This could either be using a semi permeable membrane, or a thicker matrix when injecting the cells of interest into the defect region. Bone slices were introduced as a potential alternative bone model as they had a smaller bone area to cell ratio, which may have allowed for an increase in bone remodelling. Generally, the bone slices and bone cores had very similar levels of bone remodelling, they both supported the increase in osteoid production for the triple combination experiments as well as for the HBMSC experiments. The main disadvantage of the bone slices was that as they were thinner, allowing more cells to pass through the slice into the cell culture plastic, meaning any benefit of less trabecular bone was lost as less cells were adhering and interacting in the bone slice.

Based on all the µCT analysis performed, the combination of a bone core incubated in the CAM assay was the most robust method for developing the 3D multicellular model of Osteosarcoma. As the ultimate aim for this model was to be used to test new drugs and therapies, a pilot study was performed using the drug Mifamurtide. The bone cores were inserted with the triple-cell combination, then they were either incubated in Mifamurtide prior to CAM incubation, or after removal from the CAM. The triple combination with Mifamurtide pre-incubation showed very similar results to the triple combination without Mifamurtide, while the triple-cell combination with Mifamurtide post incubation showed a small increase in bone formation compared with the

control, and both other triple combinations. This effect could be due to immune infiltrate as there have been no previous research that suggest Mifamurtide can affect bone formation. This pilot study showed there were two applicable methods that could be used to test further drugs and therapies on the bone core model. Unfortunately, the lack of robust and reproducible positive controls for bone growth and resorption has limited any conclusions that could be generated from this data. Having effective controls would allow for optimal bone formation and resorption to be determined in this model, which would allow for more accurate conclusions based on the small differences seen in the µCT data to determine whether bone remodelling had occurred. The largest changes in bone formation were seen in the bone cores incubated with osteoblasts, unfortunately these cells were slow to proliferate and as such the experiment was limited to only two bone cores. A repeat is necessary to determine if there is any significance and if this pattern is repeated. Alternatively, previous studies have shown bone formation can occur in this model when a combination of collagen sponge and BMP2 was combined [177], as such it could be repeated to induce bone formation as a positive control. A positive control for bone resorption was attempted by culturing HBMSC and MDMs in osteoclast media, with no effect. According to 2D assays (4.2.6) osteoclast generation was most effective when CD14 isolated cells were cultured in osteoclast media, as such could be a good positive control.

The combination of bone cores incubated on the CAM showed the most evidence for osteoid production compared with the other conditions tested. Unfortunately, there was no definitive analysis confirming bone production or resorption in the 3D multicellular models, which may be because the short incubation time was not sufficient for bone mineralisation. This could potentially be resolved through the use of multiple, consecutive CAM assays, but the length of time needed to establish vascularisation via this method is unknown, and it also increases the risk of contamination. Re-analysing the µCT data by looking specifically at separate bone growth or bone loss overlays may result in more differences, although this method would mean the bone loss and bone gain couldn't be directly compared potentially exaggerating misalignment effects. Other methods of analysis may be more informative in developing this 3D multicellular model of osteosarcoma, as such immunohistochemistry analysis of the bone cores and slices as performed in the following chapter.

Chapter 6 Immunohistochemistry Analysis of a 3D Multi-Cellular Model of Osteosarcoma

6.1 Introduction

Mechanical signals are reported to be important in modulating tumour behaviour in the bone microenvironment [156], thus selecting a scaffold like structure was important when initially developing a 3D multicellular model of osteosarcoma. A range of scaffolds, formed from both natural and synthetic material [150, 156], have been used in bone research, with all having different advantages and disadvantages in terms of biocompatibility, degradation and bioactivity [157, 160]. A mixture of synthetic and natural scaffolds have been developed to overcome these individual disadvantages [161], but there was limited evidence of their use in tumour models. Novel 3D models are continually evolving and becoming increasingly translationally relevant as the understanding of the tumour microenvironment increases, but currently there have been no published data using human bone as the basis for an osteosarcoma 3D model. Current models of osteosarcoma are also limited in biological activity and signalling, with no experiments combining osteosarcoma cells with structural and stromal cells found in the bone environment. With unique access to the femoral head of patients undergoing hip replacement surgery, a novel 3D multicellular model of osteosarcoma was developed, which used human bone as the structural base. The addition of stromal, immune and osteosarcoma cells, were used to replicate cellular interactions found in the osteosarcoma microenvironment. By combining human bone with primary human cells, the risk of cellular rejection was decreased, while also simulating the 3D bone structure found in patients.

Accurate and reproducible validation of the bone model was important in assessing how well it replicates the tumour microenvironment. This was assessed by histology and immunohistochemistry analysis alongside the µCT data analysed in the previous results chapter. In addition, multiplex histological analysis of 10 primary human osteosarcoma samples, were used as a basis for evaluating the similarities of the 3D bone core model with the human tumour microenvironment. As bone is a hard material, appropriate preparation needed to occur before further histological analysis. Most protocols decalcify bone before embedding in paraffin or OCT [245]. This removes any mineralisation which softens the structure so it can be cut using a standard microtome blade. Alternatively, bone can be embedded in resin without the necessity for decalcification, but this needs to be sectioned with a diamond blade, then ground down/polished before any further staining can occur [246]. While the resin embedding process has the advantage of not needing decalcification, which can affect certain future histological

stains, it is a more expensive method with specialist equipment and knowledge needed. In this thesis the decalcification ability of four different chemical methods, outlined in 2.6.1, was compared, to optimise the embedding and staining process of human bone cores, before immunochemistry analysis was performed on specific markers of interest.

6.2 Results

6.2.1 Embedding Decalcified Bone Cores in Paraffin

The human bone cores and slices were quantified by immunohistochemistry staining for various markers of interest, to do this the bone was first decalcified to enable robust sectioning and preparation of the material. This included four different decalcification methods: 10% (v/v) formic acid, a Krajian solution, 6% (v/v) TCA and an EDTA-glycerol solution (2.6.1). After decalcification the bone cores were embedded in paraffin (under vacuum), before being sectioned and stained for H+E. **Figure 6-1** shows representative images of the H+E staining, which showed very similar structural composition for all four decalcification methods, both at a low and high magnifications. Unfortunately, there were issues with the sectioning process of all four decalcification methods, particularly for formic acid, where the tissue was disintegrating closer to the defect area, where the cells were inserted, before a section could be obtained. This destruction meant only the remaining three decalcification methods could be used for further staining comparisons.

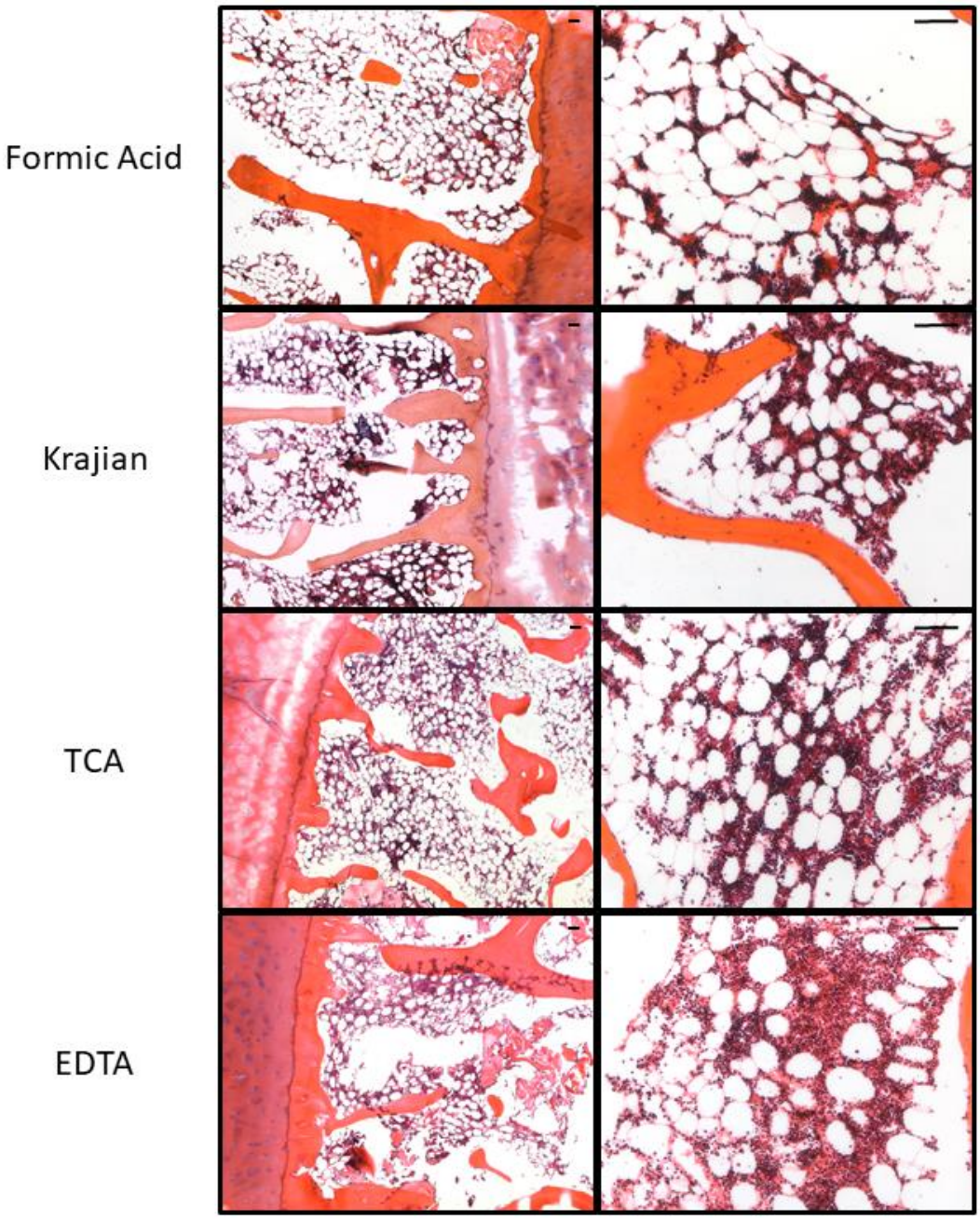

Figure 6-1. H+E staining of bone cores after decalcification and embedding in paraffin. *Images of bone cores after they have been decalcified by 10% (v/v) formic acid, Krajian solution, 6% (v/v) TCA or an EDTA-glucose solution at two different magnifications. Images are representative of N=2, with four technical replicates. Scale bar= 100 µm*

Different decalcification methods potentially affect whether certain staining protocols can be carried out, for example highly acidic decalcification methods, such as formic acid, can cleave specific antigens meaning enzymatic stains like TRAP (2.6.6) and ALP (2.6.8) may not be effective. As such, the different decalcification methods were analysed for positive TRAP staining. **Figure 6-2** are representative images of TRAP staining for the Krajian, TCA and EDTA methods. A rat femur section was used as a positive control for TRAP staining, osteoclasts are stained red/brown and

light green was used as a background stain. Although some areas of bone show non-specific staining, there was also evidence of positive TRAP staining in all three decalcification solutions, although the strongest signal can be seen in the Krajian sample.

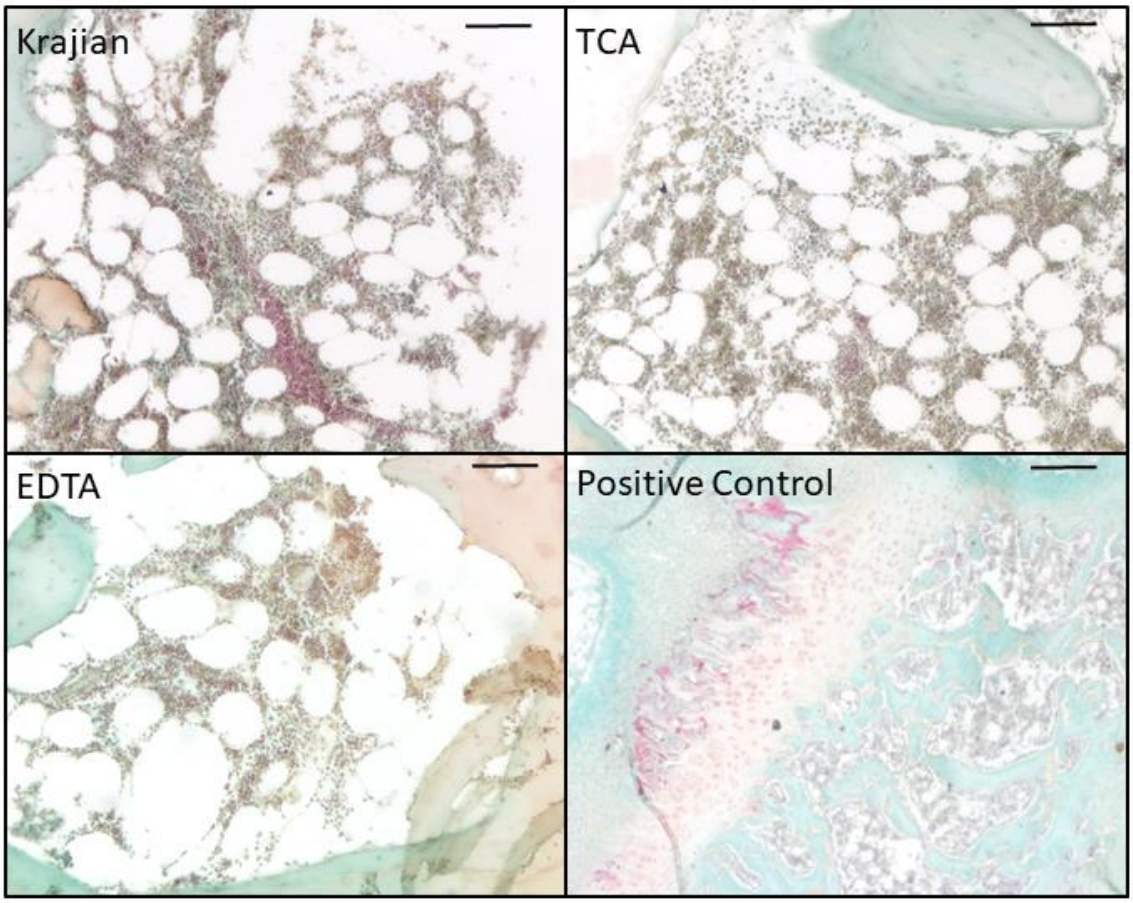

Figure 6-2. TRAP staining of bone cores after decalcification and embedding in paraffin. *Images of bone cores after they have been decalcified by, Krajian solution, 6% (v/v) TCA or an EDTA-glucose solution. Sections of rat femur were used as a positive control. Osteoclasts stained red/brown, with fast green used as a background stain. Images are representative of N=2, with four technical replicates. Scale bar= 100 µm*

While there was little difference in terms of structural and enzymatic staining, differences in immunohistochemistry staining (2.6.5) were also tested, comparing both adherence of the sectioned tissue and staining intensity. **Figure 6-3** shows representative images of CD68 staining, a macrophage marker. Clear positive staining can be seen in all decalcification comparisons, with similar colour and staining intensity. The sections also remained adherent to the slides during this longer staining protocol. Unfortunately, the main issue was the difficulty in obtaining complete sections from all decalcified bone cores during sectioning, as such the formic acid decalcified cores were not included. The bone cores were analysed by µCT before they were embedded,

confirming they had been completely decalcified, suggesting there may be a problem with the embedding process itself.

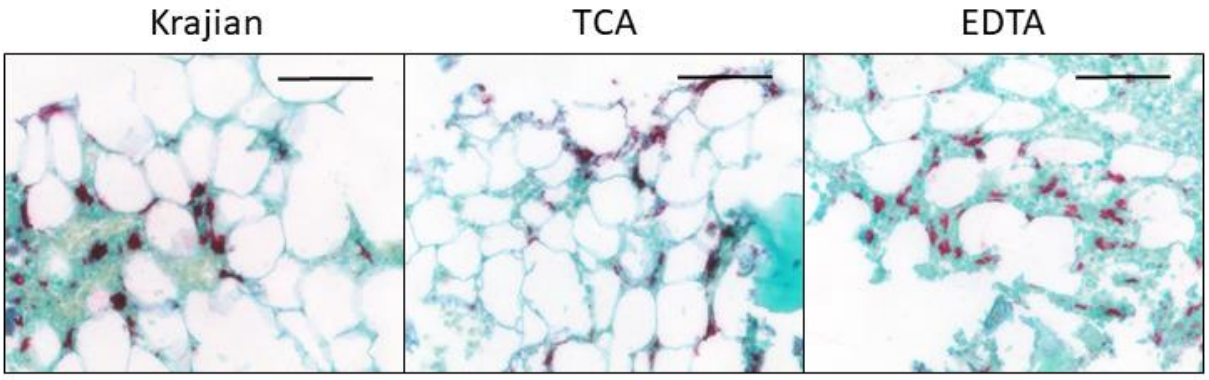

Figure 6-3. CD68 staining of bone cores after decalcification and embedding in paraffin. *Images of bone cores after they have been decalcified by, Krajian solution, 6% (v/v) TCA or an EDTA-glucose solution. CD68 positive cells are stained red, with fast green used as a background stain. Images are representative of N=2, with four technical replicates. Scale bar= 100 µm.*

An alternative embedding option was then attempted, by directly comparing OCT (2.6.3) with paraffin embedding (2.6.2). Once OCT embedding was optimised the resulting sections were stained for H+E (2.6.4) and compared. Optimisation resulted in a 20 minute incubation in OCT under vacuum before being frozen in isopentane over dry ice. **Figure 6-4** show representative images of TCA decalcified bone cores embedded in either paraffin or OCT before being stained for H+E, images were taken at various magnifications. There was no difference in clarity or morphology of the bone cores embedded in either paraffin or OCT. While the paraffin embedded samples had similar problems with tissue fragmenting when sectioning closer to the defect area as in previous studies, this was not found in the OCT embedded cores, where complete sections could be taken throughout the whole bone core. Thus, OCT was determined to be the optimal method of embedding over paraffin.

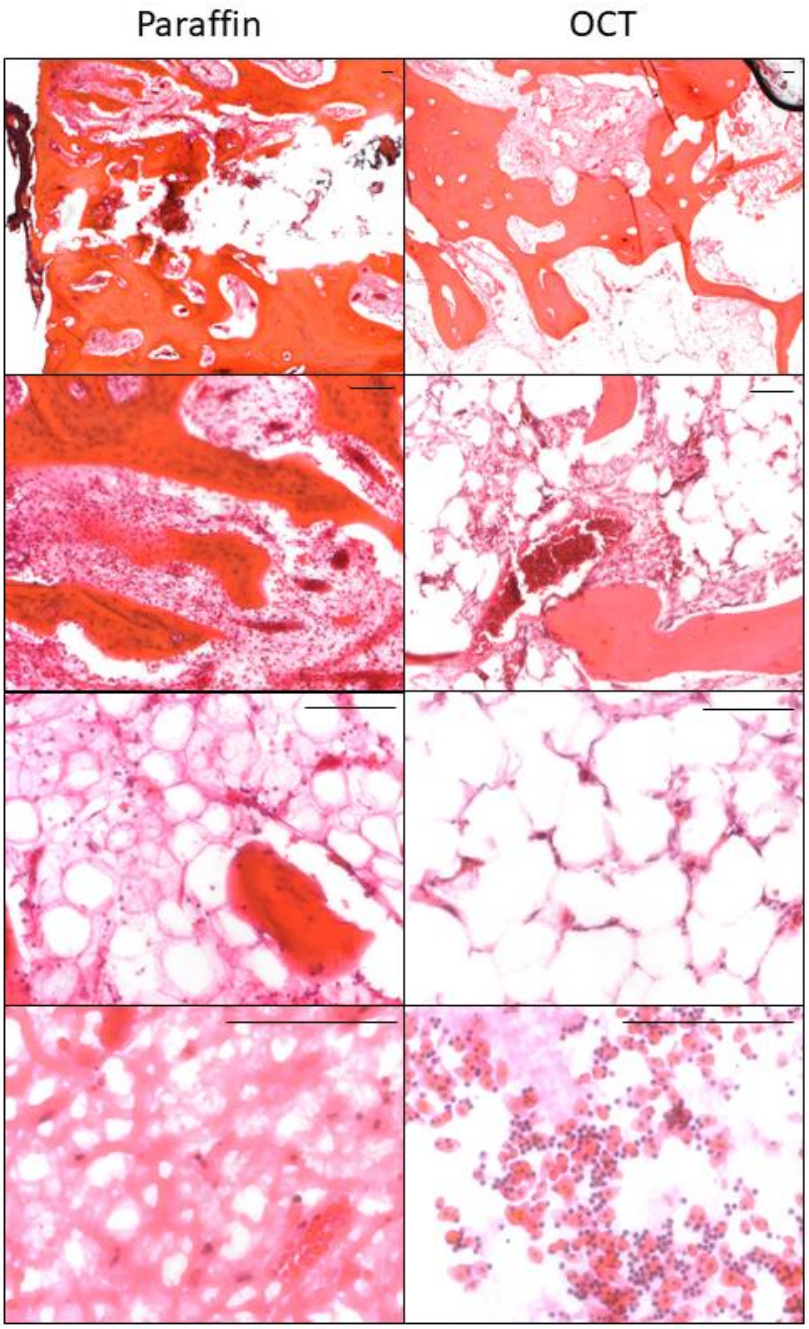

Figure 6-4. Images comparing OCT and paraffin embedding of the bone cores*. 6% (v/v) TCA decalcified bone cores were embedded in paraffin or OCT, sectioned and stained with H+E, images were taken using various objectives. Images are representative of N=4, scale bar= 100 µm.*

6.2.2 Embedding Decalcified Bone Cores in OCT

After optimising the use of OCT as the embedding medium, histological analysis was then compared for the four different decalcification methods. **Figure 6-5** are representative images of H+E staining of the four different decalcification solutions, showing similar structure and morphology for all bone cores. Unfortunately, while the sectioning of three decalcification

methods, Krajian, TCA and EDTA did improve considerably, there was still issues with the sectioning of the formic acid decalcified cores, with the sections crumbling as they got closer to the defect region. As such formic acid decalcified bone cores were not analysed in future stains.

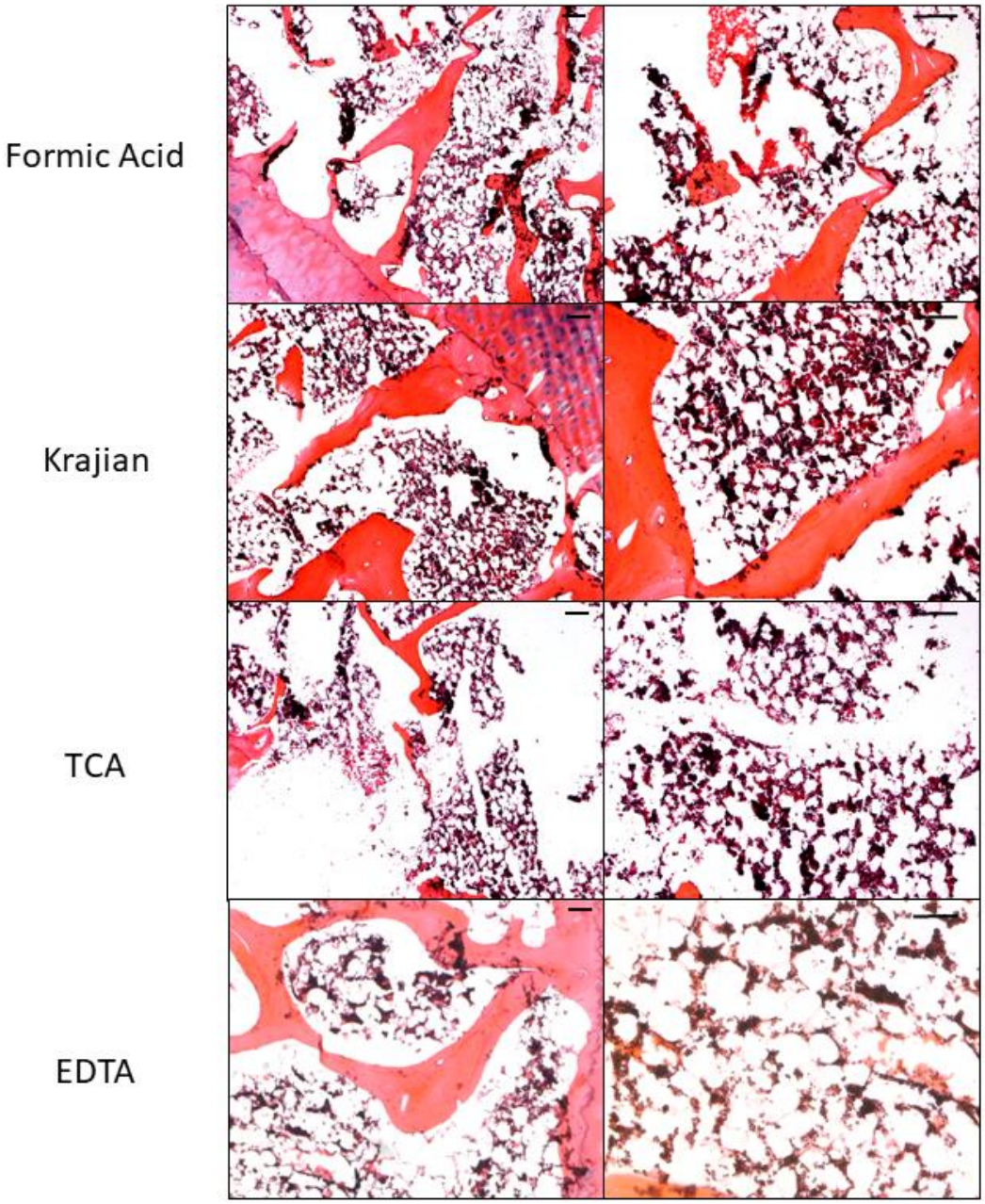

Figure 6-5. H+E staining of bone cores after decalcification and embedding in OCT. *Images of bone cores after they have been decalcified by 10% (v/v) formic acid, Krajian solution, 6% (v/v) TCA or an EDTA-glucose solution. Images are representative of N=2, with four technical replicates. Scale bar= 100 µm.*

The remaining three decalcification methods were then compared for enzymatic staining. **Figure 6-6** are representative images of TRAP staining (2.6.6), osteoclasts are stained red/brown with light green used as a background stain. Although there was evidence of positive staining in all

three decalcification methods, there was a large amount of tissue loss during the staining protocol. This was also true of longer CD68 immunohistochemistry staining protocol (2.6.5), where while there was a clear positive staining with similar intensity and morphology, over half of the sections detached and washed away during staining (**Figure 6-7**).

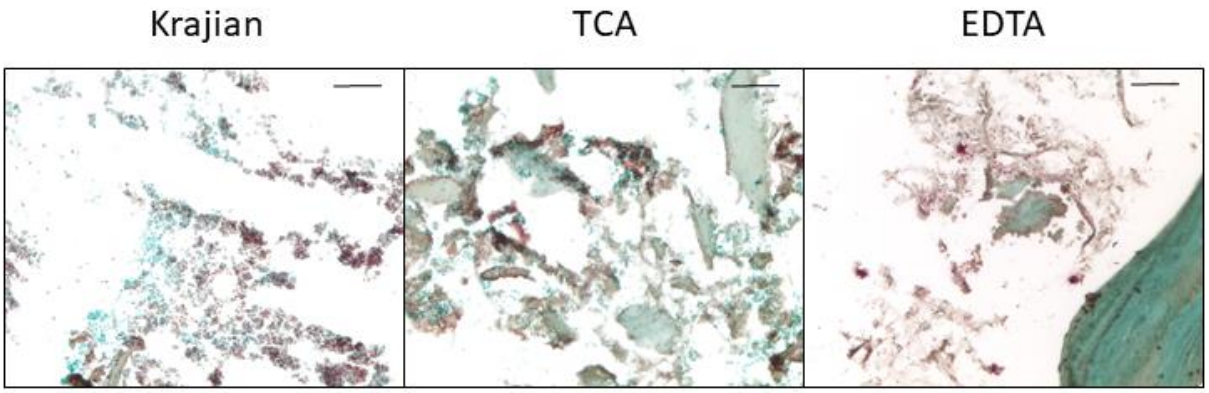

Figure 6-6. TRAP staining of bone cores after decalcification and embedding in OCT*. Images of bone cores after they have been decalcified by, Krajian solution, 6% (v/v) TCA or an EDTA-glucose solution. Osteoclasts stained red/brown, with fast green used as a background stain. Images are representative of N=2, with four technical replicates. Scale bar= 100 µm.*

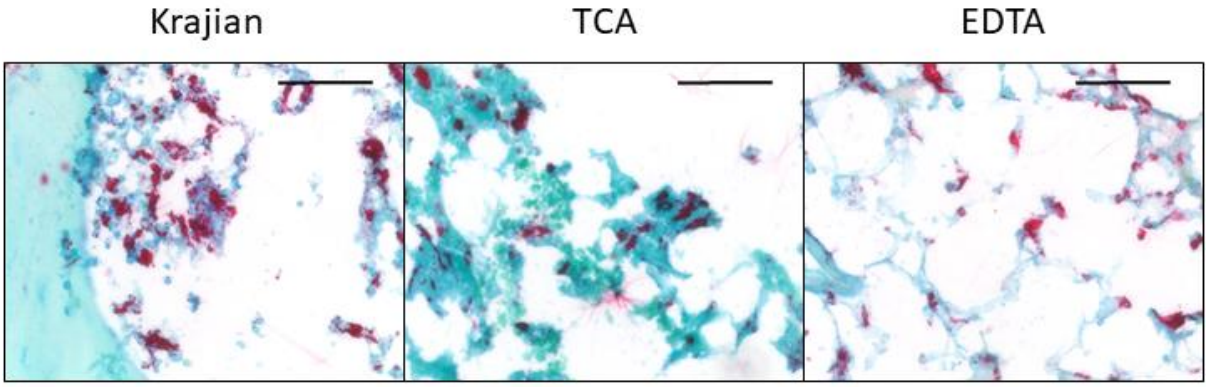

Figure 6-7. CD68 staining of bone cores after decalcification and embedding in OCT*. Images of bone cores after they have been decalcified by: Krajian solution, 6% (v/v) TCA or an EDTA-glucose solution. CD68 positive cells are stained red, with fast green used as a background stain. Images are representative of N=2, with four technical replicates. Scale bar= 100 µm*

The previous sections were attached to standard superfrost slides (MENZEL-GLÄSER). To see if adherence could be improved two new slides were tested, including 'plus gold' slides from Fisher, TOMO® slides from CellPath, alongside a tissue capture pen from Fisher. All three methods were promoted as improving the adherence of tissue, with the plus gold slides specifically referencing

bone marrow. Tissue capture pen solution was applied to standard slides to increase the adhesion of the sections. **Figure 6-8** are representative images of CD105 staining of the three adherent slides. CD105 is a marker for angiogenesis and mesenchymal stem cells and was used here to replace the CD68 staining protocol, as it was the same length. There was a clear increase in adherence of tissue when using TOMO® slides compared with both the tissue capture pen and plus gold slides. The plus gold slides did show an improvement of adherence over the tissue capture pen, but not to the same extent as the TOMO® slides. From these optimisation experiments it was concluded that the combination of TCA decalcified bone embedded in OCT and sectioned onto TOMO® slides was optimal for future staining. TCA was chosen as while there were little differences in morphology or staining intensity between the Krajian, TCA and EDTA decalcification methods, it was a simple dilution with a shorter decalcification time.

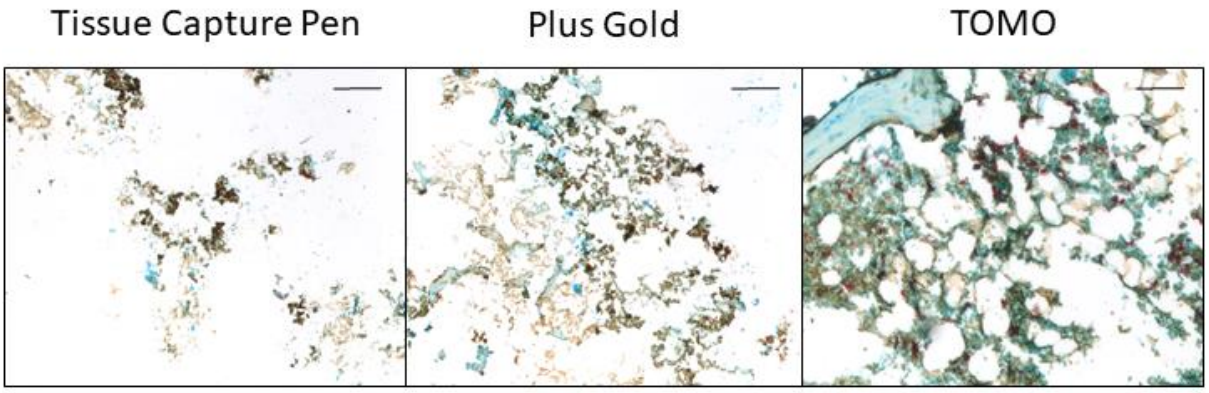

Figure 6-8. CD105 staining of bone cores after decalcification and embedding in OCT. *Images of bone cores after they have been decalcified by 6% (v/v) TCA, then sectioned onto adherent slides including those coated in a tissue capture pen, plus gold slides and TOMO® slides. CD105 positive cells are stained brown, with fast green used as a background stain. Images are representative of N=1, with three technical replicates. Scale bar= 100 µm.*

6.2.3 Histological Analysis of the 3D Bone Core Model Incubated on the CAM

After decalcification, embedding and sectioning the bone cores were stained for a range of markers including; CD68, a macrophage marker, CD105, a mesenchymal stem cell marker and RANK, which is expressed by osteoclasts. From each section an average of five images were captured using a Zeiss Axiovert microscope. These images were taken from set areas as shown in **Figure 6-9**A, to keep analysis consistent between the different conditions. The images consisted of; two taken at the sides of the defect area, two closer to the bottom of the bone core, and one or two taken in the defect region. Once the images were captured, they were analysed using ImageJ to quantify the area of positive staining. **Figure 6-9** depicts the image analysis method on one section. The original image (B) was first deconvoluted [247], with the positive red stain

separated from the other green and brown background colours (C). A threshold was then set to encompass only the positive red staining, once set this was kept for all further analysis of each antibody for the same experiment. The resulting binary image (D) was then assessed for particle analysis (E), where the pixel area of positive stain and percentage area of positive stain was recorded. The resulting data could then be combined and compared.

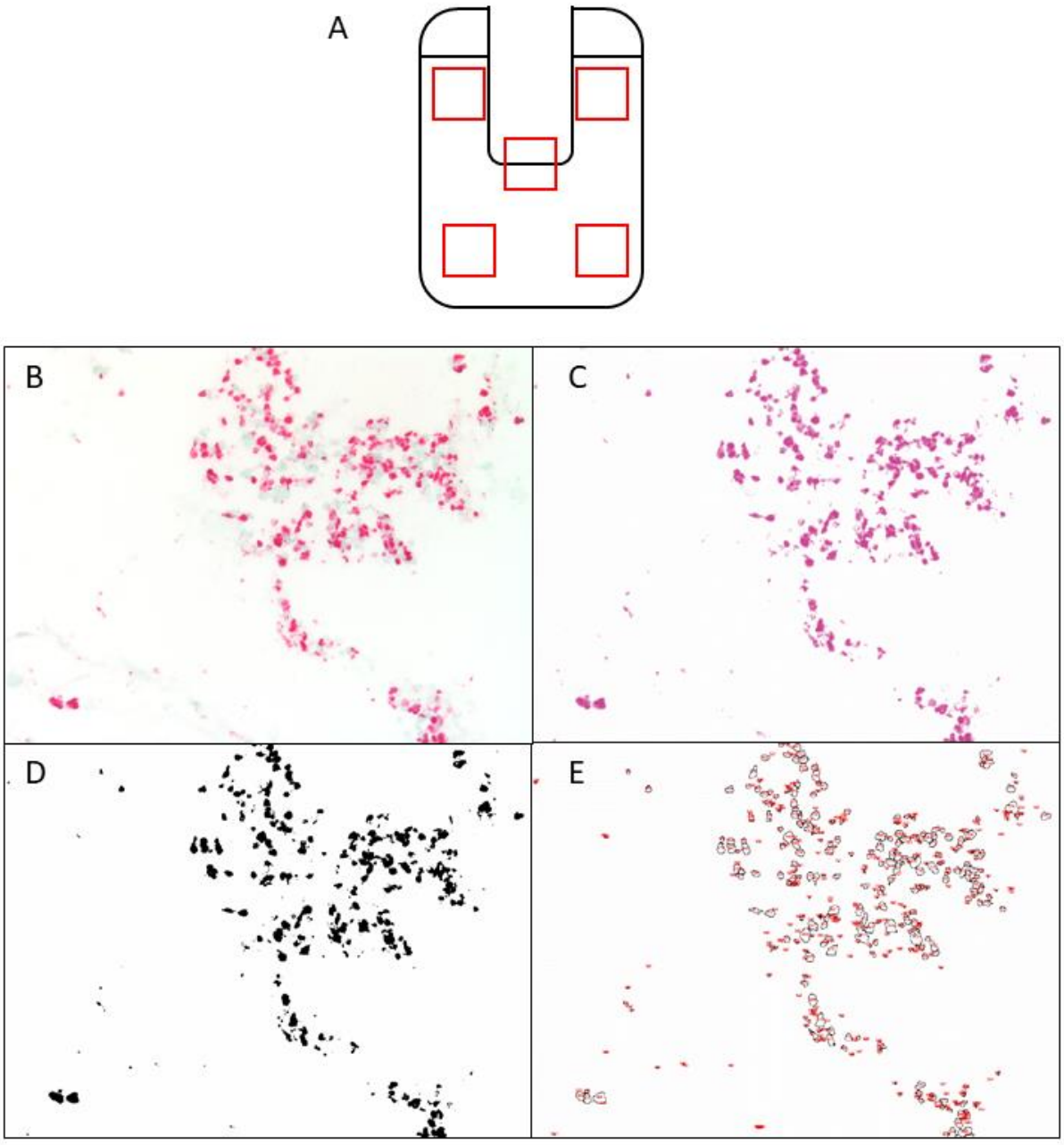

Figure 6-9. Schematic for the histological quantification analysis of bone cores. *(A) Five images from each stained section were taken using a Zeiss Axiovert microscope. (B) A representative image was first deconvoluted (C), which separated the positive red stain from green and brown background stains. These images were then (D) transformed into a binary image, then (E) assessed for particle analysis, the resulting pixel number was quantified and compared.*

The first 3D bone model consisted of a combination of MDM, Saos-2 and HBMSCs, characterised for inclusion in Chapter 3 and Chapter 4, which were inserted into bone cores (2.4.1) and cultured on the CAM assay for 10 days (2.4.3). Models were generated which included each of the cell types alone or as a triple combination, with empty bone cores being used as a control. After decalcification and embedding, the resulting sections were stained for CD68, a macrophage marker. **Figure 6-10**A shows representative images of CD68 staining (in red) for the five different conditions. A secondary antibody only control was also included to show there was no non-specific staining. These images showed clear CD68 positive staining in the MDM, HBMSC and triple combination bone cores, while also being found to a lesser extent in the control and Saos-2 bone cores. CD68 positive cells not in the defect area were also found in the resident tissue, more specifically at the top of the bone core near the cartilage layer. It was also determined that a large number of the inserted cells remained within the defect region (**Figure 6-10**B), with some interaction of the immediate surrounding tissue. The percentage area of positive stain was then calculated and compared. The deconvolution vector for 'FastRed' was used due to the strong red signal, with a threshold of 0-148. **Figure 6-10**C indicates the percentage of CD68 expression found in the whole bone core, where the triple combination showed significantly higher levels of CD68 compared with all other conditions. The MDM-only bone cores also showed significantly higher levels of expression compared with the control and Saos-2 conditions. While the majority of inserted cells remained within the defect area, it was unknown whether the presence of the cells affected the activity of resident macrophages, or if any cell migration occurred. **Figure 6-10**D shows the quantified percentage of positive staining of the surrounding resident tissue, not including images of the defect region. Here it was found that there were still differences in CD68 expression, showing a similar pattern where the MDM, HBMSCs and triple-cell combination had a higher level of expression than the control and Saos-2. The triple combination also had a significantly higher CD68 expression compared with the Saos-2-only bone cores.

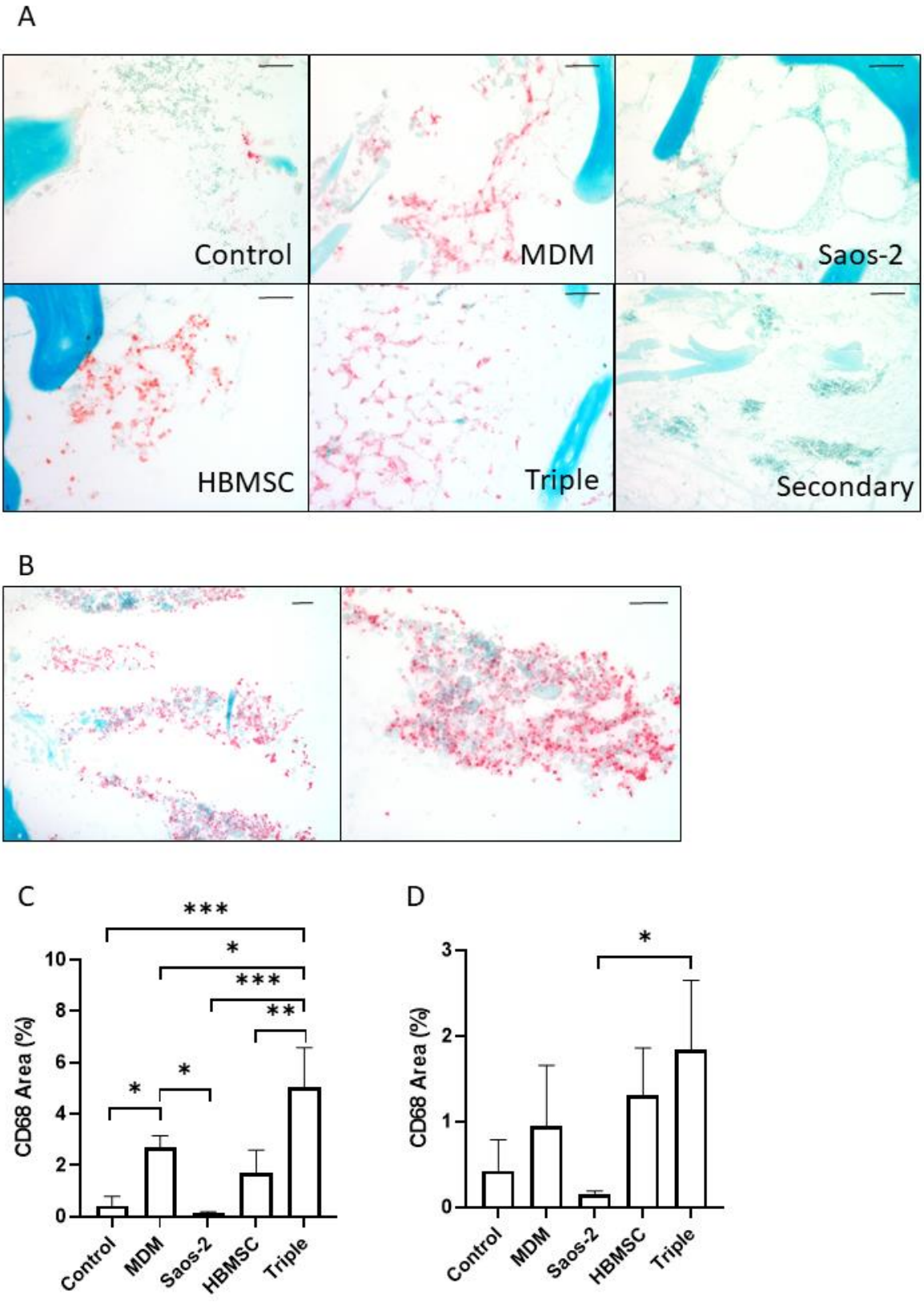

Figure 6-10. CD68 staining of bone cores after a 10 day CAM incubation with a combination of MDM, Saos-2 and HBMSCs cells. *(A) are representative images of CD68 staining (red) of the five conditions, a section was stained with the secondary antibody only as a control. These images were taken of the surrounding resident tissue, bone is stained blue. (B) are representative images of CD68 positive staining (red) found in the defect area. (C) is the quantification CD68+ staining*

*from all images taken of the bone cores. (D) is the quantification of CD68+ staining of resident tissue not including the defect area. Scale bar= 100 µm. N=3-5, data presented as mean +/- SD, statistics determined using one-way ANOVA, significance represented as *<0.05, ** <0.01, ***<0.001.*

The expression of CD105, a variable marker for angiogenesis and mesenchymal stem cells, was also assessed and quantified in these bone cores. **Figure 6-11**A shows representative images of CD105 staining in the five different conditions. A secondary antibody only control was also included to determine there was no non-specific staining occurring. These images showed clear positive staining in all conditions except for the control (no inserted cells). Images of the defect region (**Figure 6-11**B) supported the findings found in the CD68 staining, that the inserted cells generally remained within the defect region, where there was a stronger CD105 expression. The percentage area of positive staining was then analysed and compared, the deconvolution vector 'H+E Dab' was used to separate out the brown positive stain from the remaining blue and green background stains, with a threshold of 0-40. **Figure 6-11**C shows the percentage positive CD105 expression found in the whole bone core, here all bone cores inserted with additional cells showed an increased CD105 trend compared with the control bone cores. Differences between the groups were not significant, possibly due to the large variation between the bone cores of the same condition. The expression of CD105 in the surrounding resident tissue was also determined by quantifying the bone cores but not including images of the defect region (**Figure 6-11**D). This showed a lower CD105 expression in all bone cores, particularly the triple-cell combination, with very similar low levels of expression across all conditions.

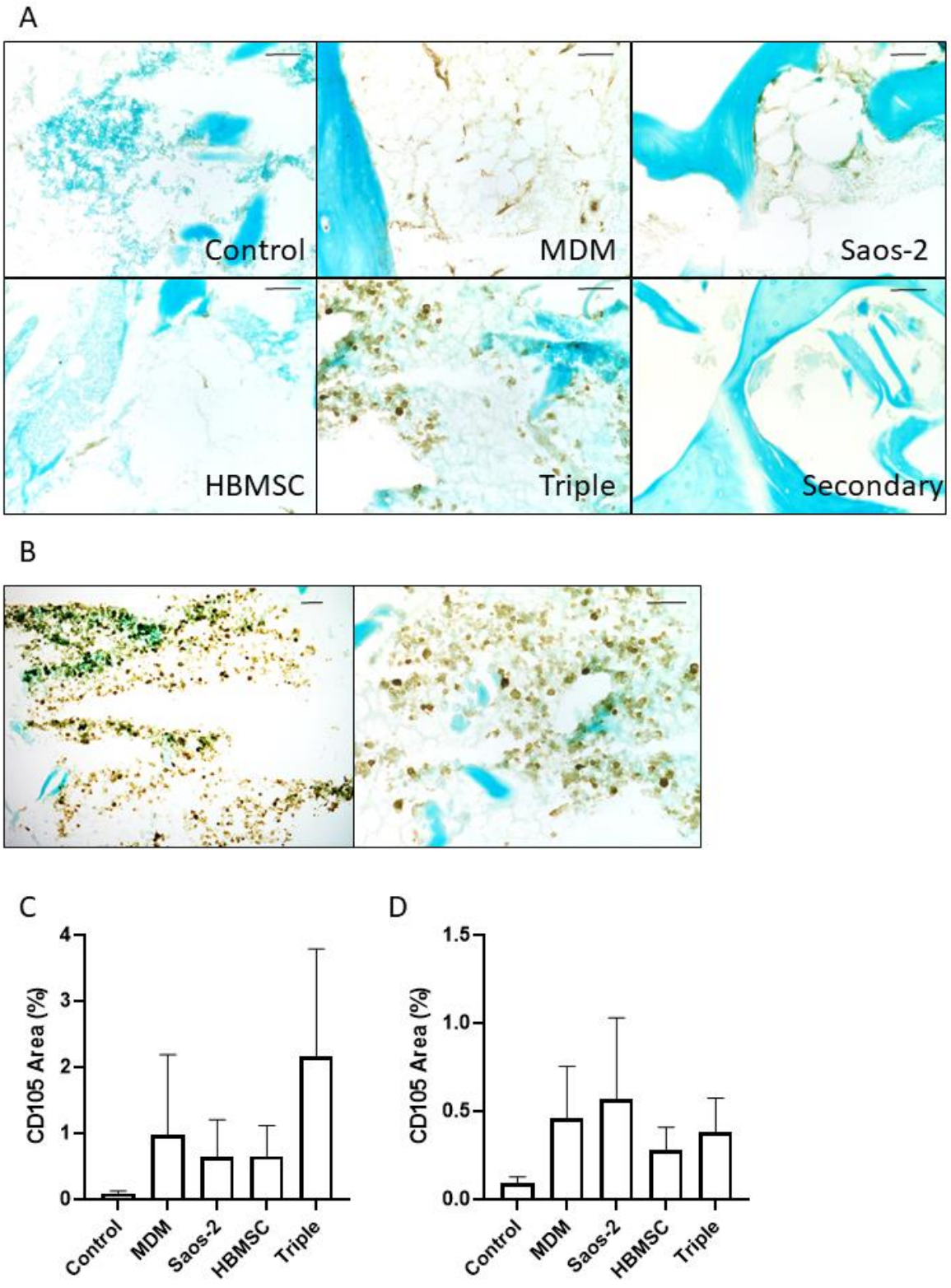

Figure 6-11. CD105 staining of bone cores after a 10 day CAM incubation with a combination of MDM, Saos-2 and HBMSCs cells. *(A) are representative images of CD105 staining (brown) of the five conditions, a section was stained with the secondary antibody only as a control. These images were taken of the surrounding resident tissue, bone is stained blue. (B) are representative images of CD105 positive staining found in the defect area. (C) is the quantification of CD105+ staining from all images of the bone cores. (D) is the quantification of CD105+ staining of resident tissue*

not including the defect area. Scale bar= 100 µm. N=3-5, data presented as mean +/- SD, statistics determined using a one-way ANOVA, no significance determined.

The expression of the osteoclast marker RANK was also analysed in the five different conditions. **Figure 6-12**A are representative images of RANK staining, which showed a low amount of positive staining that could be seen in certain areas on the MDM sample. A secondary antibody only control was also included to show there was no non-specific staining occurring. Unfortunately, no cells were found in the small defect regions of these sections, and so the level of RANK could not be compared between the defect region and the surrounding tissue. The lack of cells could suggest the sections used were not close enough to the centre of the defect, supporting the contention that the inserted cells remained within the defect region. The percentage area of RANK positive staining was analysed for the whole bone core, with the deconvolution vector 'feulgen light green' used to separate out the fainter red stain from any green and brown, the threshold was set at 0-160. The data was combined and **Figure 6-12**B showed there was no RANK staining found in all five conditions, equating to less than 0.1% of total image area.

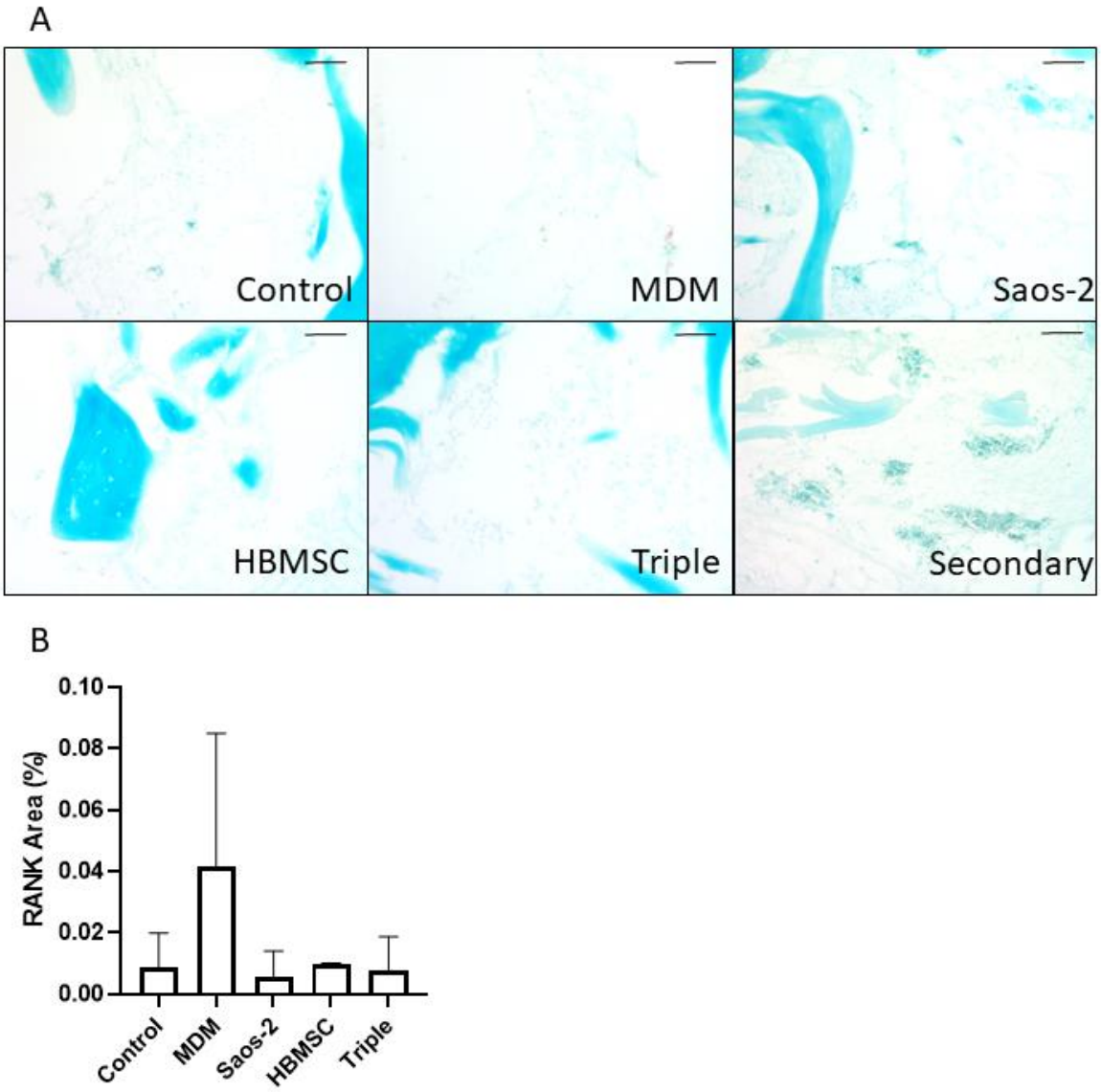

Figure 6-12. RANK staining of bone cores after a 10 day CAM incubation with a combination of MDM, Saos-2 and HBMSCs cells*. (A) are representative images of RANK staining (red) of the five conditions, a section was stained with the secondary antibody only as a control. These images were taken of the surrounding resident tissue, bone is stained blue. (B) is the quantification of RANK staining from all images of the bone cores. Scale bar= 100 µm. N=3-5, data presented as mean +/- SD, statistics determined using a one-way ANOVA, no significance determined.*

The histological analysis of the 3D bone cores has shown that expression of CD68 was higher in the triple cell combination during both the whole bone core analysis (**Figure 6-10**C) and in the resident tissue of the CAM bone cores after the defect area was removed from analysis (**Figure 6-10**D). CD105 expression in the CAM incubated bone cores also showed a higher level of expression in the triple cell combination and single cell bone cores compared to the control (**Figure 6-11**). RANK expression was low (**Figure 6-12**) with the defect areas showing no inserted

cells, suggesting further optimisation of the sectioning and staining process would be needed for this marker.

6.2.4 Histological Analysis of the 3D Bone Core Model Incubated in Long Term Culture

To determine how much the CAM vasculature influences the phenotypic changes observed in the bone cores, the triple combination of MDMs, Saos-2 and HBMSCs were introduced into bone cores (2.4.1) and cultured in basal media (instead of the CAM) for the long term culture of 20 days, before they were decalcified, embedded in OCT and sectioned. **Figure 6-13**A are representative images of CD68 staining in the control and triple combination bone cores. There were increased levels of CD68 staining found in the defect region, supporting the previous findings that a high proportion of the cells remained in the defect region during culture. The percentage area of CD68 positive staining was analysed, using the deconvolution vector 'FastRed' with a threshold of 0-162. **Figure 6-13**B showed a clear increased trend in CD68 expression in the triple combination bone cores compared with the control (no inserted cells). In comparison, when the images of the defect region were removed from the image analysis, there was very similar levels of CD68 staining in resident tissue between the triple combination and the control bone cores.

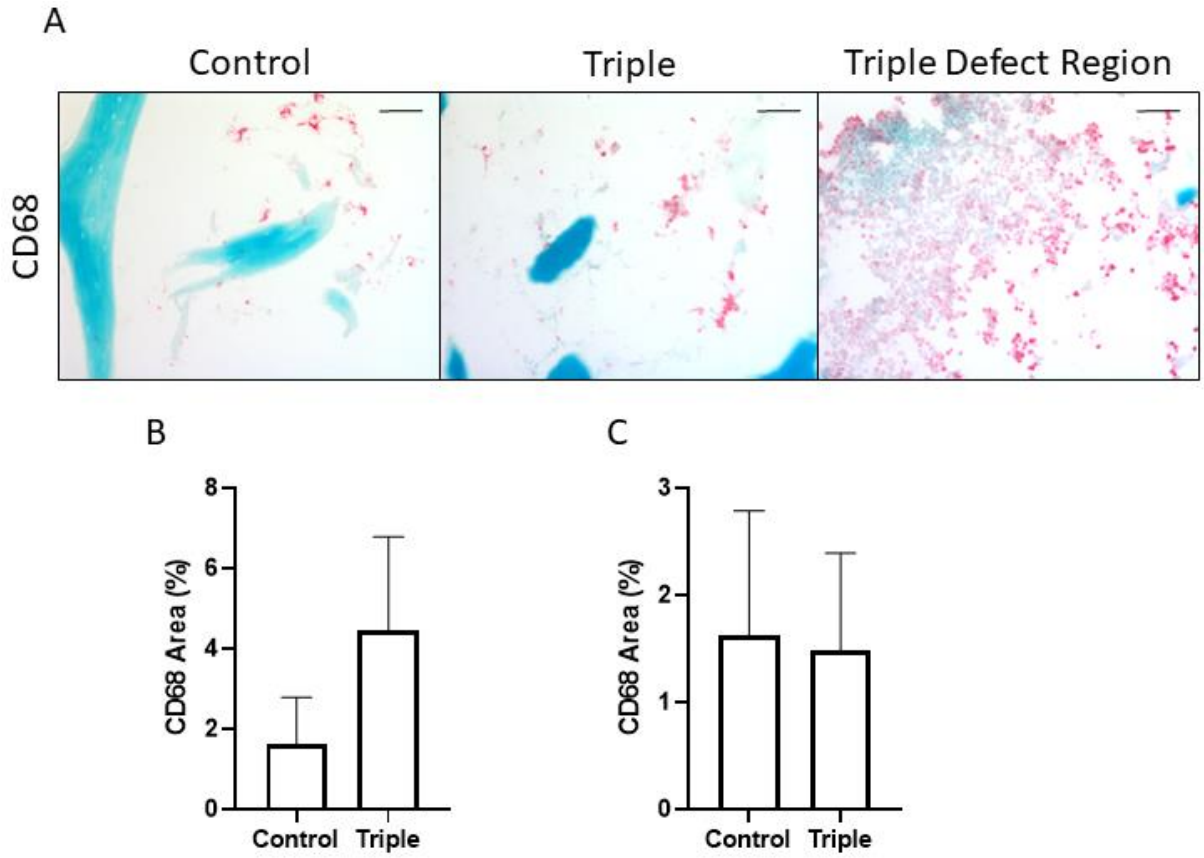

Figure 6-13. CD68 staining of bone cores after a 20 day culture in basal media with and without a combination of MDM, Saos-2 and HBMSCs cells*. (A) are representative images of CD68 staining (red) from the resident tissue surrounding the defect area of the bone cores, as well as positive staining found in the defect region of the triple combination. Bone is stained blue. (B) is the quantification CD68+ staining from all images of the bone cores. (C) is the quantification of CD68+ staining of resident tissue not including the defect area. Scale bar= 100 µm. N=2-5, data presented as mean +/- SD, statistics determined using a T test, no significance was determined.*

These long term cultured bone cores were also stained and analysed for CD105 expression. **Figure 6-14**A are representative images of CD105 expression in the control and triple-cell combination cores. Positive staining was found in the tissue surrounding the defect region, but a much stronger CD105 staining was located within the defect region of the triple-cell combination. This pattern was also found in the image analysis, which used the deconvolution vector 'H+E DAB', with a threshold of 0-30. **Figure 6-14**B shows in the whole bone core there was higher percent area staining of CD105 expression of the triple combination bone cores compared with the control. This was also seen although to a lesser extend when the defect images are removed from the analysis (**Figure 6-14**C). While neither of these were significant changes, it does suggest that there may have been interactions or migration of the inserted cells, supporting the increase of CD105 expression in the surround resident bone.

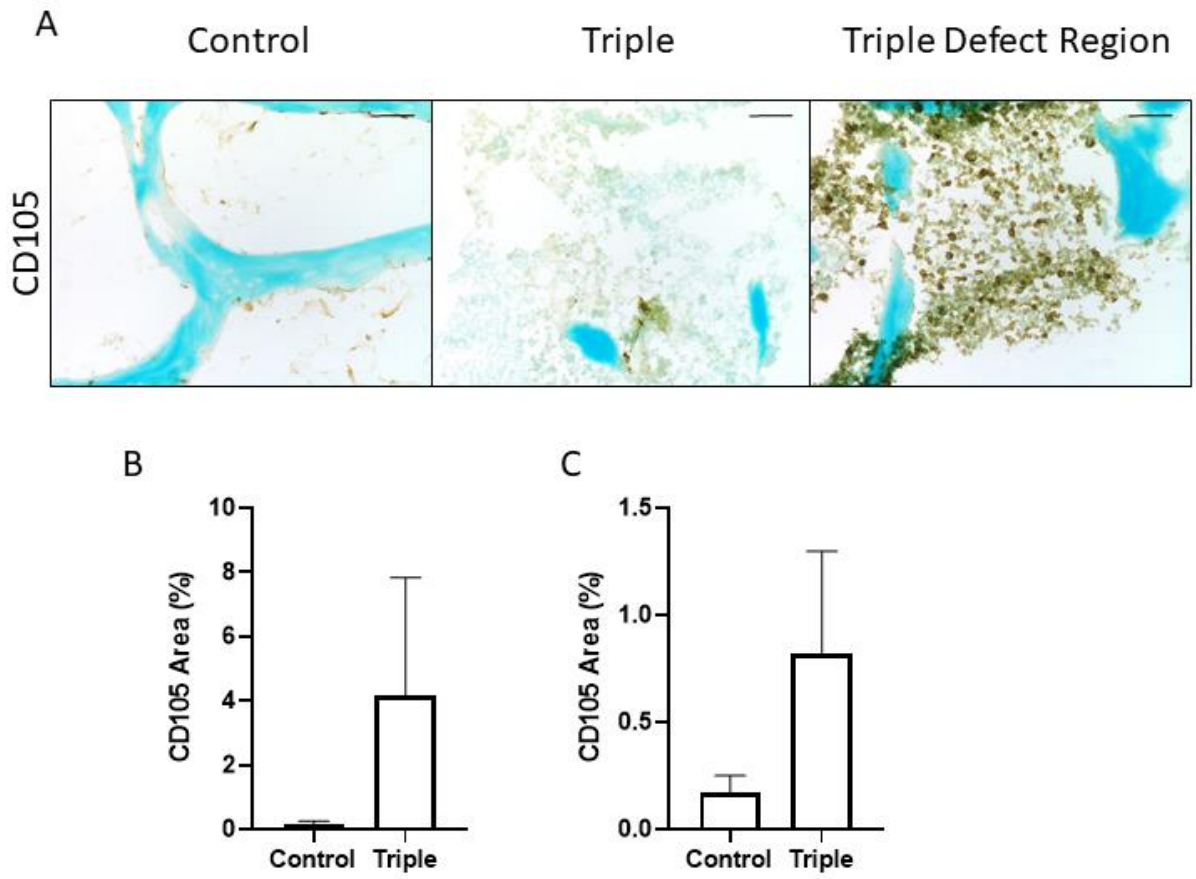

Figure 6-14. CD105 staining of bone cores after a 20 day culture in basal media with and without a combination of MDM, Saos-2 and HBMSCs cells*. (A) are representative images of CD105 staining (brown) from the resident tissue surround the defect area of the bone cores, as well as positive staining found in the defect region of the triple combination, bone is stained blue. (B) is the quantification CD105+ staining from all images of the bone cores. (C) is the quantification of CD105+ staining of resident tissue not including the defect area. Scale bar= 100 µm. N=2-5, data presented as mean +/- SD, statistics determined using a T test, no significance was determined.*

Finally, the long term cultured bone cores were also stained for RANK expression. Similarly, to the CAM analysed cores, the defect regions of these sections did not show large volumes of inserted cells, as such analysis of RANK only consisted of the surrounding resident tissue. **Figure 6-15**A are representative images of RANK signalling in the control and triple-cell combination bone cores, showing no positive signalling in the control cores with a higher level of expression in the triple-cell combination, although there are large discrepancies between the bone cores of the same condition. The images were analysed using the deconvolution vector 'feulgen light green', with a threshold of 0-160. **Figure 6-15**B illustrates an increase in RANK expression over the triple combination bone cores compared with the control, but this remained low, not exceeding 1.5% of the total image area.

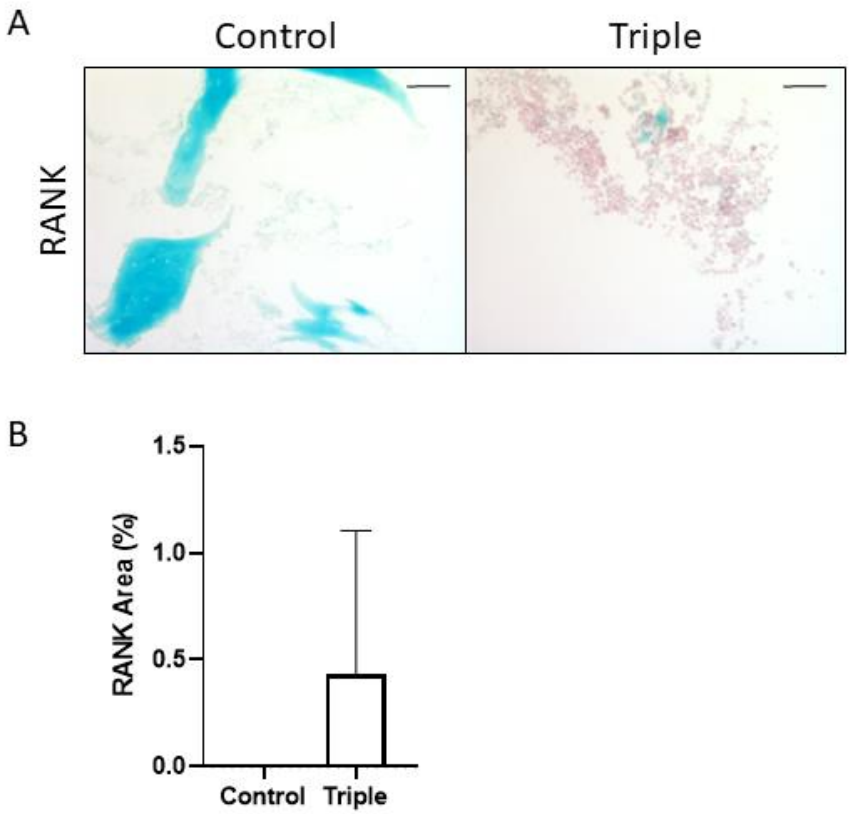

Figure 6-15. RANK staining of bone cores after a 20 day culture in basal media with and without a combination of MDM, Saos-2 and HBMSCs cells*. (A) are representative images of RANK staining (red) from the resident tissue surround the defect area of the bone cores, bone is stained blue. (B) is the quantification of RANK+ staining from all images. Scale bar= 100 µm. N=2-5, data presented as mean +/- SD, statistics determined using a T test, no significance was determined.*

Overall, the data presented here has shown that expression of CD68 was higher in the triple cell combination during whole bone core analysis compared to the control (**Figure 6-13**B), but the resident CD68 expression was similar between the control and triple cell combination (**Figure 6-13**C). Similar to the CAM data, CD105 expression in the long term culture was higher in the triple cell combination compared to the control (**Figure 6-14**). RANK expression was also very low in the long term culture bone cores (**Figure 6-15**), where the defect areas showed no inserted cells. This was similar to the CAM incubated bone cores, suggesting further optimisation would be needed for this marker.

6.2.5 Histological Analysis of the 3D Bone Slice Model

Bone cores, although designed for easy insertion of cells, were large (~8mm in width). It was unknown whether the large area of trabecular bone was affecting the migration of cells in the bone core model, potentially reducing any biological effects. Consequently, bone slices (~5 mm) were made (2.4.2), which had a lower trabecular bone surface area, and a combination of MDM,

Saos-2 and HBMSCs were inserted at the same cell number as the bone cores. Empty bone slices, not inserted with cells, were used as a control. These bone slices were then incubated on the CAM assay for 10 days before being decalcified, embedded and sectioned. **Figure 6-16** illustrates representative images of CD68, CD105 and RANK expression of bone slices cultured with the triple-cell combination or no cells as a control. The percentage area of CD68 (A) positive signalling was very similar across both bone slice conditions. Image analysis showed there was an increase in CD68 expression in the control bone cores compared with the triple combination, although this remained overall very low with less than 1.6% of the whole image area. Both CD105 (B) and RANK (C) showed similar patterns of expression, with an increase in percentage area of positive cells from the triple combination compared with the control.

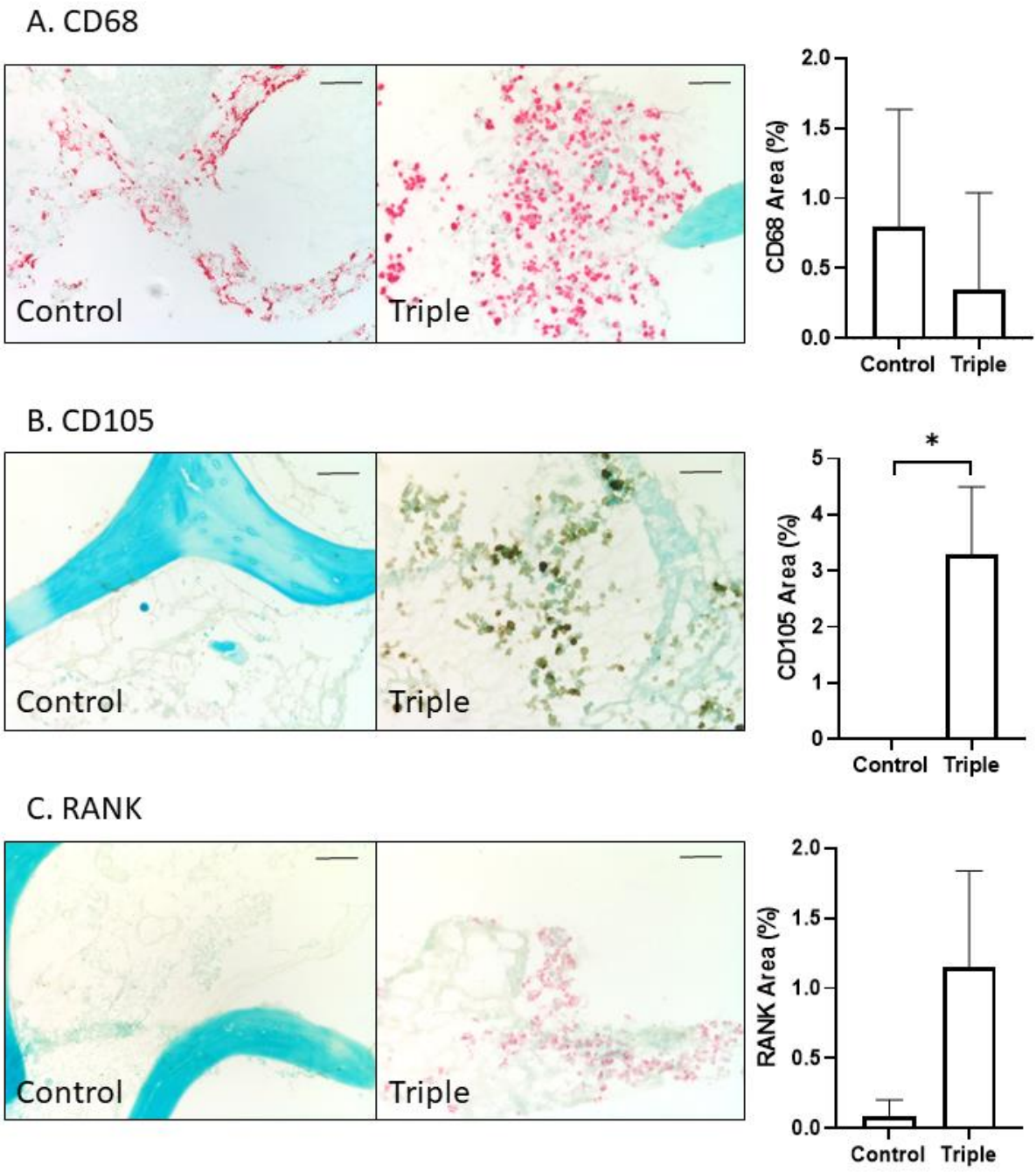

Figure 6-16. Immunohistochemistry analysis of triple combination bone slices after incubation on the CAM. *Bone slices were inserted with a combination of MDMs, Saos-2 and HBMSCs before being incubated for 10 days on the CAM. (A) are representative images of CD68 (red) staining and quantification of CD68 from all images. (B) are representative images of CD105 (brown) positive staining and quantification of CD105 from all images. (C) are representative images of RANK (red) staining and quantification of RANK from all images. Bone is stained blue. Scale bar= 100 µm. N=3-5, data presented as mean +/- SD, statistics determined using a T test, significance represented as *<0.05.*

The triple combination of cells were also inserted onto bone slices and cultured for 20 days in basal media before being decalcified, embedded and sectioned. **Figure 6-17** show representative images of CD68, CD105 and RANK staining (2.6.5). Similar to the CAM culture, there was positive CD68 (A) staining in both the control and triple combinations, although there was a clear increase in the triple combination, which differs from the CAM analysis. This was also true of the image analysis, which showed an increase in percentage area of positive CD68 cells in the triple combination compared with the control. Similar patterns could also be seen in both the CD105 (B) and RANK (C) staining, where an increase of positive staining was seen in the triple-cell combination slices compared with the control. This was again repeated in the image analysis, where both stains showed an increased trend in total percentage area in the triple combination compared with the control.

In summary, immunohistochemistry analysis suggested that incubation on the CAM resulted in similar levels of CD68 expression for both the triple combination and control bone slices, while in contrast CD105 and RANK showed a higher level of staining in the triple combination bone slices compared to the controls. Analysis of the long term cultured bone slices also showed a higher level of CD68, CD105 and RANK expression in the triple combination bone slices compared to the control bone slices. This was similar to the data generated from the bone core models, but it was noted that a high proportion of cells inserted did not remain within the trabecular bone, suggesting that the use of bone slices doesn't improve the penetration and migration of the inserted cells.

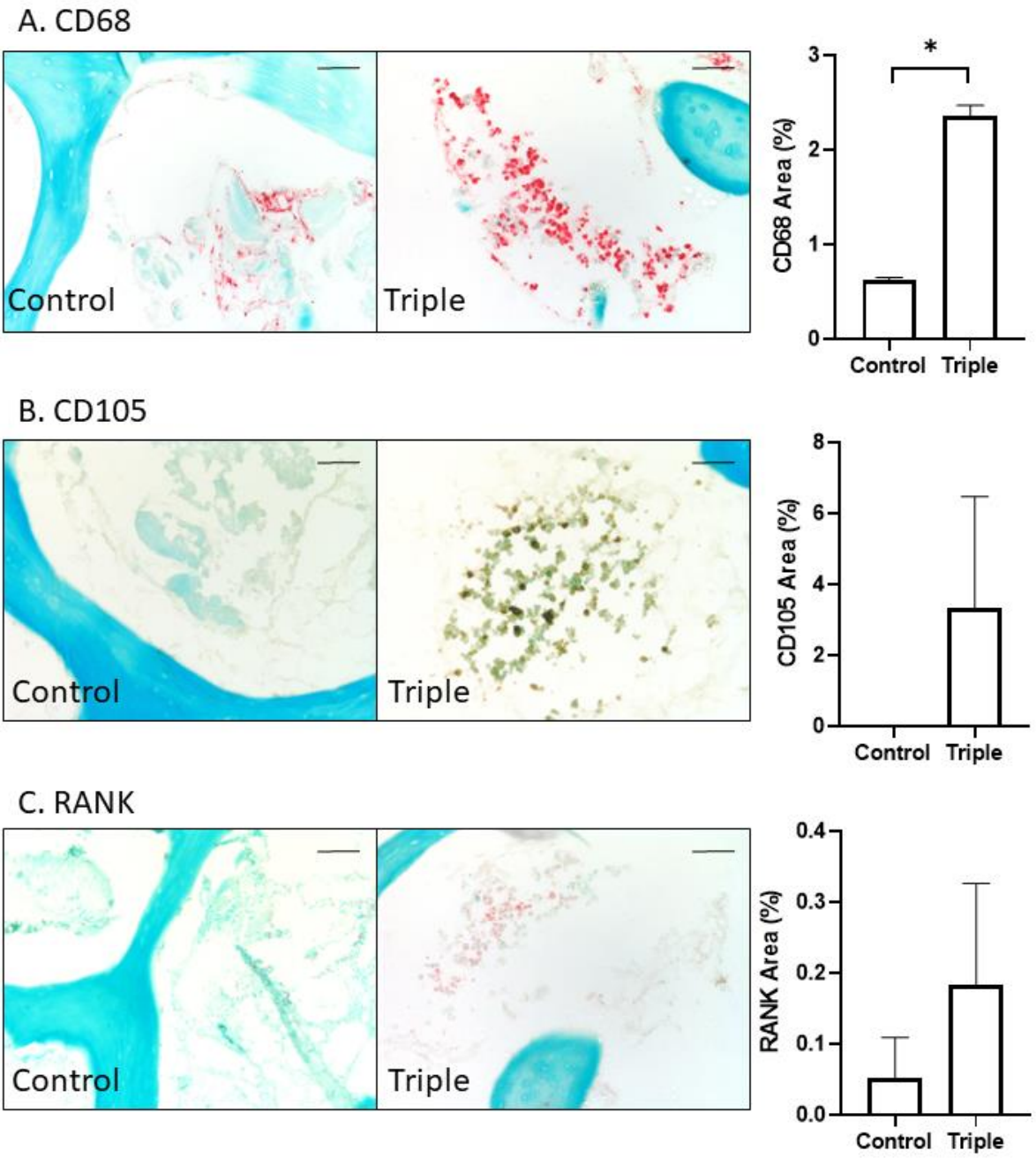

Figure 6-17. Immunohistochemistry analysis of triple combination bone slices after a 20 day incubation in basal media. *Bone slices were inserted with a combination of MDMs, Saos-2 and HBMSCs before being incubated for 20 days in basal media. (A) representative images of CD68 (red) staining and quantification of CD68 from all images. (B) are representative images of CD105 (brown) positive staining and quantification of CD105 from all images. (C) are representative images of RANK (red) staining and quantification of RANK from all images. Bone is stained blue. Scale bar= 100 µm. N=2-5, data presented as mean +/- SD, statistics determined using a T test, significance represented as *<0.05*

6.2.6 Histological Analysis of the 3D Bone Core Model after Incubation with Mifamurtide

The ultimate aim of developing a 3D multicellular model of osteosarcoma was to use it to test new drugs and therapies. In light of this, a pilot study was performed by culturing the triple-cell combination bone cores in the osteosarcoma drug Mifamurtide for 5 days before implantation onto the CAM (pre), or for 5 days after removal from the CAM (post). Empty bone cores were used as a control, alongside empty bone cores incubated with Mifamurtide. A final concentration of 0.16 µg/ml of Mifamurtide was used (diluted 1:10 with basal media), this was based on HBMSC and Saos-2 2D analysis (3.2.6 and 3.2.7). The bone cores were then decalcified, embedded and sectioned before being analysed for by immunohistochemistry (2.6.5). **Figure 6-18**A shows representative images of CD68 expression in the five different conditions, demonstrating low levels of CD68 expression in the control and Mifamurtide control bone cores, with a higher level of staining in the three triple-cell combination bone cores. Images of cells found in the defect regions of the triple combination bone cores, with and without Mifamurtide (both Pre and Post) showed similar levels of CD68 expression, although it was still stronger in the triple combination only bone cores (**Figure 6-18**B). The images were then analysed using the deconvolution vector 'FastRed' with a threshold of 0-160. Due to the similar levels of CD68 expression, images from the control and control+ Mifamurtide groups were combined for quantification. **Figure 6-18**C shows there was a significantly higher percentage area of CD68 staining in the triple-cell combination group compared with the control. These cores also demonstrated an increase in the triple-cell combination compared with the Mifamurtide treated groups, which themselves showed very similar levels of expression. Interestingly, when the defect region images were removed from the analysis the differences between the triple-cell combination bone cores with the other three conditions increased in statistical significance (**Figure 6-18**D). In contrast, the Mifamurtide Pre bone cores demonstrated a reduced expression down to a similar level to the control bone cores, and the Mifamurtide post bone cores only showed a slightly higher level of expression.

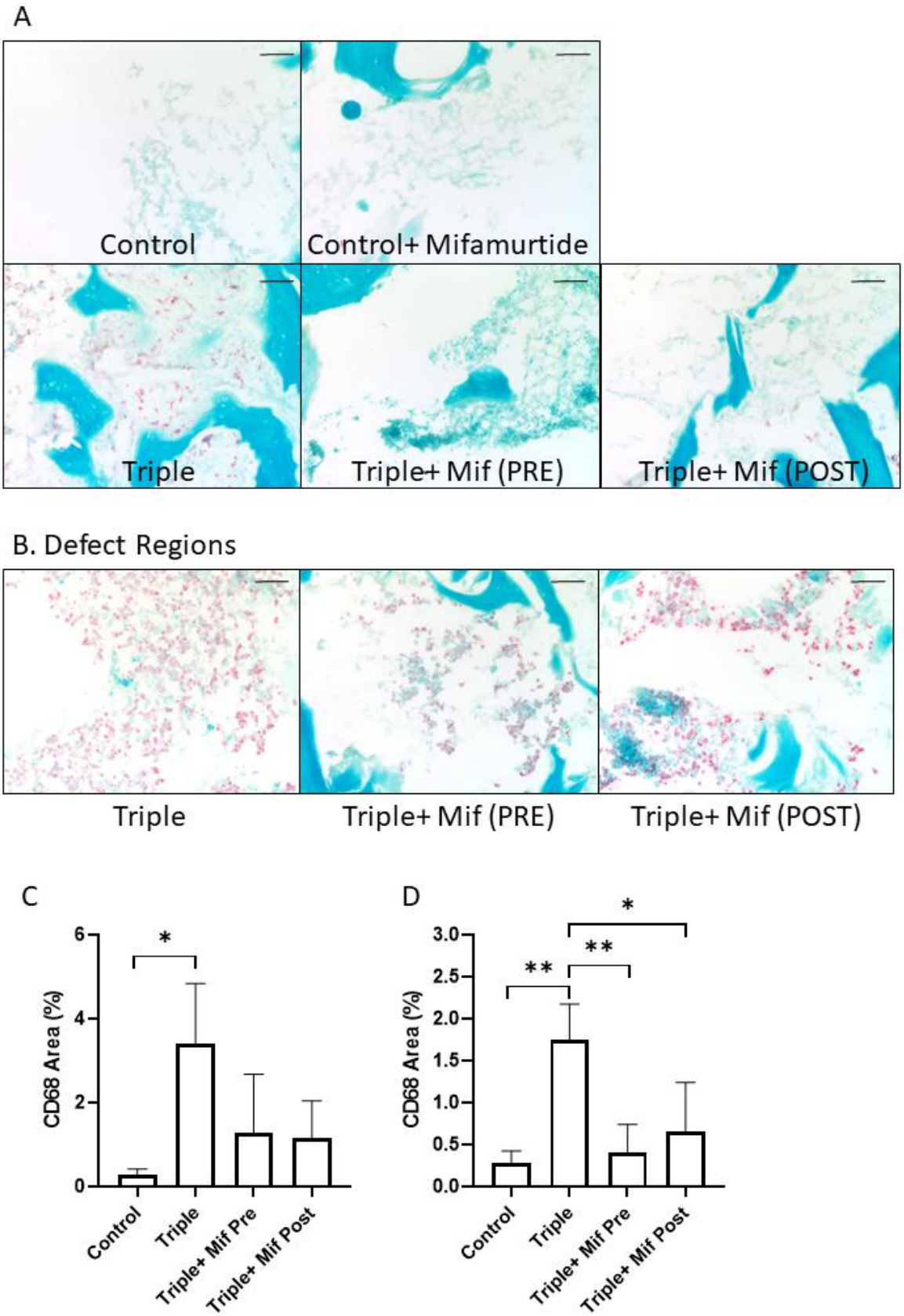

Figure 6-18. CD68 staining of triple combination bone cores after a 10 day CAM incubation and treatment with Mifamurtide*. Bone cores were inserted with a combination of MDMs, Saos-2 and HBMSCs, they were then incubated in Mifamurtide for five days before or after the CAM incubation. (A) are representative images of CD68 (red) staining from the resident tissue surround*

*the defect area, bone is stained blue. (B) are representative images of CD68 positive staining found in the defect areas. (C) is the quantification CD68+ staining from all images of the bone cores. (D) is the quantification of CD68+ staining of resident tissue not including the defect area. Scale bar = 100 µm. N=3-5, data presented as mean +/- SD, statistics determined using a one-way ANOVA, significance represented as *<0.05, ** <0.01.*

These bone cores were also analysed for CD105 expression. **Figure 6-19**A are representative images of CD105 staining in the five conditions, where both control bone cores and the Mifamurtide Post bone cores showed no positive staining. In contrast the triple and Mifamurtide Pre bone cores showed similar levels of higher CD105 expression. Differences in CD105 expression could be seen more clearly in the defect regions of the triple-cell combination bone cores, where those treated with Mifamurtide post incubation demonstrated the lowest level of expression, compared with both the triple and Mifamurtide Pre (**Figure 6-19**B). Image analysis of the bone cores was performed using the deconvolution vector 'H+E DAB', with a threshold of 0-30. Due to similar levels of CD105 expression from the control and control+ Mifamurtide these images were combined for quantification analysis. **Figure 6-19**C illustrates there was an increase in percentage area of CD105 staining of the triple combination and those cultured with Mifamurtide pre-incubation, compared with the control and the bone cores treated with Mifamurtide post-incubation. This pattern was also seen in analysis of the resident tissue, where images of the defect regions were removed prior to analysis (**Figure 6-19**D).

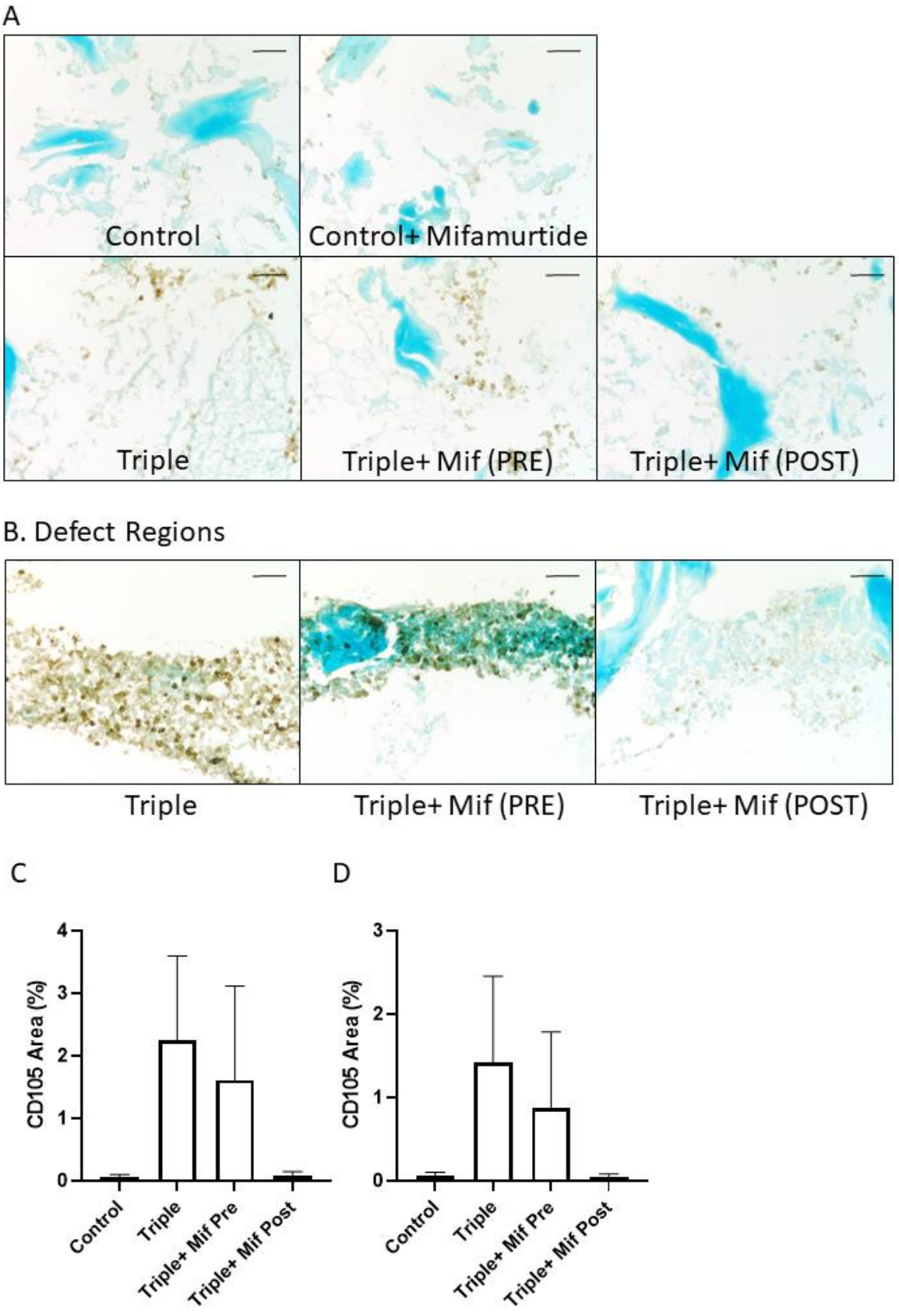

Figure 6-19. CD105 staining of triple combination bone cores after a 10 day CAM incubation and treatment with Mifamurtide*. Bone cores were inserted with a combination of MDMs, Saos-2 and HBMSCs, they were then incubated in Mifamurtide for five days before or after the CAM*

incubation. (A) are representative images of CD105 (brown) staining from the resident tissue surround the defect area, bone is stained blue. (B) are representative images of CD105 positive staining found in the defect areas. (C) is the quantification CD105+ staining from all images of the bone cores. (D) is the quantification of CD105+ staining of resident tissue not including the defect area. Scale bar= 100 µm. N=3-5, data presented as mean +/- SD, statistics determined using a one-way ANOVA, no significance was determined.

Finally, the bone cores were also stained for RANK expression. **Figure 6-20**A are representative images of RANK staining in the five different bone core conditions, which showed an increase in the triple-cell combination compared with the other four conditions. Images taken of the defect regions also illustrated a clear difference in RANK expression (**Figure 6-20**B), with the high levels in the triple-cell combination not found in the bone cores treated with Mifamurtide, both pre and post incubation. Image analysis of RANK signalling was completed, using the deconvolution vector 'feulgen light green', with a threshold of 0-160. Due to similar levels of RANK expression, images from the control and control+ Mifamurtide were combined for quantification analysis. **Figure 6-20**C demonstrated there was an increased trend in the percentage area of RANK expression of the triple-cell combination bone cores compared with the other three conditions. This pattern was also found when the defect region images were removed from the analysis, which showed a significantly higher percentage area of RANK in the triple combination cores compared with both Mifamurtide incubated bone cores (**Figure 6-20**D). This suggested that although the majority of cells inserted remained within the defect region, they did affect expression in other areas of the bone core.

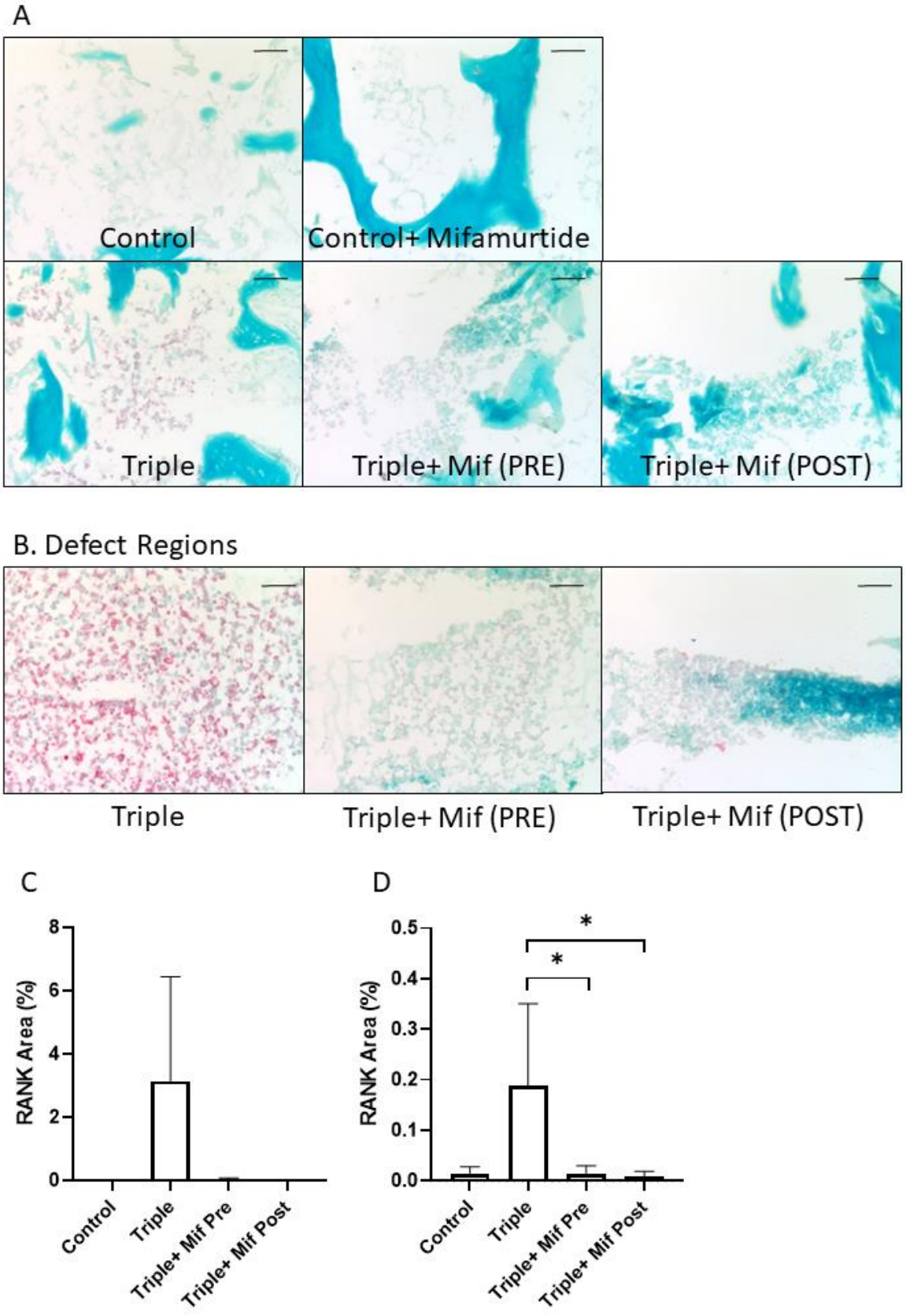

Figure 6-20. RANK staining of triple combination bone cores after a 10 day CAM incubation and treatment with Mifamurtide*. Bone cores were inserted with a combination of MDMs, Saos-2 and HBMSCs, they were then incubated in Mifamurtide for five days before or after the CAM incubation. (A) are representative images of RANK (red) staining from the resident tissue surround*

*the defect area, bone is stained blue. (B) are representative images of RANK positive staining found in the defect areas. (C) is the quantification RANK+ staining from all images of the bone cores. (D) is the quantification of RANK+ staining of resident tissue not including the defect area. Scale bar= 100 µm. N=3-5, data presented as mean +/- SD, statistics determined using a one-way ANOVA, significance represented as *<0.05.*

Culturing the triple-cell combination bone cores in Mifamurtide showed a reduced expression of all three markers analysed. CD68 expression (Figure 6-18) was higher in the triple combination compared to the control, but this was reduced when incubated with Mifamurtide, both before and after culturing on the CAM. The same pattern was seen in the level of RANK expression (Figure 6-20), which also showed a significantly higher level of expression in the triple combination compared to Mifamurtide incubated bone cores. Finally, the expression of CD105 (Figure 6-19) was higher in both the triple combination bone cores and those incubated with Mifamurtide pre-CAM culture, compared to the control and the bone cores incubated in Mifamurtide post-CAM culture, suggesting angiogenesis may have had an impact on CD105 expression.

6.2.7 Multiplex Analysis of Osteosarcoma Patient Samples

Histological analysis of the 3D bone models have shown differences in markers of interest, including CD68, CD105 and RANK, depending on the combination of cells inserted, and the method of culture (6.2.3 and 6.2.6). To assess if these differences modelled the osteosarcoma tumour microenvironment, 10 osteosarcoma primary sections were stained with 10 markers of interest (Table 2-8), including the three markers used to analyse the 3D bone models. As the data was anonymised, only the gender and age of the patients were known (Table 2-7). The staining was performed by multiplex immunohistochemistry (2.6.9) [248], where up to 8 stains were analysed in the same section to look for overlapping markers of interest. All quantification and multiplex staining was performed by the research histology department in the University Hospital Southampton. The antibodies underwent quantification analysis for up to 8 repeats to confirm markers were not lost over multiple staining cycles, and were split into two panels for analysis, panel 1: pSTAT3, CD68, HIF1α, CD32b, CD163, STAT3 and VEGF, panel 2: pSTAT3, Osteocalcin, CD105, RANK, STAT3, HIF1α, and VEGF. These markers were chosen based on their link to osteosarcoma characterisation in the literature, showing increased expression of Osteocalcin [249], RANK [250], STAT3 [251, 252], angiogenesis (which includes CD105 [253] and VEGF [254] markers), hypoxia (HIF1α) [255], and M2-like polarisation of macrophages (CD68, CD163 and CD32b) [256-258].

The resulting images were analysed and the area of positive staining was generated and compared. **Figure 6-21** and **Figure 6-22** are representative images showing the positive staining (in red) after the first and last stain. The quantification analysis was plotted next to the images to show how the level of staining changed over each repeat. The majority of antibodies showed a stable expression across multiple repeats, with the exception of pSTAT3 (**Figure 6-21**), and osteocalcin (**Figure 6-22**). The area of positive staining for pSTAT3 started to decrease dramatically during the third stain, while osteocalcin started decreasing during the 4th stain. Once the order of antibodies was determined, the 10 osteosarcoma samples were stained.

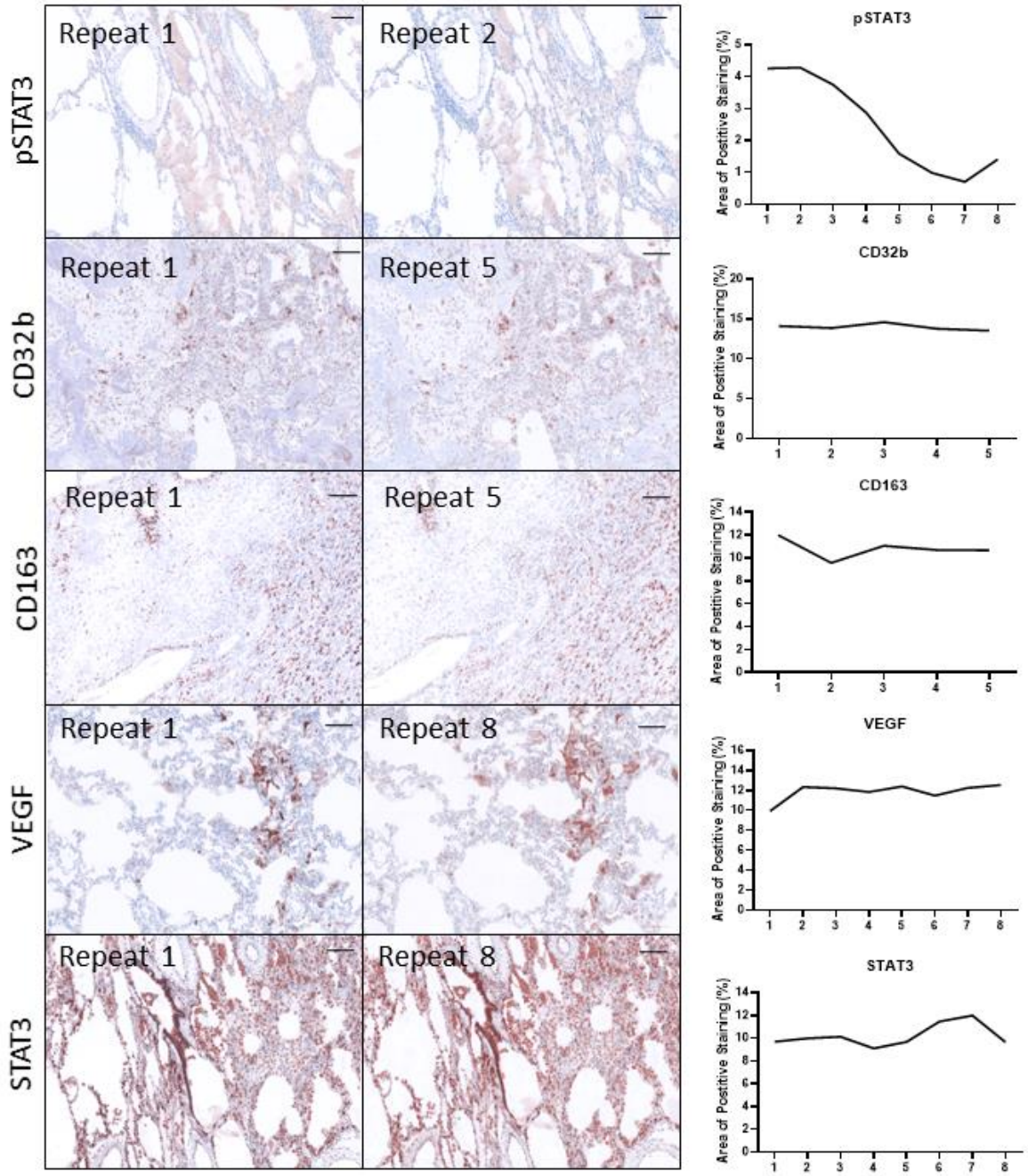

Figure 6-21. Quantification analysis of five antibodies for Multiplex analysis*. Osteosarcoma tissue was stained with pSTAT3, CD32b, CD163, VEGF or STAT3 for up to 8 times, representative images are shown for the first and last repeat of positive staining. The images of each antibody were analysed and the area of positive staining was recorded for each day. Scale bar= 100 µm.*

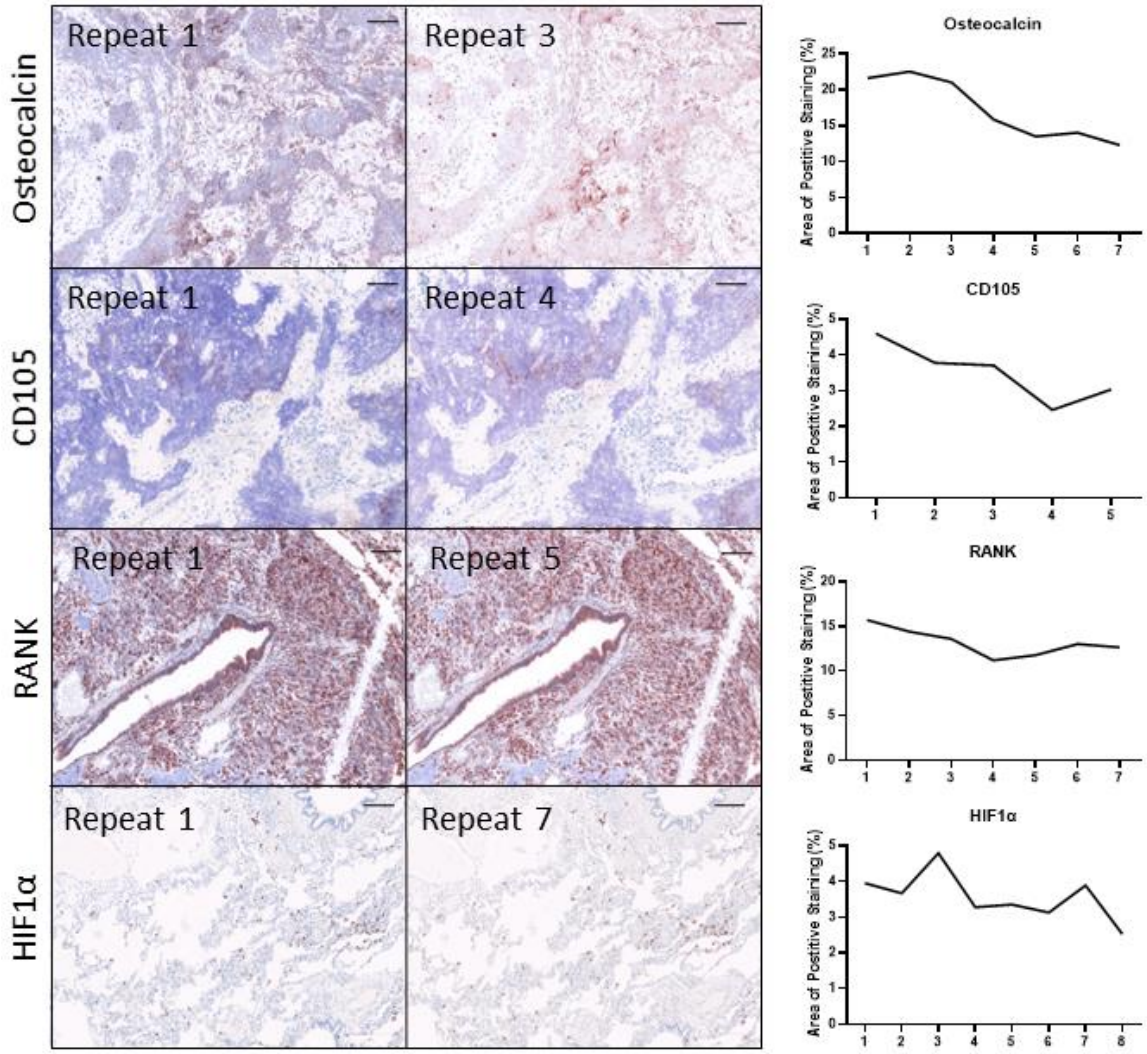

Figure 6-22. Quantification analysis of five antibodies for Multiplex analysis. *Osteosarcoma tissue was stained with osteocalcin, CD105, RANK or HIF1α for up to 8 repeats, representative images are shown on the first and last day of positive staining. The images of each antibody were analysed and the area of positive staining was recorded for each day. Scale bar= 100 µm.*

The whole tissue sample was imaged after each stain, before being analysed in ImageJ using the same method as for the 3D bone model analysis. **Figure 6-23** are representative images depicting the quantification method for analysing the multiplex images. First the colours from the initial image (A) were deconvoluted, with the positive red stain (B) separated from the other background colours. A threshold was then set to encompass only the positive red staining (C), once set this was kept the same for all further analysis of the same antibody. A threshold was also set for the blue background stain of each image (D), set at 0-228. The resulting binary images (C and E) were then assessed for particle analysis, where the area of positive stain (number of pixels) was recorded. The percentage positive area of stain was then calculated by dividing the red pixel area from the combined red and blue pixel area, to give a percentage of the whole tissue section.

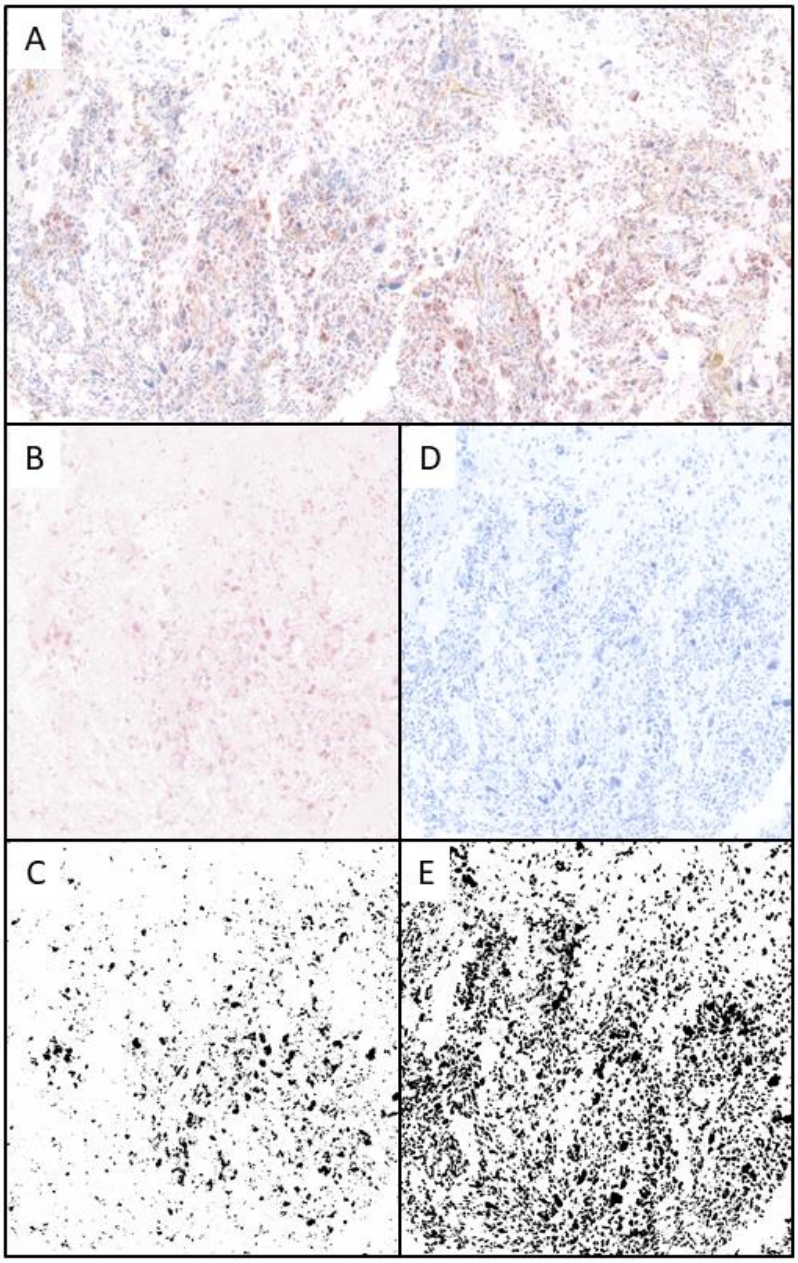

Figure 6-23. A schematic depicting the quantification of multiplex images. *The stained slides were imaged (A), then deconvoluted to separate the positive red stain (B) from the background stains (D). A threshold was then set for each colour and the number of pixels in the resulting binary images (C and E) were quantified.*

Figure 6-24 illustrates the image analysis of osteocalcin and RANK; for analysis purposes both of these stains were separated into the group's high, middle and low based on their percentage of area positivity. This system of classification was used for all stains analysed on the osteosarcoma samples. For osteocalcin the high staining was above 20% of tissue area, the middle was between 10 and 20% and low was below 6% (**Figure 6-24**A). Representative images of these groups can be seen in **Figure 6-24**C, where there was a clear decrease in osteocalcin staining (red). For RANK the

high level of staining was above 12% of tissue area, the middle between 5 and 12%, while the low was below 5% (**Figure 6-24**B). Representative images of these groups (**Figure 6-24**D) showed there was a decrease in RANK staining (red), with the low image illustrating no positive staining. There was very little overlap of osteocalcin and RANK staining on any of the 10 osteosarcoma samples, with both stains having distinct areas of positive and negative staining.

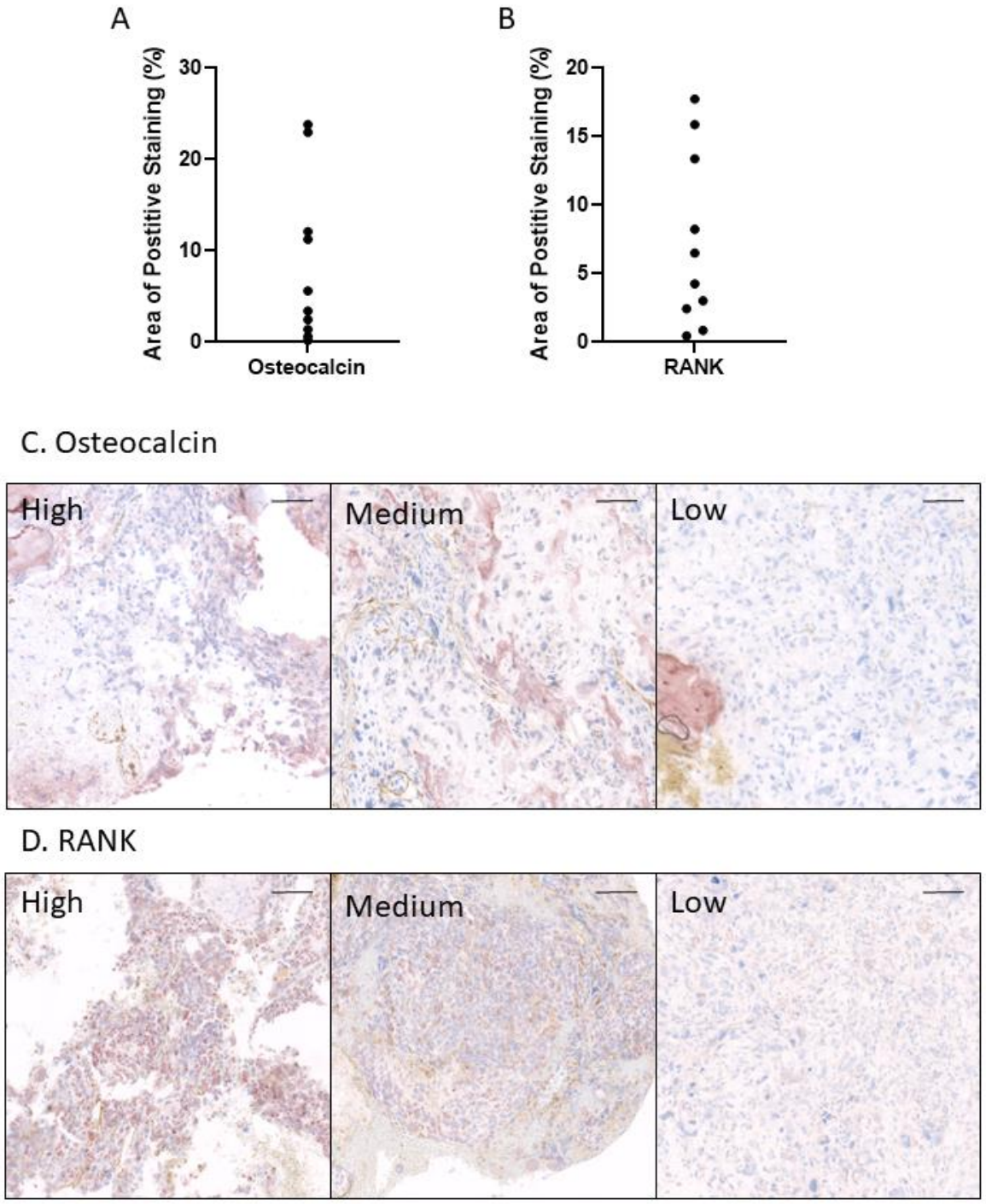

Figure 6-24. Multiplex analysis of osteocalcin and RANK from osteosarcoma patient samples. *Area positive staining of (A) osteocalcin and (B) RANK from 10 osteosarcoma patient samples. (C) Representative images of high (>20%), medium (10-20%) and low (<5%) levels of osteocalcin staining. (D) Representative images of high (>12%), medium (5-10%), and low (<5%) levels of RANK staining. Scale bar= 100 µm.*

Figure 6-25 shows the analysis of CD68, CD163 and CD32b, all of which can be used as markers of macrophages, while also being expressed on other immune cells [259, 260]. As CD163 and CD32b can be found on M2-like macrophages, a pattern of expression between these two markers was

expected, but no correlation was found between any of the three markers. The osteosarcoma samples were also grouped into high, medium, and low based on the percentage area of positive staining. For CD68 the high level of expression was above 2.5% of the tissue area, while the middle was between 1.2 and 2.5%, and the low was lower than 1.2%. Representative images of these groups can be seen in **Figure 6-25**B. While the high and middle expression images looked very similar in terms of amount of positive staining (in red), the CD68 positive cells tended to be in clusters around the tissue. This meant the high expression groups had more clusters per total tissue area than the middle group. For CD163 the high staining was above 8%, the middle between 5 and 8%, with the low below 5% of total tissue stained. Representative images of these groups can be seen in **Figure 6-25**C, where in contrast to the CD68 expression there was a general spread of CD163 positive staining (in red) across the tissue. For CD32b, all osteosarcoma samples had a very low level of staining, less than 2% of the total tissue area, but these patient samples could still be grouped into high, middle and low. The high group showed above 1% positive staining, the middle was between 0.5 and 1%, while the low group, which was lower than 0.5%, showed no CD32b positive expression. Representative images of CD32b expression can be seen in **Figure 6-25**D, but due to the low overall levels of expression no pattern of staining could be identified.

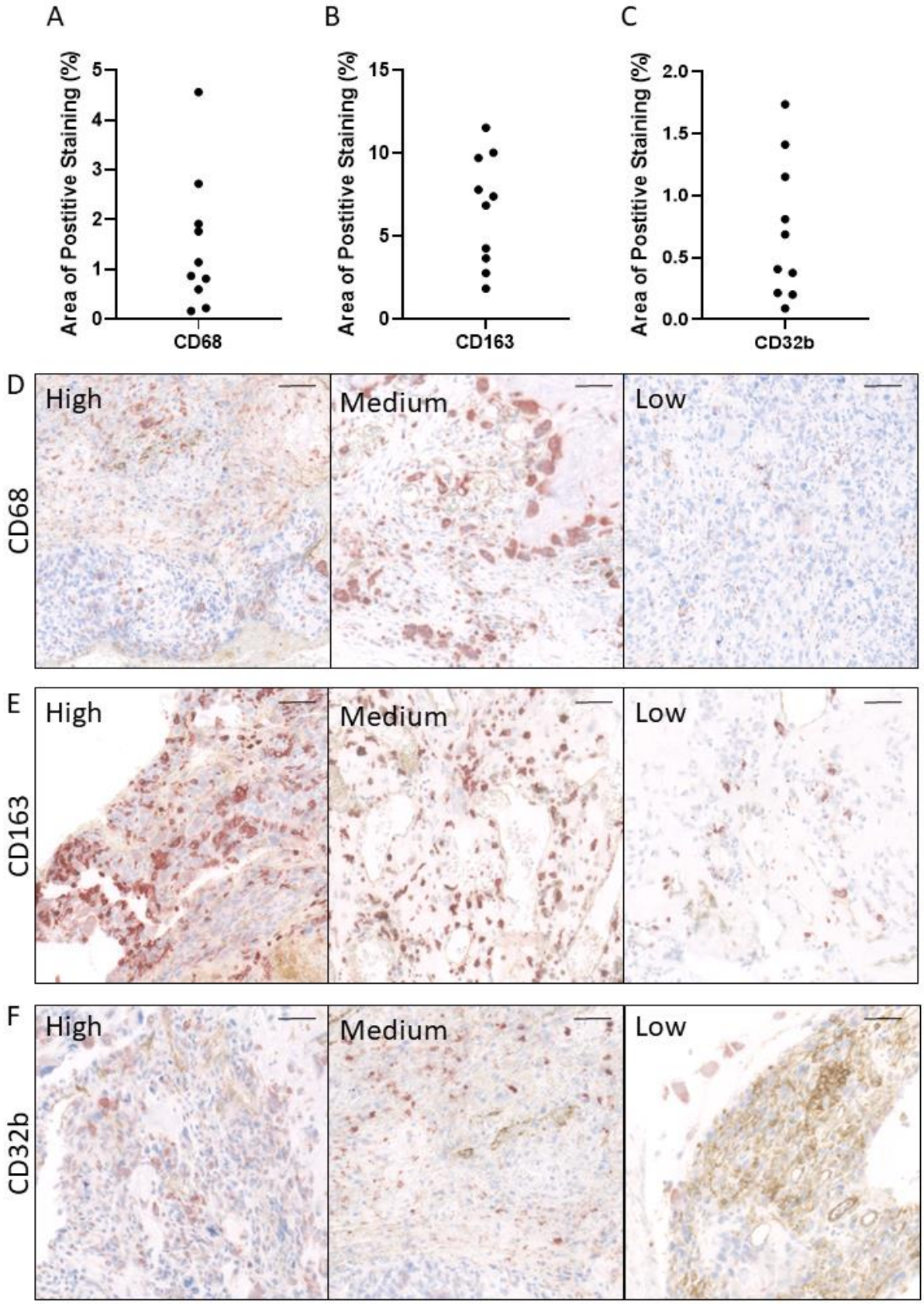

Figure 6-25. Multiplex analysis of CD68, CD163 and CD32b from osteosarcoma patient samples. *Area positive staining of (A) CD68, CD163 and CD32b from 10 osteosarcoma patient samples. (B) Representative images of high (>2.5%), medium (1.2-2.5 %) and low (<1.2%) levels of CD68*

staining. (C) Representative images of high (>8%), medium (5-8%), and low (<5%) levels of CD163 staining. (D) Representative images of high (>1%), medium (0.5-1%), and low (<0.5%) levels of CD32b staining. Scale bar= 100 µm.

The expression of CD105 was also analysed on the osteosarcoma patient samples (**Figure 6-26**). Here the amount of positive staining was split into two groups, high and low, with the high group indicating greater than 10% area positive staining of the tissue, while the low groups showed less than 5%, with some as low as 0.1%. Representative images of CD105 staining can be seen in **Figure 6-26**B, where there was a clear positive expression of CD105 staining (red) in the high image, but only a small amount of staining in the low image. There were even four patient samples which did not have any detectable staining, calculated at 0.1%.

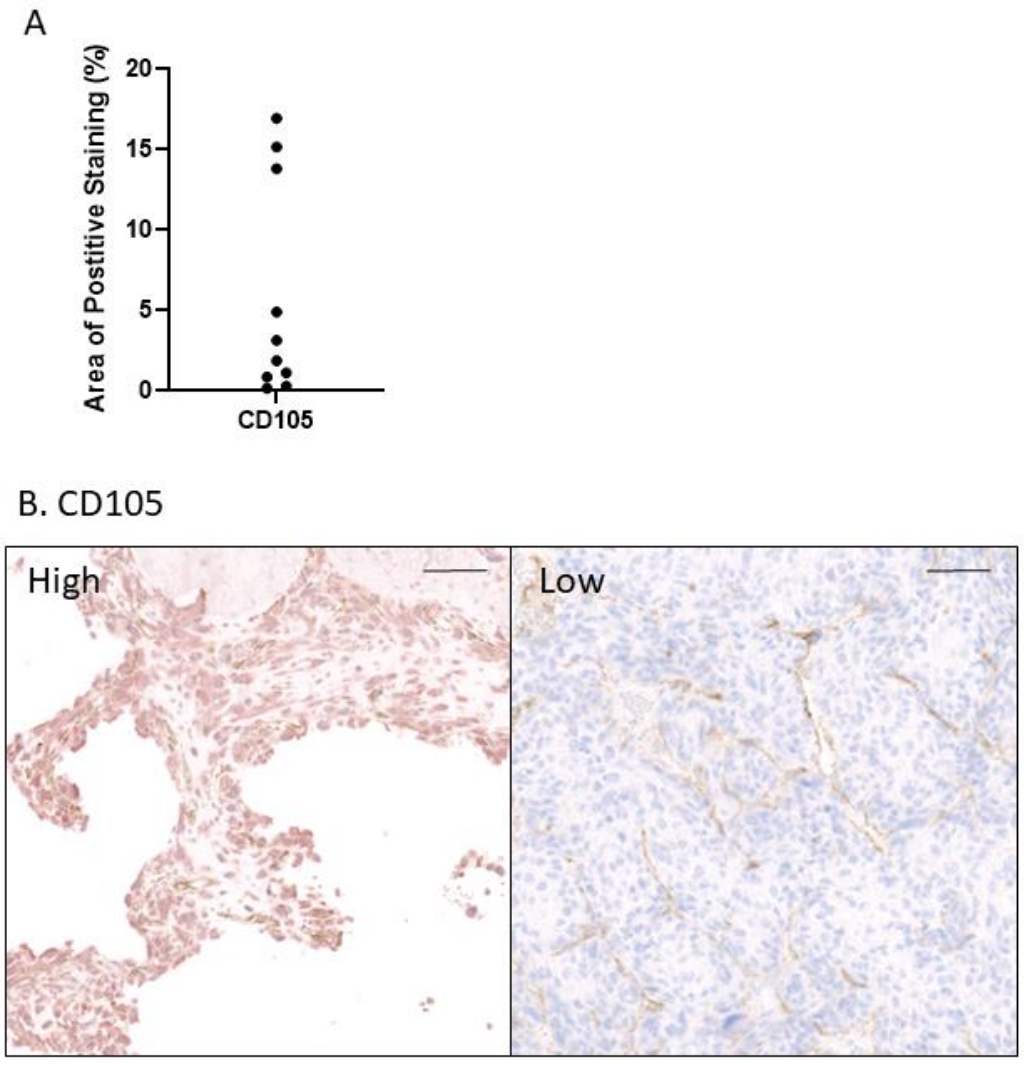

Figure 6-26. Multiplex analysis of CD105 staining from osteosarcoma patient samples. *(A) Area positive staining of CD105 from 10 osteosarcoma patient samples. (B) Representative images of high (>10%) and low (<5%) levels of CD105 (red) staining. Scale bar= 100 µm.*

Figure 6-27 shows the analysis of HIF1α and VEGF expression in the 10 osteosarcoma patients. HIF1α, a marker of hypoxia, and could also be separated into a high, middle and low level of expression. Only one patient sample had over 3% area staining, here classified as high, although it is lower than previously recorded data which showed HIF1α staining between 5 to 80% in osteosarcoma sections [261]. The middle group was classed as between 1 and 2%, while the low was below 1% total tissue area. Representative images of these groups can be seen in **Figure 6-27**C. The one patient sample with more than 3% expression showed large specific areas of HIF1α staining (in red), whereas in the middle and low groups the expression was over a broader area. VEGF, a marker of angiogenesis, was also analysed showing only 2 patient samples had high levels of VEGF, with the majority being under 3% of the total tissue. The representative images in **Figure 6-27**D also illustrated these large differences (in red), although there were similar patterns of staining between the samples. The samples with positive VEGF expression also demonstrated higher expression of HIF1α but did not correlate with any of the other markers analysed.

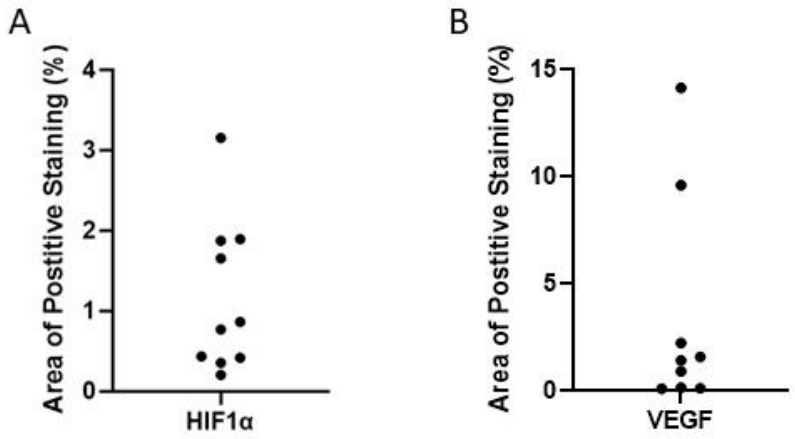

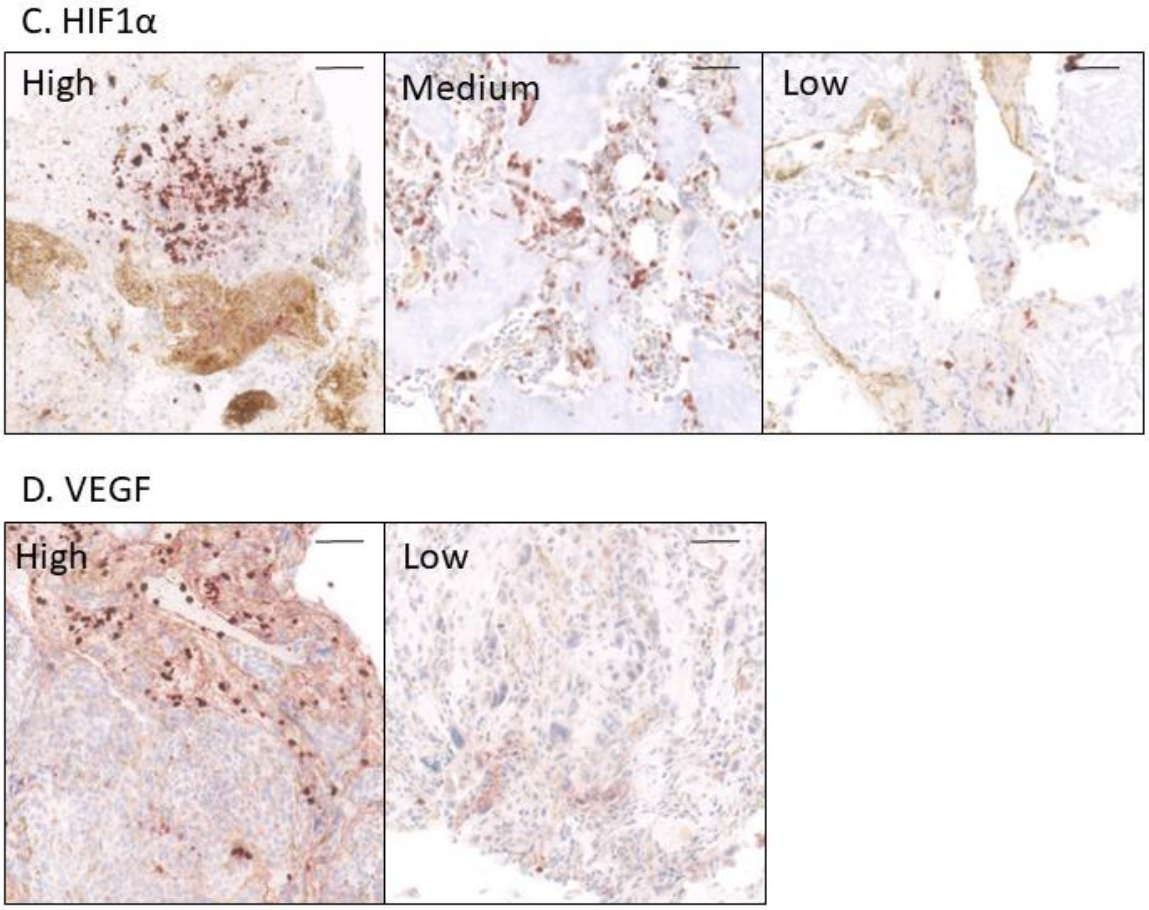

Figure 6-27. Multiplex analysis of HIF1α and VEGF from osteosarcoma patient samples*. Area positive staining of (A) HIF1α and (B) VEGF from 10 osteosarcoma patient samples. (C) Images of high (>3%), medium (1-2%) and low (<1%) levels of HIF1α staining. (D) Images of high (>5%) and low (<3%) levels of VEGF staining. Scale bar= 100 µm.*

Finally, STAT3, part of the IL-6/JAK signalling pathway, and its phosphorylated form, pSTAT3, were also analysed in the osteosarcoma samples (**Figure 6-28**). While the majority of previous stains could be clearly grouped into different levels of expression, STAT3 showed a wide range, but with less definition. A high level of STAT3 expression was broadly classed as representing more than 5% of the total area, where the highest sample reached 12% positive staining. There were also two samples which had no STAT3 staining, which was grouped into a low category. The remaining 5 samples ranged between 1 to 5% coverage. Representative images of these groups are shown in **Figure 6-28**C, where there were very clear differences in STAT3 signalling (in red). In contrast to all other stains pSTAT3 was only positive in two of the patient samples, with a very low average of 0.4% area of positivity. Interestingly, the two positive samples correspond to two of the higher STAT3 samples, but the pSTAT3 staining was seen in specific areas of tissue, (**Figure 6-28**D) which was less evident in the STAT3 images.

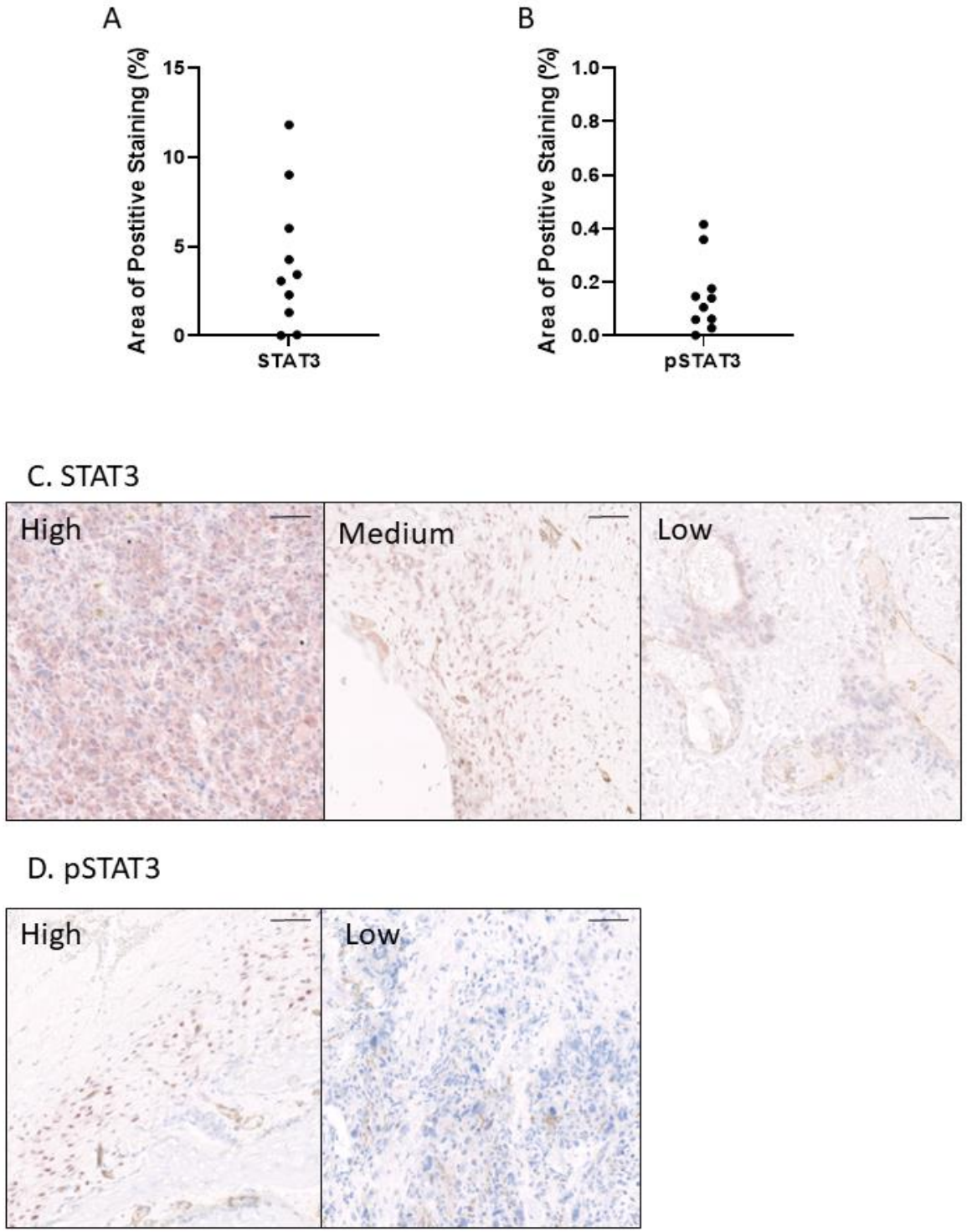

Figure 6-28. Multiplex analysis of STAT3 and pSTAT3 from osteosarcoma patient samples*. Area positive staining of (A) STAT3 and (B) pSTAT3 from 10 osteosarcoma patient samples. (C) Representative images of high (>5%), medium (1-5%) and low (<1%) levels of STAT3 staining. (D) Representative images of high (>0.3%) and low (<0.3%) levels of pSTAT3 staining. Scale bar= 100 µm.*

All the data for the 10 osteosarcoma samples was combined in heat maps to look for correlating patterns of staining (**Figure 6-29**). Generally, all stains were fairly low for the majority of the samples, although there was exceptions for most markers apart from pSTAT3. All patients underwent chemotherapy to treat their osteosarcoma, but it was unknown whether the sample was taken before or after treatment. This meant correlation between the tumour phenotype and patient treatment could not be inferred. The data was first separated by gender, and then organised by age, which ranged from 9 months to 17 years. There was no correlation found between the markers of interest and gender (**Figure 6-29**A).

When organised by age (**Figure 6-29**B), there was a small trend seen between an increase in age with an overall rise in the expression of multiple markers, although the specific markers depended on the patient sample. The exceptions to this were both the oldest and youngest patient samples, the 9 month male (M 9m) and 17 year old female (F 17Y). The youngest diagnosed patient (M 9m) had an overall consistently higher expression across all markers compared with other samples, while the oldest patient sample (F 17Y) had one of the lowest overall expression across the 10 markers. Two other samples also showed low overall expression, an 11 year old male (M 11Y) and a 12 year old female (F 12Y), which both showed a high level of osteocalcin, but very low levels of the other 9 markers. Analysis comparing overlapping positive staining for the multiple markers was not assessed due to time restrictions, this could generate further patterns of expression.

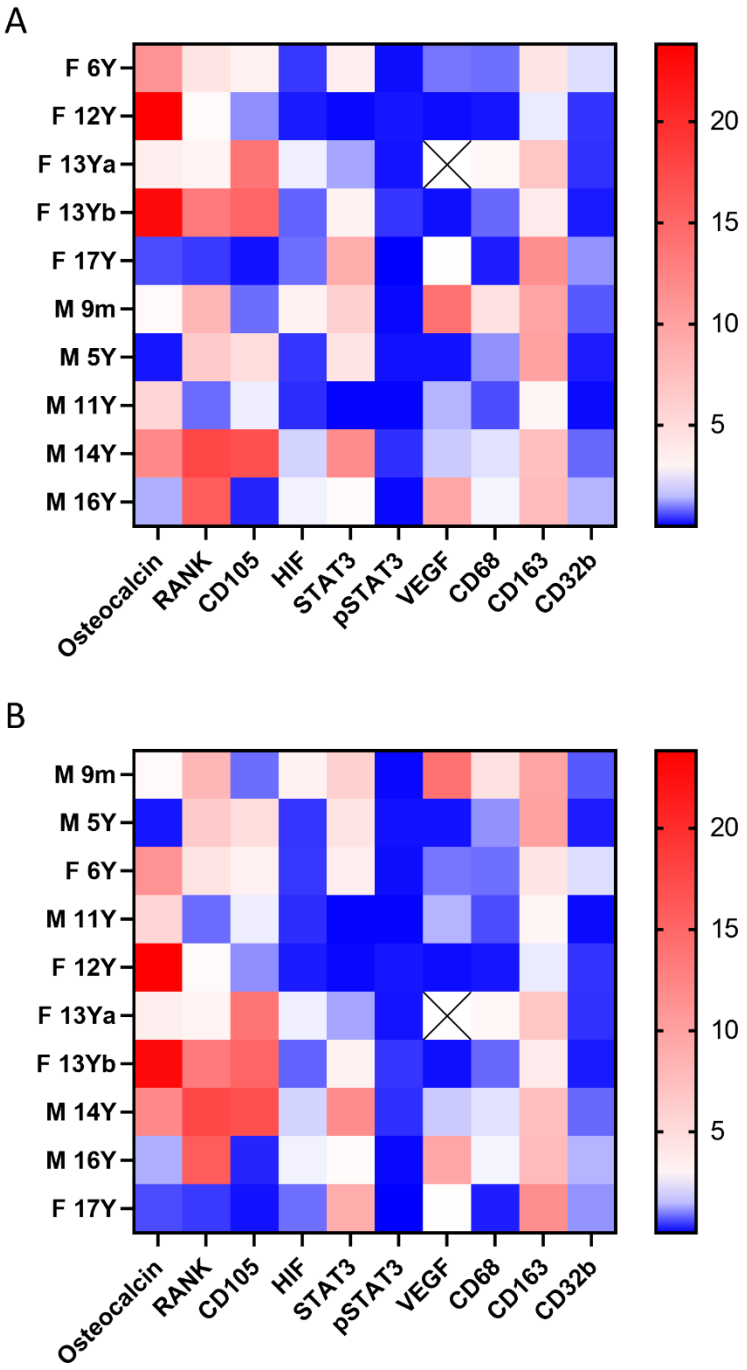

Figure 6-29. Comparative analysis of 10 markers of interest on 10 osteosarcoma patient samples. *Heat maps showing the percentage area positive of 10 different markers of interest including; osteocalcin, RANK, CD105, HIF1α, STAT3, pSTAT3, CD68, CD163 and CD32b, organised by (A) gender and (B) age.*

6.3 Discussion

After immunohistochemistry analysis of the bone models the key findings were:

- Optimal decalcification processes included 6% TCA embedded in OCT with a vacuum.
- Incubating different cell types in the bone models resulted in different characteristics.
- The drug Mifamurtide was successfully introduced to the bone core model, which resulted in changes in phenotype.

Comparison of the decalcification and embedding processes of the 3D model determined that optimal methods included the use of 6% (v/v) TCA, with OCT vacuum embedding before being sectioned on TOMO® slides (6.2 and 6.2.2). Different decalcification methods were performed based on literature analysis [245]. While no difference was found in immunohistochemistry staining for three of the methods, Krajian, TCA and EDTA (**Figure 6-5**), the choice of TCA decalcification was determined by the quicker preparation and decalcification time compared with the Krajian and EDTA methods. While paraffin embedding did result in more defined structures during staining, difficulty during sectioning meant it wasn't robust enough for further analysis. A pilot study performed in the lab attempted to resolve the issues found during paraffin sectioning by replacing the histoclear steps with chloroform, which did successfully overcome the problems during embedding. This suggested that there was an issue with the histoclear not removing all the ethanol prior to embedding in paraffin. Although paraffin sections were preferred due to their structure, and improved adhesion over the OCT samples, safety concerns with using chloroform consequently meant the use of OCT was continued.

The markers used for immunohistochemistry analysis included CD68, CD105 and RANK. Osteocalcin was also initially chosen for analysis, but optimisation could not occur within the timeframe. CD68, a macrophage marker, was used to identify MDMs inserted into the model as well as resident macrophages already present in the bone cores. CD105, also known as endoglin, is predominantly expressed on cells within the vasculature system particularly on proliferating endothelial cells [253] and on some mesenchymal stem cells [262]. This meant it could be used to assess successful vascularisation from the CAM membrane, as well as to determine whether the combination of cells inserted had affected angiogenesis. More importantly an increase CD105 has been heavily linked with endothelium of multiple tumours, suggesting there may be a link between CD105 and tumour angiogenesis [253, 263]. Finally RANK is mainly expressed on osteoclasts [264], the cell involved in bone resorption, although it has also been found on certain immune cells including dendritic cells and macrophages [265]. The combination of these three markers should give an indication of whether cell integration had been successful in the 3D bone models.

Immunohistochemistry analysis of both the CAM and long-term culture bone cores (6.2.3 and 6.2.4) have shown that the majority of the inserted cells remain within the defect region, suggesting there was limited early cell migration. While there wasn't strong evidence of cell migration, increased expression of these markers were seen in the bone core resident tissue, although more predominantly in the CAM than during long term culture. CD68 was increased in the MDM and triple-cell combination whole bone cores (**Figure 6-18**), which was expected as a macrophage marker, but it was also increased in the resident tissue of the bone cores, suggesting there was an increase in biological signalling. This was also seen in CD105 staining (**Figure 6-19**), which was increased in all bone cores except the control. These increases could be a result of biological signalling or also from cell migration, as while CD105 is a strong marker for endothelial cells, it has also been found on *in vitro* differentiated macrophages [266] as well as Saos-2 cells [267]. The very low levels of RANK signalling (**Figure 6-20**) were likely due to the depth of the section, while there was a small defect area at the top of the bone core, it wasn't far enough to show the whole defect area and consequently no inserted cells were identified. This supports the supposition that there was only a low level of cell migration during culture, enhancing the importance of sectioning in the right area. The CD68 stain for the long-term culture (**Figure 6-13**), was the only stain which conflicts with the contention of cellular migration or biological signalling. It showed that there were similar levels of CD68 expression in the tissue resident images for both the triple-cell combination and control bone cores. This could be a result of the lack of macrophage growth factors in the media, like M-CSF. While Saos-2 and HBMSCs are routinely grown in basal media this was not the case for the MDMs, and as such it could be causing MDM cell death and consequently a reduction in the CD68 stain. This was more evident in the resident tissue where there were fewer macrophages clustered together (**Figure 6-13**).

Bone slices were introduced to decrease the bone surface area to cell ratio, and aimed to improve the formation of the bone model. Unfortunately, during the insertion of cells, the smaller surface area and thickness resulted in cells travelling through the trabecular bone and remaining in the cell culture plastic, reducing the overall cell number inserted. This meant that not all bone slices had the same number of cells, which was evident in the image analysis where it resulted in large variation (6.2.5). Also, the removal of resident bone marrow stromal cells by hydrogen peroxide means any effect on resident cells could not be assessed. Consequently, as expected increased levels of CD68, RANK and CD105 were found in the triple combination compared with the control, in both CAM and long-term cultured bone slices (6.2.5).

The inclusion of Mifamurtide in the 3D bone core model resulted in a decrease in CD68 (**Figure 6-18**) and RANK (**Figure 6-20**) signalling, while CD105 (**Figure 6-19**) only showed a reduction in signalling when the bone cores were incubated in Mifamurtide after the CAM incubation.

Previous *in vitro* experiments (**Appendix 2**) indicated that the Mifamurtide used in this work resulted in death of MDMs, and this could explain the reduction in CD68, a macrophage marker. It could also explain the reduction in RANK, as osteoclasts share a common lineage to macrophages and so may be affected in the same way. These results were not expected as Mifamurtide has been shown to activate monocytes and macrophages [268], which suggests there would have been an increase in CD68 and potentially RANK. The liposomal form of Mifamurtide was designed to target monocytes and macrophages as the liposome needs to be phagocytosed for the drug to be released. While previous *in vitro* research has used Mifamurtide at varying concentrations up to 100 µM [195], early research using the liposomal form indicated concentrations as low as 1.67 µg/ml [269] for activating monocytes. This should suggest that the concentration used in this assay of 1.6 µg/ml should result in activation of macrophages. In addition, the Mifamurtide drug was initially reconstituted in 0.9% (v/v) sodium chloride for patient injection, and then further diluted in basal media not containing macrophage growth factors including M-CSF for these experiments. The lack of growth factors could also have caused cell death of the macrophages, which has previously been found in long term macrophage cultures after removal of M-CSF [270]. While the number of CD68+ macrophages were decreasing there were still visible cells found in the Mifamurtide treated bone cores, suggesting it did not affect cell death of the other inserted cells (**Figure 6-18**).

The reduction of CD105 in only one of the Mifamurtide groups was also unexpected (**Figure 6-19**), but it implied that there was either an overall decrease in endothelial cells, or more specifically a decrease in their proliferation, as CD105 is strongly expressed on proliferating endothelial cells [253]. Alternatively, as CD105 can be used as a marker for all cells inserted, there could be an overall increase of cell death. While there was a decrease in CD68 and RANK expression alongside CD105 in the Mifamurtide treated bone cores after CAM incubation (6.2.6), cells can still be seen in the defect area, suggesting the reduction was not due to extensive cell death. The first group of Mifamurtide treated bone cores was carried out before CAM incubation, and consequently before vascularisation. This meant Mifamurtide did not affect the endothelial vascular cells that were activated during the CAM culture, but they can be affected by Mifurmatide after the CAM culture. This supports the potential hypothesis that the reduction of CD105 when the bone cores were cultured in Mifamurtide after the CAM, could be caused by inhibition of endothelial cell proliferation. Further assays would need to be performed to determine how this could affect the utility of the 3D model to test osteosarcoma drugs and therapies.

Unfortunately, while quantitative analysis was carried out and determined for these three antibodies of interest, further markers could not be analysed due to time restrictions, limiting the comparative analysis that can be combined. Osteogenic differentiation and bone mineralisation

are prognostic factors in osteosarcoma development, as such osteogenic stains like ALP and osteocalcin, are important immunohistochemistry stains. These stains were initially optimised during the decalcification comparisons and should be the carried out in any future experiments. A panel of markers were initially chosen to assess the 3D bone model based on published literature, but to better determine whether the 3D bone model replicated the osteosarcoma tumour environment, these markers were analysed on osteosarcoma samples. To do this a multiplex immunohistochemistry method was chosen, as it meant only two sections were needed, allowing for analysis of multiple markers on the same cell to assess whether overlapping signalling occurred.

All markers analysed (**Figure 6-21** and **Figure 6-22**) were linked to osteosarcoma characterisation, so the markers were stained in combination to understand more complex biological interactions and signalling. Six of the antibodies were used to locate specific cells of interests. These included osteocalcin, which is expressed by osteoblasts, and has been previously found at high levels in osteosarcoma samples [249]. Although overall expression of osteocalcin was below 22% of total tissue analysed for the osteosarcoma samples tested (**Figure 6-24**), the majority showed positive expression of osteocalcin, correlating with data found in the literature. RANK is expressed by osteoclasts, which can be upregulated in the osteosarcoma environment due to an increase in bone resorption to allow for tumour growth [250]. RANK analysis of the 10 osteosarcoma patient samples (**Figure 6-24**) showed similar results found in the literature where an increase in RANK was observed in osteoclasts and their precursors, which were found in specific areas of the tumour microenvironment [250]. CD105 is an endothelial and mesenchymal stem cell marker, which has been previously linked with an increase in tumour angiogenesis [253, 263]. Although there was variable expression in CD105 for the osteosarcoma samples analysed (**Figure 6-26**), increased levels were found in three samples, which may correlate with increased angiogenesis, but further vascular markers would be needed to determine this.

Three macrophage markers were also analysed including CD68, CD163 and CD32b. While CD68 is an important general marker for macrophages, it doesn't allow for specificity of macrophage polarisation. A combination of CD68, CD163 and CD32b was used to compare whether macrophages were polarised towards the M2-like phenotype. There have been conflicting data on how the polarisation of macrophages links with osteosarcoma prognosis [100, 271], but they have been found to play key roles in the development of osteosarcoma and other cancers. Although M1-like macrophage markers could not be included in these assays, the combination of CD32b and CD163 were analysed alongside CD68 to target M2-like macrophages [256-258]. Overall, the level of CD68 remained low at less than 5% of all total tissue, located in specific areas within the samples (**Figure 6-25**). Both CD163 and CD32b showed no particular patterns of staining

compared to the CD68 staining after analysis as a single stain (**Figure 6-25**), this was most likely due to alternative CD163+ [259] and CD32+ [260] immune cells found within the osteosarcoma microenvironment also being included in the analysis. Multiple staining analysis would allow the removal of CD68-CD163+ or CD68-CD32b+ cells from the data, focusing on only the CD68+ macrophage cells. However, due to a limiting amount of time, dual staining of the multiplex analysis could not be analysed, and consequently the number of M2-like macrophages could not be compared.

Multiple marker analysis could not be assessed for any of the antibodies used, including the remaining four markers; HIF1α, VEGF, STAT3 and pSTAT3, due to time limitations. An increase in hypoxia has been reported in both the bone and tumour microenvironment, with previous studies showing HIF1α overexpression in osteosarcoma is linked to increased cell proliferation and invasion [255]. This was not seen in the osteosarcoma samples stained, which all had a generally low level of HIF1α expression (**Figure 6-27**). VEGF is a marker of vascularisation, acting as a stimulator for new blood vessel growth, which has been linked to increased growth and metastases in solid tumours [254, 272]. Studies have shown that VEGF can be used as a prognostic factor in osteosarcoma patients, with increased VEGF expression linked to a higher histological grade and consequently a poorer prognosis [273]. While both VEGF and CD105 are linked to vascularisation, they do not have correlating staining in the 10 osteosarcoma samples tested, where the patient samples that showed an increase in VEGF had two of the lowest CD105 expressions (**Figure 6-29**).

STAT3 is part of the IL-6/JAK signalling pathway. Activation of this pathway can lead to the phosphorylation of STAT3, which has been linked to onset and growth of a variety of cancers [251, 252]. STAT3 overexpression has also been correlated with the progression and poor prognosis of osteosarcoma [274]. Interestingly the osteosarcoma patient samples had very low to no positive pSTAT3 staining, with variable STAT3 expression (**Figure 6-28**D and C). The low pSTAT3 staining could suggest these samples are from patients with better prognosis, or patients who had all already undergone chemotherapy treatment before the sample was taken. Without knowing this data this hypothesis cannot be confirmed. Further analysis assessing the number of cells positive for multiple markers of interest is important in understanding the microenvironment of the osteosarcoma patient samples and would be a priority for any future work.

The three markers analysed on the 3D bone core models, RANK, CD105 and CD68, can be broadly compared against the multiplex data generated from the 10 osteosarcoma patient samples. The RANK staining of the patient samples ranged from approximately 0.5% to 18% total area staining, in comparison the 3D bone core model indicated approximately 3% RANK expression in the triple

combination. Although no established osteoclasts were found in the bone core sections, precursors of osteoclasts could account for the level of this marker, although specific regions of staining seen in the multiplex analysis were not present in the 3D bone cores. The expression of CD105 in the 3D bone core models remained low, which was similar to 7 of the osteosarcoma patient samples which showed less than 5% total expression. The remaining three patient samples had a high expression of CD105 (approximately 15%), which differed from the 3D bone core analysis. Finally, the percentage of CD68 positive cells in the triple combination 3D bone core models was approximately 5% total staining. This was similar to the multiplex analysis of CD68, where all 10 patient samples were under 5% CD68 positive staining, although the 3D bone core staining was found over a broader area compared to the specific regions found in the osteosarcoma patient samples. While a useful tool for developing and validating the 3D bone model, 10 samples alone were not enough to draw any conclusions on phenotypic expression of osteosarcoma patients, and should be assessed alongside published literature to quantify the development of the 3D multicellular model of osteosarcoma.

During the development of a 3D multicellular model of osteosarcoma it has been shown that combining bone cores with incubation on the CAM was optimal for cellular growth and development. This method resulted in changes in phenotype depending on the combination of cells inserted into the model, and has also been used to test two methods of drug delivery. Future work needs to focus on increasing the characterisation of the 3D bone core model, particularly on osteogenic markers, and comparing the resulting data to human primary samples. This will allow for future optimisation of the cellular composition inserted into the 3D bone model.

Chapter 7 Discussion

The main hypothesis for the project reported in this thesis was that a functional 3D model could be engineered to replicate aspects of the osteosarcoma tumour microenvironment, which then could be used to test new drugs and therapeutic treatments. The development of this model included combining three cell types of interest; HBMSCs, macrophages and an osteosarcoma cell line, in a human bone scaffold. Following that, the model was cultured, assessed, and quantified using μCT and histological analysis.

The aims were quantified by:

1. Characterising the cells of interest, optimising growth and differentiation conditions prior to 3D analysis. The findings were:
    - Anatomical origin of HBMSCs is important in their functionality, with differences in osteogenic, adipogenic and chondrogenic differentiation of cells from the femoral diaphysis and femoral epiphysis.
    - Tri-lineage differentiation of two osteosarcoma cell lines indicated marked differences in their ability to differentiate down the osteogenic, adipogenic and chondrogenic pathways.

2. Phenotyping monocyte derived macrophages and optimising their differentiation from different cell sources prior to 3D analysis. The findings were:
    - Macrophage differentiation from human bone marrow cells and PBMCs showed no phenotypic differences after isolation and CD14+ cell sorting,
    - Macrophage polarisation also showed no significant phenotypic differences in M1-like and M2-like macrophages differentiated from human bone marrow and PBMCs.

3. Developing a 3D multicellular bone model of osteosarcoma to investigate bone formation and resorption of the osteosarcoma environment. The findings were:
    - Integration of human bone onto the CAM assay resulted in successful avian blood vessel infiltration, with viable human cells recovered in further histological analysis, demonstrating graft viability after *in ovo* implantation.

- Micro-CT analysis of the bone models resulted in no significant change in bone formation or resorption following either CAM implantation or long-term culture in conditioned media.

4. Investigating the cellular and extracellular interaction of the 3D bone models via histological analysis. The findings were:
    - Histological analysis of the bone models resulted in significant differences in CD68, CD105 and RANK expression between the triple cell combination and their single cell type controls, demonstrating functional interaction of cells in this 3D bone model.
    - Mifamurtide was successfully introduced into the 3D bone model, resulting in changes of CD68, CD105 and RANK expression, suggesting two potential routes to validate new drugs and therapies.

7.1 Cellular Selection for the Establishment of a 3D Bone Model

A critical requirement for the success of the development of a 3D bone model of osteosarcoma, was the evaluation and consequent optimisation of the cells to be incorporated. There are many different cell types that are found in the osteosarcoma microenvironment that could be incorporated into the development of a 3D model, some of these were grouped into, osteosarcoma cells; including Saos-2 and MG63 osteosarcoma cell lines, cells found in the bone environment; including stromal cells and osteoblasts, and finally the third group discussed in 7.2 involved myeloid derived cells; including macrophages and osteoclasts. Tri-lineage differentiation of two osteosarcoma cell lines, Saos-2 and MG63, resulted in diverse characteristics, with Saos-2 showing an increased level of osteogenic differentiation (**Figure 3-2** and **Figure 3-4**), while MG63 cells showed a high level of adipogenic differentiation (**Figure 3-5**). This is different to previously published data by Mohseny et al [185], who analysed 19 different osteosarcoma cell lines for tri-lineage differentiation, and determined that MG63 cells showed only chondrogenic differentiation, while Saos-2 was able to differentiate down the chondrogenic and adipogenic pathways. Differing methodology can explain the variation found in the tri-lineage differentiation. Although in the published study the Saos-2 cells were not classed as osteogenic, the ALP basal rate of Saos-2 cells were already very high [275], thus could qualify them as osteogenic. The culture also only extended for 3 weeks before they were analysed with alizarin red, which quantifies mineralisation, compared with the 4 weeks in this thesis (2.2.9). Different results on

Saos-2 and MG63 adipogenic differentiation can also be explained by altered methodology, with both the paper and this thesis using different assorted cytokines and growth factors for adipogenic differentiation (2.2.10). Osteosarcoma tumours generate spontaneous bone growth and mineralisation as such the Saos-2 cells were selected for use in the development of a 3D bone model due to the higher osteogenic potential.

Stromal cells are an important part of the osteosarcoma tumour microenvironment. Characterisation of bone marrow by various imaging techniques have denoted specific areas of 'yellow' and 'red' bone marrow in the femoral epiphysis and femoral diaphysis/metaphysis respectively [66, 183]. Currently, no previous research has characterised the cells at these different skeletal locations at a cellular level. In order to try and replicate the stromal phenotype found in osteosarcoma patients, tri-lineage differentiation capability was assessed between HBMSCs from the FD and FE regions of the femur, alongside fetal bone marrow progenitor cells. Initial analysis of the fetal bone marrow cells showed low osteogenic potential (**Figure 3-18**), this alongside the irregular sample collections meant they were not appropriate for use in the 3D bone model. Comparing the HBMSCs from the FD and FE locations of the femur demonstrates distinct differences in osteogenic, chondrogenic and adipogenic differentiation. There was an increase in osteogenic (**Figure 3-3** and **Figure 3-4**) and chondrogenic (**Figure 3-6**) differentiation in the FD HBMSCs compared with the FE, which were also found to be at different stages of adipogenic differentiation (**Figure 3-5**). With these significant differences found in the femur, it further questions how similar HBMSCs are in other bones within the body. While adolescent osteosarcoma is generally found in the long bones [17], there are patients who develop osteosarcoma in axial locations, like the jaw and pelvis. If HBMSCs found in these locations have similar characteristics to the 'yellow' or 'red' bone marrow found in the femur, the importance of stromal cell characteristics could be evaluated. This could be particularly relevant for studying the initial incidence of osteosarcoma, particularly as many cases occur at the growth plate during 'red' to 'yellow' bone marrow conversion [276]. Due to the higher osteogenic potential of the FD HBMSCs these cells were used during the development of the 3D bone model of osteosarcoma. Osteoblasts are important cells found in the bone microenvironment, essential for bone growth, suggesting they could play a significant role in the osteosarcoma microenvironment. Unfortunately, due to low retrieval numbers and slow proliferation rate it was not realistically feasible to include these cells in the 3D bone model. Of all the cells initially analysed the osteosarcoma cell line Saos-2 and the FD HBMSCs were chosen to be included in the 3D bone model due to their enhanced osteogenic potential compared with the MG63 and FE HBMSCs respectively.

7.2 Myeloid Selection for the Establishment of a 3D Bone Model

Myeloid cells were also assessed for inclusion in the 3D bone model, these included macrophages and osteoclasts. Macrophages have been found to play a role in osteosarcoma growth and metastasis, with an increase in macrophages, particularly M2-like polarised macrophages, correlating to poorer prognosis [100]. They are also the target of the osteosarcoma drug Mifamurtide, which stimulates the macrophages in a pro-inflammatory manner, with the aim to activate an immune response against the tumour [28]. While multiple studies have assessed the phenotype of human macrophages differentiated from PBMCs [277], very few studies have analysed macrophages differentiated from human bone marrow [217]. In these experiments similar characteristics were seen between PBMC and human bone marrow derived macrophages after CD14+ isolation (**Figure 4-9**). Initially, bone marrow cultures were not CD14 selected and so also contained contaminating stromal cells (**Figure 4-1**), which has also been found in mouse bone marrow derived macrophages [222]. These contaminating stromal cells affected the overall percentage of the macrophage markers including CD14, CD11b and HLA-DR, but these differences were negated after CD14+ cell isolation (**Figure 4-9**). Polarisation of M1-like and M2-like macrophages were also compared between the PBMC and bone marrow cells (4.2.4), again resulting in similar expression of polarisation markers including; CD38, CD40 for M1-like macrophages and CD11b for M2-like macrophages. Mouse studies have shown macrophages derived from different organs, including the peritoneal cavity, bone marrow and spleen, show different phenotypes with different biological functions [278]. These differences were not seen between the human PBMCs and bone marrow, suggesting a level of homogeneity between these macrophages and monocytes. As monocytes originate from stem cells in the bone marrow this could explain the similarity of the macrophage phenotypes derived from the PBMCs and human bone marrow. PBMC derived macrophages were chosen for use in the 3D bone model due to the greater yield from one sample compared with bone marrow derived macrophages.

Osteoclasts are involved in bone resorption and are generated from a monocyte/macrophage lineage. Research has shown that osteoclasts are manipulated in the tumour microenvironment as the resorption of bone produces growth factors that enable proliferation of the tumour [59]. Osteoclast differentiation was compared between PBMCs and human bone marrow cells for potential inclusion in the 3D model (4.2.6 and 4.2.7). While differentiation from a heterogenous population was optimal for the differentiation of bone marrow cells (**Figure 4-17**), after isolating CD14+ cells a larger number of osteoclasts were generated from PBMCs compared with the bone marrow (**Figure 4-18**). While both cell sources showed osteoclast differentiation, further assays comparing the resorption ability of these cells needs to be conducted to confirm these osteoclasts were functionally active. Due to the lack of data on the activation of the osteoclasts, these cells

were not included in the development of the 3D bone model, apart from any already present in the bone structure. Alternatively, bone cores and slices were seeded with macrophages and HBMSCs, and cultured in osteoclast media to generate a positive control of bone resorption for µCT analysis. The generation of osteoclasts could prove beneficial for future development of the 3D bone model, but the combination of macrophages, HBMSCs and Saos-2 cells were optimised for use in the development of this initial 3D bone model.

7.3 Micro-CT Analysis of the 3D Bone Model

A range of scaffolds and different structures have been developed for studying cancer models [156]. Unfortunately, the majority of scaffolds still remain biologically inactive, not providing mechanical signals found in the bone microenvironment [156, 157]. For the development of a novel 3D model of osteosarcoma, cores and slices of human bone, taken from the femoral head of patients who underwent hip replacement surgery, were used as the structural component. This not only replicated the formation of bone, but also meant structural and stromal cells already present in the human bone environment, including osteoblasts and osteoclasts, were already included in the model. In this thesis bone formation and resorption was assessed by measuring changes in the bone structure after long term incubation and inclusion on the CAM. Previous research has shown the CAM is an effective way of measuring bone formation in bone cylinders [177]. By using a resolution of 18 µm the µCT scans were able to detect early stages of bone regeneration, while limiting the number of x-rays used. Typically, bone regeneration of an *in vivo* defect is analysed by measuring net bone volume within a region of interest [279, 280]. In contrast, µCT analysis conducted in this thesis measured the entire bone core or slice before and after incubation, this allowed for a relative change in bone as an output for each individual sample. This also meant that any variations in length or initial density between samples in the same group did not skew the resulting data. A region of interest encompassing approximately 1mm around the defect was also analysed for structural changes localised to the defect area.

The µCT analysis only resulted in small changes in bone structure, the majority of which was not significant (5.2). Robust positive controls for bone formation and resorption were not generated (5.2.7 and 5.2.10), and would need to be achieved for further quantitative analysis of the 3D bone model. While osteogenic and mineralisation conditioned media were ineffective in producing mineralized osteoid, successful bone formation has been previously quantified using a collagen sponge with BMP2 in human bone cylinders [177]. To generate a positive control for bone resorption, optimised osteoclast differentiation with long term incubation could be effective, as the bone models attempted may not have been in culture long enough for effective osteoclast activation and resorption to occur. Other methods to assess whether early levels of osteoid

deposition occurred prior to mineralisation, could be more applicable to the quantification of this model. This could include scanning the model at a higher resolution, but this comes with an increased x-ray dose as well as a longer exposure time, which could affect the viability and growth of the cells. Alternatively culturing CD14+ PBMCs in osteoclast media for a longer incubation time may also result in generation of biologically active osteoclasts as suggested in 4.2.6. While histological analysis can be used to look at bone formation and bone resorption in parallel, µCT analysis of the bone models included both formation and resorption as a single measurement e.g. percentage bone volume.

The selection of HBMSCs and Saos-2 cells inserted in this model were chosen in part due to higher levels of osteogenic potential during 2D characterisation, which may have enhanced osteoid deposition and consequent mineralisation. A chick embryo skeleton initiate's mineralisation over an 8-9 day period roughly 11 days post fertilisation [281]. This means an increase in bone model mineralisation would be expected over this time period. Any mineralisation could be limited by an initial resorption phase, which has been found in bone grafts known as creeping substitution. This is where cortical bone grafts were found to be vascularised by an initial osteoclast resorption phase preceding bone formation [282]. In these models' osteoclast activity would also be expected at early time points, due to osteoclast mediated removal of dead bone tissue generated by the formation of the bone cores [283]. The potential early osteoclast activity found in previous studies using the CAM, may also have been affecting remodelling in the 3D bone models. An expected overall increase in bone formation could have been inhibited by initial bone resorption. The main success of the CAM was the integration and vascularisation of the bone cores (**Figure 5-1**), which was not possible in bone cores and slices incubated in long-term culture. Consequent quantification analysis of the long term cultured bone models resulted in few differences for CD68, CD105 and RANK signalling (discussed in 7.4), with no evidence of bone formation or resorption during µCT analysis. Bone cores and slices cultured on the CAM did show initial differences. As bone slices were smaller and lighter than bone cores they generally integrated onto the CAM at the window they were inserted, whereas the heavier bone cores always travelled towards the bottom of the egg, which occasionally resulted in a lack of vascularisation.

7.4 Histological Analysis of the 3D Bone Model

In this thesis biological and cellular changes of the 3D bone models were assessed by immunohistochemistry techniques with the aim to replicate characteristics of the osteosarcoma microenvironment. Here differences were found in CD68, CD105 and RANK expression between the bone models incubated with combinations of HBMSC, Saos-2 cells and MDMs, and in those treated with and without Mifamurtide (6.2). The bone models were assessed for CD68, CD105 and

RANK expression, this allowed for the quantitative analysis of macrophages (CD68) and osteoclasts (RANK). While CD105 was initially included for use as a marker of vascularisation, research has shown CD105 is expressed on all the cells inserted into the model, this could allow it to be used as a general marker to follow cell migration. A limitation of the immunohistochemistry analysis was the lack of ability to accurately distinguish the migration of the inserted cells through the bone models. Initial pilot experiments stained the inserted cells with cell tracking dyes, including CSFE (Thermofisher, UK) and a range of Vybrant dyes (Thermofisher, UK), which labelled the cells without affecting their function or viability. Unfortunately, the resulting fluorescence was found to be stripped during the embedding procedures. The use of other cell viability dyes could be suitable to overcome this limitation, or alternatively the Saos-2 cell line could be transfected to express green fluorescent protein (GFP), although this would not be suitable for the primary HBMSC and macrophage cells, which are harder to transfect [284, 285]. Locating migrating cells in a 2D section of the model would allow us further understanding of the movement of our individual cell types, but as the model is 3D it would be more effective to investigate cell migration with the use of a 3D imaging unit like the IVIS Spectrum imaging system (Perkin Elmer). This system locates bioluminescence and fluorescent signalling from the cells and presents it on a 3D display.

Previous studies have evidenced biocompatibility between the CAM and a xenograft implant, with no avian immune response to the implantation of human bone and skin [177, 286, 287]. Evidence has also shown there can be primitive immune responses to implanted cells and tissue, although not bone related [288, 289]. A main limitation when using the CAM in this thesis, is the inability to easily distinguish between the host avian tissue and the graft human tissue, most likely due to cross-reactivity of antibodies between the species. This issue can be circumvented by the use of genetically modified chick embryos ubiquitously expressing GFP under a phosphoglycerol kinase promoter [290]. This allows the evaluation of GFP alongside a marker of interest, to determine if they are of avian or human origin, while also showing any interaction of avian and human cells, for example if the inclusion of macrophages has introduced an avian immune response in the bone model. The use of the GFP eggs for the CAM assay would also answer the question of migration, whether increases of CD68, CD105 and RANK+ cells in the resident tissue of the bone cores (6.2.3) were a result of inserted cell migration, or are avian in origin. While the fertilised eggs used in this thesis were not genetically modified to express GFP, we can still assess whether differences in our immunohistochemistry analysis were a result of the human cells. With the exception of CD68 (**Figure 6-10** and **Figure 6-18**), very low to no CD105 (**Figure 6-11** and **Figure 6-19**) and RANK (**Figure 6-12** and **Figure 6-20**) staining was found in the control bone cores in all experiments. An increase in CD105 and RANK could be seen in the resident tissue of bone cores after insertion of cells (6.2.3), which suggested there was either a biological response to the cells

inserted or they migrated through the bone core, although an indirect avian effect cannot be ruled out. The inclusion of a general human marker, for example HLA expressed on all nucleated human cells, would assess the effect of the human / avian cellular interaction occurring in the 3D bone models incubated on the CAM.

Further histological staining of the 3D bone models is important for any future work, particularly looking at osteogenic differentiation and matrix deposition, which are early markers for bone mineralisation, characteristic of osteosarcoma patients. These include biochemical staining like ALP, as well as immunohistochemistry staining of particular markers including Collagen I and osteocalcin. Further mineralisation staining methods, including Von Kossa which stains calcium deposits, cannot be performed as the bone models are decalcified before embedding. Resin embedding of the bone cores negates the need for decalcification, although it is a more expensive and skilled procedure. Ten markers of interest were initially selected for use in histological quantification of the 3D bone models, to compare their homogeny to the osteosarcoma microenvironment, although they were not all tested. These markers were imaged on ten osteosarcoma patient samples following multiplex immunohistochemistry staining (6.2.6). While single stain analysis didn't result in correlated changes between the osteosarcoma samples across the 10 markers analysed, dual and multiple overlapping stains can be quantified. This will allow for a standardised, highly reproducible and efficient quantitative analysis, and will be important in any future development of the 3D multicellular bone model of osteosarcoma.

7.5 Final Remarks

A preliminary 3D multicellular model of osteosarcoma has been developed which has the potential to be used to test new drugs and therapies. It has been shown that multiple cell types can be combined in a 3D human bone scaffold, cultured on the CAM and remain viable (6.2). Ongoing analysis would need to continue to optimise the 3D bone model, including a more detailed immunohistochemistry panel in line with a more in depth analysis of osteosarcoma patient samples. Positive µCT controls for bone formation and resorption would also need to be developed, to more accurately determine any bone remodelling response of the 3D bone models. Future experiments will also need to be conducted to optimise the different aspects affecting the osteosarcoma microenvironment. This includes optimisation of cell number for the Saos-2 cells, HBMSCs and MDMs in comparison to each other, as well as determining whether any 'pre priming' conditions are more representative of the osteosarcoma microenvironment, for example culture in osteogenic media or in a hypoxic environment.

Although there are conflicting evidence, research has shown there is an increased number of M2-like macrophages in the microenvironment, which correlate to a poorer prognosis for the patient.

Thus, it would be important to characterise any differences when M1-like and M2-like macrophages are included in the 3D bone models, alongside the HBMSC and Saos-2 cells. This would allow us to investigate whether an increased number of M1-like macrophages, which are pro-inflammatory in nature, induce an immune response in the CAM. In initial 2D experiments we determined that, of the two HBMSC types, FD cells were more osteogenic than FE cells, but this was determined after culturing in osteogenic media. In these initial 3D bone model experiments that were analysed by immunohistochemistry, the HBMSCs included were cultured in basal media. To increase osteogenic potential of the 3D bone model, the HBMSCs could be cultured in osteogenic media prior to their insertion in the 3D bone core model alongside the Saos-2 and MDMs.

Finally, the method of drug testing would need to be optimised for therapeutic effect. In this thesis we suggested two possible routes (6.2.6), incubation of the drug prior to CAM implantation, although this would be more useful for targeting early cellular responses to the drug of choice before vascularisation occurs. Or alternatively, incubation of the bone core in the drug after CAM implantation, which would be arguably more clinically relevant as the 'tumour microenvironment' would be further developed and representative after vascularisation. While further optimisation is needed we have established that the 3D multicellular bone model is a viable method of testing new drug and therapies targeted at osteosarcoma.

Appendix A Primer Efficiency

ACTB

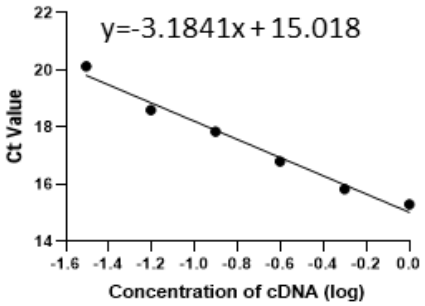

Efficiency: 2.061, 106%

ALPL

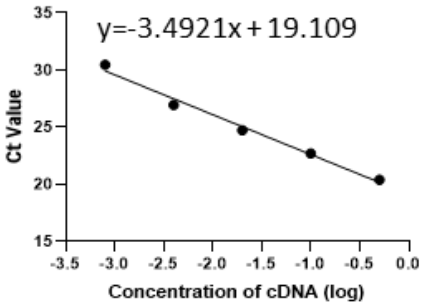

Efficiency: 1.934, 93%

COL1A1

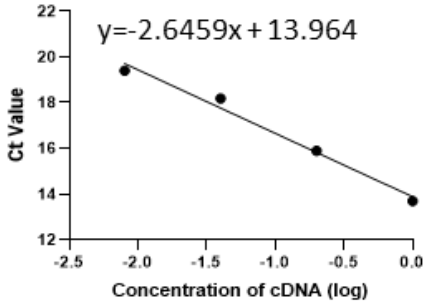

Efficiency: 2.387, 138%

PPARγ

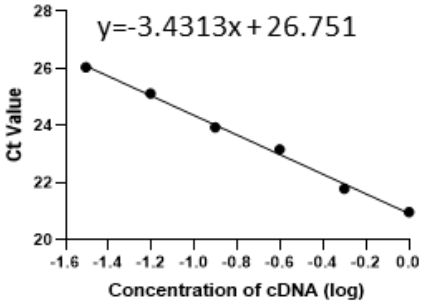

Efficiency: 1.957, 96%

FABP4

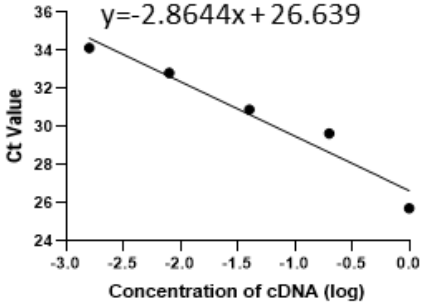

Efficiency: 2.234, 123%

SOX9

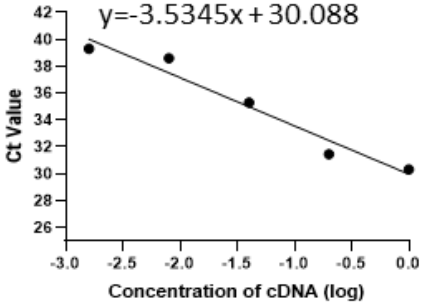

Efficiency: 1.918, 92%

Appendix 1 continued on next page

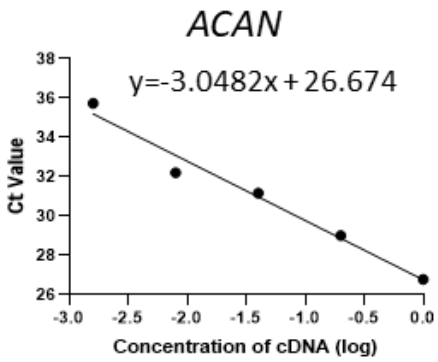

Efficiency: 2.144, 114%

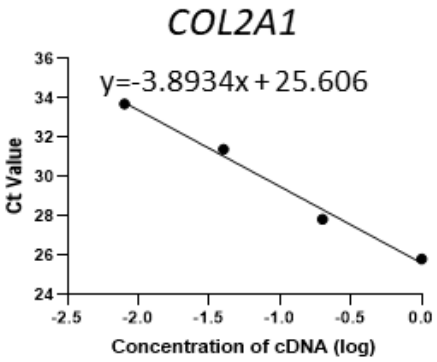

Efficiency: 1.806, 81%

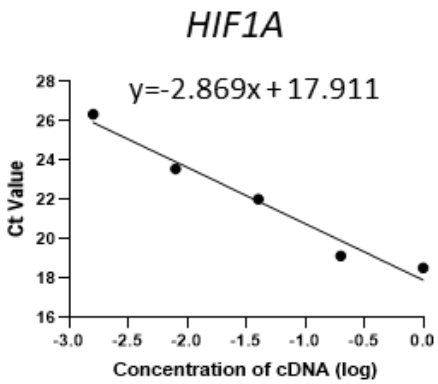

Efficiency: 2.231, 123%

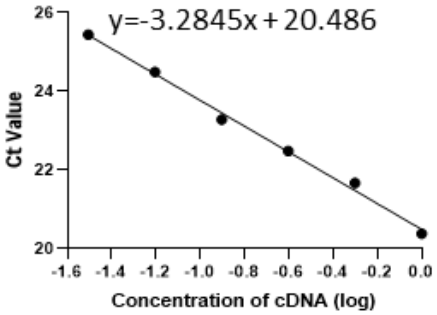

Efficiency: 2.015, 102%

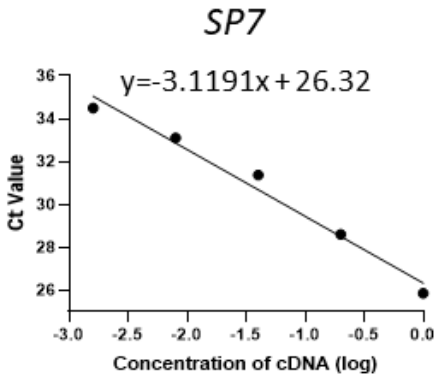

Efficiency: 2.092, 109%

Appendix 1. Efficiency of Primers used in qPCR Experiments*. The efficiency of 11 primers was calculated and converted into a percentage including:* ATCB, ALPL, COL1A1, PPARγ, FABP4, SOX9, ACAN, COL2A1, HIF1A, MKI67 *and* SP7*.*

Appendix B Effect of Mifamurtide on Macrophages

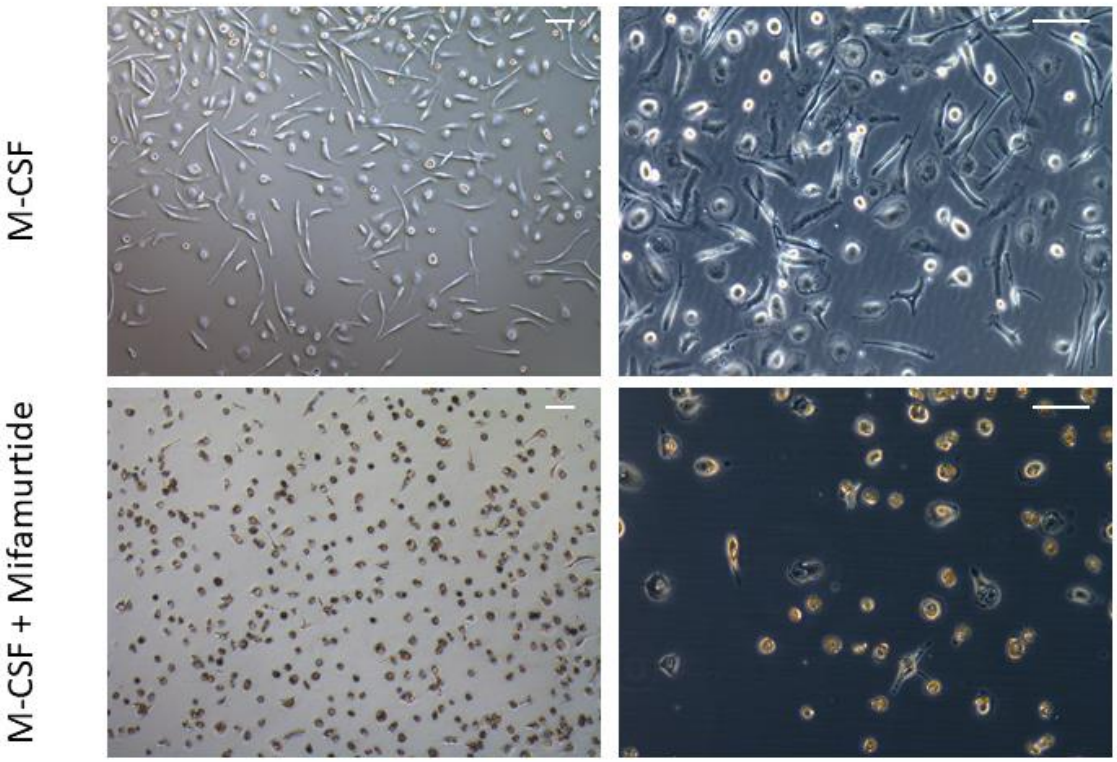

Appendix 2. Representative images of macrophages after culture with Mifamurtide. *PBMC derived MDMs were cultured in basal media with M-CSF, or M-CSF+ Mifamurtide for 7 days. Images were taken using at two magnifications. Scale bar= 100 µm.*

References

1. Patel, J., et al., *DNA damage and mitochondria in cancer and aging.* Carcinogenesis, 2020. **41**(12): p. 1625-1634.
2. Lu, T., et al., *Gene regulation and DNA damage in the ageing human brain.* Nature, 2004. **429**(6994): p. 883-91.
3. Shiloh, Y. and H.M. Lederman, *Ataxia-telangiectasia (A-T): An emerging dimension of premature ageing.* Ageing Res Rev, 2017. **33**: p. 76-88.
4. Rahner, N. and V. Steinke, *Hereditary cancer syndromes.* Dtsch Arztebl Int, 2008. **105**(41): p. 706-14.
5. Siegel, R., et al., *Cancer statistics, 2014.* CA Cancer J Clin, 2014. **64**(1): p. 9-29.
6. Bagnardi, V., et al., *Alcohol consumption and the risk of cancer: a meta-analysis.* Alcohol Res Health, 2001. **25**(4): p. 263-70.
7. van Elsland, D. and J. Neefjes, *Bacterial infections and cancer.* EMBO Rep, 2018. **19**(11).
8. *Bone sarcomas: ESMO Clinical Practice Guidelines for diagnosis, treatment and follow-up.* Ann Oncol, 2014. **25 Suppl 3**: p. iii113-23.
9. Huang, X., et al., *Risk and clinicopathological features of osteosarcoma metastasis to the lung: A population-based study.* J Bone Oncol, 2019. **16**: p. 100230.
10. Overholtzer, M., et al., *The presence of p53 mutations in human osteosarcomas correlates with high levels of genomic instability.* Proc Natl Acad Sci U S A, 2003. **100**(20): p. 11547-52.
11. Selvarajah, S., et al., *Identification of cryptic microaberrations in osteosarcoma by high-definition oligonucleotide array comparative genomic hybridization.* Cancer Genet Cytogenet, 2007. **179**(1): p. 52-61.
12. Miller, C.W., et al., *Frequency and structure of p53 rearrangements in human osteosarcoma.* Cancer Res, 1990. **50**(24): p. 7950-4.
13. Toguchida, J., et al., *Mutation spectrum of the p53 gene in bone and soft tissue sarcomas.* Cancer Res, 1992. **52**(22): p. 6194-9.
14. Wadayama, B., et al., *Mutation spectrum of the retinoblastoma gene in osteosarcomas.* Cancer Res, 1994. **54**(11): p. 3042-8.
15. Hansen, M.F., et al., *Osteosarcoma and retinoblastoma: a shared chromosomal mechanism revealing recessive predisposition.* Proc Natl Acad Sci U S A, 1985. **82**(18): p. 6216-20.
16. Wang, L.L., et al., *Association between osteosarcoma and deleterious mutations in the RECQL4 gene in Rothmund-Thomson syndrome.* J Natl Cancer Inst, 2003. **95**(9): p. 669-74.
17. Mirabello, L., R.J. Troisi, and S.A. Savage, *Osteosarcoma incidence and survival rates from 1973 to 2004: data from the Surveillance, Epidemiology, and End Results Program.* Cancer, 2009. **115**(7): p. 1531-43.
18. Guijarro, M.V., S.C. Ghivizzani, and C.P. Gibbs, *Animal models in osteosarcoma.* Frontiers in oncology, 2014. **4**: p. 189-189.
19. Ragland, B.D., et al., *Cytogenetics and Molecular Biology of Osteosarcoma.* Laboratory Investigation, 2002. **82**(4): p. 365-373.
20. Yang, Y., et al., *Genetically transforming human osteoblasts to sarcoma: development of an osteosarcoma model.* Genes & cancer, 2017. **8**(1-2): p. 484-494.
21. Smeland, S., et al., *Event-free survival and overall survival in 2,253 patients with osteosarcoma registered to EURAMOS-1.* Journal of Clinical Oncology, 2015. **33**(15_suppl): p. 10512-10512.
22. Smeland, S., et al., *Survival and prognosis with osteosarcoma: outcomes in more than 2000 patients in the EURAMOS-1 (European and American Osteosarcoma Study) cohort.* European Journal of Cancer, 2019. **109**: p. 36-50.
23. Kumar, R., et al., *Primary Osteosarcoma in the Elderly Revisited: Current Concepts in Diagnosis and Treatment.* Curr Oncol Rep, 2018. **20**(2): p. 13.
24. Iwata, S., et al., *Prognostic factors in elderly osteosarcoma patients: a multi-institutional retrospective study of 86 cases.* Ann Surg Oncol, 2014. **21**(1): p. 263-8.

25. Jimmy, R., et al., *Effectiveness of mifamurtide in addition to standard chemotherapy for high-grade osteosarcoma: a systematic review.* JBI Database System Rev Implement Rep, 2017. **15**(8): p. 2113-2152.
26. Geddes, K., J.G. Magalhães, and S.E. Girardin, *Unleashing the therapeutic potential of NOD-like receptors.* Nature Reviews Drug Discovery, 2009. **8**(6): p. 465-479.
27. Girardin, S.E., et al., *Nod2 is a general sensor of peptidoglycan through muramyl dipeptide (MDP) detection.* J Biol Chem, 2003. **278**(11): p. 8869-72.
28. Kager, L., U. Pötschger, and S. Bielack, *Review of mifamurtide in the treatment of patients with osteosarcoma.* Therapeutics and clinical risk management, 2010. **6**: p. 279-286.
29. Netea, M.G., et al., *IL-32 synergizes with nucleotide oligomerization domain (NOD) 1 and NOD2 ligands for IL-1beta and IL-6 production through a caspase 1-dependent mechanism.* Proc Natl Acad Sci U S A, 2005. **102**(45): p. 16309-14.
30. Netea, M.G., et al., *Nucleotide-binding oligomerization domain-2 modulates specific TLR pathways for the induction of cytokine release.* J Immunol, 2005. **174**(10): p. 6518-23.
31. Marina-García, N., et al., *Pannexin-1-mediated intracellular delivery of muramyl dipeptide induces caspase-1 activation via cryopyrin/NLRP3 independently of Nod2.* J Immunol, 2008. **180**(6): p. 4050-7.
32. Kager, L., U. Pötschger, and S. Bielack, *Review of mifamurtide in the treatment of patients with osteosarcoma.* Ther Clin Risk Manag, 2010. **6**: p. 279-86.
33. Múdry, P., et al., *Improved osteosarcoma survival with addition of mifamurtide to conventional chemotherapy - Observational prospective single institution analysis.* J Bone Oncol, 2021. **28**: p. 100362.
34. Smeland, S., et al., *Survival and prognosis with osteosarcoma: outcomes in more than 2000 patients in the EURAMOS-1 (European and American Osteosarcoma Study) cohort.* Eur J Cancer, 2019. **109**: p. 36-50.
35. Tacyildiz, N., et al., *The Efficiency and Toxicity of Mifamurtide in Childhood Osteosarcoma.* J Pediatr Hematol Oncol, 2018. **40**(6): p. e373-e376.
36. Brard, C., et al., *Sarcome-13/OS2016 trial protocol: a multicentre, randomised, open-label, phase II trial of mifamurtide combined with postoperative chemotherapy for patients with newly diagnosed high-risk osteosarcoma.* BMJ Open, 2019. **9**(5): p. e025877.
37. Sikic, B.I., et al., *First-in-Human, First-in-Class Phase I Trial of the Anti-CD47 Antibody Hu5F9-G4 in Patients With Advanced Cancers.* Journal of clinical oncology : official journal of the American Society of Clinical Oncology, 2019. **37**(12): p. 946-953.
38. Edris, B., et al., *Antibody therapy targeting the CD47 protein is effective in a model of aggressive metastatic leiomyosarcoma.* Proceedings of the National Academy of Sciences of the United States of America, 2012. **109**(17): p. 6656-6661.
39. Russell, R.G., *Bisphosphonates: from bench to bedside.* Ann N Y Acad Sci, 2006. **1068**: p. 367-401.
40. Ory, B., et al., *Zoledronic acid suppresses lung metastases and prolongs overall survival of osteosarcoma-bearing mice.* Cancer, 2005. **104**(11): p. 2522-9.
41. Heymann, D., et al., *Bisphosphonates: new therapeutic agents for the treatment of bone tumors.* Trends Mol Med, 2004. **10**(7): p. 337-43.
42. Horie, N., et al., *Combined effects of a third-generation bisphosphonate, zoledronic acid with other anticancer agents against murine osteosarcoma.* Br J Cancer, 2007. **96**(2): p. 255-61.
43. Meyers, P.A., et al., *Addition of pamidronate to chemotherapy for the treatment of osteosarcoma.* Cancer, 2011. **117**(8): p. 1736-44.
44. Goldsby, R.E., et al., *Feasibility and dose discovery analysis of zoledronic acid with concurrent chemotherapy in the treatment of newly diagnosed metastatic osteosarcoma: a report from the Children's Oncology Group.* Eur J Cancer, 2013. **49**(10): p. 2384-91.
45. Li, S., et al., *Addition of Zoledronate to Chemotherapy in Patients with Osteosarcoma Treated with Limb-Sparing Surgery: A Phase III Clinical Trial.* Medical science monitor : international medical journal of experimental and clinical research, 2019. **25**: p. 1429-1438.

46. Piperno-Neumann, S., et al., *Zoledronate in combination with chemotherapy and surgery to treat osteosarcoma (OS2006): a randomised, multicentre, open-label, phase 3 trial.* Lancet Oncol, 2016. **17**(8): p. 1070-1080.
47. Koshkina, N.V., et al., *Fas-Negative Osteosarcoma Tumor Cells Are Selected during Metastasis to the Lungs: The Role of the Fas Pathway in the Metastatic Process of Osteosarcoma.* Molecular Cancer Research, 2007. **5**(10): p. 991.
48. Aliper, A.M., et al., *A role for G-CSF and GM-CSF in nonmyeloid cancers.* Cancer medicine, 2014. **3**(4): p. 737-746.
49. Anderson, P.M., et al., *Aerosol granulocyte macrophage-colony stimulating factor: a low toxicity, lung-specific biological therapy in patients with lung metastases.* Clin Cancer Res, 1999. **5**(9): p. 2316-23.
50. Arndt, C.A.S., et al., *Inhaled granulocyte-macrophage colony stimulating factor for first pulmonary recurrence of osteosarcoma: effects on disease-free survival and immunomodulation. a report from the Children's Oncology Group.* Clinical cancer research : an official journal of the American Association for Cancer Research, 2010. **16**(15): p. 4024-4030.
51. Clarke, B., *Normal bone anatomy and physiology.* Clinical journal of the American Society of Nephrology : CJASN, 2008. **3 Suppl 3**(Suppl 3): p. S131-S139.
52. Yoshiko, Y., et al., *Osteoblast autonomous Pi regulation via Pit1 plays a role in bone mineralization.* Molecular and cellular biology, 2007. **27**(12): p. 4465-4474.
53. Dallas, S.L. and L.F. Bonewald, *Dynamics of the transition from osteoblast to osteocyte.* Annals of the New York Academy of Sciences, 2010. **1192**: p. 437-443.
54. Florencio-Silva, R., et al., *Biology of Bone Tissue: Structure, Function, and Factors That Influence Bone Cells.* BioMed research international, 2015. **2015**: p. 421746-421746.
55. Blanchard, F., et al., *The dual role of IL-6-type cytokines on bone remodeling and bone tumors.* Cytokine & Growth Factor Reviews, 2009. **20**(1): p. 19-28.
56. Chipoy, C., et al., *Downregulation of Osteoblast Markers and Induction of the Glial Fibrillary Acidic Protein by Oncostatin M in Osteosarcoma Cells Require PKCδ and STAT3.* Journal of Bone and Mineral Research, 2004. **19**(11): p. 1850-1861.
57. Duplomb, L., et al., *Interleukin-6 Inhibits Receptor Activator of Nuclear Factor κB Ligand-Induced Osteoclastogenesis by Diverting Cells into the Macrophage Lineage: Key Role of Serine727 Phosphorylation of Signal Transducer and Activator of Transcription 3.* Endocrinology, 2008. **149**(7): p. 3688-3697.
58. Krzeszinski, J.Y. and Y. Wan, *New therapeutic targets for cancer bone metastasis.* Trends in pharmacological sciences, 2015. **36**(6): p. 360-373.
59. Kinpara, K., et al., *Osteoclast Differentiation Factor in Human Osteosarcoma Cell Line.* Journal of Immunoassay, 2000. **21**(4): p. 327-340.
60. Broadhead, M.L., et al., *The molecular pathogenesis of osteosarcoma: a review.* Sarcoma, 2011. **2011**: p. 959248.
61. Weilbaecher, K.N., T.A. Guise, and L.K. McCauley, *Cancer to bone: a fatal attraction.* Nature reviews. Cancer, 2011. **11**(6): p. 411-425.
62. Gorlick, R., *Current Concepts on the Molecular Biology of Osteosarcoma*, in *Pediatric and Adolescent Osteosarcoma*, N. Jaffe, O.S. Bruland, and S. Bielack, Editors. 2010, Springer US: Boston, MA. p. 467-478.
63. Trivedi, S., et al., *A quantitative method to determine osteogenic differentiation aptness of scaffold.* J Oral Biol Craniofac Res, 2020. **10**(2): p. 158-160.
64. Kim, S.H., et al., *Reassessment of alkaline phosphatase as serum tumor marker with high specificity in osteosarcoma.* Cancer Med, 2017. **6**(6): p. 1311-1322.
65. Blebea, J.S., et al., *Structural and Functional Imaging of Normal Bone Marrow and Evaluation of Its Age-Related Changes.* Seminars in Nuclear Medicine, 2007. **37**(3): p. 185-194.
66. Hwang, S. and D.M. Panicek, *Magnetic resonance imaging of bone marrow in oncology, Part 1.* Skeletal Radiol, 2007. **36**(10): p. 913-20.

67. Mercier, F.E., C. Ragu, and D.T. Scadden, *The bone marrow at the crossroads of blood and immunity.* Nature Reviews Immunology, 2012. **12**(1): p. 49-60.
68. Nombela-Arrieta, C. and S. Isringhausen, *The Role of the Bone Marrow Stromal Compartment in the Hematopoietic Response to Microbial Infections.* Frontiers in Immunology, 2017. **7**(689).
69. Cuminetti, V. and L. Arranz, *Bone Marrow Adipocytes: The Enigmatic Components of the Hematopoietic Stem Cell Niche.* Journal of clinical medicine, 2019. **8**(5): p. 707.
70. Miggitsch, C., et al., *Human bone marrow adipocytes display distinct immune regulatory properties.* EBioMedicine, 2019. **46**: p. 387-398.
71. Liney, G.P., et al., *Age, gender, and skeletal variation in bone marrow composition: a preliminary study at 3.0 Tesla.* J Magn Reson Imaging, 2007. **26**(3): p. 787-93.
72. Pittenger, M.F., et al., *Multilineage potential of adult human mesenchymal stem cells.* Science, 1999. **284**(5411): p. 143-7.
73. Poggi, A. and M. Giuliani, *Mesenchymal Stromal Cells Can Regulate the Immune Response in the Tumor Microenvironment.* Vaccines, 2016. **4**(4): p. 41.
74. Orimo, A., et al., *Stromal Fibroblasts Present in Invasive Human Breast Carcinomas Promote Tumor Growth and Angiogenesis through Elevated SDF-1/CXCL12 Secretion.* Cell, 2005. **121**(3): p. 335-348.
75. Tuxhorn, J.A., et al., *Stromal Cells Promote Angiogenesis and Growth of Human Prostate Tumors in a Differential Reactive Stroma (DRS) Xenograft Model.* Cancer Research, 2002. **62**(11): p. 3298.
76. Zhang, T., et al., *Bone marrow-derived mesenchymal stem cells promote growth and angiogenesis of breast and prostate tumors.* Stem Cell Research & Therapy, 2013. **4**(3): p. 70.
77. Konopleva, M., et al., *Stromal cells prevent apoptosis of AML cells by up-regulation of anti-apoptotic proteins.* Leukemia, 2002. **16**(9): p. 1713-1724.
78. Karnoub, A.E., et al., *Mesenchymal stem cells within tumour stroma promote breast cancer metastasis.* Nature, 2007. **449**(7162): p. 557-63.
79. Cortini, M., et al., *Tumor-Activated Mesenchymal Stromal Cells Promote Osteosarcoma Stemness and Migratory Potential via IL-6 Secretion.* PloS one, 2016. **11**(11): p. e0166500-e0166500.
80. Avnet, S., et al., *Cancer-associated mesenchymal stroma fosters the stemness of osteosarcoma cells in response to intratumoral acidosis via NF-κB activation.* International journal of cancer, 2017. **140**(6): p. 1331-1345.
81. Whiteside, T.L., *The tumor microenvironment and its role in promoting tumor growth.* Oncogene, 2008. **27**(45): p. 5904-5912.
82. Ren, G., et al., *CCR2-dependent recruitment of macrophages by tumor-educated mesenchymal stromal cells promotes tumor development and is mimicked by TNFα.* Cell stem cell, 2012. **11**(6): p. 812-824.
83. Razmkhah, M., et al., *Adipose derived stem cells (ASCs) isolated from breast cancer tissue express IL-4, IL-10 and TGF-β1 and upregulate expression of regulatory molecules on T cells: Do they protect breast cancer cells from the immune response?* Cellular Immunology, 2011. **266**(2): p. 116-122.
84. Otsu, K., et al., *Concentration-dependent inhibition of angiogenesis by mesenchymal stem cells.* Blood, 2009. **113**(18): p. 4197-4205.
85. Sun, Z., S. Wang, and R.C. Zhao, *The roles of mesenchymal stem cells in tumor inflammatory microenvironment.* Journal of Hematology & Oncology, 2014. **7**(1): p. 14.
86. Johann, P.-D., et al., *Tumour stromal cells derived from paediatric malignancies display MSC-like properties and impair NK cell cytotoxicity.* BMC cancer, 2010. **10**: p. 501-501.
87. Xu, X., et al., *Isolation and comparison of mesenchymal stem-like cells from human gastric cancer and adjacent non-cancerous tissues.* Journal of Cancer Research and Clinical Oncology, 2011. **137**(3): p. 495-504.
88. Honold, L. and M. Nahrendorf, *Resident and Monocyte-Derived Macrophages in Cardiovascular Disease.* Circulation research, 2018. **122**(1): p. 113-127.

89. Biswas, S.K. and A. Mantovani, *Macrophage plasticity and interaction with lymphocyte subsets: cancer as a paradigm.* Nature Immunology, 2010. **11**(10): p. 889-896.
90. Italiani, P. and D. Boraschi, *From Monocytes to M1/M2 Macrophages: Phenotypical vs. Functional Differentiation.* Frontiers in Immunology, 2014. **5**(514).
91. Jayasingam, S.D., et al., *Evaluating the Polarization of Tumor-Associated Macrophages Into M1 and M2 Phenotypes in Human Cancer Tissue: Technicalities and Challenges in Routine Clinical Practice.* Frontiers in oncology, 2020. **9**: p. 1512-1512.
92. Ségaliny, A.I., et al., *Interleukin-34 promotes tumor progression and metastatic process in osteosarcoma through induction of angiogenesis and macrophage recruitment.* Int J Cancer, 2015. **137**(1): p. 73-85.
93. Mantovani, A., et al., *Tumour-associated macrophages as treatment targets in oncology.* Nat Rev Clin Oncol, 2017. **14**(7): p. 399-416.
94. Lewis, C.E. and J.W. Pollard, *Distinct Role of Macrophages in Different Tumor Microenvironments.* Cancer Research, 2006. **66**(2): p. 605.
95. Han, Y., et al., *Tumor-associated macrophages promote lung metastasis and induce epithelial-mesenchymal transition in osteosarcoma by activating the COX-2/STAT3 axis.* Cancer Lett, 2019. **440-441**: p. 116-125.
96. Buddingh, E.P., et al., *Tumor-Infiltrating Macrophages Are Associated with Metastasis Suppression in High-Grade Osteosarcoma: A Rationale for Treatment with Macrophage Activating Agents.* Clinical Cancer Research, 2011. **17**(8): p. 2110.
97. Noy, R. and J.W. Pollard, *Tumor-associated macrophages: from mechanisms to therapy.* Immunity, 2014. **41**(1): p. 49-61.
98. Franklin, R.A. and M.O. Li, *Ontogeny of Tumor-associated Macrophages and Its Implication in Cancer Regulation.* Trends Cancer, 2016. **2**(1): p. 20-34.
99. Gordon, S.R., et al., *PD-1 expression by tumour-associated macrophages inhibits phagocytosis and tumour immunity.* Nature, 2017. **545**(7655): p. 495-499.
100. Dumars, C., et al., *Dysregulation of macrophage polarization is associated with the metastatic process in osteosarcoma.* Oncotarget, 2016. **7**(48): p. 78343-78354.
101. Yang, D., et al., *LncRNA RP11-361F15.2 promotes osteosarcoma tumorigenesis by inhibiting M2-Like polarization of tumor-associated macrophages of CPEB4.* Cancer Lett, 2020. **473**: p. 33-49.
102. Yao, Y., et al., *The Macrophage-Osteoclast Axis in Osteoimmunity and Osteo-Related Diseases.* Front Immunol, 2021. **12**: p. 664871.
103. Lampiasi, N., R. Russo, and F. Zito, *The Alternative Faces of Macrophage Generate Osteoclasts.* Biomed Res Int, 2016. **2016**: p. 9089610.
104. Evans, K.E. and S.W. Fox, *Interleukin-10 inhibits osteoclastogenesis by reducing NFATc1 expression and preventing its translocation to the nucleus.* BMC Cell Biol, 2007. **8**: p. 4.
105. Zhao, E., et al., *Bone marrow and the control of immunity.* Cell Mol Immunol, 2012. **9**(1): p. 11-9.
106. Liu, Y. and X. Cao, *Immunosuppressive cells in tumor immune escape and metastasis.* J Mol Med (Berl), 2016. **94**(5): p. 509-22.
107. Jiang, D., et al., *Tumour infiltrating lymphocytes correlate with improved survival in patients with esophageal squamous cell carcinoma.* Scientific Reports, 2017. **7**(1): p. 44823.
108. Zgura, A., et al., *Relationship between Tumor Infiltrating Lymphocytes and Progression in Breast Cancer.* Maedica, 2018. **13**(4): p. 317-320.
109. Trieb, K., et al., *Evaluation of HLA-DR Expression and T-Lymphocyte Infiltration in Osteosarcoma.* Pathology - Research and Practice, 1998. **194**(10): p. 679-684.
110. Théoleyre, S., et al., *Phenotypic and functional analysis of lymphocytes infiltrating osteolytic tumors: use as a possible therapeutic approach of osteosarcoma.* BMC cancer, 2005. **5**: p. 123-123.
111. Alves, P.M., et al., *Evaluation of tumor-infiltrating lymphocytes in osteosarcomas of the jaws: a multicenter study.* Virchows Archiv, 2019. **474**(2): p. 201-207.
112. Shen, J.K., et al., *Programmed cell death ligand 1 expression in osteosarcoma.* Cancer immunology research, 2014. **2**(7): p. 690-698.

113. Brahmer, J.R., et al., *Safety and activity of anti-PD-L1 antibody in patients with advanced cancer.* The New England journal of medicine, 2012. **366**(26): p. 2455-2465.
114. Topalian, S.L., et al., *Safety, activity, and immune correlates of anti-PD-1 antibody in cancer.* The New England journal of medicine, 2012. **366**(26): p. 2443-2454.
115. Tawbi, H.A., et al., *Pembrolizumab in advanced soft-tissue sarcoma and bone sarcoma (SARC028): a multicentre, two-cohort, single-arm, open-label, phase 2 trial.* The Lancet Oncology, 2017. **18**(11): p. 1493-1501.
116. Jain, R.K., et al., *Lessons from phase III clinical trials on anti-VEGF therapy for cancer.* Nat Clin Pract Oncol, 2006. **3**(1): p. 24-40.
117. Konerding, M.A., E. Fait, and A. Gaumann, *3D microvascular architecture of pre-cancerous lesions and invasive carcinomas of the colon.* Br J Cancer, 2001. **84**(10): p. 1354-62.
118. Carmeliet, P., *VEGF as a key mediator of angiogenesis in cancer.* Oncology, 2005. **69 Suppl 3**: p. 4-10.
119. Dewhirst, M.W., et al., *Microvascular studies on the origins of perfusion-limited hypoxia.* Br J Cancer Suppl, 1996. **27**: p. S247-51.
120. Liu, Y., et al., *High expression levels of Cyr61 and VEGF are associated with poor prognosis in osteosarcoma.* Pathol Res Pract, 2017. **213**(8): p. 895-899.
121. Davis, L.E., et al., *Randomized Double-Blind Phase II Study of Regorafenib in Patients With Metastatic Osteosarcoma.* J Clin Oncol, 2019. **37**(16): p. 1424-1431.
122. Grignani, G., et al., *Sorafenib and everolimus for patients with unresectable high-grade osteosarcoma progressing after standard treatment: a non-randomised phase 2 clinical trial.* Lancet Oncol, 2015. **16**(1): p. 98-107.
123. Ebb, D., et al., *Phase II trial of trastuzumab in combination with cytotoxic chemotherapy for treatment of metastatic osteosarcoma with human epidermal growth factor receptor 2 overexpression: a report from the children's oncology group.* J Clin Oncol, 2012. **30**(20): p. 2545-51.
124. Fox, E., et al., *A phase 1 trial and pharmacokinetic study of cediranib, an orally bioavailable pan-vascular endothelial growth factor receptor inhibitor, in children and adolescents with refractory solid tumors.* J Clin Oncol, 2010. **28**(35): p. 5174-81.
125. Maes, C., et al., *VEGF-independent cell-autonomous functions of HIF-1α regulating oxygen consumption in fetal cartilage are critical for chondrocyte survival.* J Bone Miner Res, 2012. **27**(3): p. 596-609.
126. Ren, H.Y., et al., *Prognostic role of hypoxia-inducible factor-1 alpha expression in osteosarcoma: a meta-analysis.* Onco Targets Ther, 2016. **9**: p. 1477-87.
127. Cramer, T., et al., *Expression of VEGF isoforms by epiphyseal chondrocytes during low-oxygen tension is HIF-1 alpha dependent.* Osteoarthritis Cartilage, 2004. **12**(6): p. 433-9.
128. Hulley, P.A., et al., *Hypoxia-inducible factor 1-alpha does not regulate osteoclastogenesis but enhances bone resorption activity via prolyl-4-hydroxylase 2.* J Pathol, 2017. **242**(3): p. 322-333.
129. Pierrevelcin, M., et al., *Focus on Hypoxia-Related Pathways in Pediatric Osteosarcomas and Their Druggability.* Cells, 2020. **9**(9).
130. Ouyang, Y., et al., *Hypoxia-inducible factor-1 expression predicts osteosarcoma patients' survival: a meta-analysis.* Int J Biol Markers, 2016. **31**(3): p. e229-34.
131. Li, Y., et al., *Prognosis value of Hypoxia-inducible factor-1α expression in patients with bone and soft tissue sarcoma: a meta-analysis.* Springerplus, 2016. **5**(1): p. 1370.
132. Kapalczynska, M., et al., *2D and 3D cell cultures - a comparison of different types of cancer cell cultures.* Arch Med Sci, 2018. **14**(4): p. 910-919.
133. Uluckan, O., et al., *Preclinical mouse models of osteosarcoma.* Bonekey Rep, 2015. **4**: p. 670.
134. Guijarro, M.V., C.S. Ghivizzani, and P.C. Gibbs, *Corrigendum: Animal models in osteosarcoma.* Front Genet, 2014. **5**: p. 475.
135. Khanna, C., et al., *Metastasis-associated differences in gene expression in a murine model of osteosarcoma.* Cancer Res, 2001. **61**(9): p. 3750-9.
136. Kim, W.Y. and N.E. Sharpless, *Drug efficacy testing in mice.* Curr Top Microbiol Immunol, 2012. **355**: p. 19-38.

137. Teicher, B.A., et al., *Characteristics of human Ewing/PNET sarcoma models.* Ann Saudi Med, 2011. **31**(2): p. 174-82.
138. Becher, O.J. and E.C. Holland, *Genetically engineered models have advantages over xenografts for preclinical studies.* Cancer Res, 2006. **66**(7): p. 3355-8, discussion 3358-9.
139. Lee, E.Y., et al., *Mice deficient for Rb are nonviable and show defects in neurogenesis and haematopoiesis.* Nature, 1992. **359**(6393): p. 288-94.
140. Lin, P.P., et al., *Targeted mutation of p53 and Rb in mesenchymal cells of the limb bud produces sarcomas in mice.* Carcinogenesis, 2009. **30**(10): p. 1789-95.
141. Taneja, P., et al., *Transgenic and knockout mice models to reveal the functions of tumor suppressor genes.* Clin Med Insights Oncol, 2011. **5**: p. 235-57.
142. Walkley, C.R., et al., *Conditional mouse osteosarcoma, dependent on p53 loss and potentiated by loss of Rb, mimics the human disease.* Genes Dev, 2008. **22**(12): p. 1662-76.
143. Lavigueur, A., et al., *High incidence of lung, bone, and lymphoid tumors in transgenic mice overexpressing mutant alleles of the p53 oncogene.* Mol Cell Biol, 1989. **9**(9): p. 3982-91.
144. Rüther, U., et al., *Deregulated c-fos expression interferes with normal bone development in transgenic mice.* Nature, 1987. **325**(6103): p. 412-6.
145. Grigoriadis, A.E., et al., *Osteoblasts are target cells for transformation in c-fos transgenic mice.* J Cell Biol, 1993. **122**(3): p. 685-701.
146. Schuh, J.C., *Trials, tribulations, and trends in tumor modeling in mice.* Toxicol Pathol, 2004. **32 Suppl 1**: p. 53-66.
147. Rowell, J.L., D.O. McCarthy, and C.E. Alvarez, *Dog models of naturally occurring cancer.* Trends in molecular medicine, 2011. **17**(7): p. 380-388.
148. O'Donoghue, L.E., et al., *Expression profiling in canine osteosarcoma: identification of biomarkers and pathways associated with outcome.* BMC Cancer, 2010. **10**: p. 506.
149. Paoloni, M., et al., *Canine tumor cross-species genomics uncovers targets linked to osteosarcoma progression.* BMC Genomics, 2009. **10**: p. 625.
150. De Luca, A., et al., *Relevance of 3d culture systems to study osteosarcoma environment.* J Exp Clin Cancer Res, 2018. **37**(1): p. 2.
151. Hickman, J.A., et al., *Three-dimensional models of cancer for pharmacology and cancer cell biology: capturing tumor complexity in vitro/ex vivo.* Biotechnol J, 2014. **9**(9): p. 1115-28.
152. Martins-Neves, S.R., et al., *Therapeutic implications of an enriched cancer stem-like cell population in a human osteosarcoma cell line.* BMC Cancer, 2012. **12**: p. 139.
153. Indovina, P., G. Rainaldi, and M.T. Santini, *Hypoxia increases adhesion and spreading of MG-63 three-dimensional tumor spheroids.* Anticancer Res, 2008. **28**(2a): p. 1013-22.
154. Baek, N., et al., *Monitoring the effects of doxorubicin on 3D-spheroid tumor cells in real-time.* Onco Targets Ther, 2016. **9**: p. 7207-7218.
155. Chaddad, H., et al., *Combining 2D angiogenesis and 3D osteosarcoma microtissues to improve vascularization.* Exp Cell Res, 2017. **360**(2): p. 138-145.
156. Sitarski, A.M., et al., *3d Tissue Engineered In Vitro Models Of Cancer In Bone.* ACS Biomater Sci Eng, 2018. **4**(2): p. 324-336.
157. O'Brien, F.J., *Biomaterials & scaffolds for tissue engineering.* Materials Today, 2011. **14**(3): p. 88-95.
158. Kim, J.A., et al., *Magnesium phosphate ceramics incorporating a novel indene compound promote osteoblast differentiation in vitro and bone regeneration in vivo.* Biomaterials, 2018. **157**: p. 51-61.
159. Wang, M., *Developing bioactive composite materials for tissue replacement.* Biomaterials, 2003. **24**(13): p. 2133-51.
160. Oh, S.H., et al., *Fabrication and characterization of hydrophilic poly(lactic-co-glycolic acid)/poly(vinyl alcohol) blend cell scaffolds by melt-molding particulate-leaching method.* Biomaterials, 2003. **24**(22): p. 4011-4021.
161. Lisi, A., et al., *A combined synthetic-fibrin scaffold supports growth and cardiomyogenic commitment of human placental derived stem cells.* PLoS One, 2012. **7**(4): p. e34284.
162. Pavlou, M., et al., *Osteomimetic matrix components alter cell migration and drug response in a 3D tumour-engineered osteosarcoma model.* Acta Biomaterialia, 2019. **96**: p. 247-257.

163. Ivanov, V., et al., *Naturally produced extracellular matrix inhibits growth rate and invasiveness of human osteosarcoma cancer cells.* Med Oncol, 2007. **24**(2): p. 209-17.
164. Rubio, R., et al., *Bone environment is essential for osteosarcoma development from transformed mesenchymal stem cells.* Stem Cells, 2014. **32**(5): p. 1136-48.
165. Liu, Z. and G. Vunjak-Novakovic, *Modeling tumor microenvironments using custom-designed biomaterial scaffolds.* Current opinion in chemical engineering, 2016. **11**: p. 94-105.
166. Balke, M., et al., *Morphologic characterization of osteosarcoma growth on the chick chorioallantoic membrane.* BMC Res Notes, 2010. **3**: p. 58.
167. Murphy, J.B., *TRANSPLANTABILITY OF TISSUES TO THE EMBRYO OF FOREIGN SPECIES : ITS BEARING ON QUESTIONS OF TISSUE SPECIFICITY AND TUMOR IMMUNITY.* The Journal of experimental medicine, 1913. **17**(4): p. 482-493.
168. Ribatti, D., *The chick embryo chorioallantoic membrane (CAM). A multifaceted experimental model.* Mech Dev, 2016. **141**: p. 70-77.
169. Liao, Y.-Y., et al., *CCL3 promotes angiogenesis by dysregulation of miR-374b/ VEGF-A axis in human osteosarcoma cells.* Oncotarget, 2015. **7**(4): p. 4310-4325.
170. Deryugina, E.I. and J.P. Quigley, *Chapter 2. Chick embryo chorioallantoic membrane models to quantify angiogenesis induced by inflammatory and tumor cells or purified effector molecules.* Methods Enzymol, 2008. **444**: p. 21-41.
171. Lokman, N.A., et al., *Chick chorioallantoic membrane (CAM) assay as an in vivo model to study the effect of newly identified molecules on ovarian cancer invasion and metastasis.* International journal of molecular sciences, 2012. **13**(8): p. 9959-9970.
172. Zuo, Z., et al., *The CAM cancer xenograft as a model for initial evaluation of MR labelled compounds.* Scientific reports, 2017. **7**: p. 46690-46690.
173. Manjunathan, R. and M. Ragunathan, *Chicken chorioallantoic membrane as a reliable model to evaluate osteosarcoma-an experimental approach using SaOS2 cell line.* Biological procedures online, 2015. **17**: p. 10-10.
174. Nowak-Sliwinska, P., T. Segura, and M.L. Iruela-Arispe, *The chicken chorioallantoic membrane model in biology, medicine and bioengineering.* Angiogenesis, 2014. **17**(4): p. 779-804.
175. DeBord, L.C., et al., *The chick chorioallantoic membrane (CAM) as a versatile patient-derived xenograft (PDX) platform for precision medicine and preclinical research.* American journal of cancer research, 2018. **8**(8): p. 1642-1660.
176. Li, M., et al., *The In Ovo Chick Chorioallantoic Membrane (CAM) Assay as an Efficient Xenograft Model of Hepatocellular Carcinoma.* Journal of visualized experiments : JoVE, 2015(104): p. 52411.
177. Moreno-Jimenez, I., et al., *Remodelling of human bone on the chorioallantoic membrane of the chicken egg: De novo bone formation and resorption.* J Tissue Eng Regen Med, 2018. **12**(8): p. 1877-1890.
178. Inglis, S., et al., *Human endothelial and foetal femur-derived stem cell co-cultures modulate osteogenesis and angiogenesis.* Stem Cell Research & Therapy, 2016. **7**(1): p. 13.
179. Costa Moura, C., et al., *Quantitative temporal interrogation in 3D of bioengineered human cartilage using multimodal label-free imaging.* Integrative Biology, 2018. **10**(10): p. 635-645.
180. Gothard, D., et al., *Regionally-derived cell populations and skeletal stem cells from human foetal femora exhibit specific osteochondral and multi-lineage differentiation capacity in vitro and ex vivo.* Stem Cell Research & Therapy, 2015. **6**(1): p. 251.
181. Chang, T.C., et al., *Stabilization of hypoxia-inducible factor-1{alpha} by prostacyclin under prolonged hypoxia via reducing reactive oxygen species level in endothelial cells.* J Biol Chem, 2005. **280**(44): p. 36567-74.
182. Witte, K., et al., *Chondrobags: A high throughput alginate-fibronectin micromass platform for in vitro human cartilage formation.* Biofabrication, 2020. **12**(4): p. 045034.
183. Blebea, J.S., et al., *Structural and functional imaging of normal bone marrow and evaluation of its age-related changes.* Semin Nucl Med, 2007. **37**(3): p. 185-94.

184. Unni, K.K., *Osteosarcoma of bone.* Journal of Orthopaedic Science, 1998. **3**(5): p. 287-294.
185. Mohseny, A.B., et al., *Functional characterization of osteosarcoma cell lines provides representative models to study the human disease.* Lab Invest, 2011. **91**(8): p. 1195-205.
186. Golfier, F.o., et al., *Fetal bone marrow as a source of stem cells for in utero or postnatal transplantation.* British Journal of Haematology, 2000. **109**(1): p. 173-181.
187. Wurtz, T., et al., *Collagen mRNA expression during tissue development: the temporospacial order coordinates bone morphogenesis with collagen fiber formation.* Matrix Biol, 1998. **17**(5): p. 349-60.
188. Tontonoz, P. and B.M. Spiegelman, *Fat and beyond: the diverse biology of PPARgamma.* Annu Rev Biochem, 2008. **77**: p. 289-312.
189. Benya, P.D. and J.D. Shaffer, *Dedifferentiated chondrocytes reexpress the differentiated collagen phenotype when cultured in agarose gels.* Cell, 1982. **30**(1): p. 215-24.
190. Bi, W., et al., *Sox9 is required for cartilage formation.* Nat Genet, 1999. **22**(1): p. 85-9.
191. Lian, C., et al., *Collagen type II suppresses articular chondrocyte hypertrophy and osteoarthritis progression by promoting integrin beta1-SMAD1 interaction.* Bone Res, 2019. **7**: p. 8.
192. Kiani, C., et al., *Structure and function of aggrecan.* Cell Research, 2002. **12**(1): p. 19-32.
193. Kleinerman, E.S., et al., *Phase II study of liposomal muramyl tripeptide in osteosarcoma: the cytokine cascade and monocyte activation following administration.* J Clin Oncol, 1992. **10**(8): p. 1310-6.
194. Kleinerman, E.S., et al., *Activation of tumoricidal properties in monocytes from cancer patients following intravenous administration of liposomes containing muramyl tripeptide phosphatidylethanolamine.* Cancer Res, 1989. **49**(16): p. 4665-70.
195. Punzo, F., et al., *Mifamurtide and TAM-like macrophages: effect on proliferation, migration and differentiation of osteosarcoma cells.* Oncotarget, 2020. **11**(7): p. 687-698.
196. Zernik, J., K. Twarog, and W.B. Upholt, *Regulation of alkaline phosphatase and alpha 2(I) procollagen synthesis during early intramembranous bone formation in the rat mandible.* Differentiation, 1990. **44**(3): p. 207-15.
197. Yu, S., et al., *Lung cells support osteosarcoma cell migration and survival.* BMC cancer, 2017. **17**(1): p. 78-78.
198. Pautke, C., et al., *Characterization of osteosarcoma cell lines MG-63, Saos-2 and U-2 OS in comparison to human osteoblasts.* Anticancer Res, 2004. **24**(6): p. 3743-8.
199. Gu, R. and Y. Sun, *Does serum alkaline phosphatase level really indicate the prognosis in patients with osteosarcoma? A meta-analysis.* Journal of Cancer Research and Therapeutics, 2018. **14**(9): p. 468-472.
200. Kim, S.H., et al., *Reassessment of alkaline phosphatase as serum tumor marker with high specificity in osteosarcoma.* Cancer medicine, 2017. **6**(6): p. 1311-1322.
201. Gurevitch, O., S. Slavin, and A.G. Feldman, *Conversion of red bone marrow into yellow - Cause and mechanisms.* Med Hypotheses, 2007. **69**(3): p. 531-6.
202. Golub, E.E. and K. Boesze-Battaglia, *The role of alkaline phosphatase in mineralization.* Current Opinion in Orthopaedics, 2007. **18**(5): p. 444-448.
203. Hancke, K., et al., *Adipocyte fatty acid-binding protein as a novel prognostic factor in obese breast cancer patients.* Breast Cancer Res Treat, 2010. **119**(2): p. 367-7.
204. Jukkola, A., et al., *Procollagen synthesis and extracellular matrix deposition in MG-63 osteosarcoma cells.* J Bone Miner Res, 1993. **8**(6): p. 651-7.
205. Al Hasan, M., et al., *Type III Collagen is Required for Adipogenesis and Actin Stress Fibre Formation in 3T3-L1 Preadipocytes.* Biomolecules, 2021. **11**(2).
206. Kaur, G. and J.M. Dufour, *Cell lines: Valuable tools or useless artifacts.* Spermatogenesis, 2012. **2**(1): p. 1-5.
207. Sinha, K.M. and X. Zhou, *Genetic and molecular control of osterix in skeletal formation.* Journal of cellular biochemistry, 2013. **114**(5): p. 975-984.
208. de Azambuja, E., et al., *Ki-67 as prognostic marker in early breast cancer: a meta-analysis of published studies involving 12,155 patients.* British journal of cancer, 2007. **96**(10): p. 1504-1513.

209. Liu, H., et al., *Hypoxic preconditioning advances CXCR4 and CXCR7 expression by activating HIF-1α in MSCs.* Biochemical and Biophysical Research Communications, 2010. **401**(4): p. 509-515.
210. Cimmino, F., et al., *HIF-1 transcription activity: HIF1A driven response in normoxia and in hypoxia.* BMC Medical Genetics, 2019. **20**(1): p. 37.
211. Yoon, D.S., et al., *Interleukin-6 induces the lineage commitment of bone marrow-derived mesenchymal multipotent cells through down-regulation of Sox2 by osteogenic transcription factors.* The FASEB Journal, 2014. **28**(7): p. 3273-3286.
212. Dumars, C., et al., *Dysregulation of macrophage polarization is associated with the metastatic process in osteosarcoma.* Oncotarget, 2016. **7**(48): p. 78343-78354.
213. Sudhakaran, P.R., A. Radhika, and S.S. Jacob, *Monocyte macrophage differentiation in vitro: Fibronectin-dependent upregulation of certain macrophage-specific activities.* Glycoconjugate Journal, 2007. **24**(1): p. 49-55.
214. Vogel, D.Y., et al., *Human macrophage polarization in vitro: maturation and activation methods compared.* Immunobiology, 2014. **219**(9): p. 695-703.
215. Wang, Z., et al., *Polarization behavior of bone marrow-derived macrophages on charged P(VDF-TrFE) coatings.* Biomater Sci, 2021. **9**(3): p. 874-881.
216. Muñoz-Rojas, A.R., et al., *Co-stimulation with opposing macrophage polarization cues leads to orthogonal secretion programs in individual cells.* Nature Communications, 2021. **12**(1): p. 301.
217. Sayed, I.M., et al., *Replication of Hepatitis E Virus (HEV) in Primary Human-Derived Monocytes and Macrophages In Vitro.* Vaccines (Basel), 2020. **8**(2).
218. Abdallah, D., et al., *An Optimized Method to Generate Human Active Osteoclasts From Peripheral Blood Monocytes.* Frontiers in immunology, 2018. **9**: p. 632-632.
219. Cody, J.J., et al., *A simplified method for the generation of human osteoclasts in vitro.* International journal of biochemistry and molecular biology, 2011. **2**(2): p. 183-189.
220. Takahashi, N., et al., *Osteoclast-like cells form in long-term human bone marrow but not in peripheral blood cultures.* J Clin Invest, 1989. **83**(2): p. 543-50.
221. Kylmäoja, E., et al., *Peripheral blood monocytes show increased osteoclast differentiation potential compared to bone marrow monocytes.* Heliyon, 2018. **4**(9): p. e00780.
222. Crocker, P.R. and S. Gordon, *Isolation and characterization of resident stromal macrophages and hematopoietic cell clusters from mouse bone marrow.* J Exp Med, 1985. **162**(3): p. 993-1014.
223. Bühring, H.J., et al., *Novel markers for the prospective isolation of human MSC.* Ann N Y Acad Sci, 2007. **1106**: p. 262-71.
224. Ferrante, C.J. and S.J. Leibovich, *Regulation of Macrophage Polarization and Wound Healing.* Adv Wound Care (New Rochelle), 2012. **1**(1): p. 10-16.
225. Bondeson, J., et al., *The role of synovial macrophages and macrophage-produced cytokines in driving aggrecanases, matrix metalloproteinases, and other destructive and inflammatory responses in osteoarthritis.* Arthritis Res Ther, 2006. **8**(6): p. R187.
226. Champagne, C.M., et al., *Macrophage cell lines produce osteoinductive signals that include bone morphogenetic protein-2.* Bone, 2002. **30**(1): p. 26-31.
227. Nakagawa, H., et al., *Influence of monocyte-macrophage lineage cells on alkaline phosphatase activity of developing osteoblasts derived from rat bone marrow stromal cells.* Nihon Seikeigeka Gakkai Zasshi, 1993. **67**(5): p. 480-9.
228. Muñoz, J., et al., *Macrophage Polarization and Osteoporosis: A Review.* Nutrients, 2020. **12**(10).
229. Chamberlain, L.M., et al., *Extended culture of macrophages from different sources and maturation results in a common M2 phenotype.* Journal of biomedical materials research. Part A, 2015. **103**(9): p. 2864-2874.
230. Tarique, A.A., et al., *Phenotypic, Functional, and Plasticity Features of Classical and Alternatively Activated Human Macrophages.* American Journal of Respiratory Cell and Molecular Biology, 2015. **53**(5): p. 676-688.

231. Amici, S.A., et al., *CD38 Is Robustly Induced in Human Macrophages and Monocytes in Inflammatory Conditions.* Frontiers in Immunology, 2018. **9**(1593).
232. Zirlik, A., et al., *CD40 Ligand Mediates Inflammation Independently of CD40 by Interaction With Mac-1.* Circulation, 2007. **115**(12): p. 1571-1580.
233. Schmid, M.C., et al., *Integrin CD11b activation drives anti-tumor innate immunity.* Nature communications, 2018. **9**(1): p. 5379-5379.
234. Bar-Shavit, Z., *The osteoclast: a multinucleated, hematopoietic-origin, bone-resorbing osteoimmune cell.* J Cell Biochem, 2007. **102**(5): p. 1130-9.
235. Teitelbaum, S.L., *Osteoclasts: what do they do and how do they do it?* The American journal of pathology, 2007. **170**(2): p. 427-435.
236. Kundu, Z.S., *Classification, imaging, biopsy and staging of osteosarcoma.* Indian journal of orthopaedics, 2014. **48**(3): p. 238-246.
237. Gasser, J.A., et al., *Noninvasive monitoring of changes in structural cancellous bone parameters with a novel prototype micro-CT.* J Bone Miner Metab, 2005. **23 Suppl**: p. 90-6.
238. van Lenthe, G.H., et al., *Nondestructive micro-computed tomography for biological imaging and quantification of scaffold-bone interaction in vivo.* Biomaterials, 2007. **28**(15): p. 2479-90.
239. Müller, R., T. Hildebrand, and P. Rüegsegger, *Non-invasive bone biopsy: a new method to analyse and display the three-dimensional structure of trabecular bone*. Phys Med Biol, 1994. **39**(1): p. 145-64.
240. Bouxsein, M.L., et al., *Guidelines for assessment of bone microstructure in rodents using micro-computed tomography.* J Bone Miner Res, 2010. **25**(7): p. 1468-86.
241. Hahn, M., et al., *Trabecular bone pattern factor--a new parameter for simple quantification of bone microarchitecture.* Bone, 1992. **13**(4): p. 327-30.
242. Gerrand, C., et al., *UK guidelines for the management of bone sarcomas.* Clinical Sarcoma Research, 2016. **6**(1): p. 7.
243. Lamoureux, F., et al., *Therapeutic relevance of osteoprotegerin gene therapy in osteosarcoma: blockade of the vicious cycle between tumor cell proliferation and bone resorption.* Cancer Res, 2007. **67**(15): p. 7308-18.
244. Ohba, T., et al., *Bisphosphonates inhibit osteosarcoma-mediated osteolysis via attenuation of tumor expression of MCP-1 and RANKL.* J Bone Miner Res, 2014. **29**(6): p. 1431-45.
245. Begum, F., et al., *A novel decalcification method for adult rodent bone for histological analysis of peripheral–central nervous system connections.* Journal of Neuroscience Methods, 2010. **187**(1): p. 59-66.
246. Heck, C.T., G. Volkmann, and H.N. Woodward, *Polyester or epoxy: assessing embedding product efficacy in paleohistological methods.* PeerJ, 2020. **8**: p. e10495.
247. Ruifrok, A.C. and D.A. Johnston, *Quantification of histochemical staining by color deconvolution.* Anal Quant Cytol Histol, 2001. **23**(4): p. 291-9.
248. Tan, W.C.C., et al., *Overview of multiplex immunohistochemistry/immunofluorescence techniques in the era of cancer immunotherapy.* Cancer Commun (Lond), 2020. **40**(4): p. 135-153.
249. Agustina, H., et al., *The Role of Osteocalcin and Alkaline Phosphatase Immunohistochemistry in Osteosarcoma Diagnosis.* Pathology Research International, 2018. **2018**: p. 6346409.
250. Branstetter, D., et al., *RANK and RANK ligand expression in primary human osteosarcoma.* Journal of Bone Oncology, 2015. **4**(3): p. 59-68.
251. Horinaga, M., et al., *Clinical and pathologic significance of activation of signal transducer and activator of transcription 3 in prostate cancer.* Urology, 2005. **66**(3): p. 671-5.
252. Lee, J., et al., *Expression of activated signal transducer and activator of transcription 3 predicts poor clinical outcome in gastric adenocarcinoma.* Apmis, 2009. **117**(8): p. 598-606.
253. Minhajat, R., et al., *Organ-specific endoglin (CD105) expression in the angiogenesis of human cancers.* Pathol Int, 2006. **56**(12): p. 717-23.

254. Yang, X., et al., *VEGF-B promotes cancer metastasis through a VEGF-A–independent mechanism and serves as a marker of poor prognosis for cancer patients.* Proceedings of the National Academy of Sciences, 2015. **112**(22): p. E2900.
255. Zhang, B., et al., *Hypoxia-inducible factor-1 promotes cancer progression through activating AKT/Cyclin D1 signaling pathway in osteosarcoma.* Biomed Pharmacother, 2018. **105**: p. 1-9.
256. Vogel, D.Y., et al., *Macrophages in inflammatory multiple sclerosis lesions have an intermediate activation status.* J Neuroinflammation, 2013. **10**: p. 35.
257. Peng, H., et al., *Increased expression of M1 and M2 phenotypic markers in isolated microglia after four-day binge alcohol exposure in male rats.* Alcohol, 2017. **62**: p. 29-40.
258. Oshi, M., et al., *M1 Macrophage and M1/M2 ratio defined by transcriptomic signatures resemble only part of their conventional clinical characteristics in breast cancer.* Sci Rep, 2020. **10**(1): p. 16554.
259. Harris, J.A., et al., *CD163 versus CD68 in tumor associated macrophages of classical hodgkin lymphoma.* Diagnostic Pathology, 2012. **7**(1): p. 12.
260. Rankin, C.T., et al., *CD32B, the human inhibitory Fc-gamma receptor IIB, as a target for monoclonal antibody therapy of B-cell lymphoma.* Blood, 2006. **108**(7): p. 2384-91.
261. Liu, D.-C., et al., *HIF-1α inhibits IDH-1 expression in osteosarcoma.* Oncol Rep, 2017. **38**(1): p. 336-342.
262. Mark, P., et al., *Human Mesenchymal Stem Cells Display Reduced Expression of CD105 after Culture in Serum-Free Medium.* Stem Cells International, 2013. **2013**: p. 698076.
263. Marioni, G., et al., *CD105 is a marker of tumour vasculature and a potential target for the treatment of head and neck squamous cell carcinoma.* J Oral Pathol Med, 2010. **39**(5): p. 361-7.
264. Boyce, B.F. and L. Xing, *The RANKL/RANK/OPG pathway.* Curr Osteoporos Rep, 2007. **5**(3): p. 98-104.
265. Rigoni, T.S., et al., *RANK Ligand Helps Immunity to Leishmania major by Skewing M2-Like Into M1 Macrophages.* Front Immunol, 2020. **11**: p. 886.
266. Lastres, P., et al., *Regulated expression on human macrophages of endoglin, an Arg-Gly-Asp-containing surface antigen.* Eur J Immunol, 1992. **22**(2): p. 393-7.
267. Postiglione, L., et al., *Differential expression and cytoplasm/membrane distribution of endoglin (CD105) in human tumour cell lines: Implications in the modulation of cell proliferation.* Int J Oncol, 2005. **26**(5): p. 1193-201.
268. Pahl, J.H., et al., *Macrophages inhibit human osteosarcoma cell growth after activation with the bacterial cell wall derivative liposomal muramyl tripeptide in combination with interferon-γ.* J Exp Clin Cancer Res, 2014. **33**(1): p. 27.
269. Asano, T., et al., *Liposomal muramyl tripeptide up-regulates interleukin-1 alpha, interleukin-1 beta, tumor necrosis factor-alpha, interleukin-6 and interleukin-8 gene expression in human monocytes.* J Pharmacol Exp Ther, 1994. **268**(2): p. 1032-9.
270. Chen, Y.C., et al., *Withholding of M-CSF Supplement Reprograms Macrophages to M2-Like via Endogenous CSF-1 Activation.* Int J Mol Sci, 2021. **22**(7).
271. Yang, Y., et al., *Genetically transforming human osteoblasts to sarcoma: development of an osteosarcoma model.* Genes Cancer, 2017. **8**(1-2): p. 484-494.
272. Liu, W., et al., *Tumor-derived vascular endothelial growth factor (VEGF)-a facilitates tumor metastasis through the VEGF-VEGFR1 signaling pathway.* Int J Oncol, 2011. **39**(5): p. 1213-20.
273. Bajpai, J., et al., *VEGF expression as a prognostic marker in osteosarcoma.* Pediatr Blood Cancer, 2009. **53**(6): p. 1035-9.
274. Wang, Y.C., et al., *Clinical value of signal transducers and activators of transcription 3 (STAT3) gene expression in human osteosarcoma.* Acta Histochem, 2011. **113**(4): p. 402-8.
275. Murray, E., et al., *Characterization of a human osteoblastic osteosarcoma cell line (SAOS-2) with high bone alkaline phosphatase activity.* J Bone Miner Res, 1987. **2**(3): p. 231-8.
276. Jesus-Garcia, R., et al., *Epiphyseal plate involvement in osteosarcoma.* Clin Orthop Relat Res, 2000(373): p. 32-8.

277. Sharif, O., et al., *Transcriptional profiling of the LPS induced NF-kappaB response in macrophages.* BMC Immunol, 2007. **8**: p. 1.
278. Wang, C., et al., *Characterization of murine macrophages from bone marrow, spleen and peritoneum.* BMC Immunology, 2012. **14**: p. 6 - 6.
279. Kempen, D.H., et al., *Effect of local sequential VEGF and BMP-2 delivery on ectopic and orthotopic bone regeneration.* Biomaterials, 2009. **30**(14): p. 2816-25.
280. Lienemann, P.S., et al., *Longitudinal in vivo evaluation of bone regeneration by combined measurement of multi-pinhole SPECT and micro-CT for tissue engineering.* Sci Rep, 2015. **5**: p. 10238.
281. Kanczler, J.M., et al., *A novel approach for studying the temporal modulation of embryonic skeletal development using organotypic bone cultures and microcomputed tomography.* Tissue Eng Part C Methods, 2012. **18**(10): p. 747-60.
282. Khan, S.N., et al., *The biology of bone grafting.* J Am Acad Orthop Surg, 2005. **13**(1): p. 77-86.
283. Andreev, D., et al., *Osteocyte necrosis triggers osteoclast-mediated bone loss through macrophage-inducible C-type lectin.* J Clin Invest, 2020. **130**(9): p. 4811-4830.
284. Hamm, A., et al., *Efficient transfection method for primary cells.* Tissue Eng, 2002. **8**(2): p. 235-45.
285. Jordan, E.T., et al., *Optimizing electroporation conditions in primary and other difficult-to-transfect cells.* J Biomol Tech, 2008. **19**(5): p. 328-34.
286. Kunzi-Rapp, K., A. Rück, and R. Kaufmann, *Characterization of the chick chorioallantoic membrane model as a short-term in vivo system for human skin.* Arch Dermatol Res, 1999. **291**(5): p. 290-5.
287. Carre, A.L., et al., *Fetal mouse skin heals scarlessly in a chick chorioallantoic membrane model system.* Ann Plast Surg, 2012. **69**(1): p. 85-90.
288. Friend, J.V., et al., *Immaturity of the inflammatory response of the chick chorioallantoic membrane.* Toxicol In Vitro, 1990. **4**(4-5): p. 324-6.
289. Klingenberg, M., et al., *The chick chorioallantoic membrane as an in vivo xenograft model for Burkitt lymphoma.* BMC Cancer, 2014. **14**: p. 339.
290. Chapman, S.C., et al., *Ubiquitous GFP expression in transgenic chickens using a lentiviral vector.* Development, 2005. **132**(5): p. 935-40.